UNIVERSITY OF CALIFORNIA

Los Angeles

Real-time Laser Absorption Spectroscopy

for Polyfuel Combustion Engines

A dissertation submitted in partial satisfaction

of the requirements for the degree

Doctor of Philosophy in Mechanical Engineering

by

Kevin Keegan Schwarm

2023

ABSTRACT OF THE DISSERTATION

Real-time Laser Absorption Spectroscopy

for Polyfuel Combustion Engines

by

Kevin Keegan Schwarm

Doctor of Philosophy in Mechanical Engineering

University of California, Los Angeles, 2023

Professor Raymond M. Spearrin, Chair

This dissertation details the development and application of mid-infrared laser absorption spectroscopy sensing methods towards advancing low-carbon reciprocating engines for high-efficiency and low-emission power generation in a decarbonized energy sector. The scope of this work includes advancement in methods for fundamental spectroscopic studies, integration of advanced sensors into production reciprocating engines for characterization of combustion of low-carbon fuel blends, and computational methods advancement for high-speed real-time signal processing. A high-temperature, high-pressure optical gas cell is designed to enable controlled studies of molecular absorption spectra at high temperatures (>1200 K) and high pressures (>200 atm) to validate spectroscopic parameters at the elevated conditions in combustion engines. A novel optical approach provides access to the mid-wave infrared wherein lies the fundamental rovibrational absorption bands of combustion species critical to characterization of combustion process and emissions formation. Laser absorption sensors are developed and utilized for experimental measurements in the exhaust of a production Honda single-cylinder spark-ignition engine through design of an in-line ex-

haust sensor module to gain optical access to exhaust gases close-coupled to the exhaust valve. High-temperature opto-mechanical design and laser fiber-coupling assist in achieving robust measurements of cycle-resolved temperature and species (CO and NO) concentration at a rate of 10 kHz. The exhaust sensor is demonstrated by capturing cycle-to-cycle and intra-cycle emissions dynamics and characterizing emissions response to low-carbon fuel blends incorporating natural gas, hydrogen, and ammonia. To enable real-time measurement output at 10 kHz, computational time of the sensor data processing is reduced to sub-ms scales through the use of machine learning algorithms on an embedded processing platform. Compact neural network and ridge regression models are developed to calculate species concentration and temperature directly from transmitted laser signals, removing the need for computationally-intensive nonlinear fitting methods. The machine learning algorithms are deployed to a field-programmable gate array (FPGA) for further acceleration. Hardware-in-the-loop demonstration yields computational time and latency below 100 μs to expand use of the 10 kHz exhaust sensor for real-time sensing applications. Complementary to the sensor development work, a time-resolved chemical-kinetic model is constructed within Cantera to evaluate reciprocating engine performance and emissions during fueling with low- and non-carbon blends. The simulation model provides insights into strategies for optimization of low-carbon combustion and serves as a foundation for sensor interpretation and future work in engine optimization. Discussion of ongoing work includes the design and development of an electro-hydraulic camless valvetrain for future integration into a reciprocating engine architecture to enhance adaptability for fuel-flexible operation.

The dissertation of Kevin Keegan Schwarm is approved.

Brett T. Lopez

Tsu-Chin Tsao

Timothy S. Fisher

Raymond M. Spearrin, Committee Chair

University of California, Los Angeles

2023

TABLE OF CONTENTS

LIST OF FIGURES

LIST OF TABLES

ACKNOWLEDGMENTS

Gordillo has the answers, the candy, and the wildest stories to keep my days moving smoothly with a smile on my face. The work presented in this dissertation would never have started if not for the financial support of Southern California Edison as well as Tim and Karen Strelitz, for that I am truly grateful. Additionally, I would like to thank the National Defense Science and Engineering Graduate (NDSEG) Fellowship for the support that allowed me to pursue the research paths that interested me most.

Now, for all my peers in the Laser Spectroscopy and Gas Dynamics Laboratory, you have all made these some of the most memorable years of my life. Daniel Lee, you were my first mentor and your willingness to teach me with patience and a smile is something I aspire to every day. Chuyu Wei, as one of the smartest people I know and with a razor-sharp wit, working alongside you always has me smiling. Daniel Pineda, your mentorship during my grad school beginnings helped me in innumerable ways, and our regular trips to Sepi's helped carried me through the difficult times. Christopher Jelloian, your curiosity and ability to stay positive despite any experimental setback is infectious and always refreshing to be around. China Hagström, always a source of laughs and some of the most engaging conversational breaks from work, you're a joy to have around and I can't wait to see where youre time at MIT will take you. Anil Nair, your intelligence and drive is admirable and humbling, and our interludes huddled around the whiteboard in the lab were some of my most mentally stimulating moments. Alex Keller, your enthusiasm for your research as well as all areas of your life is a welcome presence that helps keep me balanced and living in the moment. Nick Kuenning, no matter the project I want you on my team because you keep the workdays hilarious in all the ways I didn't know I needed while also acting as my go-to person for all random issues and thought experiments. Barathan Jeevaretanam, I admire your stoic work ethic and appreciate all of our shared research efforts, but even more I appreciate your ability to get me laughing several times a day in the way only you know how. Sarah Enayati, I appreciate all of your hard work, dedication, and enthusiasm in research as well as our occasional chess matches. Ariya Olaee, always lively and one of

the most thoughtful and considerate people I know, I'm looking forward to all of our future adventures together. Griffin Houston, you're similarly lively in the most surprising ways that I'm glad I'll continue to have around during our collaborations through JPL. Yi Yan, I wish I had more time working with you, I greatly enjoyed your curiosity, hard work, and humor that you brought to the lab. Miles Richmond, I am grateful for all of your contributions to our engine research together and stoked to see you living your best life in the mountains, I will see you out there soon. Nicolas Minesi, a.k.a. Minou, your joyous dance through life is infectious and I'll do my best to carry your energy through my own time as a postdoc. Isabelle Sanders, I respect your skill and integrity as a researcher as well as your selflessness and thoughtfulness with your colleagues. You've been a dear friend both inside and outside of the lab and I'm excited for you to join me at JPL so we can continue our many shenanigans.

Fabio Bendana, David Morrow, and Travis Fujimoto, I didn't expect to form some of my deepest friendships at an engineering lab across the country but that's just what happened. Fabio, the frat boy turned scientist, I have the highest respect for your professional work and spending time joking around with you makes me feel like a child again. David, I can be discussing heartfelt issues with you one minute and wrestling outside with you the next. I miss having you around LA but I'm excited for the next time we meet and catch up on memes. Travis, you're a true friend and I value your exemplary effort to spend time with and support those close to you. I'm stoked for some camping trips with your new Tacoma. Kaelly Arellano, Sydney Lavery, and Helen Kim, thank you for keeping watch over these silly guys when they clearly can't do it themselves. I'm grateful they brought you all into my life, you're some of my closest friends and I'm looking forward to all of our upcoming travels together.

Outside of UCLA, I have been blessed with a support system that has kept me balanced and enjoying life outside of the long hours and late nights of grad school. Zak Fisher, Lucas Avidan, Christine Swartwout, you provided a warm home life and support through many ups and downs, making me feel at home in Los Angeles. Alastair Crowe and Jason Feldkamp, you

have carried the torch and I'm grateful to have you around me during some of the toughest months of my Ph.D. experience. Sydney Wilke and Alana Murray, our regular adventures and late night chats bring me to life and I cherish all of our moments together.

I also want to thank the educators that supported my path to graduate school. Scott Webber, it was in your class that I first came up with the crazy idea to pursue a Ph.D. I'm grateful for your enthusiasm and encouragement that set me on this path. Christopher Mazzurco, as both my coach and advisor you taught me how to channel my strengths, overcome my obstacles, and pursue excellence with no excuses. Without your influence I would not have made it to where I am today. Professor Michael Swain, through your mentorship I found excitement and satisfaction in the area of internal combustion engine research which I have continued to carry with me through my professional and personal life. Professor Ines Basalo, as my undergraduate advisor you gave me the encouragement to reach my potential as an engineer and the confidence to challenge myself through the pursuit of a Ph.D.

Most of all I want to thank my family. To my brother Eric Schwarm, we may have had our many fights in the back yard hitting each other with sticks and similar brotherly activities, but I have always been grateful to have you around as a friend and someone to look up to. I've been happy to share so much together, including both of us completing our Ph.D. in Mechanical Engineering in the same year (but yes, you beat me). Congrats Dr. Schwarm. To my mom, Maureen Keegan, and my dad, Tom Schwarm, you have been there behind me providing support every step of the way. From childhood through today, you have always supported me not just in my academics, but also whatever weird extracurriculars and tangents my life has taken. You have given me every opportunity to succeed and find happiness in my life. Through all the good times and the difficult ones, I have never doubted that you only want what's best for me and will continue to love and support me no matter what I choose to do with my life. I love you both very much, I'm proud to be your son, and I'm honored to have made you proud as well.

2017-Present **Ph.D. in Mechanical Engineering**

University of California, Los Angeles (UCLA)

2017-2020 **M.S. in Mechanical Engineering**

University of California, Los Angeles (UCLA)

2012-2016 **B.S. in Mechanical Engineering**

University of Miami

PEER-REVIEWED PUBLICATIONS

[1] **Schwarm, K.K.**, Spearrin, R.M. (2023). Real-time FPGA-based laser absorption spectroscopy using on-chip machine learning for 10 kHz intra-cycle emissions sensing towards adaptive reciprocating engines. Applications in Energy and Combustion Science. https://doi.org/10.1016/j.jaecs.2023.100231

[2] Wei, C., **Schwarm, K.K.**, Pineda, D.I., Spearrin, R.M. (2023). Quantitative volumetric laser absorption imaging of methane and temperature in flames utilizing line-mixing effects. Proceedings of the Combustion Institute.
https://doi.org/10.1016/j.proci.2022.07.092

[3] **Schwarm, K.K.**, Minesi, N.Q., Jeevaretanam, B., Enayati, S., Tsao, T.C., Spearrin, R.M. (2022). Cycle-resolved emissions analysis of polyfuel reciprocating engines via in-situ laser absorption spectroscopy. Proceedings of the ASME 2022 ICE Forward Conference. https://doi.org/10.1115/ICEF2022-88543

[4] Wei, C., **Schwarm, K.K.**, Pineda, D.I., Spearrin, R.M. (2021). Physics-trained neural network for sparse-view volumetric laser absorption imaging of species and temperature in reacting flows. Optics Express. https://doi.org/10.1364/OE.427730

[5] Li, J., **Schwarm, K.K.**, Wei, C., Spearrin, R.M. (2021). Robust cepstral analysis at variable wavelength scan depth for narrowband tunable laser absorption spectroscopy. Measurement Science and Technology. https://doi.org/10.1088/1361-6501/abcd6a

[6] Wei, C., **Schwarm, K.K.**, Pineda, D.I., Spearrin, R.M. (2021). Volumetric laser absorption imaging of temperature, CO and CO_2 in laminar flames using 3D masked Tikhonov regularization. Combustion and Flame. https://doi.org/10.1016/j.combustflame.2020.10.031

[7] Li, J., Nair, A.P., **Schwarm, K.K.**, Pineda, D.I., Spearrin, R.M. (2020). Temperature-dependent line mixing in the R-branch of the ν_3 band of methane. Journal of Quantitative Spectroscopy and Radiative Transfer. https://doi.org/10.1016/j.jqsrt.2020.107271

[8] Wei, C., **Schwarm, K.K.**, Pineda, D.I., Spearrin, R.M. (2020). Deep neural network inversion for 3D laser absorption imaging of methane in reacting flows. Optics Letters. https://doi.org/10.1364/OL.391834

[9] **Schwarm, K.K.**, Strand, C.L., Miller, V.A., Spearrin, R.M. (2020). Calibration-free breath acetone sensor with interference correction based on wavelength modulation spectroscopy near 8.2 μm. Applied Physics B. https://doi.org/10.1007/s00340-019-7358-x

[10] Pineda, D.I., Bendana, F.B., **Schwarm, K.K.**, Spearrin, R.M. (2019). Multi-isotopologue laser absorption spectroscopy of carbon monoxide for high-temperature chemical kinetic studies of fuel mixtures. Combustion and Flame. https://doi.org/10.1016/j.combustflame.2019.05.030

[11] **Schwarm, K.K.**, Wei, C., Pineda, D.I., Spearrin, R.M. (2019). Time-resolved laser absorption imaging of ethane at 2 kHz in unsteady partially premixed flames. Applied Optics. https://doi.org/10.1364/AO.58.005656

[12] **Schwarm, K.K.**, Dinh, H.Q., Goldenstein, C.S., Pineda, D.I., Spearrin, R.M. (2019). High-pressure and high-temperature gas cell for absorption spectroscopy studies at wavelengths up to 8 μm. Journal of Quantitative Spectroscopy and Radiative Transfer. https://doi.org/10.1016/j.jqsrt.2019.01.029

CHAPTER 1

Introduction

1.1 Motivation for on-demand distributed power generation

Global efforts to mitigate climate change and airborne pollution have led to increased use of renewable energy production methods to replace carbon-based fuel sources. Power generation through hydrocarbon fuel combustion generates pollutant emissions including carbon dioxide, carbon monoxide, unburned hydrocarbons, and oxides of nitrogen. These pollutants negatively impact air quality and human safety as well as increase the rate of climate change through the greenhouse effect. In 2015, the United Nations put forth an updated Paris Agreement [23] that established a target of limiting the increase in global temperature to 1.5 degrees Celsius above pre-industrial levels. The proposed strategy includes reducing emissions by 45% by 2030 and reaching net-zero emissions by 2050 through comprehensive action that necessitates innovation in the energy sector which is responsible for the largest share of global greenhouse gas emissions at 34%, 71% of which comes from power plants that generate heat and electricity [24]. Decarbonization of the energy sector will rely heavily on renewable energy sources including solar photovoltaics, hydro-electric turbines, and wind turbines which convert non-hydrocarbon forms of energy into usable electricity to supply the energy grid without the emissions generated in hydrocarbon combustion. Figure 1.1 highlights electricity production as the most significant application for renewables both in magnitude and year-over-year growth. Widespread use of renewables for electricity generation is enabled by large-scale infrastructure including solar panel plants, hydroelectric dams, and wind farms that can supply large amounts of energy to the centralized electrical grid.

This sector of renewable energy infrastructure has seen rapid expansion over the past few decades. Figure 1.2 illustrates the worldwide yearly growth in renewable electricity generation since 2017. Solar and wind methods have seen the largest investment, responsible for around 85% of net growth in capacity in 2022 with forecasts of increasing market share into 2024 [2].
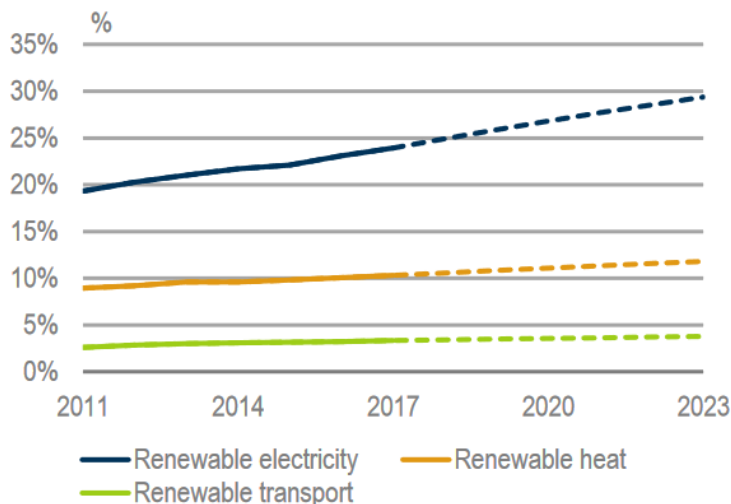
Figure 1.1: Share of renewable energy sources by sector from 2011-2017 with projections to 2023. From the International Energy Agency (IEA) 2018 market report [1].

These dominant renewable sources leverage the energy carried by naturally-occurring solar radiation and wind patterns and produce no emissions during operation unlike chemical energy conversion in fossil-fuel combustion systems. As a consequence, the energy production of solar and wind power plants is dependent on the natural cyclic variation of these sources. Timescales of variation in renewable fuel availability span from several months across seasonal changes to hours and days due to localized weather patterns and the Earth's 24-hour diurnal cycle. This inconsistency in power generation can have drastic impact on energy security across infrastructures built on the foundation of steady energy supplied by fossil fuel power plants. In their 2022 World Energy Outlook [3], the International Energy Agency (IEA) predicts that the increase in cyclic renewables will greatly increase the requirements for hourly load flexibility of power generation infrastructure. Figure 1.3 illustrates this effect,
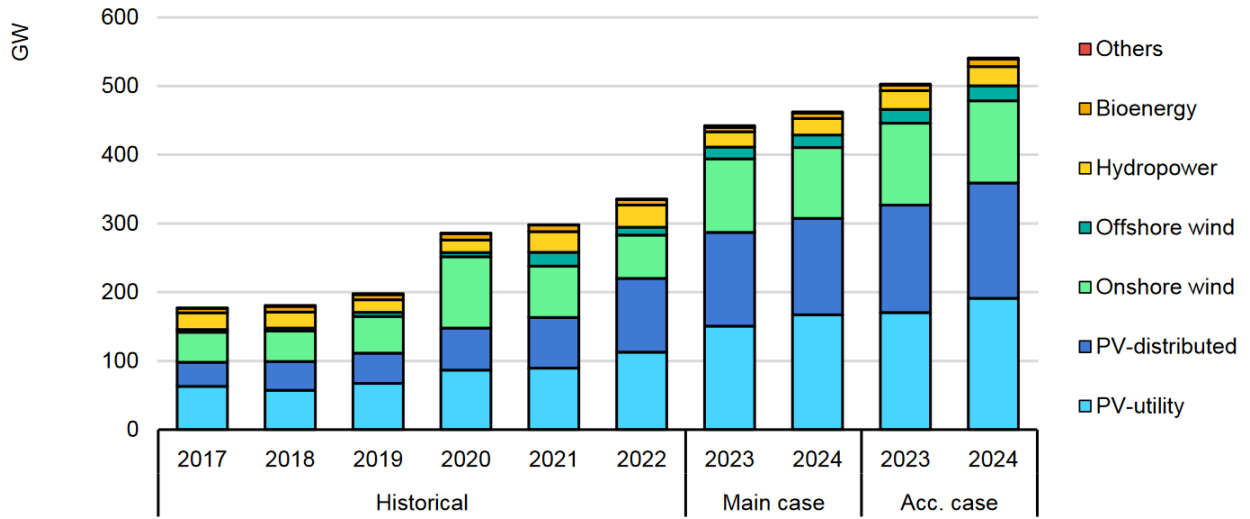
Figure 1.2: Worldwide net additions to renewable electricity generation capacity by source. From the International Energy Agency (IEA) 2023 market report [2].

showing fluctuations in net grid load after removing wind and solar output. Hour-by-hour variability in the United States extended up to 25% in 2021, with predicted increases up to 50% by 2030 if emissions targets are met through continued rewnewable energy expansion.
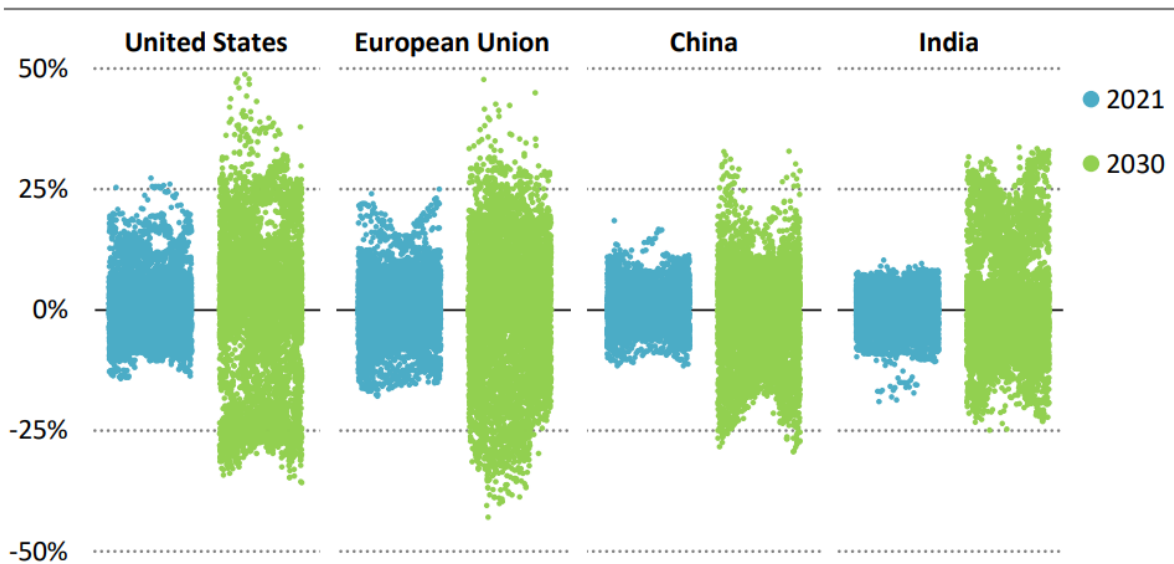
Figure 1.3: Region-specific hour-to-hour fluctuations in net electrical energy demand after subtracting wind and solar output. 2030 predictions based on successful limitation of emissions based on current regional and national pledges [3].

3

California represents a valuable case study for increased dependence on wind and solar energy for electricity generation. In 2022, 49% of California's in-state electricity generation came from renewable sources, with 27% of the total net electricity generation from solar [25]. Solar plant electricity output is constrained to daylight hours, and the increasing dependence on solar energy has exposed an imbalance between the resulting hourly electricity generation and grid demand. The daily trend has become known as the "duck curve" and is illustrated in Fig. 1.4 which displays net load on the electrical grid after subtracting renewable generation. Increasing solar plant infrastructure has expanded electricity production to meet the majority of demand between the hours of 8 am and 6 pm, however has done little to address evening and night time demand. Increasing solar production has aided in reducing mid-day net load by over 75% from 2015-2023, whereas peak load at 8 pm has only lowered by 25% over the same period. This has contributed to continued dependence on fossil fuel power plants for daily load balancing, notably natural gas-fired plants which contributed 42% of California's net electricity generation in 2022 [25].
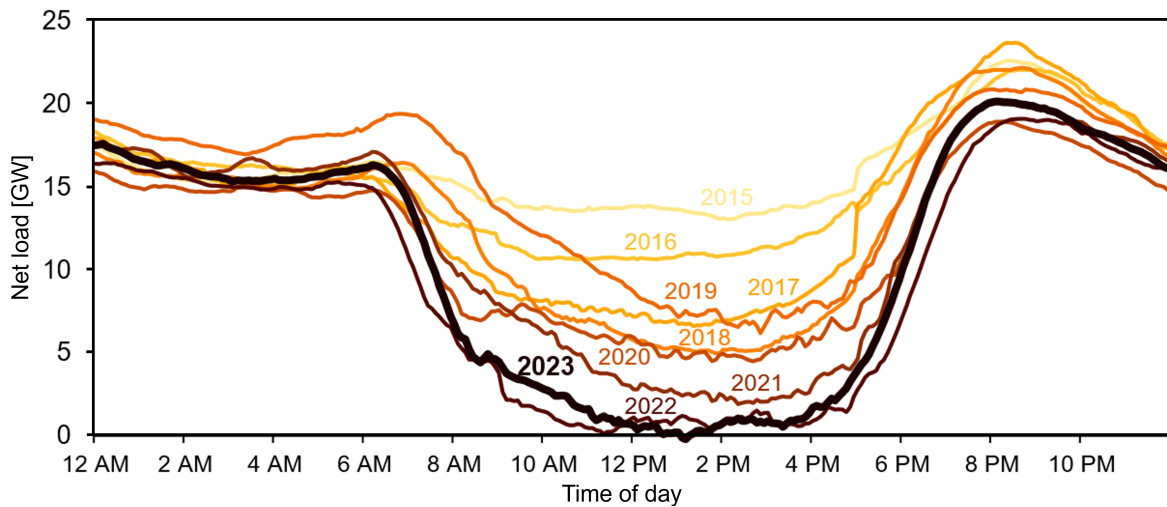
Figure 1.4: Measured net load after subtracting renewable supply for the California electric grid for the lowest-net-load day each spring (March-May) for the years 2015-2023. Adapted from [4] with data from California Independent System Operator (CAISO).

Large-scale renewable power plants coupled to a centralized electric grid provides another barrier to energy security in the face of major weather events that can disrupt electricity

4

transfer. In California, high winds and drought conditions motivate public safety power shutoffs (PSPS) to de-energize electric power lines to reduce the risk of wildfire ignition. From 2018 to 2020, the three major electric utility providers in California executed 54 PSPSs that cut power to about 3 million customers [26]. This is a challenge experienced across all centralized electric grids, with millions of customers affected by blackouts each year in the United States alone. Figure 1.5 illustrates the magnitude of energy insecurity, with on average over 10 million customers losing power every year. Weather events are responsible for the majority of power outages and are largely due to thunderstorms (47%), winter storms (32%), and tropical cyclones (20%) [5]. The types of weather events and electrical grid disruptions along with the affected infrastructure vary greatly by region and inhibit one-size-fits-all solutions to increased grid robustness and energy reliability. Resistance to disruption in the face of extreme weather events is a critical requirement for public safety, as these events necessitate uninterruptible power for time-sensitive services including emergency response and healthcare.
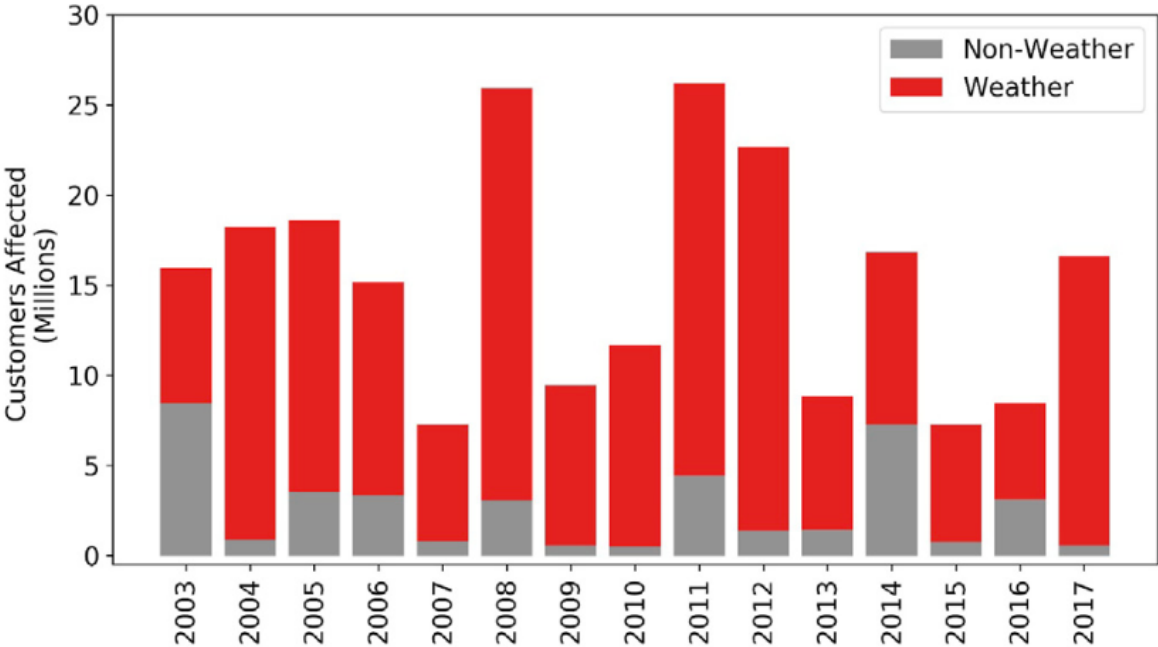
Figure 1.5: Yearly electric utility customers affected by power outages in the United States from 2003 to 2017 [5].

A centralized and decarbonized electrical grid therefore requires complementary energy technologies to improve flexibility and reliability of power generation to balance cyclic renewable energy and provide on-demand power during grid disruptions. The array of proposed solutions include:

- *Energy storage*: When power generation exceeds load demand, excess energy can be stored for later use at off-peak production hours to increase supply consistency. Methods include thermal storage of solar energy in molten salts, battery storage of excess electrical energy, and chemical storage through production of fuels such as hydrogen.

- *Localized electrical grids (microgrids)*: Segmenting large-scale electrical grids into smaller units can reduce impact of localized disruptions early in the energy flow path that supplies large areas and populations [27].

- *Distributed power generation*: Geographically distributing power generation infrastructure increases resilience to variation in centralized energy supply. Incorporating an assortment of complementary power generation methods further improves adaptability and effective load balancing.

- *On-demand standby power*: Power generation systems that can provide energy output at a moment's notice without regard to cyclic variables such as time of day or weather conditions. Rapid start-up and load adaptability help respond effectively to grid disruptions or balance variability in renewable energy output.

These individual methods are highly synergistic and a comprehensive approach leveraging all available technologies will be essential in achieving maximum resilience of decarbonized electrical grids in the future. As such, this requires research and development at all levels with consideration of the greater collaborative network, from wide-scale planning to refinement of individual energy technologies.

1.2 Internal combustion power generation engines
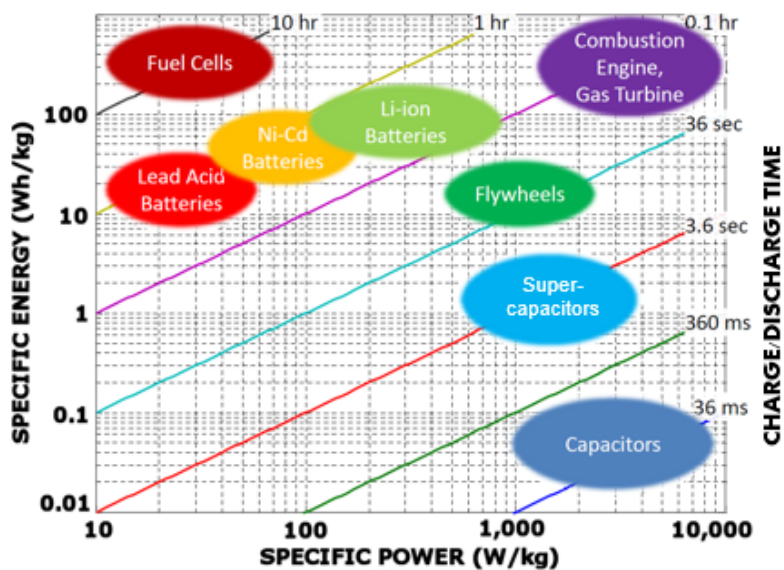
Figure 1.6: Power density and energy density of common energy storage and power generation methods, from [6].

A number of systems have been proposed for distributed, on-demand power generation in a decarbonized energy sector. Among these, fuel cells, electric batteries, and combustion engines have attracted widespread interest [28, 29, 30, 31, 32]. Fuel cells generate electrical energy by flowing fuel such as hydrogen through layers of catalysts and electrodes to generate free electrons. Hydrogen fuel cells are non-carbon systems generating no emissions, and the use of liquid or gaseous fuel aids in producing high specific energy density (see Fig. 1.6). However, low power output limits specific power density and the expensive catalyst materials leads to high system cost. Batteries provide an alternative non-carbon method for convenient direct storage for electrical energy and fast-response output. Advancements in lithium-ion battery capacities and discharge rates have made this a competitive method, with higher specific power density relative to fuel cells. The associated high mass means that the current highest performing lithium-ion batteries are limited in their specific energy density relative to fuel cells. Furthermore, battery systems rely on external power generation methods for

7

charging and so are limited in their independence. Internal combustion (IC) engines have energy density on par with fuel cells with power density surpassing both fuel cells and batteries. IC engines have characteristically faster start-up, increased load variability, and lower operating costs compared to fuel cells. Relative to battery systems, IC engines achieve higher energy and power densities with increased independence thanks to chemical fueling instead of electric charging. These characteristics support the use of IC engines as an effective power generation solution to complement renewable power plants that suffer from cyclic output variability and vulnerability to weather and grid disruptions.

Available IC engines can be grouped into (1) gas turbine engines and (2) reciprocating-piston internal combustion engines. Both systems are widely used in power generation applications, with each approach having its own advantages and drawbacks. For distributed on-demand power generation, reciprocating engines have the advantage of increased flexibility due to modularity in power plant design and load adaptability, and so are the focus for the remainder of this discussion. Reciprocating engines provide fast responsivity to sudden changes in load demand (hence their common utilization in automobiles), and maintain high efficiencies across full- and part-load conditions to effectively balance variation in load demand. The extensive portfolio of reciprocating IC engines can deliver single-engine output from kW levels to over 10 MW [8]. Higher output power plants can be constructed by grouping individual engines while requiring a lower land area than solar or wind power plants. This facilitates use as distributed power generation across a variety of applications including standby power for individual homes or industrial centers and integration into small-or large-scale electric grids to supplement renewable power plants. Critically, IC engines operate on gas or liquid fuels and are capable of delivering full output power at any instance without dependence on time of day or environmental conditions. The adaptability of reciprocating engines extends to fuels, with variable engine designs capable of operating on a wide range of fuels. This has the added benefit of integration with chemical energy storage systems where fuels produced from excess renewable electricity during peak production hours can supply

8

power generation from engines during off-peak hours or during grid disruptions. The major drawback of internal combustion for power generation is the use of conventional hydrocarbon fuels such as gasoline and diesel. Over a century of research and development has made these engines widely available for power generation applications, however the associated exhaust emissions and typical thermal efficiencies below 50% are counteractive to the targets for global emissions reduction. Implementation of reciprocating engines as low-carbon-impact on-demand power systems thus requires integration of low-carbon renewable fuels and efficient combustion to contribute to a more sustainable, decarbonized energy infrastructure.

1.2.1   Background on reciprocating engines
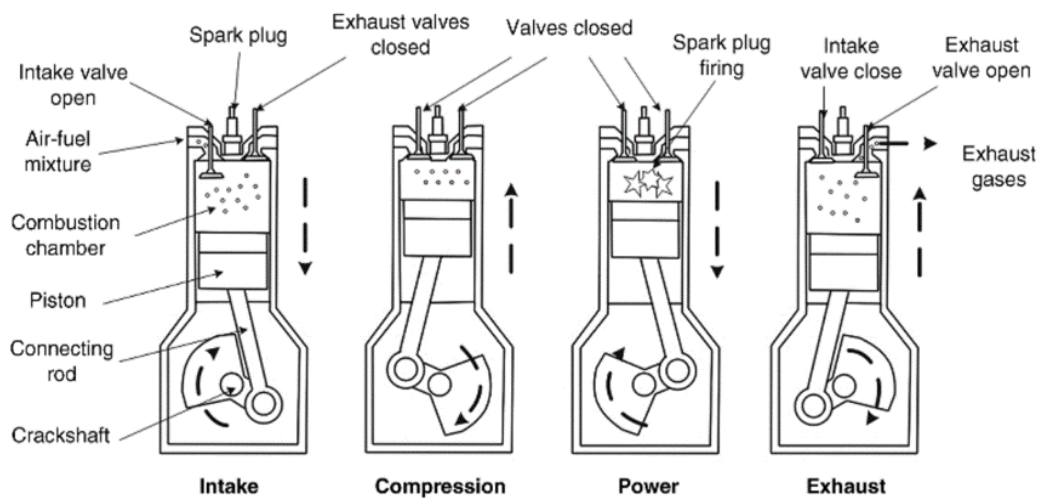
Figure 1.7: Four-stroke Otto cycle engine, from [7].

Internal combustion (IC) engines fundamentally convert chemical energy into useful mechanical energy. This occurs first through the reaction of fuel with oxygen to release heat, and the resulting high-temperature combustion gases are used to produce mechanical power. A reciprocating-piston engine relies on a moving piston to transport the working fluid and extract mechanical power by using high-pressure combustion gases to drive a rotating crankshaft. The majority of these engines operate on a four-stroke cycle shown in Fig 1.7, referring to the four movements of the internal piston comprising a single engine cycle. Four-

stroke engines can be further divided into two cycles, the diesel cycle and the Otto cycle. In the diesel cycle, combustion is initiated by injecting fuel into the high-pressure and high-temperature air within the combustion chamber at the end of the compression stroke which can be approximated as constant-pressure combustion. The Otto cycle relies on a spark to ignite a compressed, premixed fuel-air mixture at the end of the compression stroke and is treated as constant-volume combustion as illustrated in the P-V diagram in Fig 1.8. While the diesel cycle is commonly used in heavy-duty power generation due to some advantages for high cycle efficiencies, the Otto cycle has seen more use when operating on non-carbon fuels and so will be the focus of the remainder of this discussion.

The sequential processes of a four-stroke Otto cycle engine can be summarized as follows:

1. *Intake*: The intake valve opens and the moving piston draws fresh fuel-air mixture into the engine cylinder. A throttle valve in the intake controls intake gas pressure and mass flow of reactants across the intake valve.

2. *Compression*: The intake valve closes and the upward-moving piston compresses the fuel-air mixture inside the engine cylinder to elevated pressure and temperature. Compression is limited by undesirable auto-ignition of reactants prior to the desired ignition timing or during later flame propagation during the expansion stroke.

3. *Power (Expansion)*: At the end of the compression stroke, a spark ignites the compressed fuel-air mixture further increasing gas temperature and pressure within the combustion chamber. The high-pressure gas exerts force on the piston, driving it downward and applying torque to the crankshaft.

4. *Exhaust*: At the end of the expansion stroke, the exhaust valve opens and releases high-pressure combustion gases into the exhaust system. The upward moving piston expels remaining product gases from the cylinder in preparation for the intake stroke of the following cycle.
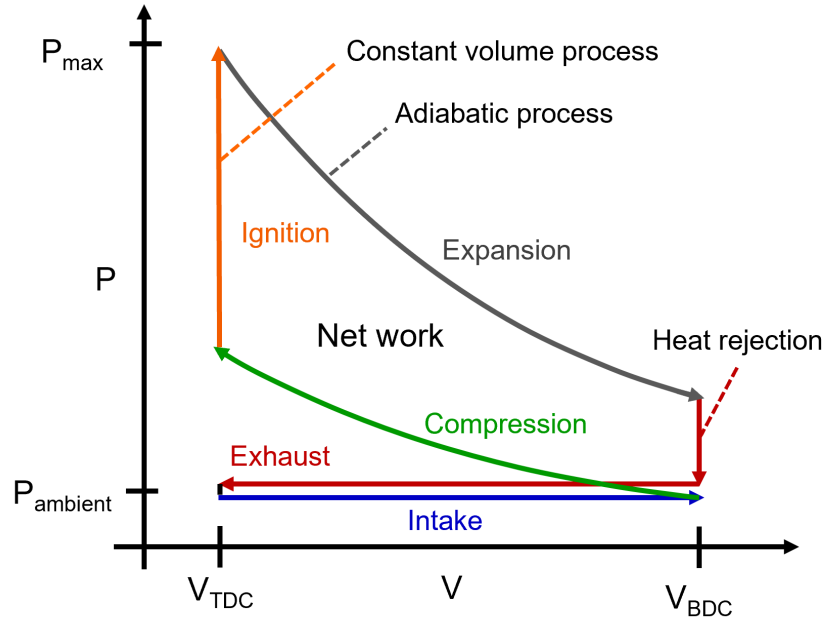
Figure 1.8: P-V diagram of an idealized Otto cycle in a 4-stroke reciprocating piston. TDC: top dead center, BDC: bottom dead center.

Net work in the Otto cycle can be visualized by the area between the power and compression strokes in the P-V diagram in Fig. 1.8, where negative work required by the piston to compress the fuel-air mixture is subtracted from the positive work generated by the high-pressure combustion products driving the piston during the power stroke. Maximum efficiency (and minimum specific emissions as a consequence) of the ideal Otto cycle is primarily a function of compression ratio (r_C) which is the ratio of the maximum internal volume to the minimum internal volume. This relationship is expressed in Eq. 1.1 where γ is the ratio of specific heats for the working gas, and illustrated visually in Fig. 1.9.

$$\eta = 1 - \frac{1}{r_C^{\gamma-1}} \tag{1.1}$$

Achieving high efficiencies and low emissions in four-stroke spark-ignition engines thus requires maximizing the compression ratio through mechanical design of the piston-cylinder geometry. Maximum compression ratio is limited by uncontrolled auto-ignition (i.e., engine

11
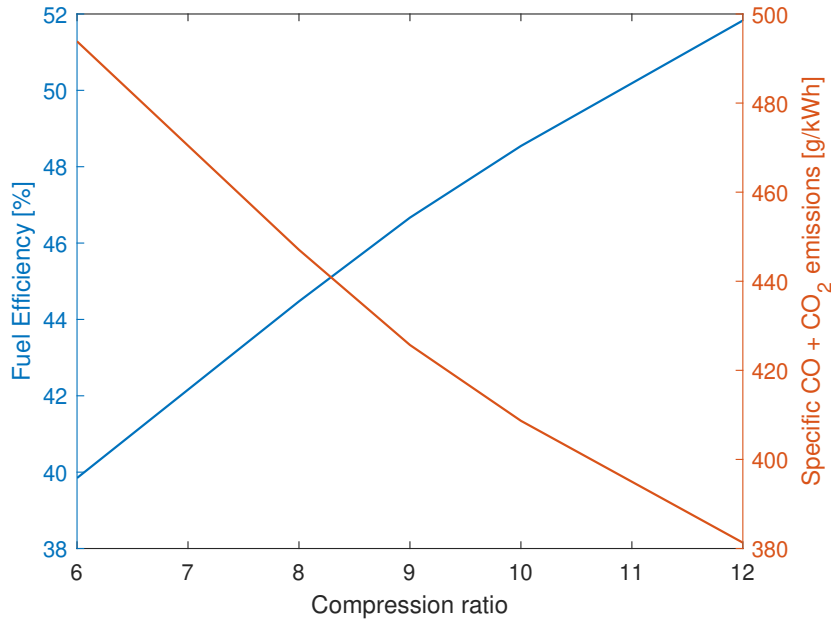
Figure 1.9: Effect of compression ratio on Otto cycle engine fuel conversion efficiency and specific emissions of CO and CO_2, simulated with a chemical kinetic model of a natural gas spark-ignition engine presented in Chapter 2.

knock) which occurs when the temperature of compressed, unburned fuel-air mixture reaches the auto-ignition temperature leading to premature ignition and in the worst cases detonations. Engine knock not only leads to reduction in engine performance due to mistimed ignition, but can also cause catastrophic damage to the engine cylinder and piston. Additional losses can contribute to lower efficiencies for a given compression ratio in Otto cycle engines. Slow combustion due to low deflagration flame speeds deviates from the constant volume assumption and requires ignition well before top dead center. This increases gas pressure and negative work during the compression stroke. Additionally, this lowers peak pressure in the expansion stroke and resulting positive work. Gas temperature and pressure is further reduced throughout the expansion stroke due to heat transfer losses to the engine cylinder and piston. At the end of the expansion stroke, the exhaust valve opens and releases combustion products which are still at elevated temperature and pressure, exhausting waste heat that is not used to apply work on the piston. Additional pumping losses occur in

the exhaust stroke and the expansion stroke, where the piston loses energy while expelling combustion products and drawing in sub-atmospheric pressure gas during the intake stroke. A total efficiency in practical engines factors in these additional losses by relating energy supplied by the fuel input to the useful work generated by the engine through Eq. 1.2, known as the fuel conversion efficiency η_f.

$$\eta_f = \frac{W_c}{m_f Q_{HV}} \tag{1.2}$$

Here, W_c is the generated work per cycle, m_f is the mass of fuel injected per cycle, and Q_{HV} is the heating value of the fuel. The fuel conversion efficiency can be separated into the combustion efficiency η_c and thermal conversion efficiency η_t of the engine, related by Eq. 1.3:

$$\eta_f = \eta_c \eta_t \tag{1.3}$$

Combustion efficiency η_c represents the fraction of energy that is supplied by the fuel that is released during combustion, given by Eq. 1.4 where $H_R(T_A)$ and $H_P(T_A)$ are the enthalpies of the reactants and products at ambient temperature T_A.

$$\eta_c = \frac{H_R(T_A) - H_P(T_A)}{m_f Q_{HV}} \tag{1.4}$$

Thermal conversion efficiency η_t relates the energy released during combustion to the net work generated by the engine, given by Eq. 1.5:

$$\eta_t = \frac{W_c}{H_R(T_A) - H_P(T_A)} \tag{1.5}$$

Increasing overall fuel conversion efficiency therefore requires complete combustion of the fuel along with minimizing thermal losses to generate maximum useful work. These efficien-

cies are influenced by mechanical design of the engine components as well as time-varying inputs during operation. Intake and exhaust port design, combustion chamber geometry, piston design, cylinder shape, and crankshaft dimensions are static factors that influence fluid motion, combustion propagation, and baseline compression ratio. Controllable inputs including intake and exhaust valve timing, intake throttle, fuel injection, and ignition timing which directly dictate fuel-air mixture preparation, combustion phasing, and fluid motion into and out of the cylinder, with valve timing additionally capable of varying the effective compression ratio. Optimization of all engine operation parameters is required to maximize fuel conversion efficiency by promoting complete combustion and maximum conversion of thermal energy into mechanical work.

1.2.2 Low-carbon reciprocating engines

	Fuel	Combustion reaction	Energy density [MJ/kg]	gCO_2/MJ
	Octane	$C_8H_{18} + 12.5\ O_2 \rightarrow 8\ CO_2 + 18\ H_2O$	47.9	64.3
Carbon reduction	Methane	$CH_4 + 2\ O_2 \rightarrow CO_2 + 2\ H_2O$	50	54.9
	Hydrogen	$H_2 + 0.5\ O_2 \rightarrow H_2O$	120	0
	Ammonia	$NH_3 + 0.75\ O_2 \rightarrow 0.5\ N_2 + 1.5\ H_2O$	18.8	0

Table 1.1: Combustion reactions, energy density, and theoretical CO_2 emissions for select fuels in the decarbonization pathway of reciprocating engines. Octane inluded as a surrogate for gasoline, and CO_2 emissions based on complete stoichiometric combustion.

A significant reduction in carbon footprint can be achieved through decarbonization of the fuels used in power generation engines. Select fuels of varying carbon content are listed in Table 1.1 with respective energy density and carbon intensity. Transitioning from liquid fuels (e.g., gasoline and diesel) to gaseous fuels such as natural gas, primarily composed of methane (CH_4), reduces carbon content and subsequent emissions of CO_2 along with particulate matter. While natural gas is a fossil fuel obtained from underground reserves, Figure 1.10 highlights alternative gaseous hydrocarbon fuels that can reduce the lifecycle carbon impact. Waste gases from industrial processes are typically burned off into the

14

atmosphere and generate high emissions without producing useful work. Burning waste gas in power generation engines generates usable electricity without producing additional emissions compared typical flaming. Renewable fuel gases including biogas can generate net-zero emissions when fueling power generation engines. Further decarbonization and elimination of CO_2 emissions can be achieved by implementing non-carbon fuels, including ammonia (NH_3) and hydrogen (H_2). These non-carbon fuels can be produced using electricity from renewable sources and act as a form of chemical energy storage when renewable electricity output outweighs demand. Coupling large-scale solar and wind power plants with chemical energy storage in the form of synthetic non-carbon fuels for later use in reciprocating engines presents a harmonious approach to providing consistent and reliable energy to the electric grid without carbon emissions.
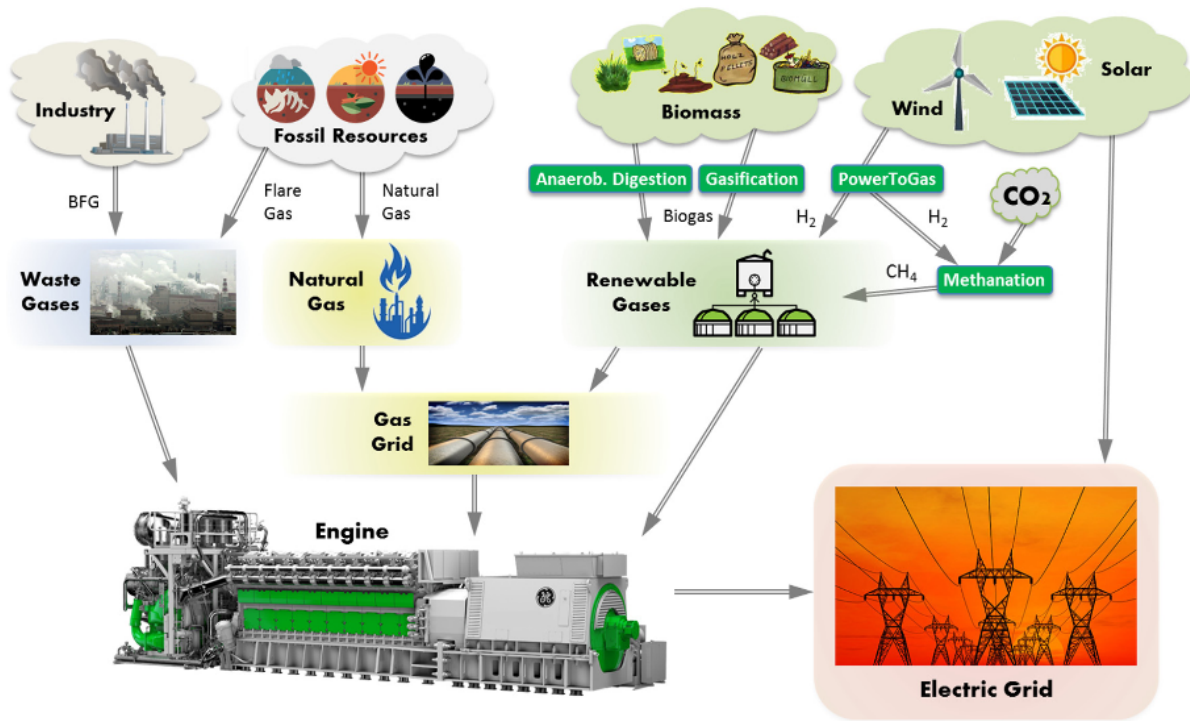
Figure 1.10: Schematic of internal combustion engine placement within the power generation infrastructure [8].

These gaseous fuels facilitate decreased carbon output among other advantages, while

also presenting new challenges compared to existing liquid fuels. The use of natural gas as a replacement for gasoline in spark-ignition engines can yield higher thermal efficiencies partially due to the higher octane number enabling higher compression ratios, and this is coupled with a simultaneous reduction in emissions of carbon oxides and unburned total hydrocarbons (THC) [33]. However, the low burning velocity of natural gas leads to high combustion instability and cyclic variation along with high THC when implementing exhaust gas recirculation (EGR) or fuel-lean equivalence ratios to reduce NOx emissions and increase fuel efficiency [34]. Improved natural gas combustion can be achieved through hydrogen addition by increasing the burning velocity and lowering the combustion duration which reduces cyclic variability and enables stable operation with fuel-lean mixtures [35]. While hydrogen-enrichment can increase thermal efficiency and reduce emissions of CO, CO_2, and THC, it can also lead to high NOx emissions through higher combustion temperatures. Additionally, hydrogen engines have reduced power output due to hydrogen's lower energy density compared to conventional fuels [35, 36]. The reactivity of hydrogen-rich fuel-air mixtures also requires careful management of operation parameters such as valve and ignition timing, equivalence ratio, and engine load to limit dangerous and destructive instances of backfire and knock [37]. Ammonia retains the non-carbon benefit of hydrogen without these safety concerns thanks to a lower flame speed, narrow flammability limits, and high auto-ignition temperature. However, ammonia is highly toxic. Consequently, unburned ammonia is a major concern which can occur with incorrect valve timing, fuel-rich operation, or low-temperature combustion at fuel-lean conditions [38]. The use of a combustion promoter such as hydrogen can lower unburned NH_3 however comes with a trade-off of high NOx emissions observed in hydrogen- and ammonia-fueled engines [21, 39].

Ideal power generation engines in a low-carbon fuel landscape should be capable of fuel-flexible operation for reliable power generation despite variations in fuel quality, composition, and availability. The spectrum of renewable, low-carbon, and non-carbon fuels have widely varying compositions and combustion behavior [8]. Pure fuels such as hydrogen and am-

Compound	Molar fraction
Hydrocarbons	
Methane	0.75 – 0.99
Ethane	0.01 – 0.15
Propane	0.01 – 0.10
n-Butane	0.00 – 0.02
Isobutene	0.00 – 0.01
n-Pentane	0.00 – 0.01
Isopentane	0.00 – 0.01
Hexane	0.00 – 0.01
Heptane plus higher hydrocarbons	0.00 – 0.001
Nonhydrocarbons	
Nitrogen	0.00 – 0.15
Carbon dioxide	0.00 – 0.30
Hydrogen sulfide	0.00 – 0.30
Helium	0.00 – 0.05

Table 1.2: Typical ranges of constituent molar concentrations in natural gas obtained from reserves, from [22].

monia have greatly different flame speeds, emissions profiles, and safety risks thus requiring significantly different engine configurations. The family of renewable and gaseous hydrocarbon fuels also vary widely in composition depending on the source, and so also require variable operation parameters to burn efficiently in reciprocating engines. Natural gas alone can fluctuate greatly in volume fraction of hydrocarbon and non-hydrocarbon constituents (see Fig. 1.2) depending on geographic location. Blending of fuels, such as hydrogen addition as a combustion promoter for methane or ammonia, has demonstrated success in narrowing the range of combustion characteristics for more reliable performance with lower emissions. Polyfuel engines improve the practicality of fuel-flexible power generation, however additional work is needed to characterize polyfuel combustion and achieve optimal efficiencies. The multi-variate and nonlinear nature of reciprocating engine performance and exhaust emissions has required decades of research and development to achieve today's levels of performance when operating with traditional fuels. Similar optimization over the multitude of possible low-carbon fuel blends requires comparable effort and resources to character-

ize the limitations and convoluted chemical kinetics to provide practical engines that meet accelerating efficiency and emissions requirements.

1.2.3 Adaptive combustion engine strategies

Utilizing alternative fuels in reciprocating engines traditionally requires significant modifications to operating parameters and hardware design, making high-efficiency fuel-flexible engines difficult to achieve. Increasingly modular engine geometries and variable control improves adaptability to different fuels, particularly if polyfuel blending is incorporated to tailor the combustion behavior and narrow the range of required modifications. Electronically-controlled spark ignition enables adaptation to varying flame speeds to optimize combustion and piston phase matching. Optimal ignition timing achieves maximum power output and efficiency while preventing engine knock and thermal NOx generation at early ignition or incomplete combustion at delayed ignition. Electronic fuel injection with variable spray geometries promotes fuel-air mixing or stratification and equivalence ratio adjustability. This enables execution of multiple combustion modes to maximize combustion efficiency with minimal emissions across varying fuel compositions with differing stoichiometric air-fuel ratios. Variable valve actuation (VVA) systems provide additional control over gas flow into and out of the cylinder, with modern VVA capable of modifying all aspects of intake and exhaust valve lift, duration, and phase [40]. This improves volumetric efficiency of the intake stroke and reduces exhaust heat rejection across the engine load and rpm range. Additionally, variable valve lift can remove the need for intake throttle valves while simultaneously increasing fuel-air mixing and turbulence to promote fast and complete combustion.

When combined, these variable systems provide comprehensive control over fluid motion and combustion within the engine cylinder and enable a multitude of techniques to optimize fuel-flexible reciprocating engines. Exhaust gas recirculation (EGR) with VVA or alternative systems dilutes the reactant mixture with exhaust gas to lower peak temperatures and reduce NOx in high-temperature fuel mixtures as with hydrogen addition [41, 42]. Variable com-

pression ratio (VCR) systems or effective compression ratio (ECR) adjustment through VVA can increase efficiency for all fuel compositions and octane ratings by operating at maximum allowable compression ratio before knock occurs across varying loads [43, 44]. The theoretical Otto cycle itself can be manipulated with VVA, for example implementing the over-expanded Miller/Atkinson cycle to increase efficiency by increasing the expansion stroke relative to the compression stroke through early or delayed closing of the intake valve [45]. These methods in concert can also improve the performance of lean-burn or low-temperature combustion which operates near the lean limit and promotes complete combustion while limiting thermal NOx formation [46, 47].

The efficacy of these modular systems and combustion techniques can be increased in a transient real-world environment by implementing adaptive modeling and control schemes to respond to fluctuations in fuel content, load demand, and environmental conditions. Online calibration and modern IC engine control algorithms such as adaptive control and model predictive control (MPC) show potential to improve transient engine performance and have demonstrated efficiency gains and emissions reduction through real-time optimization [48, 49, 50]. These control methods leverage a combination of combustion models and sensor inputs. Model predictive control has seen increasing use in reciprocating engine systems due to it's ability to handle multiple constraints and nonlinearities and achieve fast response times with predictive action [49]. Emissions production in reciprocating engines is highly nonlinear, and a key aspect of successful MPC is a predictive model of nonlinear engine dynamics to estimate control variable effects and resulting emissions. Advancement in IC engine combustion models can improve understanding of fundamental combustion processes in-cylinder for improved predictive action while offloading effort from time-intensive offline experimental calibration studies. Machine learning has seen increasing use in this area to provide online learning algorithms to inform and update model-based control to improve adaptation over time based on online sensor inputs [48, 51, 52]. The addition of sensor feedback for closed-loop model inputs and error compensation improves performance when

model estimators do not fully capture system outputs in a real-world engine subject to the breadth of transient disturbances influencing combustion performance.

1.3 Motivation for high-speed exhaust sensing

Recent efforts towards the advancement of low-emission fuel-flexible engines have established engine-out emissions as a primary target for further characterization and optimization across the wide range of fuel composition and engine operating inputs (e.g., ignition timing, valve timing). Emissions formation is a highly nonlinear process influenced by complex combustion chemical kinetics convoluted with heat transfer and fluid dynamics within the engine cylinder. Current efforts in chemical kinetic and computational fluid dynamic studies of low-carbon fuel combustion seek to improve fundamental knowledge in this area and evaluate approaches for low-carbon IC engines. Experimental engine studies provide necessary measurement data to evaluate how these models translate to combustion processes within real engines and highlight areas for improvement. Exhaust emissions analyzers in experimental research relate pollutant profiles to tunable engine operating parameters and fuel composition. These same analyzer methods are then used in offline calibration of production engines to generate engine operating maps that dictate tunable parameter set points for the range of operating conditions experienced by real-world engines. Power generation engines typically operate at speeds of 1000-3600 rpm with cycle frequencies of 8-30 Hz corresponding to cycle periods of 33-120 ms. Cycle-to-cycle variation in performance and emissions occur at these rates due to unsteady combustion or transient conditions such as engine start-up and load response. The timescales of emission formation are even smaller, with rapid chemical evolution during the expansion stroke that persists into the 8-30 ms exhaust stroke during which the exhaust valve is open and combustion gases are released into the engine exhaust. Time-resolved quantitative measurements of species concentrations at the ms-timescales of combustion and exhaust processes are necessary for full characterization of emissions formation to improve

combustion models and for optimization of engine control parameters.

High-speed exhaust diagnostics provide further benefit in real-time optimization strategies such as MPC both to refine the predictive models and supply emissions data feedback. Engine parameters including ignition, fuel injection, and valve actuation can be adjusted on a cycle-to-cycle basis, and fast-response adaptation is guided by sensor inputs to inform updated control models with a combination of open-loop, feedforward, and feedback control. The array of sensor targets includes load demand, intake air flow, engine speed and engine temperature among others. Advanced systems include in-cylinder diagnostics such as pressure transducers to evaluate peak in-cylinder pressure and heat release rates during combustion. In engine exhaust, the most common diagnostic is the electrochemical O_2 sensor, which guides air-fuel ratio by reacting to concentrations of O_2 in the exhaust indicative of fuel-lean or fuel-rich conditions. High-speed measurements of other species concentrations in the exhaust stream are increasingly important to develop the next generation of power generation engines with ultra-low emissions. Exhaust emissions of carbon oxides (CO_2 and CO), nitrogen oxides (NO_2 and NO), and unburned fuel (CH_4, THC, NH_3) are primary metrics for low-carbon engines and must be precisely controlled, ideally with cycle-to-cycle response rates. While adaptive control algorithms and electronically-controlled components already provide fast-response control capability for internal combustion engine operating parameters, the potential for real-time emissions reduction and optimization is hindered by a lack of fast real-time emissions sensing capability.

1.3.1 Emissions sensing techniques

Characterization of IC engine exhaust emissions typically involves sampling and ex situ analysis of the exhaust stream with a multitude of sensing techniques [42, 41, 53, 54]. Specific measurement techniques for emissions detection in engine exhaust gases include:

- *Gas chromatography (GC)*: In gas chromatography, an inert carrier gas carries individ-

ual samples of exhaust gas through a sampling tube (i.e., column) where the sample gas interacts with the internal chemical coating and affects residence time in the column. A detector (often flame ionization detectors) at the column exit records passing molecules over time. Measurement of the species-dependent residence times enables calculation of specific emissions concentrations within the convoluted gas mixture. This method is often used for methane and volatile organic compounds. (VOCs) [55].

- *Flame ionization detectors (FID)*: Flame ionization detectors utilize a hydrogen flame to generate ions during the combustion of hydrocarbons in the sampled exhaust gas stream. A tubular electrode around the flame region attracts ionized carbon atoms that impact the electrode and generate signal current. FID is used for exhaust measurements of unburned hydrocarbons, both methane and non-methane.

- *Chemiluminescence detectors (CLD)*: Chemiluminescence detection relies on chemical reactions induced by an added reagent to excite target species molecules which subsequently emit light at specific wavelengths when they return to the ground state. This method is widely used for NO and NO_2 detection in exhaust gas and uses ozone (O_3) as the reagent to react with NO to form excited NO_2.

- *Electrochemical (EC) sensors*: This is a broad family of sensors that is based on configurations of electrolytes and electrodes that promote oxidation-reduction reactions to generate current signals proportional to the target species concentrations. In exhaust gas analysis, these are commonly used as O_2 and NOx sensors.

- *Nondispersive infrared (NDIR) sensors*: NDIR sensors measure the total molecular absorption (i.e., attenuation) of a broadband infrared light source over specific spectral ranges corresponding to strong absorption bands of target molecules. This is a common method for several combustion species that exhibit strong absorption in the infrared including CO, CO_2, THC, and N_2O.

- *Fourier-transform infrared (FTIR) spectroscopy*: FTIR spectrometers similarly measure infrared molecular absorption of broadband light sources. FTIRs capture a larger spectral range and with spectrally-resolved measurements enabled by the moving-mirror interferometer which requires Fourier-transform of the interference pattern to generate a spectrum. These systems are used for a variety of species in exhaust gases such as carbon oxides, nitrogen oxides, hydrocarbons, and water.

- *Laser absorption spectroscopy (LAS)*: LAS employs lasers to probe molecular absorption features of target species, typically with lower spectral range and higher resolution than FTIR and NDIR systems. LAS is less common than the other absorption methods in production gas analyzer systems, but has been used for detection of nitrogen oxides, carbon oxides, and hydrocarbons. Notably, LAS provides a means for in situ gas analysis by directing a laser beam through the flow-field of interest. This method will be discussed further in Chapter 3.

Many of these measurement techniques are integrated into production gas analyzer systems for use across a variety of combustion systems, and typically rely on gas sampling lines to transport exhaust gases from the engine exhaust system to the measurement unit. This at-line or ex situ sensing configuration limits temporal resolution due to gas mixing during transit coupled with bandwidth limitations in the sensor methods themselves. Additionally, gas sample transit time and measurement signal processing produce high latency well above the 100 ms regime of reciprocating engine cycles. These characteristics are impediments in the desire for exhaust emissions sensors to provide (1) cycle-resolved characterization of emissions dynamics and (2) low-latency measurement feedback for potential use in real-time optimization strategies. Relocation of the measurement region for in-situ sensing near the exhaust port improves performance in both of these areas providing the bandwidth of detection methods are sufficiently high. Recent advancements in this area to provide cycle-resolved emissions data include sampling systems with <10 ms response time [56] and NDIR probes with kHz-rate time resolution [57, 58]. Laser absorption spectroscopy has distinct advan-

tages for in-situ exhaust sensing. LAS is quantitative without the need for calibration, can be deployed in-situ with no sample pre-treatment, has been demonstrated up to MHz-rates in combustion systems, and is sensitive to trace (ppm) emissions [59, 60]. This technique has already been demonstrated to provide cycle-resolved species and temperature measurements in the intake, cylinder, and exhaust of reciprocating piston engines with in-situ deployment removing the time-averaging and sampling latency experienced by standard exhaust gas analyzers [61, 62, 19, 63]. However, further advancement of LAS detection systems is necessary to improve robustness and computational efficiency to enable real-time detection in the harsh exhaust systems of production reciprocating engines.

1.4   Scope and organization

This dissertation details the advancement of real-time laser absorption spectroscopy for cycle-resolved emissions characterization and real-time data transfer for polyfuel combustion engines. Key contributions include (1) development of a high-temperature and high-pressure gas cell for mid-infrared absorption spectroscopy studies at conditions ($>$1000 k, $>$100 atm) relevant to reciprocating engine combustion gases (2) design of an opto-mechanical sensing system capable of sustained operation near the exhaust port in production engines to enable cycle-resolved emissions (CO and NO) at 10 kHz and (3) acceleration of LAS signal processing via machine learning and embedded electronics for real-time data reduction with sub-ms computational time. Chapter 2 discusses constant volume and time-resolved chemical kinetic modeling of low-carbon fuel blends in reciprocating engines to investigate impact on engine performance and emissions. Chapter 3 presents an introduction into mid-infrared laser absorption spectroscopy, including theory and methods used in the development of the exhaust sensing strategy. Chapter 4 details the design of a high-temperature and high-pressure optical gas cell for fundamental mid-infrared spectroscopy studies at over 1200 K and 200 atm which is used to develop LAS sensors for harsh environments as in engine exhaust systems.

Chapter 5 describes a custom exhaust sensor module developed for in-situ integration of mid-infrared LAS into the exhaust pipe of reciprocating engines and its application for 10 kHz emissions sensing and analysis of low-carbon polyfuel operation. Chapter 6 discusses the signal processing acceleration for back-end latency reduction for the LAS exhaust sensor achieved through end-to-end machine learning on a field-programmable gate array (FPGA). Lastly, Chapter 7 summarizes the findings in this work and presents ongoing efforts to further sensor development and complementary engine systems including the development of an electro-hydraulic camless valvetrain.

CHAPTER 2

Chemical-kinetic modeling of polyfuel combustion in reciprocating piston engines

2.1 Introduction

The combustion of fuels within real reciprocating engines involves a convolution of fluid dynamics, chemical kinetics, and heat transfer. Each of these processes is sensitive to mechanical engine design, operating conditions, and fuel type. This results in a notoriously nonlinear multivariate system that limits the ability to deconvolve fundamental subprocesses from experimental measurements of global engine performance. In-depth understanding of these fundamental processes is required for efficient advancement of reciprocating engines for adaptation to the evolving low- and non-carbon fuel landscape. Fluid and chemical modeling of in-cylinder combustion, often through reacting computational fluid dynamics (CFD) simulations, facilitates granular analysis at high spatial and temporal resolution and provides insights into methods to improve combustion efficiency and engine performance. These models are limited in their representation of real engines in part by (1) boundary condition assumptions dictated by lack of information or need to reduce computational complexity and (2) limited knowledge of the thermal and chemical kinetic properties of the reacting mixtures. Modeling methods benefit from parallel experimental work focused on fundamental combustion processes, parametric engine studies and high-resolution diagnostics to provide reference data to refine model assumptions and fundamental knowledge of fuel chemistry. Recent simulation efforts in the area of low-carbon reciprocating engines

has increased community understanding of fuel chemistry with low-carbon fuels including natural gas, hydrogen, and ammonia [64, 65, 66, 67, 68]. Advanced combustion models are necessary to inform low-emission engine operating strategies and interpret diagnostic results to efficiently optimize adaptive polyfuel engines.

In this chapter, recent work in low-carbon fuel chemical kinetics is leveraged to develop a combustion model of an Otto cycle engine to evaluate performance and emissions response to low-carbon fueling with natural gas blends including hydrogen (H_2) and ammonia (NH_3). A first-order model simulates constant-volume equilibrium to evaluate fundamental differences in gas properties and emissions resulting from polyfuel combustion. A second-order model is then presented which adds temporal dependence to the constant volume assumption and chemical-kinetic evolution, similar to previous works modeling reciprocating engine combustion utilizing the Cantera simulation environment [69, 70]. Boundary conditions and engine-relevant inputs are added to represent an experimental reciprocating engine which serves as the test bench for the duration of this work. The models presented here serve to predict experimental engine response to polyfuel operation, interpret experimental diagnostic results, and inform future development directions.

2.2 Modeling theory

The modeling is performed in the Cantera framework, which is an object-oriented software tool with built-in functions and numerical solvers for computational analysis of thermodynamic, chemical kinetic, and transport processes [71]. A simulation within Cantera can be defined by (1) the network of Cantera objects with the underlying assumptions and solvers and (2) the chemical-kinetic mechanism that specifies species, reactions, and material properties. The Ideal Gas Reactor serves as the central Cantera object in this study, with the state defined by mass of contents m [kg], reactor volume V [m^3], temperature T [K], and species mass fractions Y_k. The content gases are homogeneous and treated as ideal per

27

Eq. 2.1, where p is the gas pressure, n is the number of moles, and R is the universal gas constant:

$$pV = nRT \tag{2.1}$$

The volume of the reactor is constant unless a moving wall is specified, in which case the volume change is expressed by Eq. 2.2 where $f_w = \pm 1$ based on direction of motion, A_w is the surface area, and $v_w(t)$ is the time-dependent velocity.

$$\frac{dV}{dt} = \sum_w f_w A_w v_w(t) \tag{2.2}$$

Mass is conserved within the reactor and any connected inlets or outlets as in Eq. 2.3:

$$\frac{dm}{dt} = \sum_{in} \dot{m}_{in} - \sum_{out} \dot{m}_{out} \tag{2.3}$$

The change in total internal energy of the reactor contents is expressed as a function of state variables in Eq. 2.4

$$mc_v \frac{dT}{dt} = -p\frac{dV}{dt} + \dot{Q} + \sum_{in} \dot{m}_{in}\left(h_{in} - \sum_k u_k Y_{k,in}\right) - \frac{pV}{m}\sum_{out} \dot{m}_{out} - \sum_k \dot{m}_{out} - \sum_k \dot{m}_{k,gen}u_k \tag{2.4}$$

Where h is the specific enthalpy, c_v is the specific heat capacity at constant volume, $\dot{Q}$ is the heat transfer rate, u_k is the specific internal energy of species k, and $\dot{m}_{k,gen}$ is the rate at which species k is generated from homogeneous phase reactions. The rate of change of each species k is given by Eq. 2.5:

$$m\frac{dY_k}{dt} = \sum_{in} \dot{m}_{in}(Y_{k,in} - Y_k) + \dot{m}_{k,gen} \tag{2.5}$$

Species-specific thermodynamic properties along with chemical reactions and transport properties are specified in the kinetic mechanism used to define the gases within the reactor.

Mechanism	Species	Reactions	Reference
GRI 3.0	53	325	[72]
USC II	111	784	[?]
CRECK	159	2,459	[73, 74, 75, 76]

Table 2.1: Chemical kinetic mechanisms considered for this simulation study.

A number of kinetic mechanisms have been developed to replicate low-carbon fuel combustion such as USC II and GRI-Mech 3.0. In this study, we utilize a more expansive detailed kinetic mechanism from the CRECK Modeling Group (compared to other considered mechanisms in Table 2.1) that incorporates recent literature updates up to 2020 for simulation of up to C_3 hydrocarbons including NH_3 and a NOx sub-mechanism [73, 74, 75, 76], comprised of 159 species and 2,459 reversible reactions. The increase in computational run-time is acceptable as the simplified zero-dimensional model has lower baseline runtime compared to CFD models, and more detailed mechanisms can increase precision of such simplified models [77]. Thermodynamic reference-state properties of molar heat capacity $\hat{c}_p^{\circ}(T)$, molar enthalpy $\hat{h}^{\circ}(T)$, and molar entropy $\hat{s}^{\circ}(T)$ for each species are defined by the NASA 7-coefficient polynomial parameterization [78] through Eqs. 2.6-2.8.

$$\frac{\hat{c}_p^{\circ}(T)}{R} = a_0 + a_1 T + a_2 T^2 + a_3 T^3 + a_4 T^4 \tag{2.6}$$

$$\frac{\hat{h}^{\circ}(T)}{RT} = a_0 + \frac{a_1}{2}T + \frac{a_2}{3}T^2 + \frac{a_3}{4}T^3 + \frac{a_4}{5}T^4 + \frac{a_5}{T} \tag{2.7}$$

$$\frac{\hat{s}^{\circ}(T)}{R} = a_0 ln T + a_1 T + \frac{a_2}{2}T^2 + \frac{a_3}{3}T^3 + \frac{a_4}{4}T^4 + a_6 \tag{2.8}$$

Species specific transport properties are included in the mechanism, and in this case the Lennard-Jones collision diameter is used to calculate mixture-averaged collision frequency for reactions in the spatially homogeneous gas mixture. The reactions in the mechanism are defined by the species and coefficients such as in Eq. 2.9:

$$a[A] + b[B] \longrightarrow c[C] + d[D] \tag{2.9}$$

The rate of change in concentration of species A is given by Eq. 2.10:

$$\frac{d[A]}{dt} = k_f[A]^a[B]^b \tag{2.10}$$

where k_f is the forward reaction rate defined by the Arrhenius equation with pre-exponential factor A, temperature exponent n, and activation energy E_a in Eq. 2.11:

$$k_f = AT^n exp(-E_a/RT) \tag{2.11}$$

The kinetic mechanism includes adjustments to the various types of reaction rates represented by the Arrhenius equation, including pressure dependence when available.

2.3   Constant volume equilibrium

The combustion of fuel within the Otto cycle can be approximated as constant volume combustion. The fundamental combustion properties and product species concentrations of potential fuels can be characterized by a first-order kinetic model by simulating equilibrium species concentrations in a constant volume, ideal gas reactor. Initial composition is defined with molar ratios of fuel and air (O_2 and N_2) for a prescribed equivalence ratio. Initial temperature and pressure are set as 750 K and 15 atm, respectively, to represent gas conditions at the end of the compression stroke and just prior to ignition within a reciprocating engine. Chemical equilibrium composition and thermodynamic properties are found by minimizing the Gibbs free energy defined by Eq. 2.12:

$$G(p, T) = U + pV - TS = H - TS \tag{2.12}$$

Chemical equilibrium is calculated with a built-in iterative solver in Cantera to determine the state at which the kinetic system reaches a minimum Gibbs free energy as in Eq. 2.13:

$$dG_{mix} = 0 = \sum_i dN_i [\hat{g}_{i,T}^\circ + RT ln(P_i/P^\circ)] \tag{2.13}$$

where N_i is the number of moles of species i, $\hat{g}_{i,T}^\circ$ is the reference molar Gibbs free energy, P_i is the partial pressure, and P° is the reference pressure.
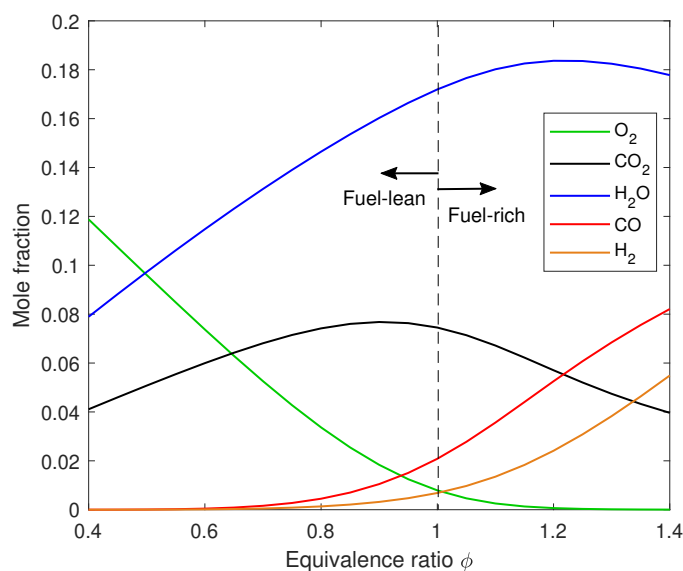
Figure 2.1: Major species concentrations as a function of equivalence ratio resulting from constant volume equilibrium simulation of fuel-air combustion of natural gas.

Figure 2.1 displays molar concentrations of major species resulting in a constant volume equilibrium simulation of natural gas-air combustion at a range of equivalence ratio. In this study, natural gas is defined as a simplified yet representative composition of 94% CH_4, 4% C_2H_6, and 2% C_3H_8. Major products CO_2 and H_2O are present at all equivalence ratios and peak at near-stoichiometric conditions. Fuel-lean conditions ($\phi < 1$) contains excess O_2 relative to stoichiometric combustion, and so results in high equilibrium O_2 concentrations and low concentrations CO and H_2 which are indicators of incomplete hydrocarbon oxidation. At fuel-rich conditions ($\phi > 1$) these trends are reversed, generating high concentrations of

CO and H_2 which are regulated emissions.
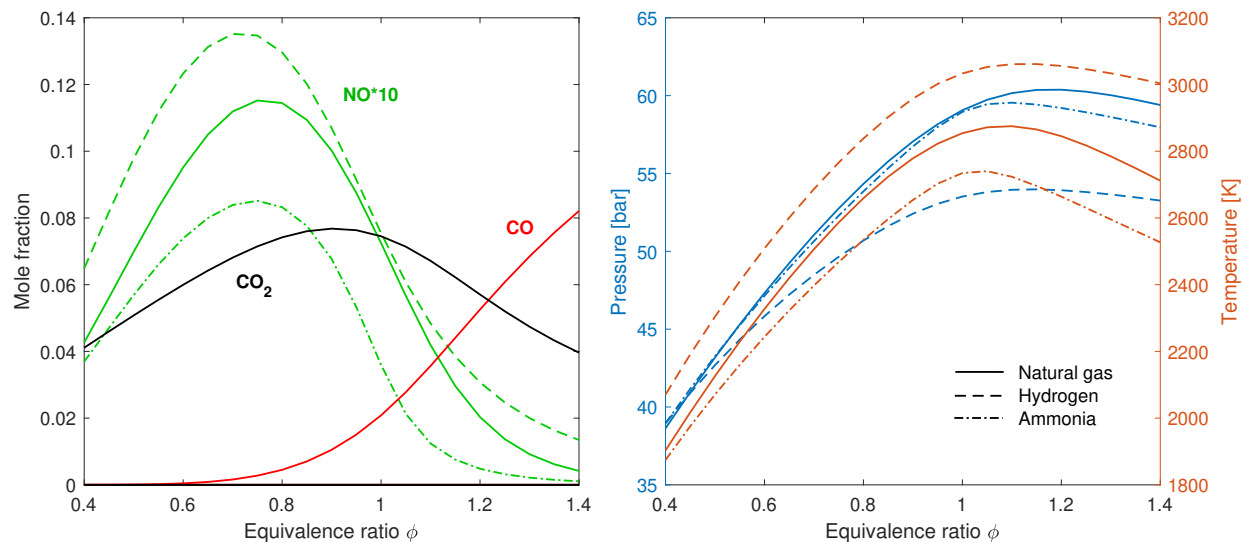
Figure 2.2: Constant volume equilibrium simulation of fuel-air combustion of natural gas, hydrogen, and ammonia as a function of equivalence ratio ϕ. *Left:* Species concentrations of critical emissions. *Right:* Equilibrium gas pressure and temperature.

Figure 2.2 shows the resulting equilibrium conditions of constant volume equilibrium for air pure natural gas, hydrogen, and ammonia in air as a function of fuel-air equivalence ratio. For all fuels, equilibrium gas pressure and gas temperature peaks around an equivalence ratio of 1-1.2, corresponding to full oxidation of fuel and resulting heat release. At higher equivalence ratios there is not enough oxygen to for complete oxidation and at lower equivalence ratios the fuel is fully oxidized in excess oxygen, however the lower fuel content yields a lower heat release. The left of Fig. 2.2 displays equilibrium concentrations of regulated emissions, with the most notable difference observed with CO_2 and CO. Natural gas generates concentrations of over 7% and 2% respectively at a stoichiometric equivalence ratio of 1. As a stable final product, CO_2 emissions are sizeable throughout and peak near a ϕ of 0.9. The intermediate CO is an indicator of incomplete oxidation in hydrocarbon fuels. As expected, CO is present in low concentrations at fuel-lean equivalence ratios and increases with higher fuel content. By contrast, both hydrogen and ammonia are non-carbon fuels and consequently produce neither CO_2 nor CO across all equivalence ratios. The formation

of nitric oxide (NO) is shared amongst all fuels and peaks around an equivalence ratio of 0.7-0.8. The formation of thermal NO occurs due to reactions between nitrogen and oxygen at high temperatures, and typically peaks at slightly fuel-lean conditions where excess oxygen is present and equilibrium temperatures are high due to adequate fuel heat release. The magnitudes of NO across the fuels mirrors the differences in adiabatic constant volume flame temperature. The discrepancies between the fuels vary with equivalence ratio, which indicates that chemical composition is relevant in addition to the equilibrium temperature.
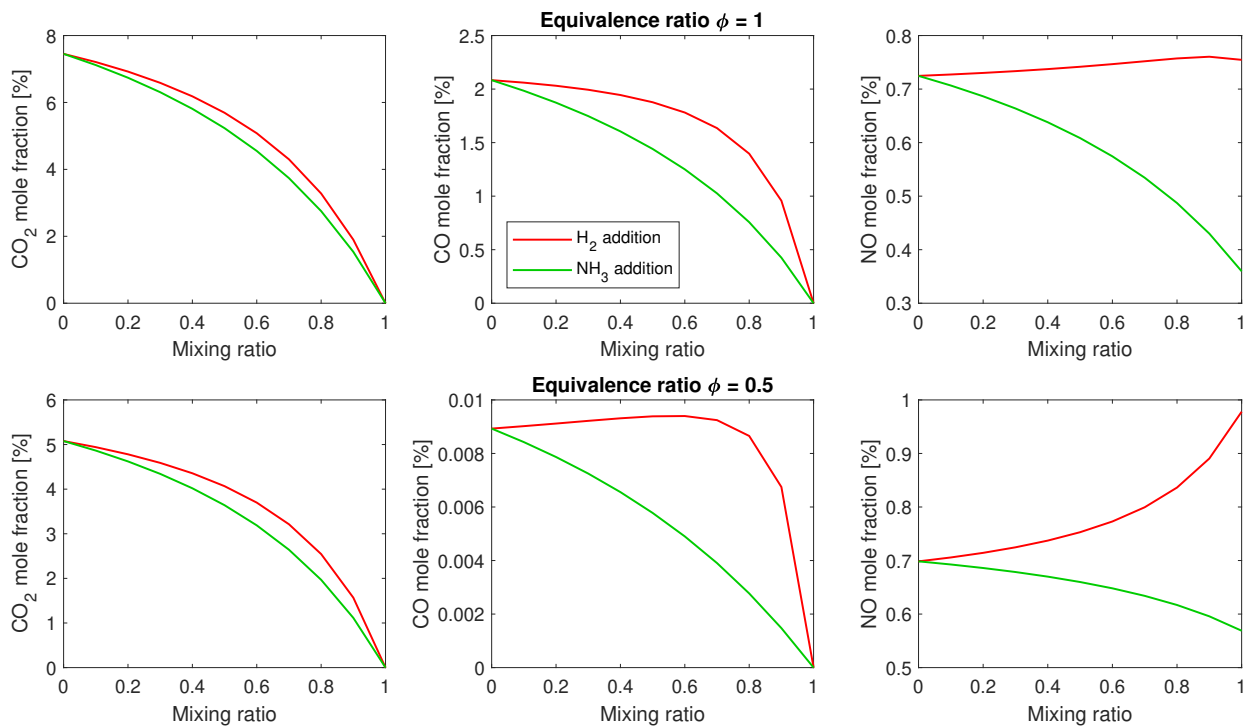
Figure 2.3: Equilibrium emissions concentrations for constant volume natural gas-air combustion with varying mixing ratios of H_2 and NH_3.

The influence on these target emissions can be examined further with respect to mixing ratios of non-carbon fuel additives (H_2 and NH_3) in natural gas, as is a common practical implementation of polyfuel engine strategies to reduce emissions of natural gas engines which are already well established. Figure 2.3 shows the effect of non-carbon fuel blending on emissions of CO_2, CO, and NO at stoichiometric ($\phi = 1$) and fuel-lean ($\phi = 0.5$) conditions. Both
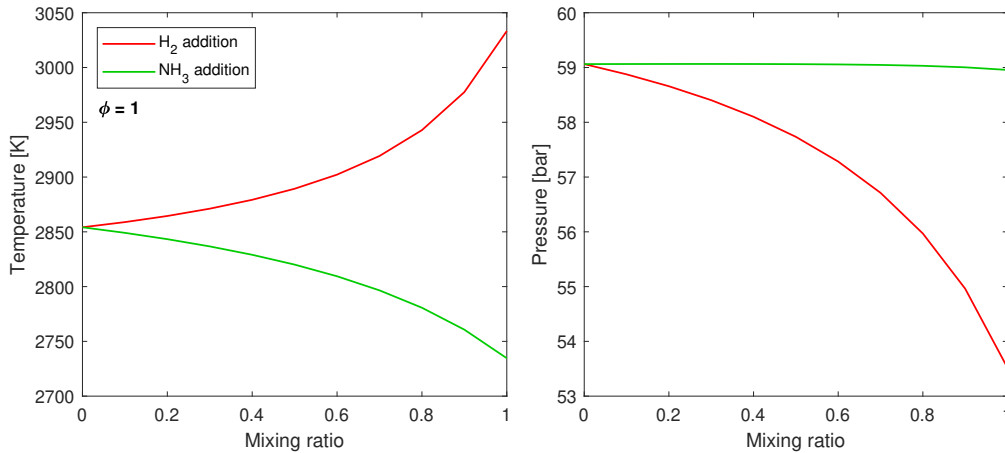
Figure 2.4: Equilibrium gas temperature and pressure for constant volume natural gas-air combustion with varying mixing ratios of H_2 and NH_3 and an equivalence ratio of 1.

additives lead to similar reductions in CO_2, with 50% reduction achieved with around 70-80% addition at both equivalence ratios. Conversely, both additives show differing effects on CO and NO emissions. Hydrogen-addition leads to a more nonlinear reduction in CO relative to ammonia, with a small increase observed at mixing ratios below 0.6 at an equivalence ratio of 0.5. Equilibrium NO shows stark differences between the two non-carbon fuels, which NH_3 leading to reduction at all conditions and H_2 consistently increasing NO concentrations. Similar dependence is observed with the equilibrium temperature and pressure in Fig. 2.4 for a stoichiometric equivalence ratio. Hydrogen increases adiabatic flame temperature and decreases pressure due to higher initial molar concentration and heat release coupled with a reduction in product moles at stoichiometric conditions relative to natural gas. Ammonia has a minimal effect on equilibrium pressure, however the lower heating value reduces equlibrium temperature relative to natural gas.

2.4 Kinetic engine modeling

Reciprocating engines are highly dynamic systems involving a convolution of time-dependent heat transfer, fluid dynamics, and chemical kinetics. Therefore additional model fidelity be-

yond first-order equilibrium analysis through temporally-resolved simulation more precisely captures the formation of emissions during polyfuel engine operation. A second-order model with temporal analysis can be used to assess engine performance metrics such as fuel conversion efficiency, output power, and specific emissions used to relate emissions with useful work produced by power generation engines. The constant volume equilibrium model was thus refined to simulate time-resolved thermochemical evolution within the combustion chamber of a reciprocating piston engine. The engine-specific boundary conditions reflect those of a Honda EU7000is Otto cycle engine that serves as the basis for experimental testing in Chapter 5, with details shown in Table 2.2 for convenience.

Model	Genconnex Honda EU7000is
IC engine	GX390T2
Cycle	4-stroke
Bore x Stroke	88 x 64 mm
Displacement	389 cm^3
Compression ratio	8.2:1
Cylinders	1
Valves per cylinder	2
Engine speed	3,300 rpm
Fuel	Natural gas
Equivalence ratio	1
Rated output	5.5 kW
Fueling method	Carburetor
Ignition method	Spark ignition
Ignition timing	20° BTDC

Table 2.2: Genconnex Honda EU7000is engine specifications.

Figure 2.5 shows a schematic of the Cantera model used to simulate Otto cycle engine combustion. The combustion chamber is a spatially homogeneous constant volume reactor, with contents treated as an ideal gas. The reactor is surrounded by adiabatic walls with the exception of the moving piston which transfers heat from the combustion chamber to standard ambient conditions. The piston is a moving wall which varies the volume of the reactor as a function of time in accordance with the mechanical dimensions of the engine
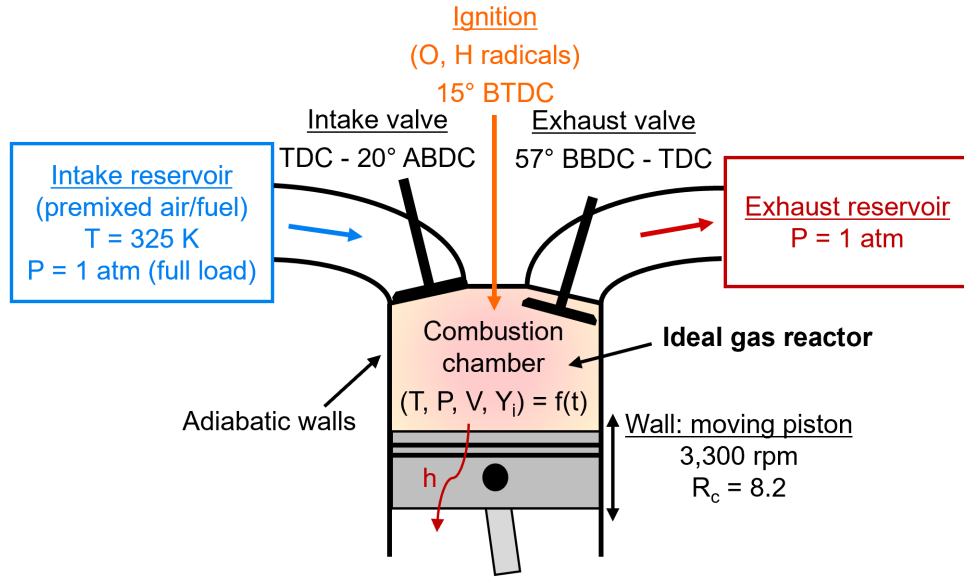
Figure 2.5: Schematic of the Cantera model to simulate time-resolved combustion in a reciprocating piston Otto-cycle engine.

(i.e., bore, stroke, compression ratio, and engine speed). The intake and exhaust valves are treated as two-way valves with constant flow coefficients for simplicity. Valve timing is informed by measurements of the experimental engine crankshafts, with modifications to match the limitations of the Cantera model. Mass flow rate through the valves is defined by Eq. 2.14 where K_v is the flow coefficient, P_1 is the upstream pressure, and P_2 is the downstream pressure.

$$\dot{m} = K_v(P_1 - P_2) \tag{2.14}$$

The exhaust manifold pressure is set to 1 atm, and the intake manifold pressure reflects throttle position and applied load, with 1 atm reflecting maximum power output. Temperature of the intake manifold is 325 K to reflect elevated temperatures during engine operation. The intake fuel-air mixture is homogeneous with molar concentrations determined by fuel-air equivalence ratio and chosen fuel type, representing the carburetor-based fuel-air mixing in the experimental engine. The Cantera framework is limited in its ability to simulate an

electric spark to serve as the ignition source. In this model, the spark is simulated by injecting a small mass ($< 3 \cdot 10^{-6}$ kg) of O and H radicals, with relative molar concentrations matching the composition of the fuel-air mixture. This is the minimum mass required to initiate combustion within the reactor, and variations in total mass and composition have minimal effect on the engine performance and emissions formation at this scale. Injection in the spatially zero dimensional combustion chamber leads to combustion speed faster than the observed combustion duration in real engines with spatially-propagating flames. Simulated ignition timing is delayed by 5 crank angle degrees, although the homogeneous combustion remains a key consideration when interpreting the model results. The time-dependent kinetic model uses the CVODE package within the SUNDIALS suite to solve the system of ordinary differential equations [79]. Backward differential formulas used to evaluate the stiff chemical kinetic equations, with variable-timestep integration used to predict temporal evolution dictated by the governing equations for the Cantera reactor system.

2.4.1 Time-resolved cycle analysis
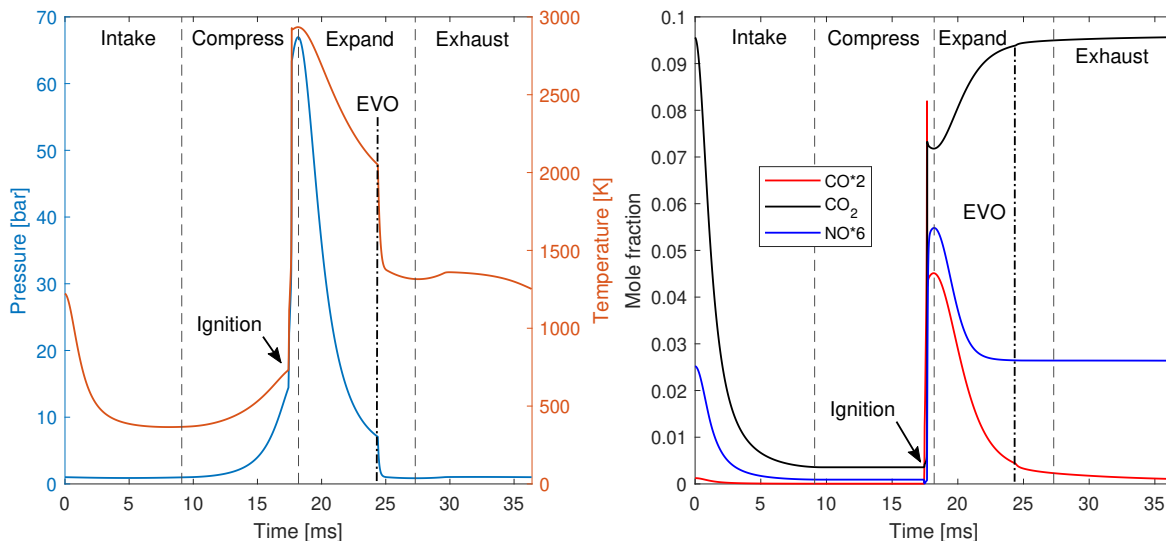
Figure 2.6: Time-resolved simulation results for in-cylinder pressure, temperature, and select species concentrations for stoichiometric natural gas-air fueling at 3,300 rpm.

Figure 2.6 shows simulated in-cylinder conditions during one full cycle with stoichiometric natural gas-air fueling as is the standard operating regime of the Honda EU7000is engine. At the baseline 3,300 rpm, each engine cycle lasts 36.4 ms. The left of Fig 2.6 displays in-cylinder temperature and pressure, highlighting the steep rise after ignition to peak values of over 2900 K and 67 bar. Temperature and pressure decrease over the expansion stroke until the exhaust valve opens leading to a sharp decrease associated with rapid expansion down to ambient pressure in the exhaust manifold. The right of Fig 2.6 displays the corresponding temporal evolution of critical emissions. A rapid evolution occurs at the time of ignition leading to increased CO_2 and NO concentrations, as well as a peak and decay of CO as a major combustion intermediate. Nonlinear species evolution persists throughout the expansion stroke, highlighting the importance of time-resolved chemical kinetic analysis. Species concentrations are dynamic immediately after ignition, with gradual decreases in CO and NO mirroring the increase in CO_2. One notable observation is the respective timescales, where CO and CO_2 do not reach equilibrium before the exhaust valve opens unlike NO formation which is most active at high temperatures at the early phase of the expansion stroke, reaching equilibrium before the exhaust valve opens.
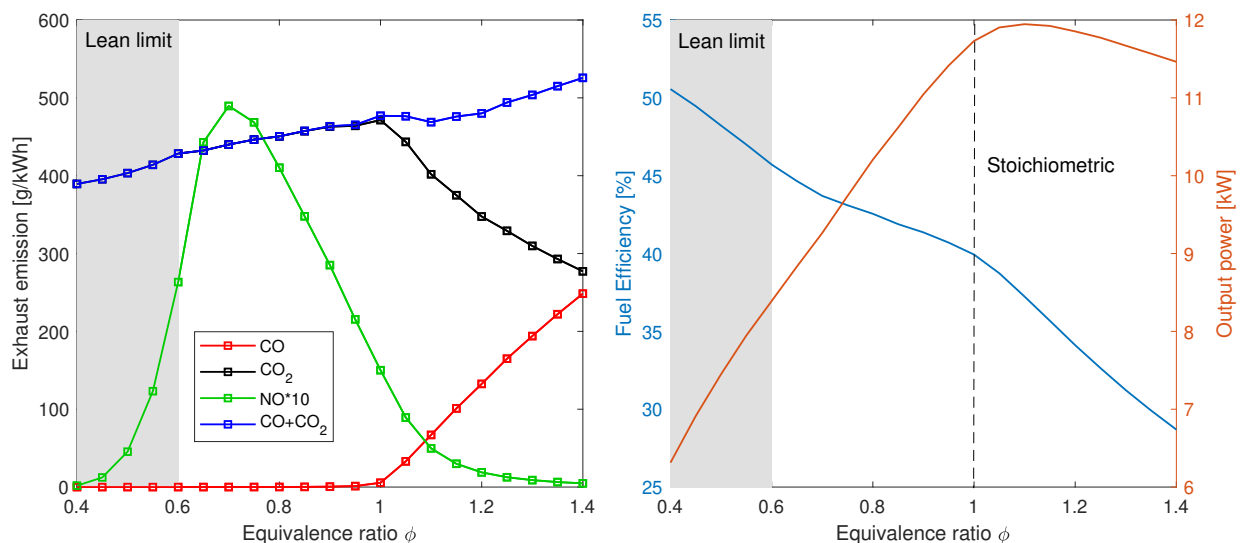
Figure 2.7: Simulated specific emissions, fuel efficiency, and output power for natural gas-air fueling in the reciprocating engine simulation.

38

Integration over the P-V diagram across the engine cycle yields net work acting on the piston and can be used to calculate output power at the simulated 3,300 rpm and can be related to the fuel input to calculate fuel conversion efficiency of the cycle through Eq. 1.2. The right of Fig. 2.7 shows the dependence of engine cycle output power and fuel conversion efficiency as a function of equivalence ratio in the time-resolved simulation. Maximum power is achieved at slightly fuel-rich conditions, whereas fuel conversion efficiency steadily increases with reduced fuel content in the reactant mixture. The left of Fig. 2.7 shows the corresponding specific emissions of NO and carbon oxides. At fuel-rich conditions, incomplete oxidation leads to a near-linear increase in specific CO emissions. Combined carbon oxide emissions increase steadily with increasing fuel content. Conversely, fuel-lean conditions increase specific NO emissions which peak around $\phi = 0.7$. Figure 2.7 illustrates the motivation for current efforts in achieving ultra-lean, low-temperature combustion in reciprocating engines. Fuel-lean operation increases fuel conversion efficiency and reduces carbon emissions per useful work provided by the engine. If engines can operate reliably at equivalence ratios below 0.5, then this additionally removes the high NO generation typical of slightly fuel-lean combustion. High-efficiency and low-emission lean-burn engines do not come without a penalty, in this case reduced power density and in practice, reduced reliability and combustion consistency which lead to the lean operability limit in natural gas engines at equivalence ratios of around 0.5-0.6.

2.4.2   Low-carbon fuel blending

The kinetic model can be used to predict engine response to blending of non-carbon fuels (H_2 and NH_3) into the natural gas fuel line of the Honda engine. The simulated fuel efficiency and power output of the engine during polyfuel operation is displayed in Fig. 2.9. Both non-carbon fuels exhibit similar trends, leading to appreciable increases in efficiency and decreases in power. These can be attributed to the leaner fuel-air mixture, as well as the lower volumetric energy density of hydrogen and ammonia relative to natural gas. Figure 2.8
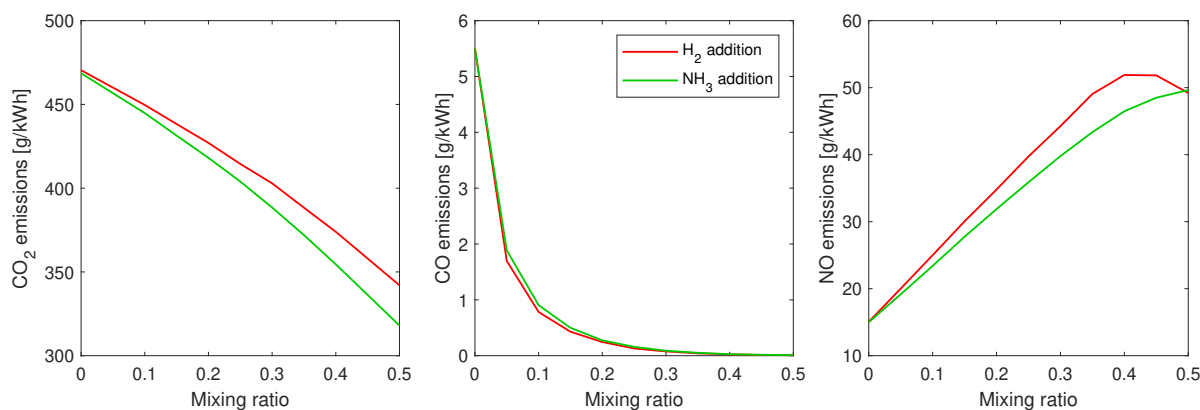
Figure 2.8: Specific emissions during simulated engine operation with varying mixing ratios of non-carbon fuels within the natural gas fuel input. Equivalence ratio of 1.
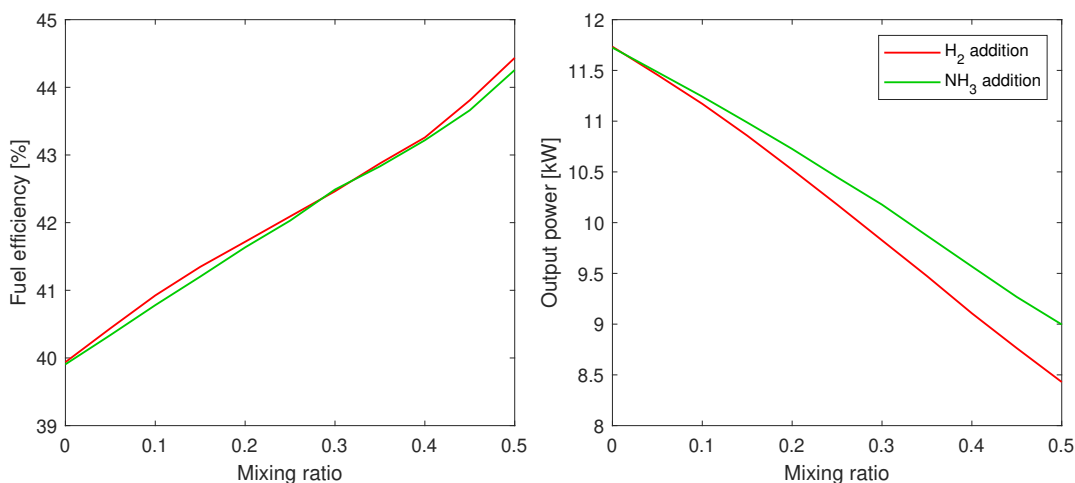
Figure 2.9: Fuel conversion efficiency and output power during simulated engine operation with varying mixing ratios of non-carbon fuels within the natural gas fuel input.

displays the effect of blending on specific emissions during unmodified engine operation. As expected, CO_2 emissions steadily decrease with non-carbon fuel addition with similar trends observed in the equilibrium simulation. However, CO and NO emissions display differing behavior in the kinetic simulation. Just 5% addition of H_2 or NH_3 lead to over 60% reduction in specific CO emissions, suggesting that kinetic effects lead to efficient CO suppression with non-carbon additives even at small concentrations. Similarly, NO formation deviates from equilibrium simulation, where both additives greatly increase specific emissions with similar

magnitude. A noteworthy effect of non-carbon addition to the simulated engine is that volumetric gas mixing via carburetion does not take into account the difference in stoichiometric air-fuel ratios between the three fuels. Hydrogen and ammonia require lower relative volumes of air for stoichiometric combustion, and so blending of these fuels in a carbureted engine calibrated for natural gas combustion has an effect of leaning the fuel-air mixture which leads to reduced carbon emissions and higher NO emissions at near-stoichiometric operation. This contributes to the peak and decay of NO emissions with hydrogen addition above 40% where the mixture has leaned beyond peak NO production. However, this cannot fully explain the magnitude of increase in NO emissions, particularly with ammonia addition. Across all equivalence ratios, equilibrium simulation predicts lower NO formation with ammonia which contradicts the dramatic increase in the engine simulation and suggests that kinetics within the engine cycle promote NO formation with ammonia fueling. The kinetics of nitric oxide production in air-breathing combustion systems due to high-temperature reactions between nitrogen and oxygen is often referred to as "thermal NOx" and is modeled by the extended Zeldovich mechanism in Eqs. 2.15-2.17, where the rate of change in NO concentration is given by Eq. 2.18:

$$N_2 + O \xrightleftharpoons{k_1} NO + N \tag{2.15}$$

$$N + O_2 \xrightleftharpoons{k_2} NO + O \tag{2.16}$$

$$N + OH \xrightleftharpoons{k_3} NO + H \tag{2.17}$$

$$\frac{d[NO]}{dt} = k_{1f}[N_2][O] + k_{2f}[N][O_2] + k_{3f}[N][OH] - k_{1r}[NO][N] - k_{2r}[NO][O] - k_{3r}[NO][H] \tag{2.18}$$

However, simulated and experimental ammonia combustion leads to higher NO production than predicted by the Zeldovich mechanism. This observation is often attributed to
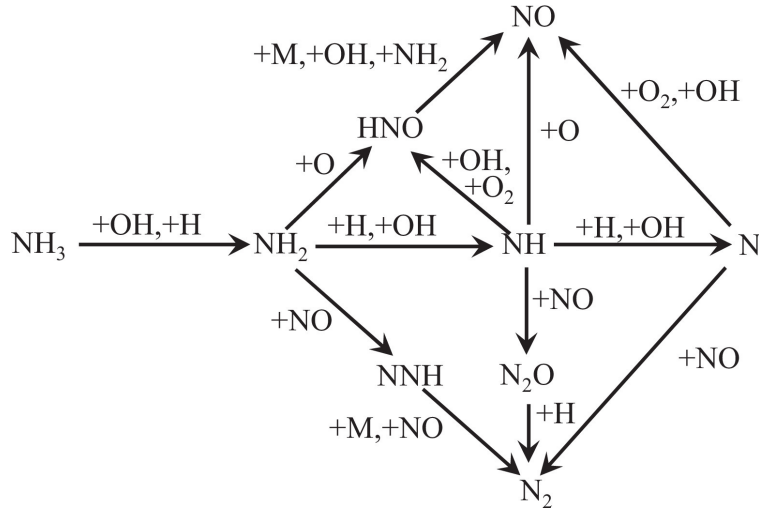
Figure 2.10: Ammonia oxidation pathway from Miller et al. [9] and obtained from [10].

kinetics in the NH_3 oxidation pathway (shown in Fig. 2.10 and dubbed "fuel NOx". The composition of radicals influences the relative strengths of channels in the oxidation pathway, with recent studies suggesting that the HNO channel dominates NO formation in ammonia combustion, particularly at lean equivalence ratios [10]. The chemical kinetics of ammonia oxidation is an active research area, and robust characterization will be critical for the practical use of ammonia in low-emission engines.

2.4.3 Polyfuel engine tuning

Optimization of polyfuel reciprocating engines requires tuning of critical engine operating parameters. Of these parameters, compression ratio is most critical as this defines the theoretical maximum efficiency of the Otto cycle. Compression ratio is limited by autoignition behavior of fuels, quantified by the octane rating, and fuel blends with different chemical compositions will lead to variable octane ratings and tolerance for high compression ratios. Variable valve timing and similar tunable engine architectures can implement variable compression ratio (VCR) combustion to respond to changes in fuel composition. The kinetic simulation model can be used to explore the response of engine performance metrics
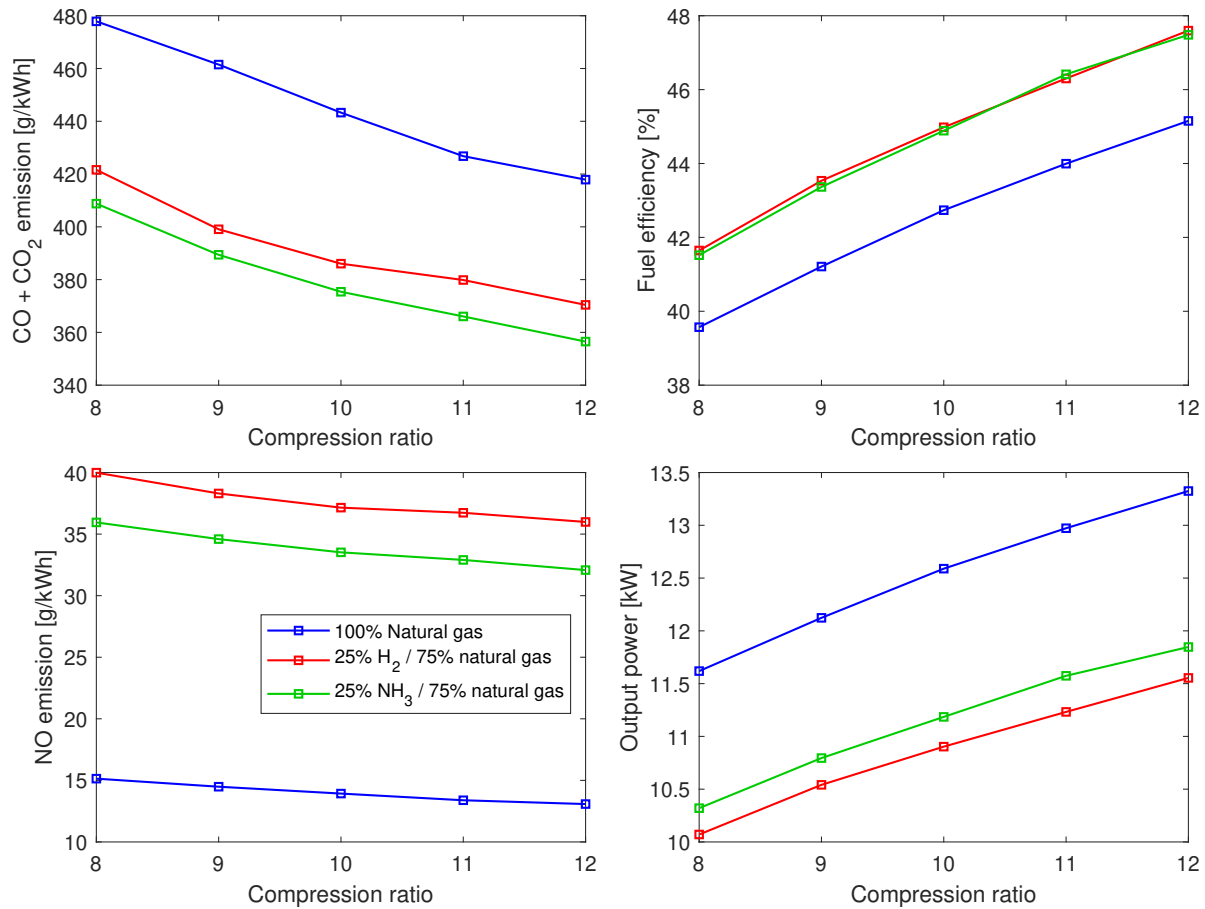
Figure 2.11: Simulated engine specific emissions, efficiency, and output power as a function of compression ratio. Evaluated at an fuel-air equivalence ratio of 1 with pure natural gas and 25% by volume addition of H_2 and NH_3.

to changes in compression ratio, with a simulation survey presented in Fig. 2.11. As predicted, increasing compression ratio leads to increased fuel conversion efficiency for natural gas as well as blends with 25% hydrogen and ammonia. Similarly, higher compression ratios produce greater power density in the engine for a given fuel. As an added benefit, higher compression ratios comprehensively reduce specific carbon and NO emissions across all fuels. On a molar concentration basis, exhaust emissions of CO and CO_2 are largely stable, while NO concentration increases slightly with higher peak in-cylinder temperatures. However, the increase in power output is more significant and provides the reduction in specific emis-

sions output which is a more useful metric to evaluate emissions impact in power generation applications.
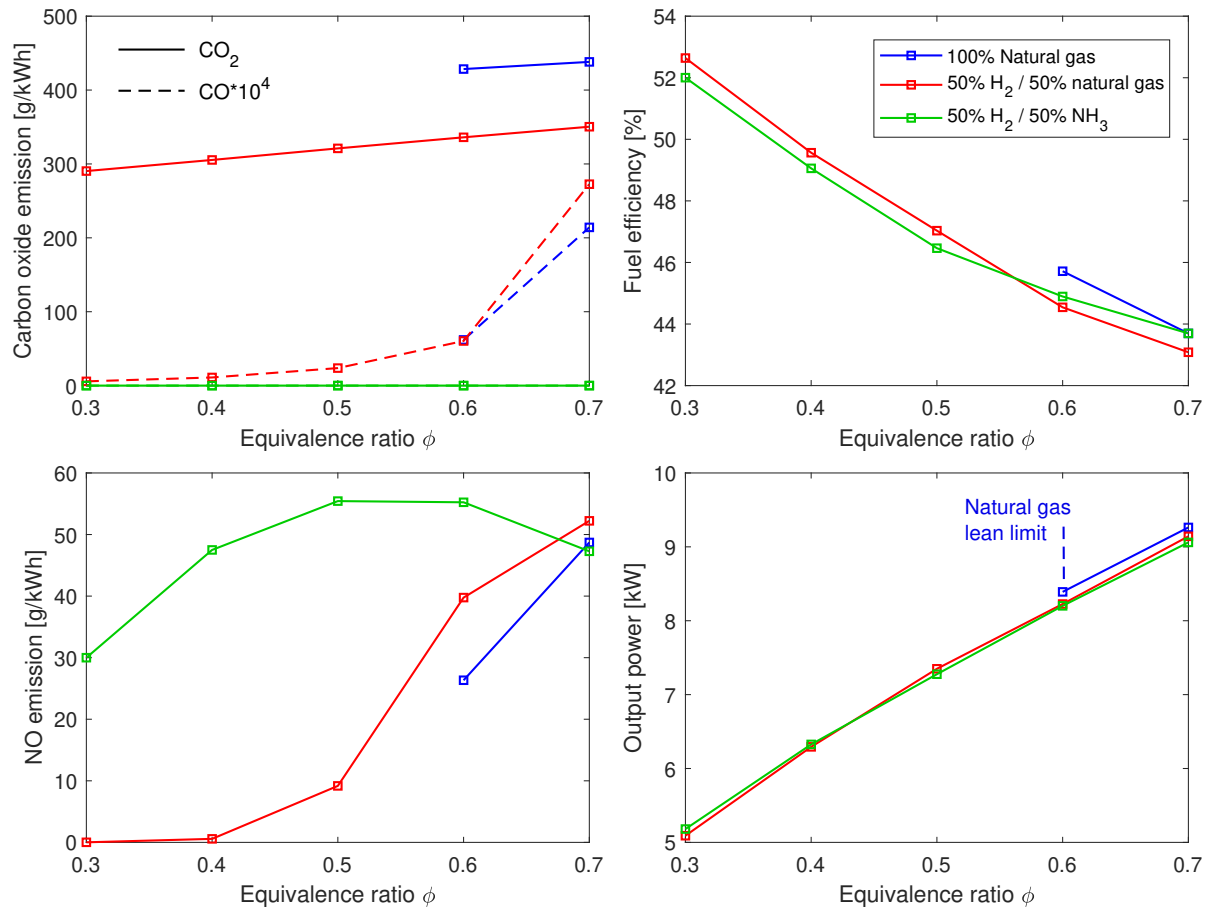
Figure 2.12: Simulated engine specific emissions, efficiency, and output power as a function of equivalence ratio adjusted to match differing stoichiometry of the fuel blends. 50% hydrogen blends with natural gas and ammonia shown alongside pure natural gas for reference, with natural gas limited to equivalence ratios above 0.6 to match experimental observations in literature.

The high NO emissions typical of hydrogen and ammonia fueling in this simulation study as well as in the literature presents a major drawback to these non-carbon fuels. Several approaches exist to mitigate these emissions including exhaust gas recirculation and exhaust aftertreatment systems. Ultra fuel-lean engines enabled by electronic fuel injection and strategic charge heterogeneity have been a subject of interest as a way to promote fuel

efficiency and complete combustion while operating at low combustion temperatures thus mitigating NO formation. Hydrogen addition has shown promise in extending the lean operability limit of other low-carbon fuels including natural gas and ammonia, increasing the reliability and consistency of lean-burn low-emission engines. Figure 2.12 displays simulation results for lean operation with 50% hydrogen addition to natural gas and ammonia, with air-fuel ratios adjusted to match the differing stoichiometry of the simulated blends. Lean operation is associated with lower engine power density and higher fuel conversion efficiencies, and all fuels exhibit similar trends. Extended lean limits enabled by hydrogen addition further reduce power output, but provide appreciable gains in fuel efficiency. Fuel efficiency gains are coupled with reduced specific carbon oxide emissions with lower equivalence ratios. The blend of 50% H_2 and 50% NH_3 has particular benefit as a non-carbon fuel thereby removing carbon emissions entirely. However, the same blend suffers from higher NO emissions relative to both pure natural gas and the 50/50 H_2/natural gas mixtures at lean conditions. Specific NO emissions with 50/50 H_2/NH_3 peak at an equivalence ratio around 0.5-0.6, and remain higher throughout realistic lean operation relative to the lean limit of natural gas. Hydrogen addition to natural gas provides the most effective reduction in NO at lean conditions. While NO emissions are higher at modest lean condition, the extended lean limit enables reduction far below the emissions of pure natural gas and the H_2/NH_3 blend. Hydrogen addition to natural gas for lean combustion presents an achievable pathway low-emission engines with comprehensive emissions reduction coupled with increases in efficiency. Hydrogen-ammonia mixtures are more recently explored in the literature and the chemistry and practical limitations are less well characterized, but the simulation indicates that it could be a powerful combination for high-efficiency, low-emission engines when paired with exhaust aftertreatment to lower NO emissions and forced induction for higher engine power density.
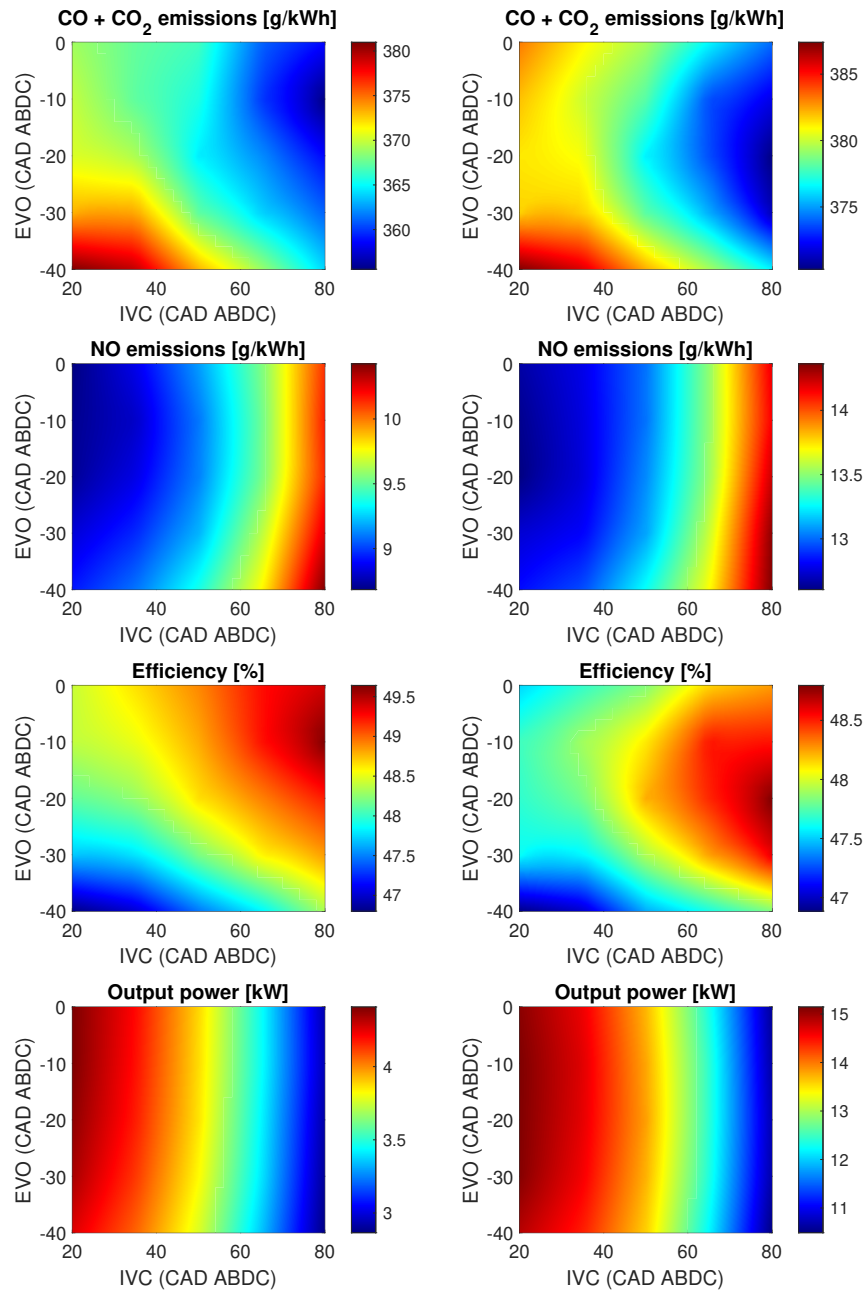
Figure 2.13: Simulated performance maps for specific emissions, fuel efficiency, and output power as a function of intake valve closing time (IVC) and exhaust valve opening time (EVO) evaluated at engine speeds of 1000 rpm (left) and 3600 rpm (right). Simulated at $\phi = 1$ for 25% hydrogen, 75% natural gas with a compression ratio of 12.

The time-dependent control parameters of the kinetic model allow further investigation on methods to optimize polyfuel combustion under transient engine conditions such as load demand and engine speed. Variable valve actuation systems provide control over fluid motion that influences combustion conditions and thermal efficiency with effects on specific emissions, fuel conversion efficiency, and power output. Timing of the intake and exhaust valves modify effective compression and expansion ratios in the engine from the geometric baseline values dictated by the mechanical design of the cylinder, piston, and crankshaft assembly. This capability allows for adaptation of compression ratio for alternative fueling constraints, and modification of the ideal Otto cycle with tradeoffs in efficiency and net work. Alteration of the intake valve closing time (IVC) and the exhaust valve opening time (EVO) can be used to shorten the compression ratio relative to the expansion ratio in the engine cycle, known as the Miller/Atkinson cycle which increases efficiency relative to the Otto cycle at the cost of lower power output [80, 47, 45]. As fluid motion is dependent on engine load and speed, precise timing of valve actuation must be modulated based on engine operating conditions. Figure 2.13 displays this effect with performance maps of specific emissions, fuel efficiency, and power output as a function of IVC and EVO for two different engine speeds (1000 rpm and 3600 rpm) typical of power generation engines. Across both engine speeds, power output is primarily a function of IVC, which dictates reactant mass and energy input per engine cycle. Similarly, specific NO emissions increase as power drops off at late IVC timing. Fuel conversion efficiency and specific carbon emissions conversely benefit from late IVC, benefiting from the over-expanded Miller/Atkinson cycle. These metrics also display significant dependence on EVO timing and engine speed. Kinetic evolution of carbon oxides persists late in the expansion stroke when the exhaust valve opens, whereas nitric oxide formation occurs earlier in the combustion process. The exhaust valve opening time balances full expansion of the exhaust gases with a need to vent pressure before the exhaust stroke and reduce pumping losses. At low engine speeds, the exhaust valve can open closer to the end of the expansion stroke and still have adequate time to evacuate high-pressure gases

before the start of the exhaust stroke. This is evident in Fig. 2.13 where EVO must be advanced at higher engine speeds for optimal fuel efficiency and specific CO and CO_2 emissions. The real-time tunability of valve actuation systems augments adaptive engine performance to balance efficiency and power output under variable engine requirements during load balancing and on-demand power applications. Characterization of the resulting tradeoffs in specific emissions, which are heavily influenced by fuel composition with diversity in relative carbon oxide and nitric oxide emissions, is necessary to evaluate the optimal valve actuation strategy.

2.5   Model limitations

The second-order chemical-kinetic model of polyfuel operation of the Honda engine provides additional insights into relevant thermochemistry and guidance on engine operation to maximize performance with minimal emissions. However, as with any model, the assumptions lead to limitations in model accuracy. Particularly, the simulation treatment of the following physical processes within the combustion chamber are worth noting:

- *Fluid dynamics*: The simulation treats the working fluid as static and homogeneous and does not account for fluid dynamics that occur in a real engine. This is relevant to flow into and out of the intake and exhaust valves, and charge mixing within the cylinder due to directional and turbulent flow. While computational fluid dynamics (CFD) aid in simulating these effects, reacting flows in reciprocating engines are notoriously complex and the high-fidelity models presented in the literature is outside the scope of this work.

- *Spatial dependence*: The spatially zero-dimensional reactor omits complex fluid mixing as well as spatial flame propagation from the ignition site at the spark plug. Flame speeds and combustion duration within reciprocating engines is a key factor that affects performance and emissions. Low flame speeds of natural gas and ammonia are

inhibitors to efficient combustion and a motivator for hydrogen addition which increases flame speed and subsequently peak in-cylinder temperatures and pressures which leads to higher NO formation that would be captured by this simulation.

- *Heat transfer*: While heat transfer occurs between the piston and the in-cylinder reacting mixture, this does not fully capture heat transfer effects in the combustion chamber. Additional cooling at the walls especially at the large surface area-to-volume ratio during ignition cools the mixture and quenches flames near the cylinder walls, leading to lower combustion efficiency and higher unburned hydrocarbons.

- *Spark ignition*: The Cantera framework does not support electronic spark ignition within the reactor volume. This was simulated with O and H radicals with constant number density to simulate decomposition of the fuel-air mixture. While the relative radical concentrations had no observable effect on thermochemistry during this study, it is a representation and does not capture real-world difficulties with ignition of low-reactivity fuels such as natural gas and ammonia especially at fuel-lean conditions which convolute with the aforementioned physical processes and lead to cyclic instability and lean operability limits.

These assumptions limit the application of lower-order chemical kinetic models to predict practical difficulties in real-world engines. Additionally, the idealized model overpredicts in-cylinder pressure and temperature, as well as power output and efficiency due to the fewer losses considered in the simulation. The model is not intended to serve as a precise replication of reciprocating engine dynamics, and despite the limitations it provides valuable insight into fundamental combustion chemistry with non-carbon fuel blends and strategies to maximize performance and minimize emissions. Used in concert with experimental measurements of polyfuel engines, this provides a path to interpret experimental results and refine the chemical kinetic mechanisms and model assumptions to better simulate the effects of low- and non-carbon fuel inputs for faster and more reliable polyfuel engine development.

2.6 Conclusions

In this study, chemical kinetic models are presented to simulate the impact of low-carbon fuel blends of natural gas, hydrogen, and ammonia in reciprocating-piston spark-ignition engines. The Cantera simulation environment is used in conjuction with a detailed chemical-kinetic mechanism to calculate species evolution and thermal gas properties at constant-volume equilibrium and a time-resolved engine simulation. Equilibrium simulations illustrate fundamental differences in oxidation of the pure low-carbon fuels relevant to combustion applications. Expansion to a time-dependent reactor network to represent major reciprocating engine components and processes enables temporal analysis of species evolution and assessment of specific emissions, engine efficiency, and output power. The time-resolved engine simulation exposes significant kinetic effects on emissions formation that are not captured in equilibrium simulations. Hydrogen and ammonia addition to natural gas without engine modification provides near-linear reduction in power and CO_2 emission with corresponding increases in fuel conversion efficiency and NO emissions. The most potent benefit observed is a drastic reduction in CO emissions even at low additive volume fractions. The engine model is used to investigate potential approaches to optimize low-carbon polyfuel combustion, with maximization of compression ratio providing comprehensive benefit to all fuel blends. Fuel-lean equivalence ratios facilitated by hydrogen addition to natural gas and ammonia shows potential for high fuel conversion efficiency and emission reduction. Tailoring of fuel component mixing ratios may benefit the high CO_2 and NO emissions observed with lean combustion of natural gas and ammonia, respectively. Complementary engine technologies such as exhaust aftertreatment and forced induction may assist in mitigating emissions and power loss in these lean-burn polyfuel engines. Sensitivity to valve timing was also explored with the model, and showed that engines equipped with variable valve actuation systems can leverage higher efficiencies of the Miller/Atkinson cycle by modulating intake valve closing and exhaust valve opening times. This demonstrates potential to improve overall engine adaptability to transient requirements in load balancing and on-demand power generation,

but requires tuning with respect to engine speed and consideration of fuel composition to balance tradeoffs in specific emissions. These insights provided by the engine simulation model are valuable for refining combustion strategies for high-efficiency and low-emission engines fueled with low-carbon blends. The time-resolved speciation is synergistic to the high-speed exhaust sensors that are developed in the remainder of this dissertation, serving as foundation to interpret experimental engine measurements and informing refinement of the simulation mechanics.

CHAPTER 3

Background on mid-infrared laser absorption spectroscopy

Laser absorption spectroscopy (LAS) has seen increasing use over the past few decades as a diagnostic tool to characterize thermochemistry in complex, reacting flows typical of combustion systems. LAS provides certain advantages as an optical diagnostic, facilitating non-intrusive in-situ measurements in harsh environments that present logistical and material challenges in alternative techniques. The underlying measurement principle provides calibration-free measurements of crucial gas properties (e.g., temperature, species concentration, pressure, velocity) within convoluted reacting mixtures. High-bandwidth optoelectronics help achieve MHz-rate measurement temporal resolution to capture dynamics at the timescales of combustion cycles and chemical-kinetic evolution. Recent advances in laser and detector systems have expanded usable hardware from the visible and near-infrared regime historically driven by the telecommunications industry to the mid-wave infrared (3-8 µm). This allows application of LAS methods to target the fundamental rovibrational absorption bands of several species valuable for combustion and emissions analysis (e.g., carbon oxides, nitrogen oxides, hydrocarbons). Figure 3.1 displays the mid-infrared absorption strength of a selection of these species at elevated temperature of 1000 K. The fundamental absorption bands exhibit orders of magnitude higher absorption strength relative to near-infrared bands, which increases measurement sensitivity and lowers optical packaging constraints. Leveraging these advancements in photonics facilitates sensitive tracking of combustion reactants (CH_4, NH_3), intermediates (CO), products (CO_2), and pollutants (NO,

NO$_2$, N$_2$O) to characterize combustion progress and emission formation. This chapter discusses the fundamental science of laser absorption spectroscopy and details the experimental methods used to perform measurements of thermometry and species concentrations which serve as the basis for the sensor development targeted for exhaust analysis in reciprocating engines.
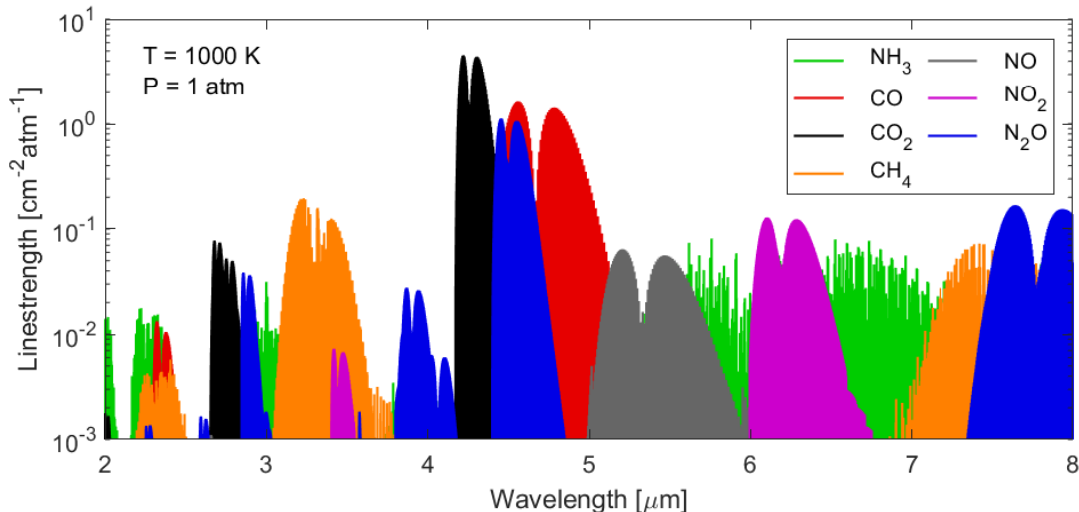
Figure 3.1: Infrared absorption linestrengths of species relevant to low-carbon combustion at elevated temperature (1000 K). Spectral simulation parameters obtained from the HITEMP and HITRAN databases [11, 12].

3.1 Fundamentals

Laser absorption spectroscopy is a technique that leverages the unique characteristics of light-matter interactions of specific molecules across the elecromagnetic spectrum. The energy stored in molecules is contained in a series of quantized energy states across different modes including molecular translation, rotation, vibration, and electronic states. These quantum energy states are determined by molecular structure, and so each specific molecule has a unique set of these energy states. Absorption occurs when a molecule transitions from an initial energy state to a higher energy state by absorbing a photon with energy corresponding

to the difference between these two states. Photon energy is determined by electromagnetic frequency (or alternatively wavelength) and specific wavelengths of light that resonate with the changes in energy states of molecules can be related through Planck's Law in Eq. 3.1:

$$\Delta E = E_{upper} - E_{lower} = \frac{hc}{\lambda} = hc\bar{\nu} \tag{3.1}$$

where h is Planck's constant ($6.33 \cdot 10^{-34}$ J·s), c is the speed of light ($3 \cdot 10^8$ m/s), λ is the wavelength of light typically expressed in nm or µm, and $\bar{\nu}$ is the spatial frequency of light in wavenumber [cm^{-1}]. The unique energy state distribution of specific molecules results in an equally unique distribution of resonant wavelengths of light, often referred to as the "spectral fingerprint". In the infrared region, these wavelengths resonate with rovibrational molecular transitions, so-called as they are single transitions comprised of changes in both rotational and vibrational quantum energy states.

Absorption spectroscopy is governed by the Beer-Lambert Law in Eq. 3.2 which relates molecular absorption to the attenuation of light traveling through an absorbing medium.

$$T_\nu = \left(\frac{I_t}{I_0}\right)_\nu = exp(-k_\nu L) \tag{3.2}$$

T_ν is the fractional transmission of light at frequency ν with I_0 and I_t as the incident and transmitted light intensity, respectively. k_ν is the spectral absorption coefficient [cm^{-1}] and L is the optical path length [cm] over which absorption occurs (i.e., absorption path length). The product $k_\nu L$ is the spectral absorbance, also referred to as α_ν. For a system of discrete transitions j of species i, the total spectral absorbance can be related to gas properties through Eq. 3.3:

$$\alpha_\nu = -ln\left(\frac{I_t}{I_0}\right)_\nu = \sum_j PX_i S_j(T)\phi_j(\nu, T, P, X_i)L \tag{3.3}$$

Here, P is the gas pressure [atm], T is temperature [K], and X_i is the mole fraction of the absorbing species i. $S_j(T)$ [cm^{-2}atm^{-1}] is the temperature-dependent absorption linestrength,

and ϕ_j is the normalized lineshape function. The temperature-dependent linestrength for each transition j at temperature T is based on fundamental quantum properties through Eq. 3.4:

$$
\begin{aligned}
S_j(T) = & S_j(T_0) \frac{Q(T_0)}{Q(T)} \left(\frac{T_0}{T}\right) exp\left[-\frac{hcE_j^{"}}{k}\left(\frac{1}{T} - \frac{1}{T_0}\right)\right] \\
& \cdot \left[1 - exp\left(\frac{-hc\nu_{0,j}}{kT}\right)\right]\left[1 - exp\left(\frac{-hc\nu_{0,j}}{kT_0}\right)\right]^{-1}
\end{aligned}
\tag{3.4}
$$

where T_0 is the reference temperature, Q is the species partition function, $E_j^{"}$ is the lower state energy of the transition, $\nu_{0,j}$ is the center frequency of the transition, and k is the Botlzmann constant $(1.38 \cdot 10^{-23}$ J/K$)$. The normalized lineshape function ϕ models the spectral dependence of absorbance for a given transition and by definition integrates to 1:

$$
\int_{-\infty}^{+\infty} \phi \, d\nu = 1
\tag{3.5}
$$

In combustion gas flows this lineshape function is typically modelled by the Voigt function ϕ_V in Eq. 3.6 which is a convolution of Gaussian and Lorentzian distributions arising from Doppler and collisional broadening, respectively.

$$
\begin{aligned}
\phi_V(\nu) &= \phi_D(\nu_0)\frac{a}{\pi}\int_{-\infty}^{+\infty}\frac{exp(-y^2 dy)}{a^2 + (w-y)^2} \\
&= \phi_D(\nu_0)V(a,w)
\end{aligned}
\tag{3.6}
$$

where $\phi_D(\nu_0)$ is the Doppler linecenter magnitude, a is the Voigt "a" parameter, w is the nondimensional line position, and y is the integral variable:

$$
\phi_D(\nu_0) = \frac{2}{\Delta\nu_D}\sqrt{\frac{ln2}{\pi}}
\tag{3.7}
$$

$$
a = \frac{\sqrt{ln2}\Delta\nu_C}{\Delta\nu_D}
\tag{3.8}
$$

$$w = \frac{2\sqrt{ln2}(\nu - \nu_0)}{\Delta\nu_D} \tag{3.9}$$

$$y = \frac{2u\sqrt{ln2}}{\Delta\nu_D} \tag{3.10}$$

The values $\Delta\nu_D$ and $\Delta\nu_C$ are the Doppler and collisional widths, defined as full-width at half-maximum (FWHM) and given by Eqs. 3.11 and 3.12:

$$\Delta\nu_D = \nu_0(7.1623 \cdot 10^{-7})\sqrt{\frac{T}{M}} \tag{3.11}$$

$$\Delta\nu_C = P\sum_i X_i 2\gamma_{k-i} \tag{3.12}$$

where M is the molecular weight of the absorbing species. The collisional width for species i depends on the broadening coefficients $2\gamma_{k-i}$ with all other present species k and is given by Eq. 3.13:

$$2\gamma_{k-i} = 1.013 \cdot 10^6 \sigma_{ki}^2 \sqrt{\frac{8}{\pi\mu_{ki}kT}} \tag{3.13}$$

Here, σ_{ki} is the optical collision diameter and μ_{ki} is the reduced mass. The temperature dependence of collisional broadening is modeled by the power law in Eq. 3.14 with knowledge of the temperature exponent N:

$$2\gamma(T) = 2\gamma(T_0)\left(\frac{T_0}{T}\right)^N \tag{3.14}$$

These equations provide the theoretical basis of laser absorption spectroscopy grounded in quantum mechanics and gas dynamics. Theoretical calculations and fundamental spectroscopy studies provide values for these physical parameters which are used in subsequent sensor applications to interpret measurement signals and infer gas properties. Experimental techniques such as scanned-wavelength direct absorption spectroscopy help simplify the computational interpretation of measurement signals for straightforward data reduction and is discussed in the next section.

3.2 Scanned-wavelength direct absorption spectroscopy
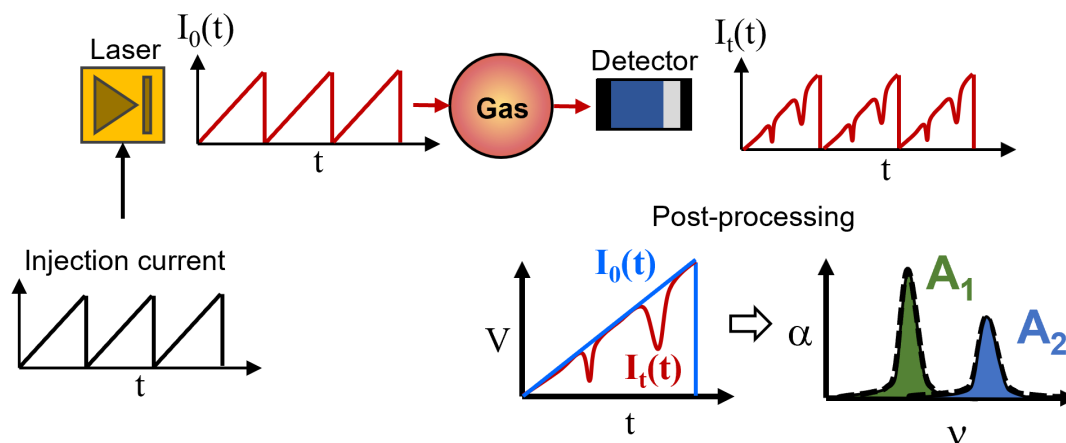
Figure 3.2: Simplified schematic of the scanned-wavelength direct absorption technique in LAS.

Scanned-wavelength direct absorption spectroscopy (DAS) is one of the most widely used LAS techniques as it provides simplicity in optical setup and signal post-processing. Mid-infrared DAS typically utilizes tunable semiconductor lasers including diode lasers, interband cascade lasers (ICLs) and quantum cascade lasers (QCLs). These lasers generate output light with narrow frequency content, making them suitable to probe individual absorption transitions with high spectral resolution. Wavelength-scanning is achieved by modulating the injection current of the laser, which generates a simultaneous modulation of output light intensity and wavelength. In a typical DAS experiment, illustrated in Fig. 3.2, the laser light is modulated at wavelengths that resonate with absorption transitions of the target molecules. This output light is directed through the gas flow of interest, and the transmitted light intensity is collected by a photodetector. In signal post-processing, the incident and transmitted intensity signals can be compared to reconstruct the time-domain absorption against the baseline intensity. With knowledge of the laser tuning characteristics, this allows domain transfer into the spectral domain and calculation of spectral absorbance α_ν through the Beer Lambert Law in Eq. 3.3. Scanning over the entire absorption feature allows integration of the lineshape function to calculate a total absorbance area A which

simplifies Eq. 3.3 into a direct and linear relationship with gas properties:

$$A = \int_{-\infty}^{\infty} \alpha_\nu d\nu = \int_{-\infty}^{\infty} -\ln\left(\frac{I_t}{I_0}\right)_\nu d\nu = X_i S(T) PL \tag{3.15}$$

This integration step removes the dependence of the measurement on specific spectral lineshape parameters and need for calibration or knowledge of complete gas composition and relevant collisional broadening parameters. To simplify computational lineshape integration while increasing SNR in the presence of experimental or optical noise, integration can be performed through a nonlinear fitting of the measured absorbance with analytical expressions that approximate the Voigt profile [81, 82]. When gas temperature is unknown, it can be calculated through simultaneous measurement of two absorption transitions of the same molecule through Eq. 3.16, known as two-line thermometry.

$$R = \frac{A_1}{A_2} = \frac{S_1(T)}{S_2(T)} = f(T) \tag{3.16}$$

By calculating the ratio R of the absorbance areas of two lines (1 and 2), all factors of pressure, pathlength, and concentration are removed and this ratio becomes solely a function of temperature which can be solved with a simple bisection method. An accurate measurement of temperature with this method depends on the sensitivity of the ratio R to temperature which is dictated by the difference in lower state energy of the two measured absorption transitions as in Eq. 3.17.

$$\left|\frac{dR/R}{dT/T}\right| \approx \left(\frac{hc}{k}\right) \frac{|E_1'' - E_2''|}{T} \tag{3.17}$$

This DAS method therefore provides a straightforward method to calculate gas temperature and species concentration with a simple optical arrangement. A measurement principle grounded in physical properties of light and molecular energy states and simplified with lineshape integration in the DAS technique provides quantitative measurements in unknown gas compositions without the need for calibration. This makes the technique ideal for detection

of trace emissions concentrations in reciprocating engine exhausts with complex reacting mixtures, and so is the focus of LAS sensor development in the following chapters.

CHAPTER 4

High-pressure and high-temperature gas cell for absorption spectroscopy studies at wavelengths up to 8 µm

*The contents of this chapter have been published in the journal **Journal of Quantitative Spectroscopy & Radiative Transfer** under the full title 'High-pressure and high-temperature gas cell for absorption spectroscopy studies at wavelengths up to 8 µm' [83].*

This chapter details the design of an optical gas cell to facilitate mid-infrared spectroscopic sensor development for reciprocating engine applications. Measurement precision depends on confidence in spectroscopic parameters of targeted absorption transitions. This motivates validation studies for field-deployable sensors, especially in high-temperature applications where mid-infrared absorption spectra are less well characterized. The optical gas cell facilitates validation of the these absorption spectra of emissions species at temperatures from room temperature to over 1200 K, which covers the range of exhaust gas temperature expected (and later measured) in reciprocating engines.

4.1   Introduction

Many fields utilize spectroscopy for measuring gas properties. The quantitative value of spectroscopic measurements, and gas properties inferred from them, depends on the ac-

curacy of underlying spectroscopic parameters (e.g. line intensities, line-shape characteristics) and their dependence on thermodynamic state (i.e. temperature, pressure) [84]. Thermodynamically-controlled, optically-accessible gas cells provide a stable environment for experimental determination of such spectroscopic properties.

In the field of combustion, absorption spectroscopy is a valuable tool for studying high-temperature gas dynamics, enabling in-situ species-specific measurements of gas properties [59]. Developing quantitative absorption-based sensors for combustion applications requires a detailed understanding of the fundamental spectroscopic parameters of relevant species at high temperatures and high pressures reflective of practical combustion systems. Optically-accessible gas cells capable of sustaining simultaneous high-pressure and high-temperature conditions are important for studying the spectroscopic characteristics of these species.

In recent years, multiple gas cell designs have been demonstrated to allow spectroscopic studies at elevated temperatures and/or pressures [85, 86, 87, 88, 89], commonly employing ceramic materials and sapphire in their construction [87, 88]. The high melting point of ceramics and strength and thermal shock resistance of sapphire are ideal for high-temperature environments (>1000 K). Gas cells built using ceramic construction with sapphire windows have been used to obtain spectroscopic measurements at temperatures up to 1700 K [88]. Few designs have been shown to simultaneously withstand high pressures (>50 atm). Notably, Christiansen et al recently demonstrated the first recorded spectroscopic measurements of CO_2 at >1000 K and >100 atm using a cell designed with sapphire windows bonded to ceramic tubes [87]. These designs enable novel spectroscopic studies of numerous near-infrared (and some mid-infrared) molecular absorption bands.

However, for many combustion-relevant species, fundamental vibrational frequencies lie in the mid-infrared region beyond the transmission window of sapphire. The high absorption strength of these fundamental bands is important in enabling sensitive measurements in applications with short optical pathlengths or small molecular concentrations [59]. Sapphire
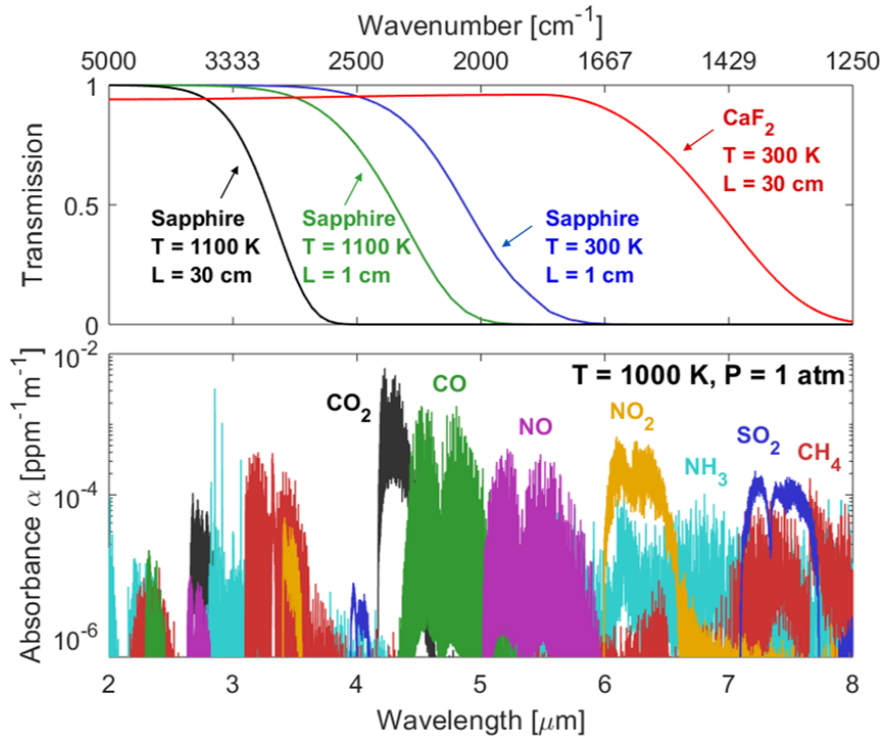
Figure 4.1: Transmission of light through sapphire [13] and calcium fluoride [14] (top) compared to absorption spectra of species relevant to combustion [15] (bottom).

optical windows—which exhibit exceptional transmission in the near-wave infrared—become opaque in the mid-wave infrared ($\sim$5 μm). Moreover, elevated temperatures shift the sapphire transmission cut-off towards shorter wavelengths [90]. As a result, gas cell designs with sapphire windows do not facilitate spectroscopic investigations of many fundamental absorption bands of interest, especially at high-temperature conditions typical of combustion systems. This limitation is displayed in Fig. 4.1, where the strong absorption bands of key species (e.g. CO, NO, NO_2) are inaccessible in part or whole to existing gas cell designs with sapphire windows.

Unfortunately, optical materials that transmit beyond the transmission range of sapphire are generally less robust and require particular concern at elevated temperature. In this work, we present a gas cell that utilizes calcium fluoride (CaF_2) rods. Although using CaF_2 presents its own challenges (which are addressed in this paper), the material transmits light up to 8 μm

in wavelength and thus enables measurements of numerous strong fundamental absorption bands (even at high temperatures) not accessible with existing cell designs. The present gas cell also uses Inconel 625 rather than a ceramic material for the non-optical cell components within the heating zone. This alloy exhibits higher strength at high temperatures than other commonly used metals and is more ductile and elastic than ceramics, thus fatiguing at lower rates [91]. This paper discusses the design of this high-temperature, high-pressure gas cell and the unique technical aspects involved with its construction and operation. The cell is validated for use in spectroscopic measurements by evaluating the temperature uniformity over a range of test conditions and comparing measurement results of well-known spectra to simulations using the current HITEMP [12] and HITRAN [18] databases. The experimental setup is then demonstrated to measure the absorption spectra of CO and CH_4 in the mid-wave infrared at conditions not previously explored, highlighting the unique capabilities of the cell and revealing spectroscopic features not previously observed.

4.2   Gas Cell and Experiment Design

The mechanical design and material selection of the gas cell enable operation at high temperatures (>1200 K), high pressures (>200 atm), and transmission up to 8 μm. Due to compromises in material properties at elevated temperature, these design targets are more difficult to achieve simultaneously. An important objective in the cell design was thus to achieve simultaneous operation at >1000 K in temperature and >100 atm in pressure while accessing the wavelength domain from 0.3–7.5 μm. Fig. 4.2 shows physical details of the gas cell along with relevant mechanical design calculations. The cell body is made from Inconel 625 alloy, chosen for its machinability, ductility, high corrosion resistance, and high thermal conductivity that promotes a uniform temperature over the test region. Additionally, Inconel 625 exhibits high strength and maintains this strength at elevated temperatures, unlike other commonly used metals [17]. Coned and threaded metal-to-metal seals are used (High

Pressure Equipment Co.) with the exception of the cap, which uses an O-ring seal.
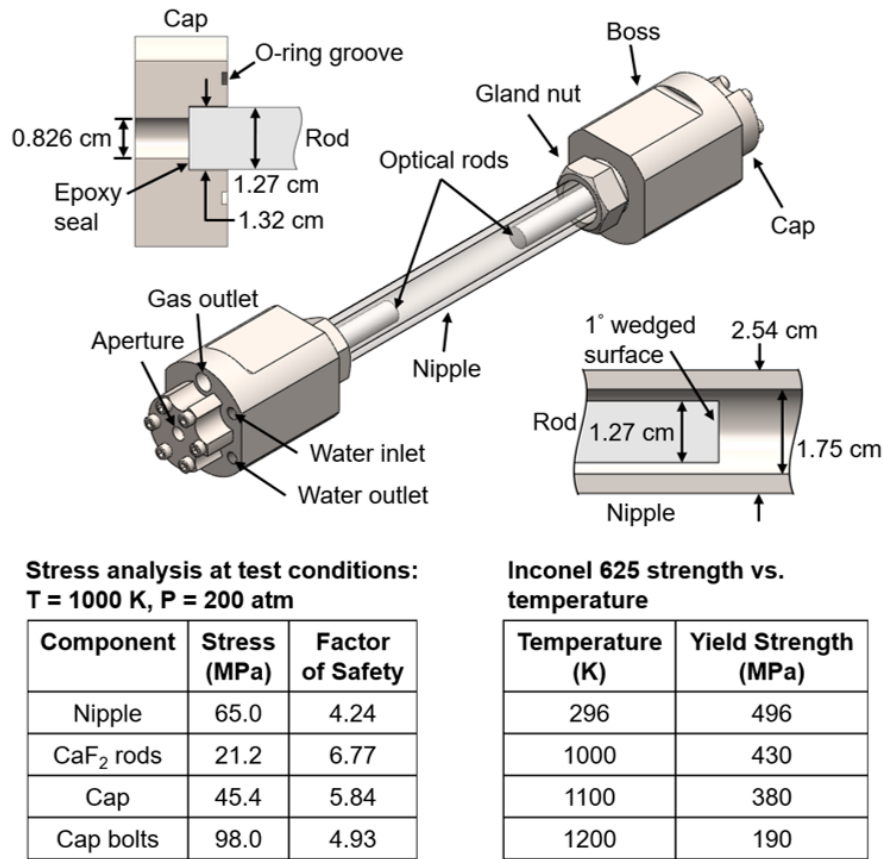
Figure 4.2: Detailed view of the high-pressure, high-temperature gas cell with critical design considerations and material data [16, 17].

A critical design consideration in the gas cell is sealing the optical component to the metal body, while accessing the thermally-uniform, high-temperature test section. The optical components used in this gas cell are interchangeable CaF_2 or sapphire rods 15.0 cm in length, which allow for a low-temperature seal outside of the heating zone, while spanning the thermal gradient of the furnace to access the test section. A 1° wedged surface at one end of each rod reduces constructive and destructive optical interference. CaF_2 is chosen because of its ability to transmit light at wavelengths up to 8 μm. However, CaF_2 is less robust than sapphire [16], especially at elevated temperatures, having lower strength, higher sensitivity to thermal shock, and susceptibility to degrading reaction with water vapor [92].

Sensitivity to thermal shock is associated with relatively high thermal expansion and low thermal conductivity. Clearance around the rod within the cap allows thermal expansion without creating additional stresses. The design of the boss component includes water cooling channels that maintain the caps at low enough temperatures such that they can be sealed by silicon O-rings rated to 478 K. A high-temperature epoxy (EPO-TEK T7109), limited to sustained operation below 573 K, bonds the interchangeable optical rods to the caps and also seals the gas cell. These sealing surfaces lie outside of the heating zone of the furnace and the water cooling prevents failure of these seals, even when the furnace temperature exceeds 1200 K.

Since the rods are bonded only to the caps—which are removable—the gas cell can be easily modified for different applications. When transmittance in longer wavelengths is not required, the CaF_2 rods can be replaced with sapphire rods for increased durability. Additionally, rods of different lengths can be installed for pathlength modification as may be appropriate for different applications.

The gas cell is housed inside an insulated, temperature-controlled furnace with eight heating coils, capable of maintaining an internal temperature of 1473 K. The critical dimensions are shown in Fig. 4.3. The heating zone comprises an internal cavity surrounded by insulation. The measurement pathlength of the gas cell is small relative to the length of the heating zone, promoting a steady, uniform temperature in the test region. Cooling channels in the cell are located near the boundary of the heating zone.

Chilled laboratory water delivered to the cooling channels at 8 gallons per hour in each boss maintains the operating temperature of the caps under the limits of the O-rings and epoxy. Temperatures are monitored with multiple K-type thermocouples attached to the nipple of the gas cell and equally spaced over the test region. Their positions are shown in Fig. 4.3. The cap temperatures are also monitored to ensure safe operating conditions for the seals during experiments. All thermocouples used have an accuracy of 0.75% for the expected operating temperature range and these uncertainties are shown as error bars in
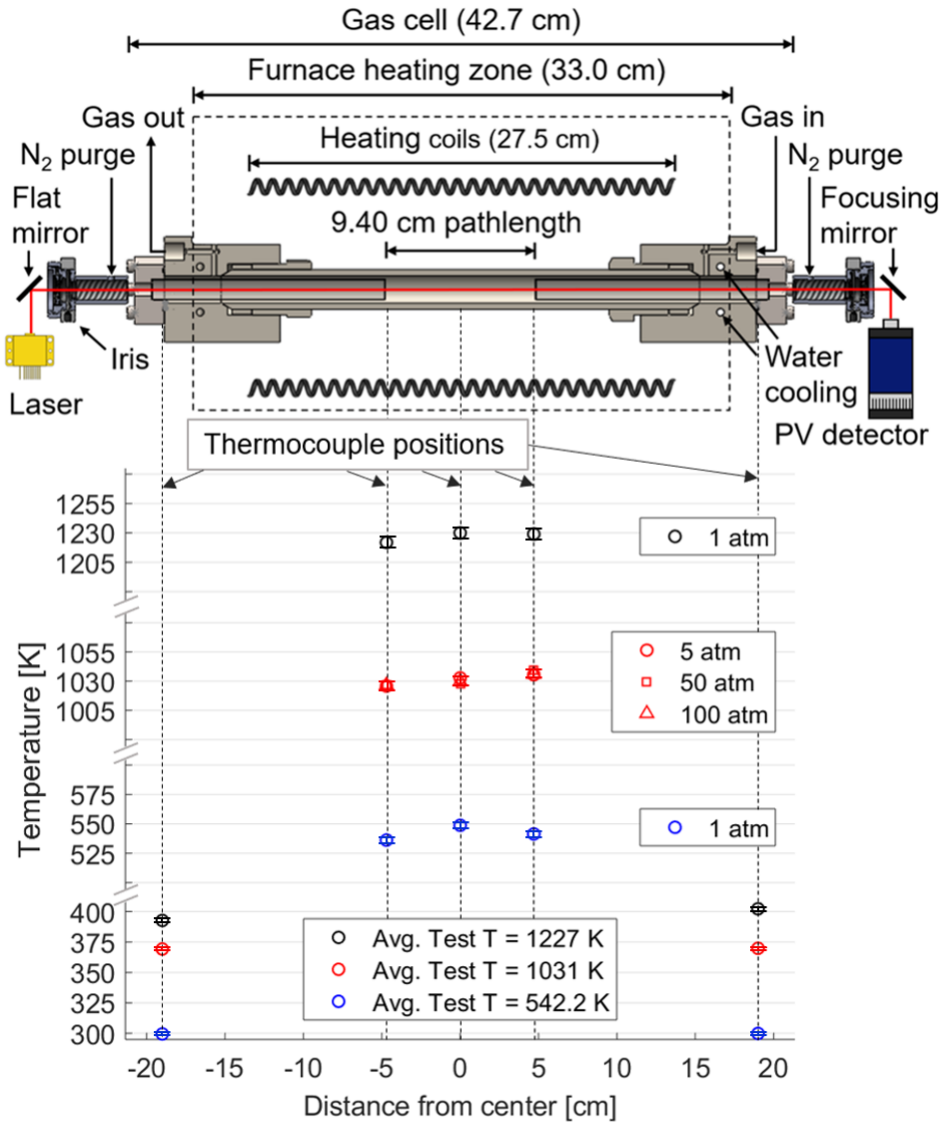
Figure 4.3: Schematic of experimental setup for spectroscopic measurements through the high-P/T gas cell, displayed with measured temperatures at representative operating conditions

Fig. 4.3. The test gas is introduced to the test cavity via channels in the boss as shown in Fig. 4.3, and delivered to the gas cell through stainless steel tubing connected to a gas manifold. Pressure transducers connected to this manifold provide measurements of the pressure inside the gas cell. For test pressures up to 3000 psig, variable capacitance pressure transducers (Setra GCT-225) are used with an accuracy of $\pm 0.25\%$ of the full scale. For test

pressures below 1000 Torr, a dual capacitance manometer (MKS Baratron 627B) is used with an accuracy of $\pm 0.12\%$.

The optical rods traverse the thermal gradient of the heating zone and form the optical pathlength (9.4 cm). This short pathlength is conducive to studying strong fundamental rovibrational transitions in the mid-infrared. The length of the rods also reduces the likelihood that the windows will crack during high pressure experiments. At elevated temperatures, changes in the optical pathlength due to thermal expansion must be considered. For example, it was determined that for sapphire rods, the pathlength increases by $2.7 \pm 0.5\%$ at 1230 K; with the uncertainty due to variation in data for the different coefficients of thermal expansion. As mentioned, CaF_2 degrades significantly in the presence of moisture above 873 K [92], and more slowly at lower temperatures, so a purge system was developed, as shown in Fig. 4.3, to supply a continuous flow of dry inert N_2 to the outside surface of these rods to prevent degradation of the optical surface by humid ambient air. This purge system includes irises on one end that promote the N_2 flow towards the rods while allowing optical access to the gas cell.

4.3   Validation Testing

The sealing of the gas cell—and subsequent purity of the mixtures under investigation—is critical to the accuracy and reliability of spectroscopic measurements. Typical measurement durations span about 20–90 seconds, from the introduction of the test gas into the cell to the capture of the data. The effect of leak rate on the measurement must be negligible at pressures of interest. The tightness of the gas cell was evaluated under expected operating conditions (high pressures, high temperatures). Under vacuum, the leak rate was measured as 6 mTorr/min at 300 K and 38 mTorr/min at 1000 K. Under 103 atm pressure at 1000 K, the leak rate is approximately 0.3 atm/min (or 0.26%/min) with pure helium as the test gas. At the maximum design and test pressure of 204 atm and 300 K, the leak rate was

approximately 0.4%/min. It should be noted that given the leak rates at these high pressures, the user must exercise caution and properly exhaust the leaked gases from the laboratory.

A known and uniform gas temperature (monitored by aforementioned thermocouples shown in Fig. 4.3) in the test section is also critical for accurate and reliable measurements. For a test temperature of 542 K, the uniformity over the test region reported by the thermocouples is ±7 K; this number incorporates both the aforementioned sensor accuracy and the variation in measurement across the cell. At a test temperature of 1031 K, the temperature gradient shows no strong relationship with gas pressure, and the average temperature uniformity is ±9 K. At a test temperature of 1227 K, the uniformity over the test region is ±10 K. For temperatures above 600 K, the inherent uncertainty in each thermocouple (±0.75%) exceeds these non-uniformities. The use of thermocouple measurements on the outside of the cell to infer the gas temperature and temperature uniformity inside the cell is justified with a more detailed thermal analysis outlined in the appendix of this manuscript. At the highest temperatures, the water cooling is able to maintain an average cap temperature of 397 K, below the rated temperatures of the epoxy window seals and the cap O-rings.

4.4   Spectroscopic Measurements

To test and further validate the gas cell capabilities, we conducted infrared laser absorption measurements of CO and CH_4 at (1) high temperatures and low pressures, (2) low temperatures and high pressures, and (3) simultaneous high temperatures and high pressures. For all measurements, a scanned-wavelength direct absorption technique was utilized with laser output line-width significantly more narrow than the measured spectral features.

Absorption of several lines of the vibrational overtone band of CO near 2.3 μm were measured with a diode laser in pure (99.5%) CO at 1227 K and 755 Torr using sapphire rods, representing an upper limit in temperature of the cell. These absorbance measurements, along with corresponding simulations made with HITEMP 2010 [12], are shown in
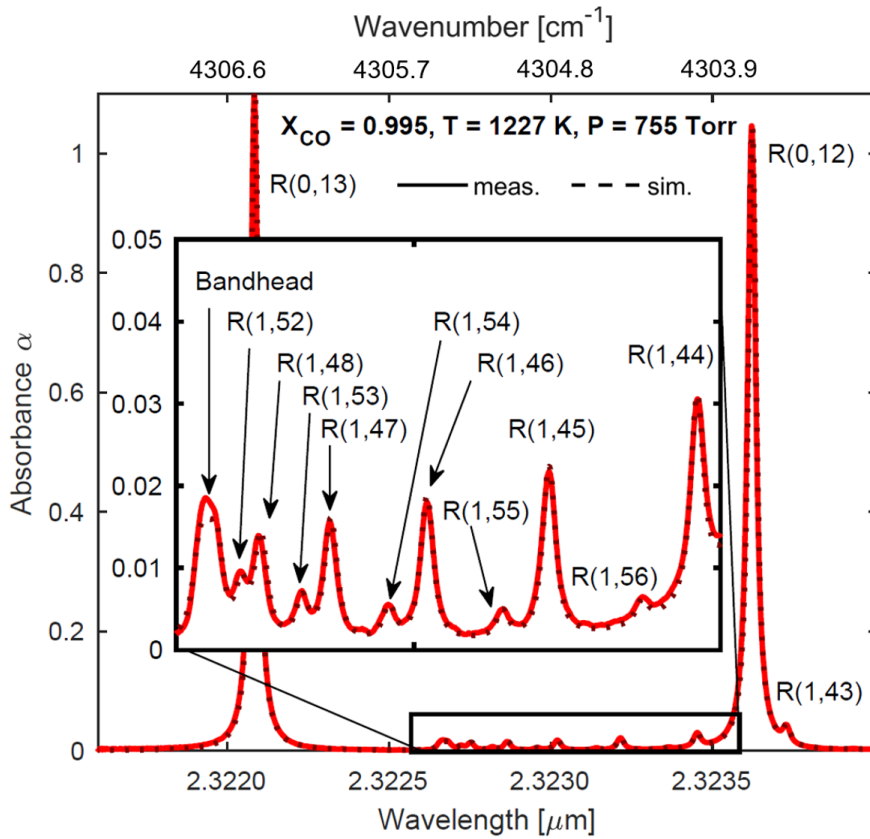
Figure 4.4: Absorbance of the first overtone bandhead of CO at 1227 K with corresponding simulation based on HITEMP 2010 [12].

Fig. 4.4. For the simulation shown, CO-CO line-broadening parameters were approximated using CO-N_2 parameters provided by Hartmann et al [93]. The spectra shown include the well-characterized R(0,12) and R(0,13) lines, the line-strengths of which are reported with 1% uncertainty in the HITRAN database [18]. Given the pressure, path-length, and mole fraction known within 0.12%, 0.5%, and 0.1%, respectively, a direct gas temperature can be determined based on the integrated absorbance areas of these well-known lines. This inference using the isolated R(0,13) line yields a mean temperature measurement of 1217±14 K, which is within the uncertainty of the thermocouple measurement of 1227±10 K. Weaker but discernible spectral lines shown include R(43)–R(48) and R(52)–R(56) with minimum detectable absorbance of approximately 5e-4. Some disagreement is observed in the bandhead, which includes the R(49)–R(51) lines. Data such as these are useful for the refinement

and development of improved high-temperature spectroscopic models.
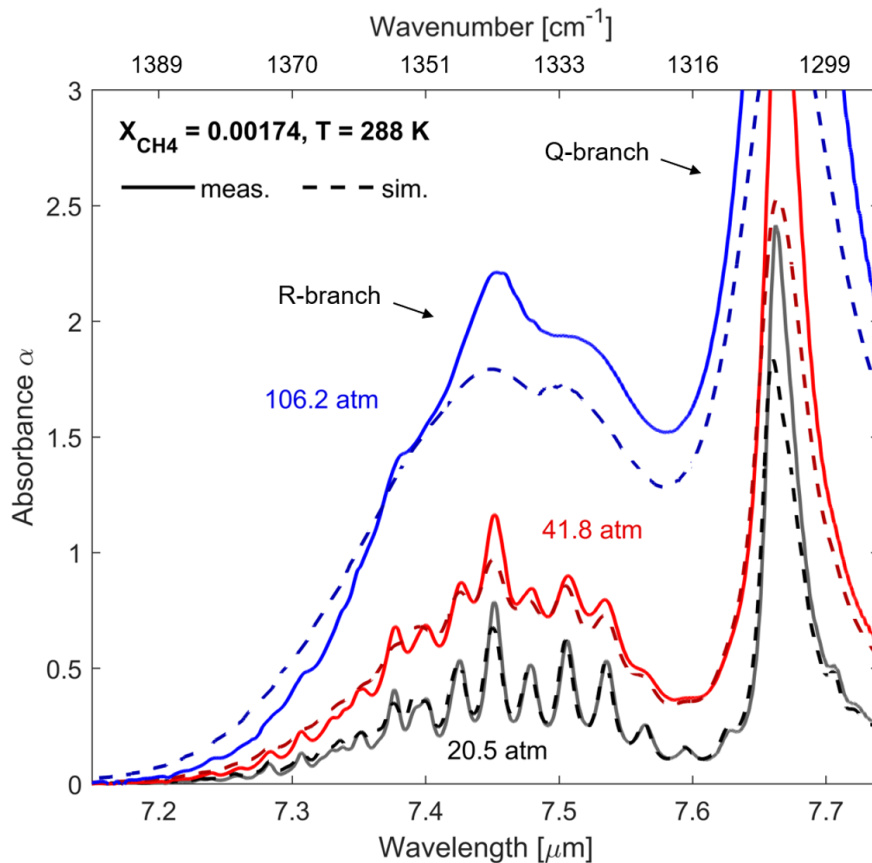
Figure 4.5: Absorbance of the ν_4 band of CH_4 at 288 K and pressures up to 106 atm with corresponding simulations based on HITRAN 2016 [18].

To demonstrate pressure capability and wavelength range, absorption of the ν_4 band of CH_4 was measured using an EC-QCL [94, 95] with a tuning range of 7–7.8 μm (1280–1427 cm^{-1}), and the results are shown in Figs. 4.5 and 4.6. The broad tuning range of the laser enabled spectral resolution of a large fraction of the absorption band. The test gas mixtures comprised small concentrations of CH_4 in an N_2 bath gas created manometrically. These measurements were compared to simulations based on the HITRAN 2016 database [18].

For the low-temperature measurements at 288 K shown in Fig. 4.5, the measured absorbance in the R-branch generally matches the simulation at pressures up to ~20 atm,

while the simulation underpredicts the measurement in the Q-branch. This underprediction may be attributed to line mixing effects that shift absorption intensity from weak lines to strong lines and are more pronounced in crowded spectra [96]. This trend increases in magnitude and is seen in the R-branch as well as the test pressure is increased. At high pressures, line mixing is evident at all test temperatures, as seen in the left of Fig. 4.6. The measured peak absorbance near 7.66 μm (1305 cm^{-1}) and 7.46 μm (1340 cm^{-1}) is consistently greater than that predicted by simulation, while for the weaker portions of the band at wavelengths lower than around 7.46 μm (1350 cm^{-1}), the measurement is lower than predicted. Pieroni et al. [97] and Tran et al. [98] observed similar trends in the ν_3 and ν_4 bands of CH$_4$, supporting the line mixing observations noted here.

To demonstrate and validate the simultaneous high-temperature and high-pressure capability of the cell, absorption of the P(0,31) line of the fundamental vibrational band of CO was measured in a mixture of 0.4% CO in 99.6% N$_2$ at 1031 K and various pressures up to 102.4 atm. This well-characterized CO line has been previously used for measurements in high-pressure combustion environments [99] owing to its relatively high linestrength and isolation from neighboring lines, and thus may be considered a more reliable validation benchmark. The measurement range covers 4.978–4.980 μm (2008–2009 cm^{-1}), which is limited by the scanning range of the DFB-QCL. Absorption measurements are displayed alongside simulations based on the HITEMP 2010 database in Fig. 4.6. Generally, the gas cell measurements show good agreement with simulation. It should be noted that at very high pressures, the background signal used to yield absorbance was observed to attenuate independent of absorption (possibly due to refraction through the dense gas). To account for this effect, the gas cell would be filled with a non-absorbing bath gas (in this case N$_2$) to the target pressure to reproduce this effect and collect a reliable background signal [100].

71
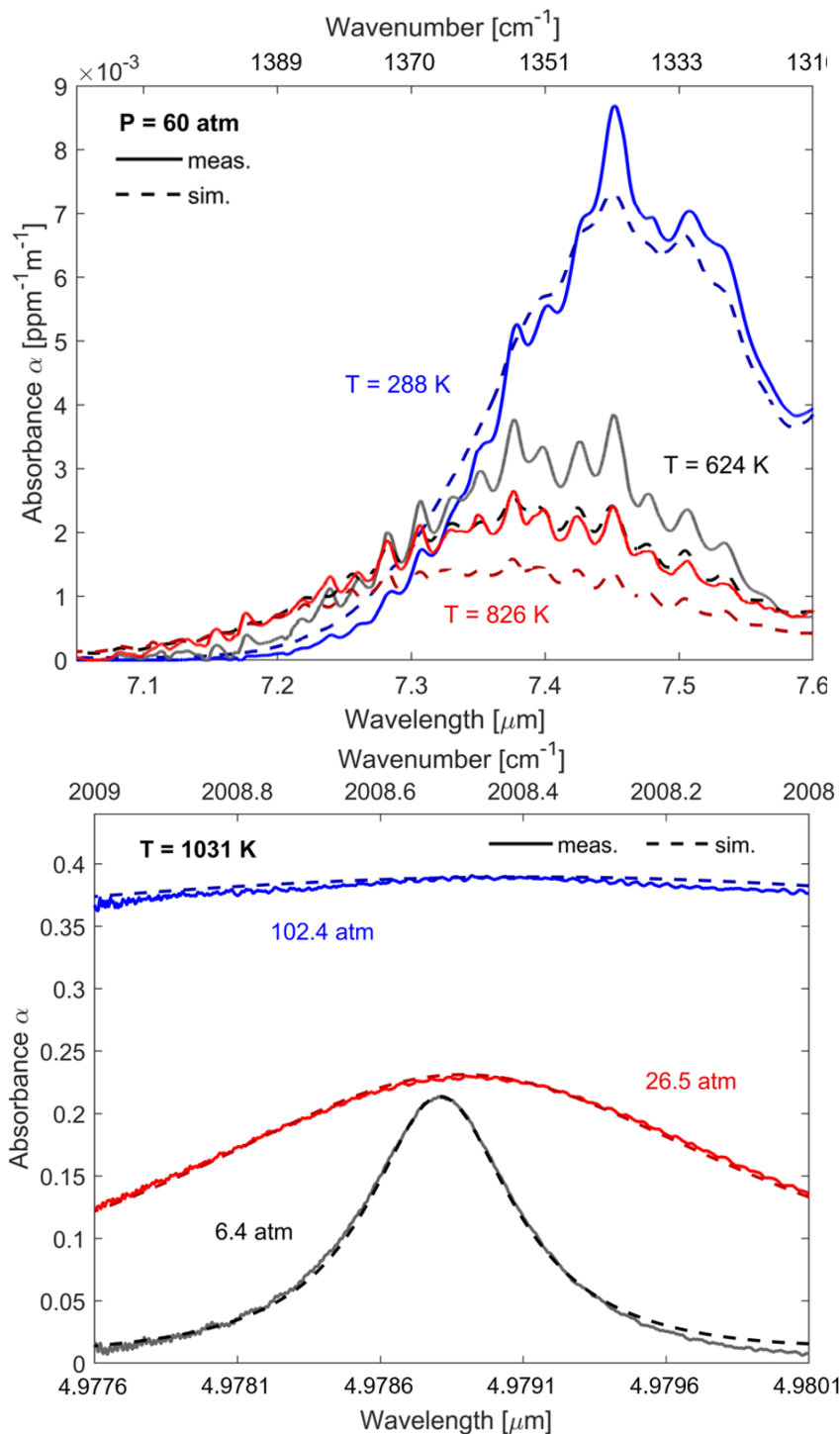
Figure 4.6: Simultaneous high-temperature and high-pressure measurements of the R branch of the ν_4 band of CH_4 (top) and the P(0,31) transition of CO (bottom) with corresponding simulations based on HITRAN 2016 (CH_4) [18] and HITEMP 2010 (CO) [12].

The absorbance of the R-branch of CH_4 at 60 atm and various temperatures is shown in the left of Fig. 4.6. The plots show a clear relationship between increasing gas temperature and the increasing underestimation of molecular absorption in the R branch of the ν_4 band of CH_4 by the simulation. This trend is not fully explained by line mixing alone, as increased temperature reduces gas density. Rather, this disagreement suggests the existence of high lower-state energy lines not listed in the current HITRAN database which are only active at higher temperatures. This suggestion is supported by the recent work of Ghysels et al. [89], who performed measurements of the $2\nu_3$ band of CH_4 near 1000 K. They found significant differences between measured absorption features and those predicted by simulations at high temperatures, attributed in part to missing lines active at elevated temperature.

4.5   Conclusions

An optically-accessible gas cell design presented in this paper demonstrates a capability of sustaining simultaneous high-pressure and high-temperature conditions for well-controlled spectroscopy studies. When access to the mid-wave infrared is needed, the use of CaF_2 optical rods facilitates spectroscopic measurements up to 8 μm. This extends the accessible wavelength range beyond that provided by sapphire optics by approximately 3 μm, enabling studies of the fundamental vibrational absorption bands of several species critical to combustion processes. The use of this gas cell for sensitive spectroscopic measurements was validated with an evaluation of leak-tightness and temperature uniformity over the test region for a wide range of pressures and temperatures, along with satisfactory measurement of a well-understood fundamental transition of CO at high temperatures and high pressures. A maximum test pressure of 204 atm and test temperature of 1227 K highlight the range of the cell when focusing on one state variable, while simultaneous high-temperature (1031 K) and high-pressure (102.4 atm) measurements using the CaF_2 rods were also demonstrated.

The utility of this gas cell design to investigate non-ideal spectroscopic phenomena at

extreme conditions was proven by example measurements. Namely, novel measurements of of the ν_4 band of CH_4 at various high-temperature and high-pressure conditions were made, showing evidence of line mixing effects and missing lines not accounted for in current spectroscopic databases. Future studies using this unique cell design will directly inform the improvement of spectroscopic models at conditions relevant to combustion and other high-temperature environments where quantitative sensing depends on the accuracy of the underlying spectroscopic properties.

CHAPTER 5

Cycle-resolved emissions analysis of polyfuel reciprocating engines via in-situ laser absorption spectroscopy

*The contents of this chapter have been published in the conference proceedings **Proceedings of the ASME 2022 ICE Forward Conference** under the full title 'Cycle-resolved emissions analysis of polyfuel reciprocating engines via in-situ laser absorption spectroscopy' [19].*

5.1   Introduction

Internal combustion (IC) engines are widely used for transportation but also provide efficient on-demand distributed electrical power in case of power outages. However, in these applications, gasoline or diesel fuel usage is slowly decaying owing to high carbon emissions. Policymakers have encouraged shifting towards natural gas (NG) because of its lower CO_2 emission factor; natural gas emits 25% less CO_2 than gasoline for the same heat release [101]. Natural gas engines are commercially available, but if tuned incorrectly for a given load or fuel blend, can suffer from poor performance and cycle-to-cycle variability caused by combustion instabilities, especially when operating fuel-lean for increased efficiency [33]. Further reducing engine carbon footprint can be achieved by employing renewable or carbon-free fuels, such as ammonia (NH_3) and hydrogen (H_2) [102]. However, IC engines running on neat NH_3 or NH_3/H_2 mixtures present some disadvantages, including potentially increased NO_x emissions and limited availability relative to their natural gas counterparts.
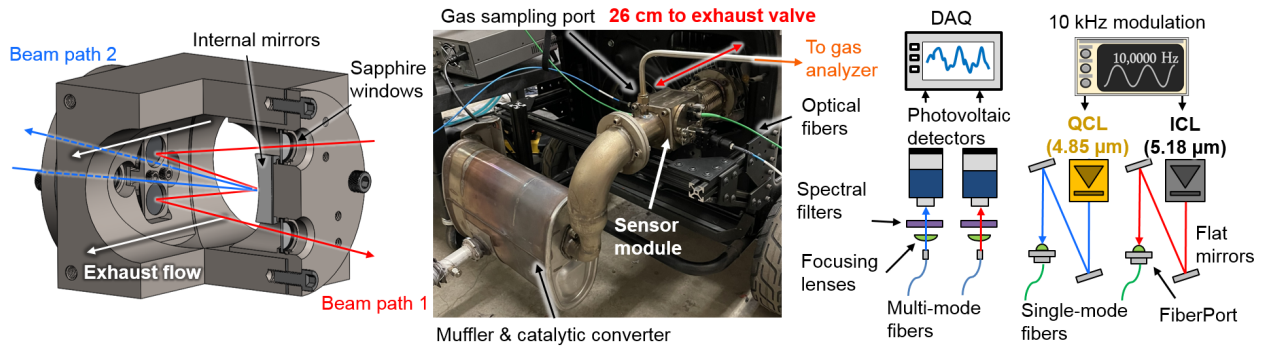
Figure 5.1: *Left*: Design model of exhaust sensor module with optical arrangement for multi-path, multi-pass beam geometry. *Middle*: Sensor including optical fibers and kinematic mounting system installed with the modified exhaust pipe on the Honda EU7000is electricity generator. *Right*: Optical breadboard setup with light sources and optics.

Stable combustion of pure NH_3 in IC engines is difficult to achieve, and experiments in research engines tend to use the addition of H_2 to enhance ignition performance. Mercier et al. showed that partial on-board cracking of pure NH_3 (to form H_2) improved the engine stability, even at low loads [21]. When blending 5–10% H_2 in NH_3 by volume, indicated thermal efficiencies of approximately 36% near stoichiometric air-to-fuel ratio operation were achieved [21, 103], comparable to typical efficiencies of NG engines [33]. Recent progress demonstrated that brake-specific CO_2 emissions could be reduced by 28% by blending 50% NH_3 by volume in natural gas while maintaining stable performance in a 6-cylinder engine originally employed for city buses [20]. With fixed timing of ignition and fuel injection, Moreno et al. found that H_2 addition to CH_4 decreased the brake-specific CO_2 emissions but increased the brake-specific NO emissions, although this could be mitigated by running the engine at leaner conditions [104]. Blending NH_3 and H_2 in natural gas represents a potential strategy for easing transitions to carbon-free combustion while also providing engine operators with the flexibility to quickly respond to new policies and fluctuations in fuel availability / cost-efficiency, which often occur on faster timescales than those of engine or generator replacement. Thus, there is a need to improve the performance and adaptability of IC engine architectures that can sustain reliable and efficient operation with a wide variety

of low-carbon fuel compositions.

IC engine operation with varying load, RPM, and fuel composition is well established, with a variety of methods available that aid the implementation of these novel fuels. For instance, variable spark timing is essential to account for the wide range of ignition delays encountered in NH_3/H_2 blends [103]. Further optimization can be achieved using variable valve actuation (VVA) systems that can adjust one or several parameters of the valve lift profile (e.g., amplitude, duration, and timing). Among the several VVA types explored thus far, the camless VVA system provides superior control flexibility of the entire valve lift profile [105]. For real-time engine optimization in response to varying fuel-blend composition or user demand, spark timing and valve actuation must heavily rely on feedback control informed by sensors which monitor engine performance and emissions in the exhaust manifold. If fed with low-latency intra-cycle data, the camless concept can rapidly adapt ignition, fuel, and valve control to respond to higher-frequency ($>$Hz) combustion behaviors. Such an increased level of performance can only be achieved if the VVA system is paired with sensors that are fast ($>$kHz), quantitative, and capable of reliable operation in the harsh conditions of an IC engine exhaust manifold. In addition to measurement time resolution, the coupling of such sensors as close as possible to the combustion source, such as with minimal distance between the exhaust valve and an exhaust gas sensor, is critical to fast control.

Exhaust measurements can be performed with well-established gas analyzers, which typically include electro-chemical (EC) sensors, non-dispersive infrared (NDIR), and flame ionization detectors (FID). Electro-chemical sensors are cheap, low power, and compact, but struggle in species sensitivity and selectivity, especially when faced with a moist high-temperature environment [106]. For this reason, the exhaust gas typically must be treated (usually desiccated to remove water) to prevent contamination or measurement interference. Non-dispersive infrared sensors for species detection rely on broadband light absorption for enhanced selectivity, although application is limited to certain strongly-absorbing species (e.g., CO_2). Moreover, routine calibration is also usually required for these sensors as their

response tends to deviate with time and use. In addition to the aforementioned difficulties, typical time-resolution of conventional sensors is commonly on the order of seconds and cannot resolve the Hz- to kHz-scale processes of interest in combustion systems that can affect performance. Recently, some NDIR sensors have been developed for kHz-rate measurements of gas properties in IC engines [107, 58]. However, these systems still require calibration to be quantitative and are limited in their target species due to interference associated with poor spectral resolution.

This work details the development of an in-situ exhaust manifold sensor for time-resolved measurement of exhaust gas properties in production-grade IC engines. The work presented here is part of a broader effort to provide rapid detection and feedback of regulated emissions to a camless VVA system to offer efficient fuel flexibility. The sensor is based on time-resolved laser absorption spectroscopy, which is particularly well-suited to this application owing to its calibration-free, quantitative, and high temporal resolution capability up to and above kHz measurement rates. A high-temperature fiber-coupled sensor module enables close coupling to the engine exhaust valve to access combustion exhaust gases immediately after leaving the cylinder. This close-coupled approach reduces sensor latency and increases the quantitative value in measured gas properties and their connection to the in-cylinder combustion processes. The high temporal response reveals more granular emissions evolution by tracking both cycle-to-cycle and intra-cycle variation. We demonstrate the capabilities of this sensor by performing in-situ measurements of gas temperature, carbon monoxide, and nitric oxide in the exhaust pipe of an EPA-certified Honda GX390T2 four-stroke engine, see Fig. 5.1, operating on natural gas (NG) and low-carbon fuel blends incorporating NH_3 and H_2 (up to 10% volume fraction). The high-temperature durability of the sensor coupled with a large dynamic range resulted in cycle-resolved measurements revealing significant combustion inconsistencies and differences in emissions among the various fuel blends, enabling new opportunities for further optimization by incorporating VVA with real-time control.

5.2 Sensor Methodology

5.2.1 Laser Absorption Spectroscopy

Laser absorption spectroscopy (LAS) is an optical diagnostic technique that has been used extensively for quantitative analysis of combustion gases, and detailed discussions of the relevant theory can be found in the literature [59]. In scanned-wavelength direct absorption LAS, a narrow-linewidth laser is tuned across wavelengths corresponding to absorption transitions of target molecules. The laser output beam is directed through the flow of interest, and the transmitted light intensity is recorded on a photodetector. The attenuation of the laser radiation due to molecular absorption can be related to gas properties through the Beer-Lambert Law, shown in Eq. 5.1:

$$A = \int_{-\infty}^{\infty} \alpha(\nu)d\nu = \int_{-\infty}^{\infty} -\ln\left(\frac{I_t}{I_0}\right)_\nu d\nu = X_i S(T) PL \tag{5.1}$$

I_0 represents the incident laser output intensity during modulation while I_t represents the measured transmitted intensity after the light passes through the absorbing medium. Spectral absorbance $\alpha(\nu)$ across the absorbing region is calculated with these recorded signals, where ν [cm^{-1}] is the wavenumber. By integrating over a single spectral line, one can calculate an absorbance area A [cm^{-1}] which can be related to absorbing species mole fraction X_i through Eq. 5.1 with the knowledge of temperature-dependent linestrength $S(T)$ [cm^{-2}·atm^{-1}] (from spectral databases), gas pressure P [atm] (measured or known), and absorption pathlength L [cm] (known from system design).

Gas temperature, when unknown, can be calculated using a two-line thermometry technique [84]. By taking the ratio R of the absorbance areas of two lines (A and B) from a single species, as in Eq. 5.2, the dependence on pressure, pathlength, and concentration in the Beer-Lambert law are removed, and this ratio becomes solely a function of temperature. To achieve a sensitive temperature measurement, the two lines should have differing

dependencies on temperature and this can be achieved by targeting transitions with a large difference in lower state energy.

$$R = \frac{A_A}{A_B} = \frac{S_A(T)}{S_B(T)} = f(T) \tag{5.2}$$

Therefore, the simultaneous measurement of two absorption transitions of the same species provides a straightforward measurement of gas temperature and species concentration. By spectrally-resolving these individual absorption transitions, this method is species-specific, calibration-free, and quantitative. Notably, LAS is readily configurable in non-intrusive, in-situ optical arrangements [59], so high-precision quantitative measurements are possible with minimal disruption to the flow of combustion gases and overall packaging of production IC engines.

5.2.2 Spectroscopic Approach

The emergence of mid-infrared photonics has extended applications of LAS to cover the fundamental rovibrational absorption bands of important combustion species [59]. The inherent high absorption strength of these bands enables increased sensitivity for trace gas detection and use in harsh environments, which is advantageous for deployment in IC engine exhaust systems. Carbon monoxide (CO) and nitric oxide (NO), whose fundamental bands lie near $5\,\mu m$, are the selected species for detection in the IC engine exhaust, as these species both serve as markers of combustion performance and are regulated as exhaust emissions [108]. Furthermore, recent studies into polyfuel combustion involving natural gas, NH_3, and H_2 have highlighted CO and NO_x production as areas requiring further investigation to optimize in-cylinder combustion and facilitate use of these fuels in practical engines subject to emissions regulations [33, 21, 103, 20, 104].

Figure 5.2 shows the target absorption transitions, selected for their absorption strength and lack of spectral interference by other absorbing species (e.g., H_2O, CO_2). CO detection
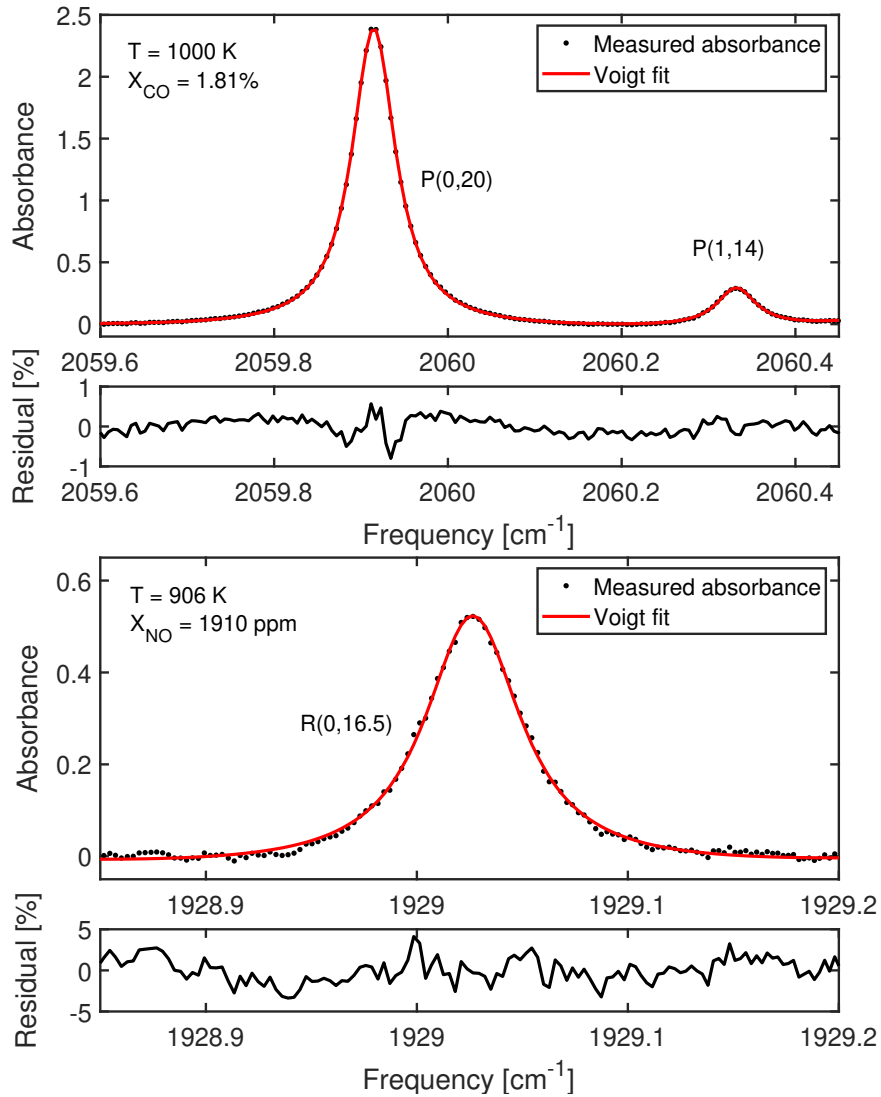
Figure 5.2: Representative absorption spectra of carbon monoxide *(top)* and nitric oxide *(bottom)* measured in the engine exhaust and fitted by voigt lineshapes.

is accomplished through simultaneous measurement of the P(0,20) and P(1,14) transitions near 2059.9 cm^{-1} and 2060.3 cm^{-1}, respectively. A quantum cascade laser (QCL, ALPES Lasers) near 4.85 µm is current-modulated to scan both transitions at a rate of 10 kHz. A Voigt lineshape function is simultaneously fitted to each transition (see Fig. 5.2) to extract the absorbance areas which are subsequently used to infer gas temperature and CO mole fraction through Eqs. 5.1 & 5.2. This line pair has been demonstrated previously to provide precise

measurement of temperature and CO mole fraction in convoluted combustion gases [109, 110]. The NO absorption transition selected for this application is the R(0,16.5) transition near 1929.0 cm^{-1}, which is similarly spectrally-resolved at a rate of 10 kHz with an interband cascade laser (ICL, Nanoplus) near 5.18 μm. After extracting absorbance area via Voigt lineshape fitting shown in Fig. 5.2, the NO mole fraction is calculated through Eq. 5.1 using the gas temperature determined from the CO spectrum. This absorption transition has also previously been measured with success in combustion and IC engine exhaust studies, validating its selection for this application [111, 61]. An exhaust gas pressure of 1 atm is assumed for the mole fraction calculation, and spectroscopic parameters used for extraction of temperature and mole fraction are taken from the HITEMP database, as well as a recent study by Almodovar et al. [12, 112, 113].

5.2.3 Optomechanical Sensor Design

The integration of laser absorption sensors in the exhaust system of a production IC engine faces practical challenges—to achieve intra-cycle resolution of the exhaust pulses, and to minimize sensor latency for feedback on combustion events, the sensing location must be as close to the exhaust valve as possible with minimal disturbance to the flow path. When applied to a continuously operating IC engine, this requires sensor operation at sustained high temperatures and vibration, presenting an exceptionally harsh environment for optics and photonics. Additionally, the sensor integration must be accomplished without compromising engine operation or performance.

The exhaust sensor module design is shown in Fig. 5.1 and is inspired by the work of Diemel et al. [61] with important distinctions enabling operation at higher temperatures. The stainless steel central body and removable port plugs form a compact module that houses the necessary optical elements around a central 50-mm bore to maintain smooth flow of the exhaust gases. The integrated optics form two orthogonal beam paths for simultaneous sensing with two light sources. Optical access is achieved with 1-mm thick, 12.7-mm diam-

eter sapphire windows. The windows are secured in place with retaining rings and graphite gaskets. Silver-coated mirrors are mounted inside the module to facilitate multi-pass beam geometries to extend the optical pathlength and increase measurement sensitivity. The internal mirrors are secured with custom stainless steel clamps and graphite gaskets. The harsh exhaust environment precluded the use of high-temperature epoxies, so mechanical clamping mechanisms and graphite gaskets are used for all mounted optics to create a secure hold and stable alignment while simultaneously preventing fracture of the optics due to differential thermal expansion. This arrangement also allows for easy disassembly and reconfiguration of the optical paths or materials for alternative sensing strategies. The temperature uniformity within the measurement region was evaluated by translating a K-type thermocouple across the 50 mm bore at various load conditions. The steady-state radial temperature is uniform with the exception of a temperature drop-off starting 6 mm from the wall, with wall temperatures 10–13% lower than the measured core temperature depending on the load condition. This minor boundary temperature non-homogeneity has a negligible impact on the absorbance, and was therefore neglected in the LAS post-processing.

The first beam path (#1 in Fig. 5.1) employs a White-cell multi-pass arrangement, which facilitates long optical pathlengths in small volumes [114, 115]. This design features a system of three concave mirrors with matching radii of curvature corresponding to the separation distance. The laser beam enters on one side of the mirror arrangement, undergoes a series of internal reflections, and exits on the same side as the entrance through a second window. The number of internal reflections and achievable optical pathlength is adjustable and set by the angles of the pair of mirrors on the left in Fig. 5.1. The configuration shown has 12 internal passes for an aggregate 61.6 cm pathlength. The second beam path (#2 in Fig. 5.1) uses a simpler, dual-pass configuration with a single internal reflection and resulting aggregate optical pathlength of 11.9 cm. Input light for each path is delivered with single-mode solid-core InF_3 fibers and aspheric collimators to maintain 2-mm diameter Gaussian beams introduced to the multi-pass cells. An adjustable lens tube with a calcium fluoride

plano-convex lens focuses the outgoing light into a 200-µm diameter multi-mode solid-core InF$_3$ fiber. The optical fibers are secured to kinematic optic mounts fastened to aluminum slip plate positioners, which together enable five degrees of freedom (X-, Y- and Z- translation, pitch, and yaw) for fine-tuning of the optical alignment. The schematic on the right of Fig. 5.1 shows the major photonic elements that interface with the exhaust sensor module and are located on a mobile breadboard away from the harsh combustion environment, a configuration enabled by the complete fiber-coupling system. The output beams of the QCL and ICL are each coupled into the single-mode fibers with fiberport alignment stages. The transmitted beams carried by the multi-mode fibers are focused on to two photovoltaic detectors (Vigo PVI-4TE-5) by CaF$_2$ plano-convex lenses mounted to alignment stages that also hold the aspheric fiber collimation packages and narrow-bandpass spectral filters to isolate the laser radiation from the thermal emission of the combustion gases.

The integration of the sensor module into the existing engine exhaust system of the test engine (detailed in Sec. 5.3) involved replacing the stock exhaust pipe with a custom-fabricated exhaust system, shown in the center of Fig. 5.1. A pipe expander mounted to the exhaust port expands the flow diameter from 27 mm to 50 mm while retaining the original O$_2$ sensor. A flexible pipe coupling connects the pipe expander to the exhaust sensor module while damping engine vibrations. This setup places the optical measurement location 26 cm downstream of the exhaust valve. A gas sampling port 5.5 cm downstream of the optical measurement is used to siphon exhaust gases to an emissions gas analyzer, detailed in Sec. 5.3. Downstream of the sensor module, the flow diameter is reduced to 27 mm for mating with the stock muffler and catalytic-converter assembly. This maintains emissions compliance of the engine after integration of the optical diagnostics. This modified exhaust system is secured with vibration-damping mounts to a support structure added to the engine frame for minimal increase of the engine footprint and retention of the original wheel-mounting and mobility.

By integrating the sensor in-stream with close proximity to the exhaust valve, exhaust

gas transit time is short and results in minimal latency relative to combustion. This latency or exhaust gas transit time can be estimated with some simplifying assumptions. First, during the initial opening of the exhaust valve, or blowdown phase, the pressure differential between the high-pressure cylinder and the low-pressure exhaust pipe leads to choked flow across the valve [116]. Second, in-cylinder gas properties including the specific heat ratio can be estimated from combustion simulations. Lastly, with changing cross-sectional areas between the valve and sensor location, gas expansion can be approximated with quasi-1D compressible flow relations. For the test engine used in this work, when assuming 1 mm valve lift and choked flow through the exhaust valve with measured gas properties, in-cylinder combustion gases travel through the modified exhaust pipe and reach the optical line-of-sight within an estimated 7 ms. This corresponds to a conservative estimate of average gas velocity of approximately 40 m/s for the leading edge of the exhaust impulse. Notably, commercial exhaust gas analyzers that rely on gas sampling (and pre-conditioning) from the exhaust stream involve much longer gas transit times on the order of seconds or longer. In-situ measurements using laser absorption reduce the sensor latency due to gas transit from second-scale to ms-scale and on the same order of magnitude as the engine piston motion, which is critical for fast control schemes.

5.3   Experimental Setup

The engine selected for demonstration with the developed laser absorption sensor is a Honda EU7000is generator driven by a single-cylinder SI engine (GX390T2) originally designed for gasoline but modified for natural gas-fueling by Genconnex. This is a commercially-available, EPA-certified engine representing the target application for a fast-response exhaust sensor integrated with real-time control for practical power generation. Table 5.1 lists specifications of the test engine. Aside from the exhaust system modifications detailed in Sec. 5.2.3 to incorporate the LAS sensor module, the engine is maintained in its original configuration.

Model	Genconnex Honda EU7000is
IC engine	GX390T2
Cycle	4-stroke
Bore x Stroke	88 x 64 mm
Displacement	389 cm^3
Compression ratio	8.2:1
Cylinders	1
Valves per cylinder	2
Engine speed	3,300 rpm
Fuel	Natural gas
Equivalence ratio	1
Rated output	5.5 kW
Fueling method	Carburetor
Ignition method	Spark ignition
Ignition timing	Fixed at constant load

Table 5.1: Genconnex Honda EU7000is engine specifications.

While originally controlled by electronic fuel injection, the natural gas conversion now relies on a pressure regulator and orifice to introduce fuel into the intake pipe upstream of the throttle valve. The engine electronic control unit (ECU) adjusts the throttle valve automatically to increase the amount of fuel/air mixture supplied to the engine to match the required power output while remaining at a constant 3,300 rpm. The ECU also adjusts spark timing based on the load applied to the generator and a predetermined engine map. The O_2 sensor is required for engine operation; however, it does not affect the ignition timing. The overhead intake and exhaust valves are pushrod-driven and have fixed valve lift profiles across the engine operating range.

The experimental setup for this investigation is shown in Fig. 5.3. The fuel is supplied by tanks of compressed natural gas, anhydrous ammonia, and hydrogen. Natural gas flowrate is monitored by a thermal-based mass flow meter (Omega FMA 1800) with an accuracy of $\pm 1\%$ of the full scale (50 slm N_2 equivalent). Blending of the natural gas with either NH_3 or H_2 is accomplished with a thermal-based mass flow controller (MKS GE50A) with an accuracy of ± 0.2 % of the full scale (20 slm N_2 equivalent) for the flowrates used in this study. The fuel
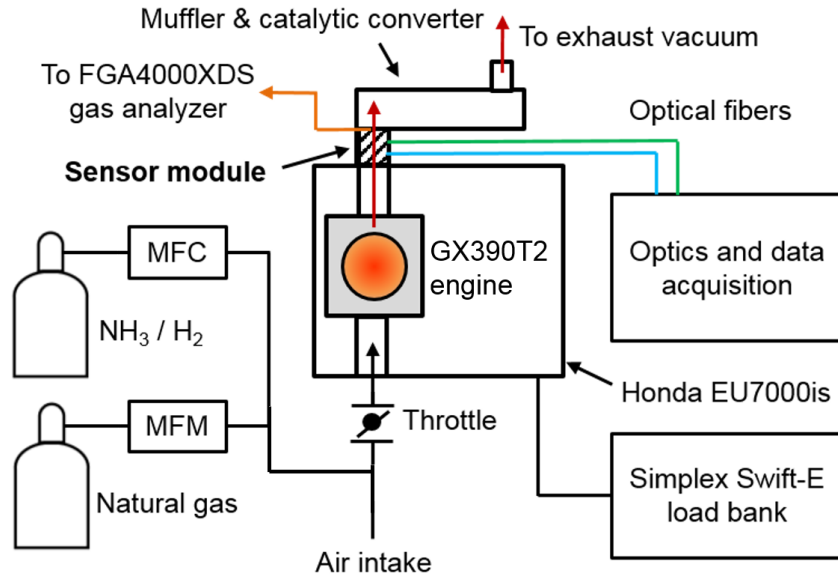
Figure 5.3: Experimental setup for testing with the EU7000is generator.

blending manifold connects to a 3 m long fuel hose leading to the EU7000is fuel intake. The engine exhaust is connected to a vacuum pump system to safely evacuate the gases from the laboratory. A portable resistive load bank (Simplex Swift-e) with a 10-kW capacity is used to apply the desired electrical load to the generator.

A mobile cart next to the test engine holds the breadboard-mounted photonics along with all other optoelectronics and the data acquisition system (National Instruments PXI-6115) controlled through LabVIEW. The optical fibers run between the cart-mounted breadboard and the exhaust sensor module during engine firing. A portion of the exhaust gas is siphoned off from the gas sampling port and transported through a 8 m long sampling tube to an exhaust gas analyzer (Infrared Industries FGA4000XDS). The gas analyzer measures CO and NO_x concentrations with an accuracy of 0.1% and 50 ppm, respectively. The analyzer relies on a NDIR sensor for the CO measurement and an EC sensor for NO_x, with a response time of 2 s.
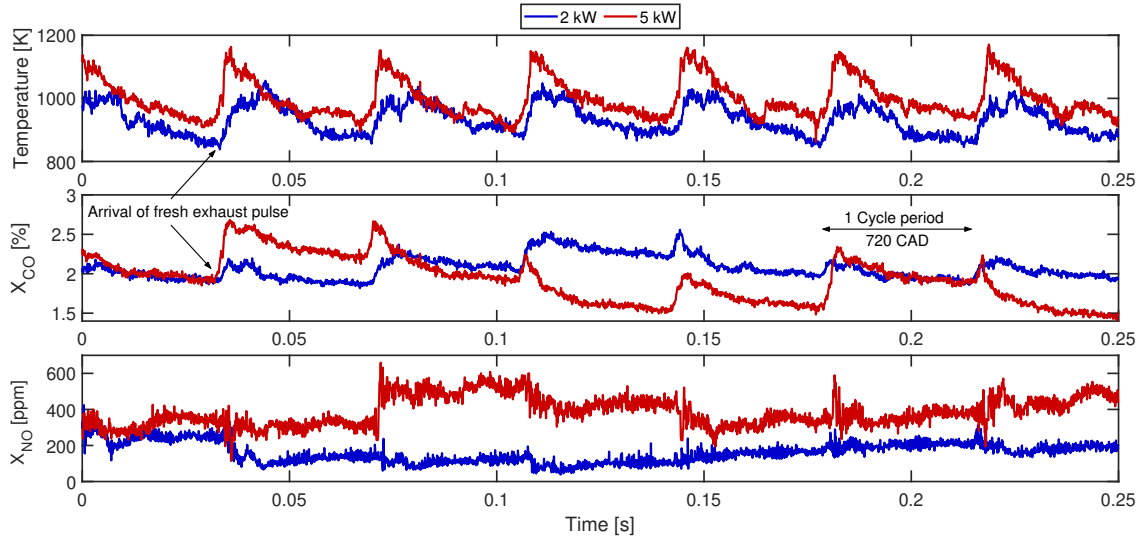
Figure 5.4: Cycle-resolved measurements of exhaust gas temperature, carbon monoxide, and nitric oxide. Engine running on pure natural gas at 3,300 rpm and two applied load conditions, 2 and 5 kW.

5.4   Results

5.4.1   Cycle-resolved Exhaust Sensing

The capability of the developed laser absorption sensor was first tested on the GX390T2 engine fueled with pure natural gas under varying load conditions. With the LAS temporal resolution of 0.1 ms and the engine operating at its standard 3,300 rpm (or cycle frequency of 27.5 Hz), this corresponds to 364 data points per cycle or a resolution better than 2 crank angle degrees (CAD). Figure 5.4 shows sample measurements captured in the engine exhaust at both high and low load. The temperature trace shows clear cyclic variation at the engine frequency of 27.5 Hz. The sharp increase corresponds to fresh exhaust gas traveling through the sensor line of sight when the exhaust valve opens at the beginning of the engine exhaust stroke. Within individual 36 ms cycles at 5 kW load, peak temperature consistently reaches over 1150 K and decreases by over 200 K due to expansion and cooling of the combustion gases as the cylinder depressurizes. Higher temperatures are consistently observed at 5-kW operation compared to the 2-kW operation, as expected due to increased reactant initial
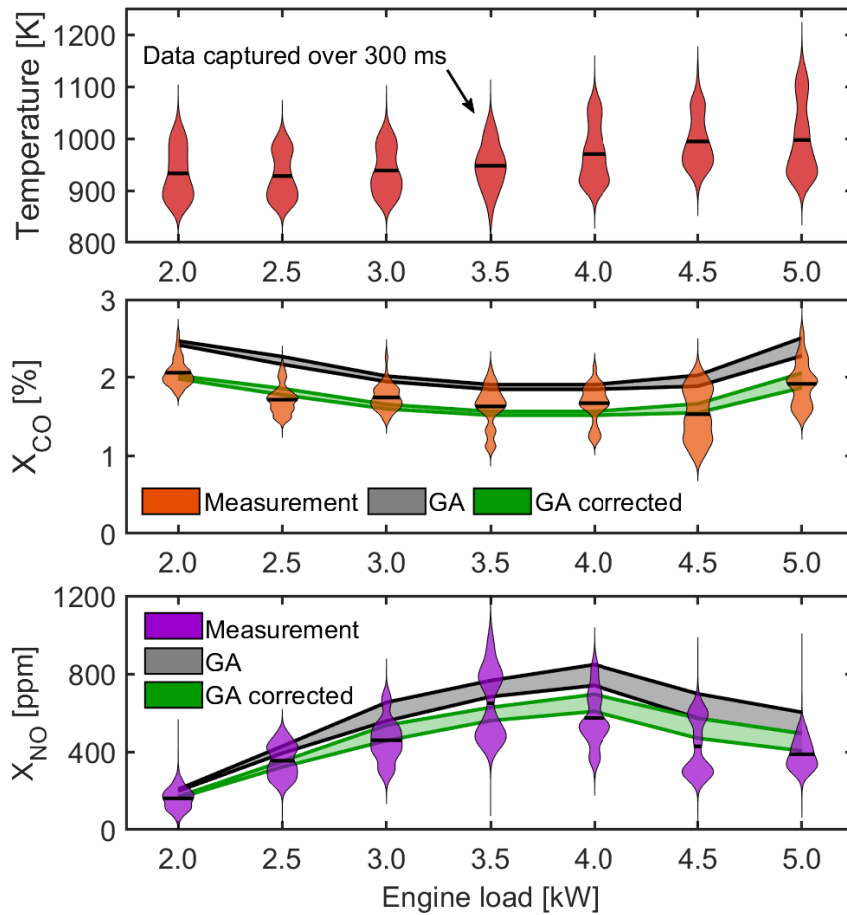
Figure 5.5: *From top to bottom:* temperature, carbon monoxide concentration, and nitric oxide concentration measured in the exhaust gas from 2- to 5-kW loads. Engine running on pure natural gas with simultaneous sampling with the FGA4000XDS gas analyzer (GA). Analyzer readout data shown in grey, with data corrected for loss in water concentration shown in green. Solid black lines within violin plots represent mean values.

pressure and subsequent in-cylinder combustion temperatures. Consecutive exhaust-pulse temperatures for the same condition show consistent profile characteristics and peak temperatures, with fluctuations likely due to inhomogeneity in combustion and transport out of the cylinder. The sensor similarly captures the cycle-resolved characteristics of CO and NO exhaust emissions which are highly dynamic in this engine. The measured CO mole fraction mirrors the intra-cycle peak and decay of measured temperature. This could potentially be due to the retrofitted nature of the test engine which has not advanced the spark timing

to account for slower natural gas flame speeds compared to gasoline. The required spark advance can reach up to 10 CAD [33], and the omission of this adjustment could lead to the combustion reaction persisting after the exhaust valve opens which is supported by the observation of CH emission through the sapphire windows during engine firing. A different trend is observed in the measured NO mole fraction, where intra-cycle variations are less significant compared to the cycle-averaged concentrations. This may suggest that the majority of its formation occurs earlier in the expansion stroke, with remaining temporal evolution potentially due to chemistry in the exhaust pipe or heterogeneous distribution of NO in the cylinder.
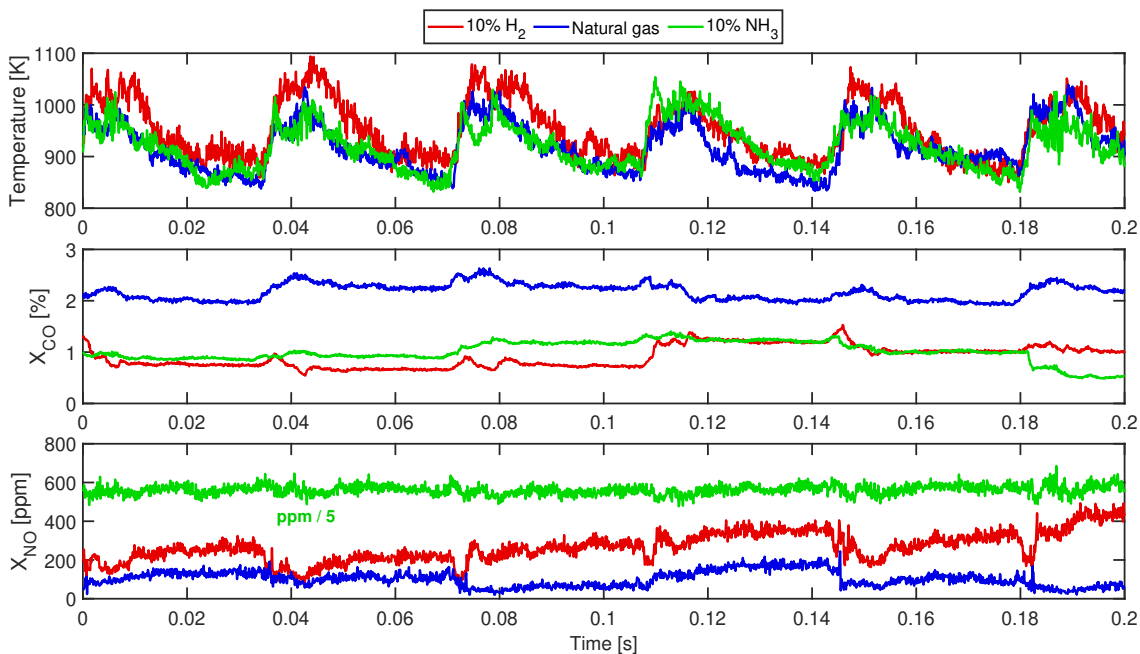
Figure 5.6: Cycle-resolved measurements of exhaust gas temperature, carbon monoxide, and nitric oxide. Engine running with 2 kW applied load and three fuel conditions: 100% natural gas, natural gas with 10 vol. % ammonia, and natural gas with 10 vol. % hydrogen. Nitric oxide emissions for 10% NH$_3$ fueling are scaled for presentation.

While measurement traces of CO and NO exhibit a certain degree of intra-cycle variation, they mostly show an exceptionally high cycle-to-cycle variation at all load conditions despite the relative consistency in measured temperature. Between the two conditions in Fig. 5.4,

there is little difference in mean CO concentration observed in the exhaust, although the data suggest cycle-to-cycle variation is higher during 5-kW operation. Within the 250-ms period presented in Fig. 5.4 for a 5-kW load, the cycle-average CO concentration reaches a maximum of 2.4% and a minimum of 1.7%. Similar cycle-to-cycle variations are encountered in the NO exhaust with maximum and minimum emissions averages of 510 and 310 ppm. These combustion inconsistencies are commonly observed in SI natural gas engines, especially those retrofitted from gasoline engines, but cannot be resolved by conventional exhaust gas analyzers.

The effect of applied load on measured exhaust conditions is illustrated further in Fig. 5.5, containing data captured over a 300-ms measurement interval or approximately 8 engine cycles. The data distributions are represented by violin plots which are wider for higher statistical occurrence. As load increases, both mean and peak temperatures increase steadily up to $\sim$1000 K and $\sim$1200 K, respectively. The measured mole fraction shows more dynamic behavior across the load range, with CO and NO exhibiting inverse dependencies. Minimum CO emissions occur in the 3.0–4.5 kW range, with those same conditions corresponding to peak NO production. This load dependence is expected in SI engines with limited adaptability and the need to strike a compromise across the operating range [116].

Gas analyzer readings are displayed in Fig. 5.5, with the grey shaded region representing the spread of readout values observed over a 30-s interval. The analyzer captures the same trends across the load range visible in the LAS measurements, and agrees reasonably well in magnitude, although on average displays slightly higher concentrations across the range ($\sim$15%). One noteworthy difference between the exhaust sensors is that the gas analyzer relies on a mass-weighted average measurement while LAS uses a non-temporally averaged line-of-sight measurement decoupled from exhaust mass flow rate. Furthermore, the gas analyzer NO_x sensor is sensitive to not just NO, but also NO_2, which can account for >10% of total NO_x emissions; this percentage increases with elevated levels of NO_x [117]. With the gas analyzer separated from the exhaust by 8 m of tubing, any chemistry occurring after the

exhaust gases pass the optical measurement location can lead to discrepancies in both the measured CO and NO concentrations. Most significantly, the gas analyzer includes a filter for removing water vapor prior to exhaust gas measurement. Water concentration can be significant in this case, ~18% in stoichiometric natural gas combustion, and so correcting for this loss in exhaust gas content yields data shown in green in Fig. 5.5. These data more closely agree with those of the LAS sensor which is deployed in the untreated exhaust stream where water vapor is still present. It should be noted that the gas analyzer was calibrated with a certified emissions mixture prior to testing.

The most significant difference in the two emissions sensors is the capture of intra-cycle and cycle-to-cycle trends with the LAS sensor, which enables additional dimensions of analysis critical for real-time engine optimization and control applications. According to the gas analyzer reading, CO exhaust varies from 1.9% to 2.5% across all loads. This 0.6% CO variation is lower than the amplitudes measured by the LAS sensor within a single 300-ms period, spanning from 1% to 2.2% CO for the 3.5–4.5 kW loads. The same observation can be made regarding the NO measurements at each load, with typical 250–800 ppm variations measured by LAS. This highlights a high degree of combustion inconsistency in this commercially-available, EPA-certified engine that is undetected by the gas analyzer. It is notable that the regulated emissions generally exhibit more cycle-to-cycle variation than the measured temperature, indicating the high sensitivity of species formation to operating conditions in this test engine. The high-bandwidth data provide a means to reduce variation through systematic engine refinement, particularly if coupled with real-time control. One such example is the implementation of throttling with a variable lift intake valve. This technique increases fuel/air mixing and turbulence, promoting (i) homogeneous combustion, (ii) higher burning velocities, and (iii) more consistent cycle-to-cycle combustion. Throttling can be tuned in real-time and across the entire operating range of the engine and has been shown to reduce brake-specific fuel consumption by up to 10% [118].

The uncertainty in the measured temperature and mole fraction from the LAS sensor was

calculated via the method put forth in Nair et al. [60] for scanned-wavelength direct laser absorption experiments and based on the Taylor series method of uncertainty propagation. This uncertainty accounts for noise in the measured raw intensities and subsequent extraction of absorbance areas in addition to uncertainty in physical parameters used to determine temperature and mole fraction through Eqs. 5.1 & 5.2, including pressure, pathlength, and tabulated spectroscopic parameters. The temperature uncertainty is dominated by the uncertainty in the measured absorbance area of the weaker P(1,14) transition of CO, and the maximum uncertainties are observed at engine operating conditions associated with low exhaust temperatures and low CO emissions. During standard operation with natural gas fuel, temperature uncertainty lies between 25 K and 31 K with the larger uncertainty corresponding to the minimum intra-cycle temperatures. Maximum uncertainties are reached during 10% NH_3/NG fueling (see Sec. 5.4.2) and range from 40 K to 55 K. The P(0,20) absorption remains high across all operating conditions and leads to a more consistent uncertainty in measured CO mole fraction of 2.9% of the measured value. The uncertainty in NO mole fraction is dependent on engine operating conditions and the large range in resulting NO emissions. An uncertainty of 26 ppm corresponds to minimal NO production (<100 ppm) at low load and pure natural gas fueling, whereas uncertainty at 10% NH_3/NG fueling and maximum NO production (<3400 ppm) is approximately 180 ppm. These uncertainties translate to detection limits (1σ) of 0.07% and 26 ppm for CO and NO mole fraction, respectively.

5.4.2   Polyfuel Emissions Analysis

The application of the LAS exhaust sensor for polyfuel IC engines was investigated by operating the test engine with low-carbon fuel blends of natural gas mixed with NH_3 and H_2 at concentrations up to 10% by volume. Figure 5.6 shows cycle-resolved exhaust measurements of select blends compared to pure natural gas fueling. Across the fuel blending matrix, applied load was kept constant at 2 kW, resulting in consistent ignition timing. The measured temperature remains largely similar between the three fuels even at 10% blending,
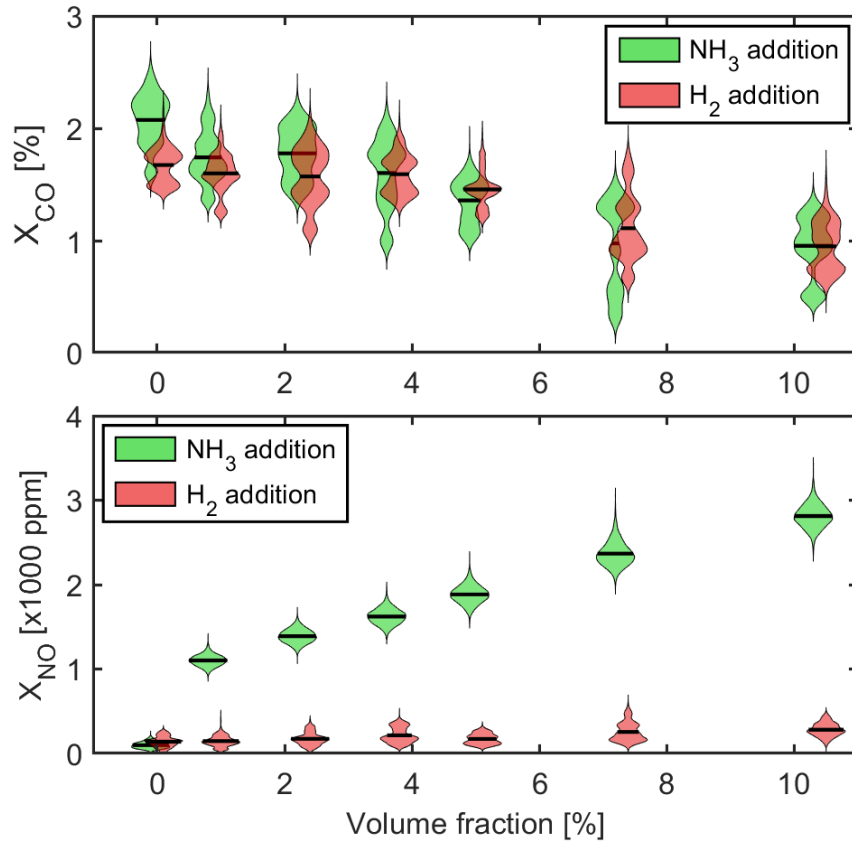
Figure 5.7: Measured exhaust CO concentration *(top)* and NO concentration *(bottom)*, collected over 300-ms interval. Engine load is 2 kW and the fuel is natural gas blended with varying concentrations of either NH_3 or H_2. Volume fractions are matched between the different blending constituents, with data shown offset for visibility.

with slightly higher temperatures observed in individual H_2-enriched cycles due to the higher flame temperatures of H_2 combustion [119].

The effect of NH_3 and H_2 addition in this particular engine is much more drastic for the CO and NO emissions. Both additives reduced CO emissions by approximately a factor of 2 at 10% blending concentrations. There is a relatively small difference in CO reduction between H_2/NG and NH_3/NG blends in these cases, and neither blend shows a substantial change in the cycle-to-cycle consistency. Emissions of NO, however, show stark differences between the two blends. H_2 addition led to an appreciable increase in NO production by a factor of 2 over pure natural gas, however the NH_3/NG blending resulted in an order

of magnitude increase. Additionally, the cycle-to-cycle consistency of NO emissions was noticeably greater during NH_3/NG fueling.

The measured emissions of the test engine fueled with these alternative blends as a function of volume fraction is displayed in Fig. 5.7. Both H_2 and NH_3 addition led to suppression of CO emissions at similar magnitudes. However, H_2/NG blends far outperformed NH_3/NG for minimizing NO emissions. The trends in NH_3 blends corroborate those reported by Oh et al., who reported mild variations in CO emissions and significant increases in NO emissions within 0–10% NH_3 addition while keeping NH_3 slip low [20]. It should be noted that the tests presented in this work were performed at low loads due to safety concerns fueling with premixed H_2/NG mixtures, including the possibility of flashback into the intake pipe upon intake valve opening events. Had the tests been performed at higher loads, then the increase in NO formation with increasing H_2 volume fraction may be more appreciable due to the likely increased in-cylinder combustion temperatures.

The trends of Fig. 5.7 suggest that at these conditions, the reduction in CO emissions is largely driven by the reduced carbon input and that the chemical effect of NH_3 or H_2 addition have similar impact (within the 10% addition). The reduction of CO emissions for H_2 blends was observed in a previous study by Aksu et al. and solely attributed to the reduction of carbon input in the fuel stream [120]. The CO exhaust is, however, marked here with a factor-of-two reduction ($\sim$2% to $\sim$1%) while NG intake is diminished by only 10%. Thus, the reduced CO emissions cannot solely be attributed to the decreased natural gas intake. The similarity of H_2 and NH_3 blends is, upon a first order analysis, unsurprising given that NH_3 is essentially an H_2 carrier and, at high temperature, undergoes H-abstraction associated with H_2 production (among others) [121, 122]:

$$NH_3 + O_2 \longrightarrow NH_2 + HO_2 \tag{R1}$$

$$NH_3 + OH \longrightarrow NH_2 + H_2O \tag{R2}$$

$$NH_3 + H \longrightarrow NH_2 + H_2 \tag{R3}$$

Therefore, CH_4 combustion is likely acting as a trigger for NH_3 splitting via the generation of H and OH radicals that accelerate Reactions R1-R3, generate H_2, and may explain the similarities between the two blends. However, the differences in NO production between the blends can be attributed to different mechanisms. While H_2 combustion often leads to increased thermal NO_x production through higher combustion temperatures, in ammonia combustion NO_x formation is typically governed by fuel NO_x via the HNO pathway, $NH_3 \rightarrow NH_2 \rightarrow HNO \rightarrow NO$ [10]. The measurement results suggest that at this operating condition, fuel NO_x is much more dominant than thermal NO_x. A full chemical kinetics investigation of $H_2/NH_3/NG$ blends is beyond the scope of this paper, however.

The exhaust behaviors observed during polyfuel operation provide insight into paths for further combustion optimization in this engine. Hydrogen-enrichment has demonstrated value in improving combustion stability and efficiency in natural gas SI engines through increased flame speed and radical generation even at 10% H_2 in natural gas [33, 123]. However, in this study, we observed no significant improvement on cycle-to-cycle consistency due to hydrogen addition. The adjustment of spark timing and additional turbulence and mixing through intake valve variation through real-time control can be used to maximize the benefit of H_2 addition while monitoring thermal NO_x generation. Incorporating NH_3 into NG or H_2 fueling presents additional challenges due to low flame speeds and high fuel-NO_x emissions [20]. The incorporation of tri-fuel operation and control over on-board NH_3 cracking with feedback control informed by real-time emissions measurements can aid to minimize NO_x formation through suppression of the HNO pathway while promoting oxidation of alternatively generated N_2O [103, 21, 10, 9]. The engine also displayed a dependence of exhaust emissions on ambient conditions on the order of 10-20%, as evident with the difference in 0% blending cases between the NH_3/NG and H_2/NG datasets in Fig. 5.7. For practical engine applications, operating environments can vary greatly due to seasonal or geographic changes, day-to-day weather, and time of day. To ensure optimum engine operation for all conditions,

the ability of the sensor to resolve these differences across a range of relevant timescales in exhaust emissions enhances the ability of any control system to adapt the system operation.

5.5 Conclusion

An in-situ laser absorption sensor has been developed for cycle-resolved measurements of exhaust gas properties in production IC engines and demonstrates the potential impact of high-speed, quantitative LAS exhaust sensors for real-world implementation. In this work, the LAS sensor captured intra-cycle, cycle-to-cycle, and engine load-dependent variation of CO, NO, and temperature in the exhaust of an EPA-compliant natural gas-fueled, Otto-cycle engine. This capability revealed combustion inefficiencies and inconsistencies associated with natural gas spark-ignition engines, and showed that NO and CO cycle-to-cycle emission variability is significant. The cycle-resolution was enabled by locating the exhaust sensor in-line with minimal distance from the engine exhaust valve leading to a reduction in sensor latency by 3 orders of magnitude over commercial on-line analyzer systems. The close-coupling of the sensor was achieved through a ruggedized optomechanical design that enabled prolonged operation (>10 hours) at the sustained high temperatures (>1000 K) near the exhaust valve without any wear or deterioration of the sensor module. This novel sensor capability provides a quantitative, time-resolved capture of exhaust dynamics that is currently unavailable for production engines.

The utility of the sensor in polyfuel applications was demonstrated by capturing the response of the test engine to low-carbon natural gas blends incorporating NH_3 and H_2. At low load, both blends similarly halved CO exhaust for only 10% admixture. A differing response was observed in the NO emissions, with H_2 and NH_3 addition leading to a factor of 2 and an order of magnitude increase, respectively. Cycle-to-cycle combustion variability was largely unaffected from blending in this study. Low detection limits of 0.07% CO and 25 ppm NO, coupled with a large dynamic range, enabled analysis of significantly different fuel

97

chemistry in these polyfuel blends while remaining sensitive to cycle-level inconsistencies. It is expected that the combined durability, low-latency, and quantitative value of the developed LAS sensor will enable more direct and rapid optimization of low-carbon polyfuel combustion in production IC engine systems.

CHAPTER 6

Real-time FPGA-based laser absorption spectroscopy using on-chip machine learning for 10 kHz intra-cycle emissions sensing towards adaptive reciprocating engines

*The contents of this chapter have been published in the journal **Applications in Energy and Combustion Science** under the full title 'Real-time FPGA-based laser absorption spectroscopy using on-chip machine learning for 10 kHz intra-cycle emissions sensing towards adaptive reciprocating engines' [124].*

6.1 Introduction

Reciprocating piston internal combustion (IC) engines and their characteristic load-variability, response speed, power density, and adaptability offer an effective and economical solution to distributed, load-matching power generation to compliment cyclic or intermittent renewable energy sources [8]. New targets for low-carbon-footprint IC engines necessitate increased fuel efficiency, reduced exhaust emissions, and enhanced low-carbon fuel flexibility. To this end, a growing number of engine adaptation strategies leverage electronically-controlled fuel injection, ignition timing, and variable valve actuation (VVA) systems to achieve high performance and low emissions over a wide range of loads. Comprehensive manipulation over charge preparation, ignition, and effective cylinder geometry maximizes combustion perfor-
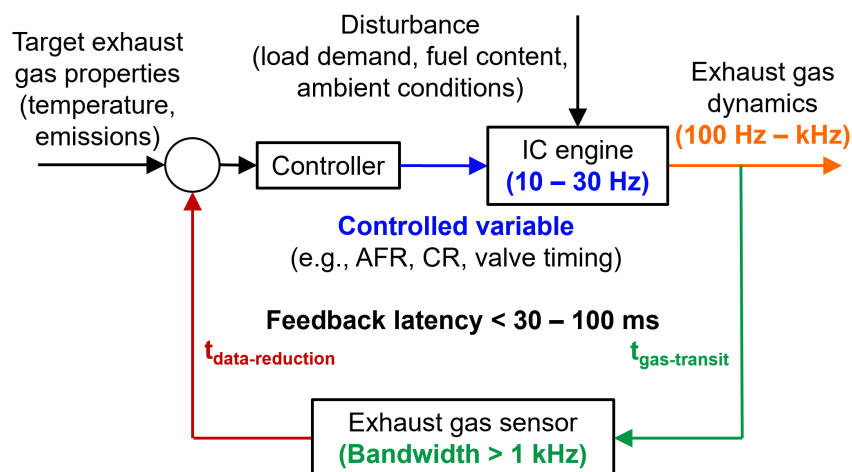
Figure 6.1: Simplified control diagram for closed-loop feedback control of internal combustion engines relative to exhaust emissions measured by a high-speed sensor. Highlights indicate required sensor response and latency for intra-cycle sensing and cycle-to-cycle adaptation relative to characteristic frequencies of power generation engines (1200-3600 rpm). AFR: air-to-fuel ratio, CR: compression ratio.

mance through methods such as variable compression ratio (VCR), exhaust gas recirculation (EGR), cylinder deactivation, and homogeneous charge compression ignition (HCCI) [40, 125, 34, 42]. The multitude of parameters in adaptive engine architectures demands precise control for real-time adjustments and optimization with respect to disturbances in load demand, fuel content, and ambient conditions [126, 50, 34].

Effective closed-loop control requires high-bandwidth and low-latency sensors capable of capturing transient intra-cycle behavior (∼kHz) and transferring critical measurements at sub-cycle latency for robust prevention of catastrophic failure through cyclic instability and engine knock [8, 48, 127, 128]. Figure 6.1 illustrates the representative timescales in reciprocating engines that typically operate around 1200-3600 rpm (cycle frequency of 10-30 Hz). Instabilities and auto-ignition knock can occur when pushing the compression ratio to maximize efficiency and can develop within a few cycles, demanding cycle-to-cycle response and real-time latency within 100 ms or less. Variable combustion performance and exhaust emissions occur at similar timescales during transient operation due to start-up and shut-down,
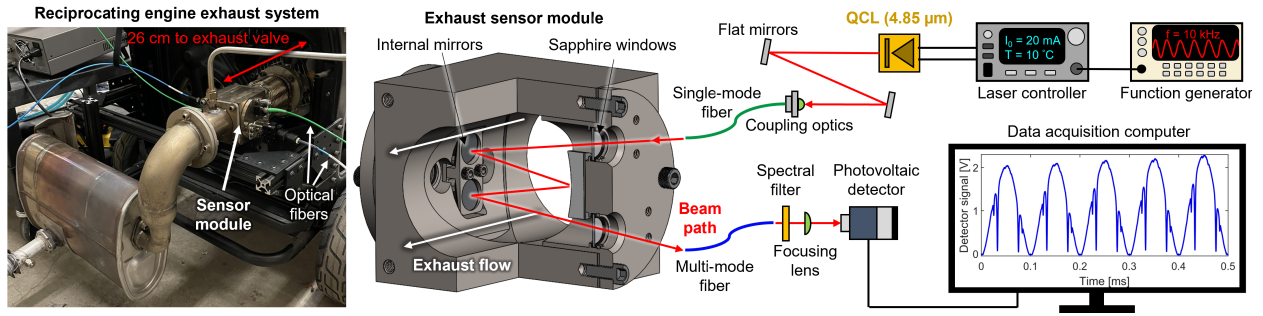
Figure 6.2: *Left*: In-line exhaust sensor module [19] installed on the Honda EU7000is electricity generator. *Right*: Schematic of exhaust CO sensing system including sensor module fiber-coupling to the light source and detector as well as laser modulation and data acquisition electronics.

load inconsistency, and fuel quality [8]. Transient intra-cycle exhaust gas indicators (e.g., temperature and emissions) of sub-optimal performance have elevated frequency content and require kHz sensor bandwidth.

Numerous sensing methods for on-line analysis of reciprocating engine exhaust have been employed including nondispersive infrared (NDIR) sensing, flame ionization detectors (FID), electrochemical sensors, fourier-transform infrared (FTIR) spectroscopy, and chemiluminescence detectors (CLD) [42, 41, 53, 54]. The reliance on gas sampling and ex situ analysis for most sensors leads to time-averaged emissions data with high latency due to gas transit times, exhaust gas mixing, and measurement integration time. Latency on the order of seconds allows for some engine tuning, but ex situ measurement prevents cycle-to-cycle adaptation as well as intra-cycle resolution, ultimately requiring more conservative design and operations to prevent fast-occuring non-idealities (such as knock) near performance limits. Improvement in real-time exhaust sensing for fast-response closed-loop control requires in-situ sensing close-coupled to the engine cylinder or exhaust manifold with kHz measurement rates to capture intra-cycle dynamics of exhaust gas properties as they evacuate the cylinder. Such close-coupling is a requisite for low latency associated with cylinder-to-sensor gas transit time. Additionally, and critically, real-time sensing also requires high-throughput data reduction and transfer methods to relay kHz-rate sensor feedback with sub-100 ms

latency thereby facilitating cycle-to-cycle engine adaptation.

Recent advancements in in-situ sensing have provided cycle-resolved emissions data using optical techniques. This includes NDIR probes with kHz-rate time resolution [57, 58] and multiple laser absorption spectroscopy (LAS) techniques which can be deployed without the need for calibration or sample pre-treatment [59]. Notably, the high-speed tunability of semiconductor lasers enables up to MHz-rate spectrally-resolved measurements in combustion systems, and operation in the mid-wave infrared provides access to the strong fundamental vibrational absorption bands yielding sensitivity to trace (ppm) emissions at practical optical pathlengths [59, 60]. These advantages have been leveraged to provide cycle-resolved quantitative species and temperature measurements in the intake, cylinder, and exhaust of reciprocating piston engines [61, 62, 19, 63, 129]. Recent work (opto-mechanical setup depicted in Fig. 6.2) utilized scanned-wavelenth direct absorption spectroscopy (DAS) to achieve transient exhaust gas temperature and emissions concentrations at 10 kHz in a production reciprocating engine with <10 ms cylinder-to-sensor latency [19]. LAS inherently provides high front-end sensor bandwidth owing to the fundamental limits set by the speed of light and high-bandwidth opto-electronics. However, back-end latency and data throughput are constrained by the complex signal post-processing procedure which typically involves computationally-intensive nonlinear spectral fitting to extract temperature and species concentrations from raw signals. The corresponding computational time leads to data reduction processes that fail to match the necessary real-time data throughput when kHz sensor bandwidth is required to capture intra-cycle dynamics and low-latency is required for cycle-to-cycle control.

In recent years, a number of methods have been explored to translate LAS signal processing algorithms to embedded platforms to increase the bandwidth and reduce latency for real-time sensor implementation. Close-coupling the data reduction procedure with the analog-to-digital converters (ADC) used to record raw LAS signals from the photodetector reduces data transfer load and resulting latency between electronic processing and control

systems by lowering required communication bandwidth from MHz-rate (raw signal sampling rate) to kHz-rate (measured gas properties). Field-programmable gate arrays (FPGA) are well suited to this application as their high data bandwidth and computationally-efficient configurability help prevent data backlog when interfaced with high-speed (MHz) ADC applications. This approach is highlighted by some recent real-time LAS efforts using FPGA processors. Xu et al. [130] utilized a combined FPGA and digital signal processor (DSP) arrangement for real-time inference of temperature and H_2O concentration via DAS with lasers scanned at 5 kHz. The FPGA performs down-sampling and pre-processing of the acquired raw signals which are then transferred to the DSP to perform fitting of the absorption lineshapes. Xia et al. [131] similarly utilized an FPGA to accelerate the demodulation of high-frequency (>100 kHz) wavelength modulation spectroscopy (WMS) signals across several channels to lower back-end computational load and enable kHz-rate tomographic imaging of flame temperature. Multi-chip data acquisition and processing configurations require optimized and synchronized inter-communications that can compromise computational precision and introduce additional data transfer latency, and this can be alleviated by maximizing single-chip contribution towards end-to-end signal interpretation. Guo et al. [132] developed a portable real-time sensor with 7 kHz 2f/1f WMS and FPGA-based demodulation of raw signal harmonics for a <5 s response time measuring ppm concentrations of NH_3 within flue gas. Similarly, Xu et al. [133] utilized an FPGA-based WMS demodulator for a gas temperature sensor, achieving a 4 kHz measurement rate (0.25 ms temporal resolution) and reducing computational time required to capture the peak WMS signal by three orders of magnitude relative to a typical least-squares fitting method.

Further acceleration of LAS data reduction can be achieved through the application of machine learning techniques to replace the computationally-intensive spectral fitting or demodulation procedures [134, 135, 136]. Zhang et al. [137] developed an artificial neural network (ANN) to improve the efficient interpretation of 2f/1f WMS signals and calculate path-integrated absorbance from 100 sets of WMS signals within 0.4 s. Yi et al. [138] applied

transfer learning for multiple machine learning regressors to infer gas temperature directly from raw transmission signals in DAS to bypass the standard nonlinear fitting of absorption lineshapes. Tian et al. [139] similarly leveraged fully-connected feedforward and convolutional neural networks for end-to-end DAS data reduction to infer ppm-level concentrations of methane and acetylene within 0.5 ms, representing a reduction in computational time of two orders of magnitude relative to spectral fitting. While training machine learning models can require significant computational resources and data to train effectively, post-training they can be effectively implemented on embedded platforms such as FPGAs [140, 141, 142]. Notably, Huang et al. [143] successfully replaced a typical quadrature demodulator with an FPGA on-chip feedforward neural network to extract peak WMS signals from raw signals, yielding improved SNR and a reduction in required signal sampling period by a factor of four.

The work presented here integrates and builds upon several of the aforementioned laser absorption spectroscopy methods by applying machine learning models for FPGA on-chip end-to-end data reduction of mid-infrared transmission spectra to infer gas temperature and species concentration in real-time at 10 kHz in the exhaust of reciprocating piston engines. The effort aims to achieve intra-cycle gas property resolution and sufficiently low latency for cycle-to-cycle feedback and control. This article describes the detailed methods, integration approach, and performance of the data reduction scheme applied to an in-situ laser absorption exhaust sensor for cycle-resolved emissions analysis in a production reciprocating piston engine. Ridge regression and fully-connected feedforward neural network models are trained on experimental and simulated data to infer exhaust temperature and CO concentration directly from transmitted DAS scans resulting from a quantum cascade laser wavelength-scanned across two absorption lines of carbon monoxide near 4.9 µm. The effects of down-selecting data points of the raw signals and adjusting model complexity are investigated with respect to utilization of the FPGA hardware and prediction accuracy. The integrated methods and their respective bandwidth and latency characteristics are tested via
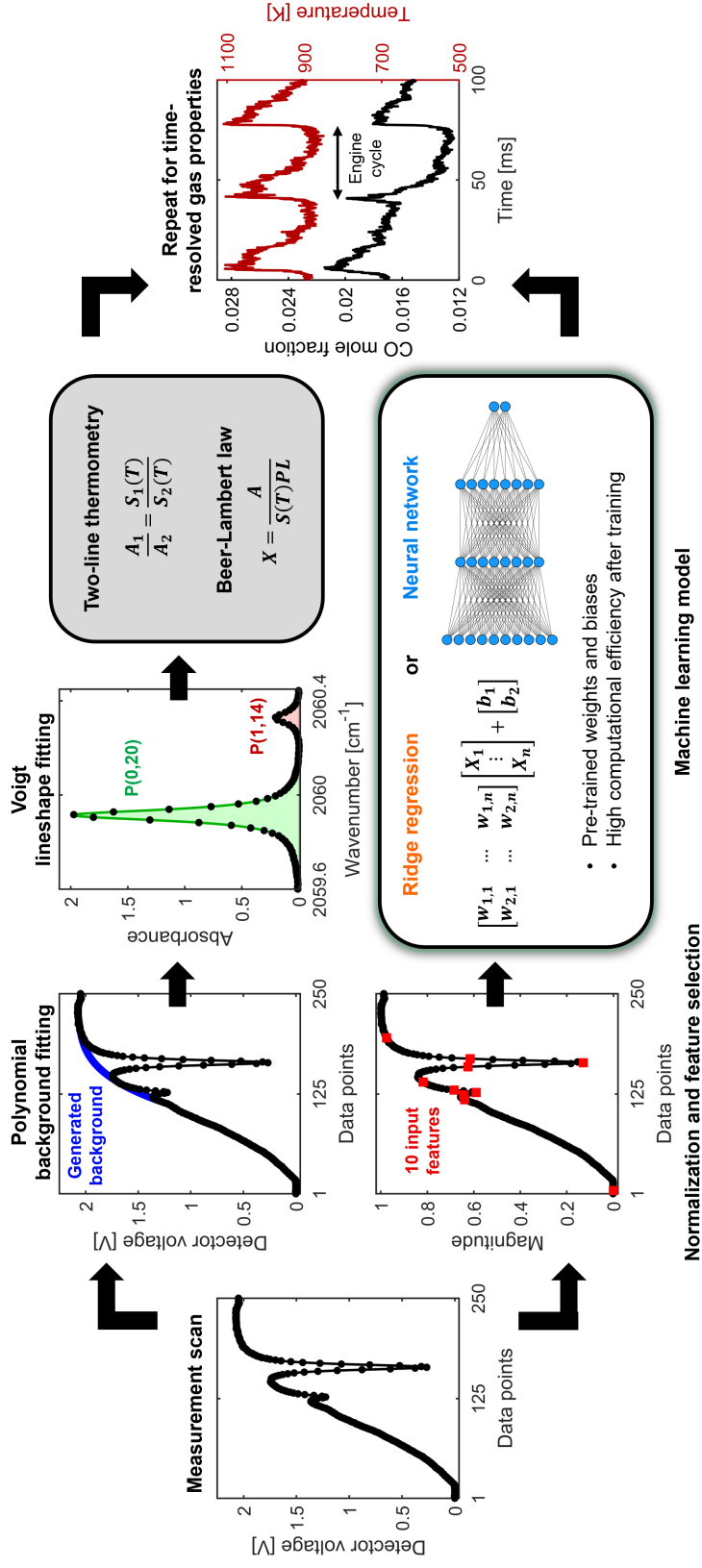
Figure 6.3: *Top*: Signal processing procedure to infer gas temperature and CO concentration from transmitted laser scans through spectral fitting of the two absorption features. *Bottom*: Alternative signal processing via machine learning to infer gas properties directly from 10 select features of the transmitted laser scan.

a controlled real-time hardware-in-the-loop system using a Xilinx Kintex-7 FPGA to demonstrate performance using real-world engine exhaust data. This work expands the capability of LAS for real-time emissions characterization at the relevant timescales of reciprocating IC engines to enable the advancement of adaptive engine architectures.

6.2 Laser absorption exhaust gas sensor

In this section we describe the basics of the spectroscopic measurement technique including the theoretical basis and experimental configuration. The hardware required for coupling the laser absorption sensor to the production IC engine is also detailed.

6.2.1 Scanned-wavelength direct absorption spectroscopy

In scanned-wavelength direct absorption spectroscopy (DAS), a narrow-linewidth laser is modulated via the injection current to produce wavelength-scanning in a spectral region that resonates with a molecular absorption transition of the target molecule. When the modulated laser beam is directed through a gaseous flow that contains absorbing molecules, the incident light intensity I_0 is attenuated and the transmitted light intensity I_t is recorded on a photodetector. This wavelength-dependent attenuation defines a spectral absorbance α_ν in the wavenumber domain, which can be directly related to gas properties through the Beer-Lambert Law for a single absorption transition, shown in Eq. 6.1:

$$A = \int_{-\infty}^{\infty} \alpha_\nu d\nu = \int_{-\infty}^{\infty} -\ln\left(\frac{I_t}{I_0}\right)_\nu d\nu = X_\mathrm{i} S(T) P L \tag{6.1}$$

Integration of the spectral absorbance yields an integrated absorbance area A [cm^{-1}] which is linearly dependent on absorbing species mole fraction X_i, temperature-dependent linestrength $S(T)$ [cm^{-2}·atm^{-1}], gas pressure P [atm], and absorbing pathlength L [cm].

If gas temperature and consequently $S(T)$ is unknown, two absorption transitions of

the same species can be targeted simultaneously to employ the two-line thermometry technique [84]. Taking the area ratio R in Eq. 6.2 removes the dependence on pressure, pathlength, and concentration and relies solely on the relative linestrengths and therefore temperature.

$$R = \frac{A_A}{A_B} = \frac{S_A(T)}{S_B(T)} = f(T) \tag{6.2}$$

Through these two equations, this technique provides a straightforward method to infer temperature and species mole fraction through simultaneous measurement of two spectrally-resolved molecular absorption transitions by a wavelength-scanned laser. By spectrally-resolving these individual absorption transitions and relating them to tabulated linestrengths from spectral databases, this method is species-specific, calibration-free, and quantitative. Temporal resolution is limited only by laser tunability and the ability to capture two transitions in a single modulation period, resulting in kHz to MHz response depending on the targeted spectral range [60]. Notably, LAS is readily configurable in non-intrusive, in-situ optical arrangements [59], so high-precision quantitative measurements are possible with minimal disruption to the flow of combustion gases and overall packaging of IC engines.

6.2.2 Experimental setup

The scanned-wavelength direct absorption method was implemented in a sensor module for cycle-resolved exhaust gas sensing in reciprocating engines which serves as the direct application for the data reduction scheme presented in this work. Relevant details of the experimental setup for this sensor are illustrated in Fig. 6.2 and discussed in this section as context for the presented data reduction method. It should be noted that the sensor module is similar to that descibed in our prior work involving characterization of polyfuel combustion emissions [19]. The sensor utilizes a quantum cascade laser near 4.9 μm to target the P(0,20) and P(1,14) rovibrational absorption transitions of carbon monoxide (CO). Wavelength-scanning of the laser was performed at a frequency of 10 kHz with a sinusoidal

waveform delivered by a function generator to the laser controller. The laser output is delivered via a single-mode optical fiber to a custom sensor module placed in-line in the engine exhaust pipe 26 cm downstream of the exhaust valve. This sensor module provides optical access and internal optics for multi-path and multi-pass optical arrangements for sustained operation in production reciprocating piston engines. The laser beam targeting CO performs two traverses of the 50 mm pipe diameter and a multi-mode optical fiber is used to collect and deliver the transmitted light to a photovoltaic detector. Transmitted intensity signals are recorded by the data acquisition computer at a sample rate of 5 MHz. The recorded data provide measured gas temperature and CO mole fraction at a temporal resolution of 10 kHz, which corresponds to 364 data points per engine cycle when operating at 3300 rpm. This enables the capture of intra-cycle and cycle-to-cycle dynamics and was used to analyze the exhaust gas behavior of an EPA-certified single-cylinder spark-ignition engine (Honda EU7000is) fueled with natural gas and blends containing ammonia (NH_3) and hydrogen (H_2).

The established spectral-fitting routine used to interpret the transmitted intensity signals involves a sequence of operations as illustrated in the top pathway of Fig. 6.3. After isolating a single transmitted laser scan from the ADC data stream, a background intensity signal is generated by fitting a 3rd order polynomial to the non-absorbing regions. These signals are used to calculate measured absorbance and then converted to the spectral (i.e., wavenumber [cm^{-1}]) domain with a pre-recorded etalon signal which characterizes the laser wavelength-scanning. The integrated absorbance areas for the two CO absorption lines are calculated through simultaneous nonlinear fitting of Voigt lineshapes to the two transitions using the analytical approximation from McLean et al. [82]. These areas are used to calculate gas temperature through two-line thermometry as in Eq. 6.2, with the bisection method used to solve the nonlinear equation. After temperature is determined, the mole fraction of CO is calculated through the Beer-Lambert Law in Eq. 6.1. For each individual transmitted scan, this procedure to infer mole fraction and temperature requires an average of over 45 ms

when executed in MATLAB 2022a on a quad-core Intel Core i7-1165G7 CPU at 4.07 GHz with 16 GB of RAM. While pipelining the procedure into sequential steps can improve data throughput, execution times of individual processes such as the 14 ms required for Voigt lineshape fitting are orders of magnitude higher than the 100 µs required to achieve a 10 kHz throughput to match the laser modulation rate. This time-intensive signal post-processing of the transmitted DAS signals therefore limits the practical integration in fast-response feedback control where 10 kHz throughput real-time data reduction is necessary to prevent data backlog or lowering of the modulation rate and therefore lowering temporal resolution. Similarly, back-end latency due to computational time and data transfer must also be lowered below the engine cycle period (36 ms) to facilitate cycle-to-cycle adaptation.

6.3 Machine learning data reduction

6.3.1 Machine learning approach

The use of machine learning (ML) models to replace the spectral fitting routine can reduce the computational time by simplifying the data reduction to a sequence of matrix operations which infer gas properties directly from the transmitted scan signals. However, reduction in computational load must not come at the expense of the model prediction accuracy meeting requirements of the sensor application. The ML data reduction must retain the precision to characterize intra-cycle gas dynamics without bias due to variable exhaust temperature and composition. Two types of regression models, a linear regression and a fully-connected feed-forward artificial neural network, were developed and rigorously tested for this application. The basic mechanics of both models are illustrated in Fig. 6.4. The linear regression is one of the simplest and most widely used regression models, and for multiple linear regression (MLR) the predictions are generated through a single linear combination of the input feature vector with corresponding feature weights and addition of a bias term for each output variable as in Fig. 6.4 [144]. The optimal weights and biases are found through a training process

(discussed in Sec. 6.3.3) on a training dataset composed of a large volume of input feature vectors paired with corresponding output vectors. Ridge regression is a variation of linear regression that incorporates L2 (i.e., Tikhonov) regularization within the training process and prevents over-fitting by penalizing large feature weights through an addition to the cost function as in Eq. 6.3 [145]:

$$P_i = \lambda \sum_{j=1}^{n} w_{i,j}^2 \qquad (6.3)$$

The penalty term P_i is calculated for a given output variable i with the penalty strength determined by the regularization parameter λ where values close to zero approach the non-regularized linear regression.

Relative to ridge regression, neural networks require a more complex training process and increased computational load in the prediction calculation, but tend to have higher prediction accuracy and generalization across a variety of non-linear applications. Convolutional and fully-connected feed-forward neural networks have been demonstrated previously to predict species concentration from transmitted scanned-wavelength direct absorption signals with high accuracy [139], with the fully-connected variant yielding the highest prediction accuracy, motivating its selection in this work. In this neural network architecture, depicted in Fig. 6.4, an initial input layer is composed of the input features, the final output layer produces the regression output variables, and hidden layers in the middle perform the intermediate computations. As the name implies, the individual nodes that make up each layer receive inputs from each node in the preceding layer, and direct their output to each node of the proceeding layer. Figure 6.4 outlines the computational flow in the hidden layer nodes. An initial summing function calculates a linear combination of all previous node values with corresponding weights and the addition of a bias term. Next, an activation function introduces nonlinearity into the system by deviating the node output away from a simple linear combination, in this case via the piecewise linear function Leaky ReLU (Rectified Linear Unit). Granular analysis reveals a computationally-straightforward method for output
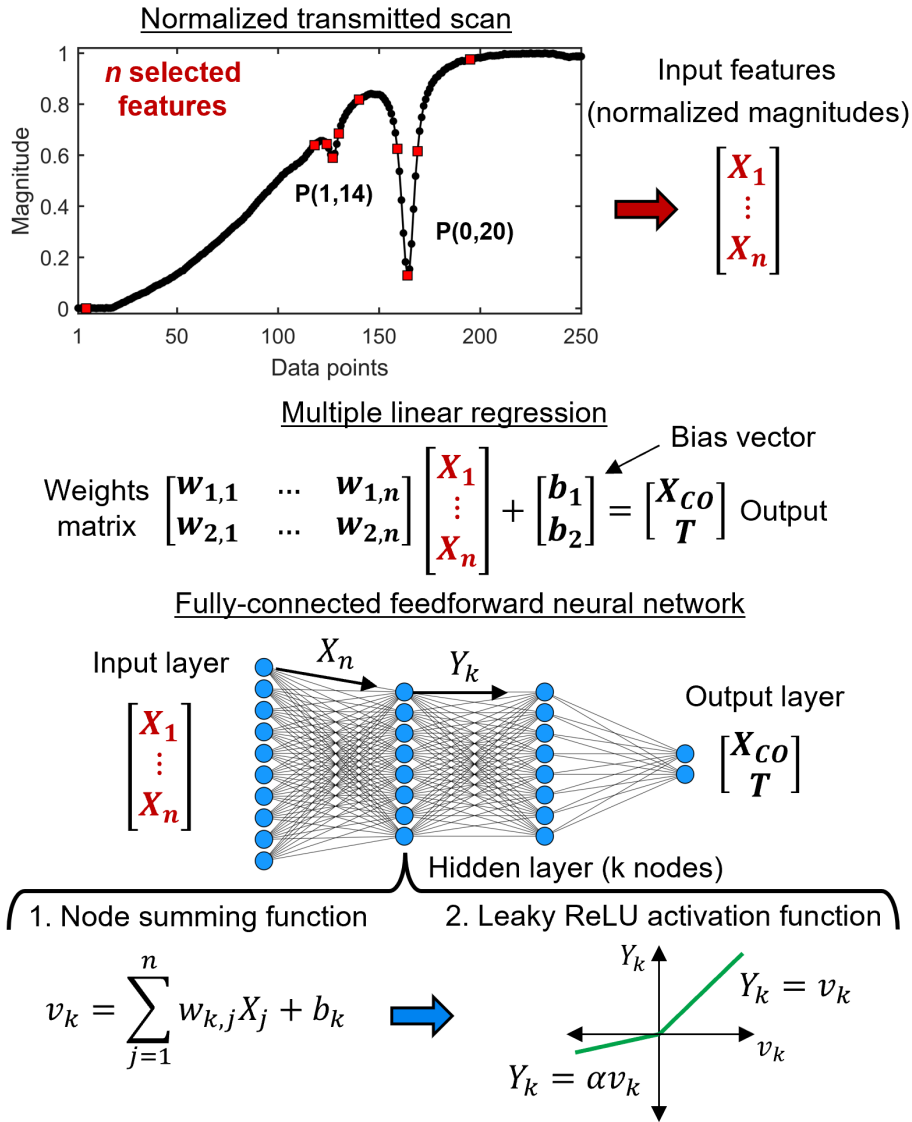
Figure 6.4: *Top*: Input feature selection corresponding to normalized magnitudes of select data points in the transmitted laser scan. *Middle*: Matrix representation of linear regression to generate X_{CO} and T from input features. *Bottom*: Neural network regression schematic including hidden layer computations to generate node outputs Y_k from node inputs X_n and Leaky ReLU slope α. For both models, weights (w) and biases (b) are determined through model training.

prediction relative to nonlinear spectral fitting. However, computational effort is front-loaded in the training and optimization process to converge on optimal weight and bias terms. Layer configuration, hyperparameters, and training data have significant influence on both the ridge

111

regression and neural network model performance and are discussed in the following sections.

6.3.2 Training data
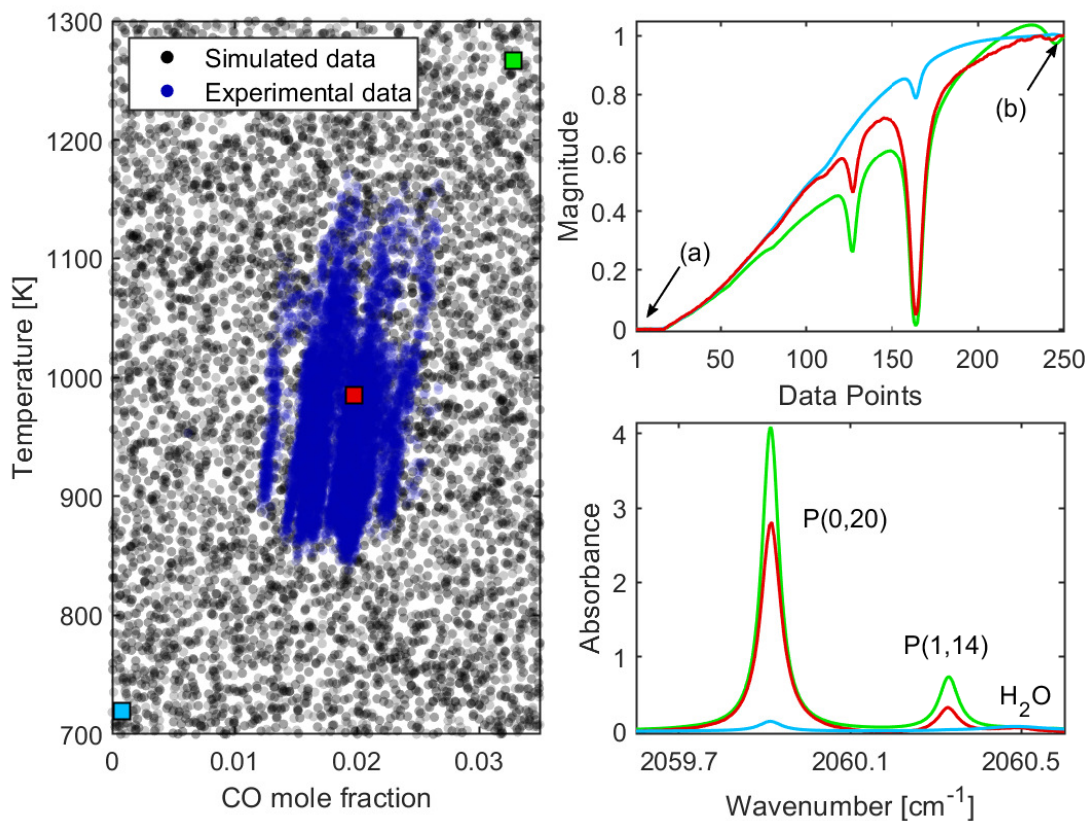
Figure 6.5: *Left*: Distribution of temperature and CO mole fraction for simulated and experimental training data. Example points are highlighted with square markers. *Right*: Training scans *(top)* and absorbance spectra *(bottom)* corresponding to the highlighted example points. The first and last data points in the training scans marked by (a) and (b) are used for scan normalization. Absorption due to H_2O is shown alongside the target CO absorption features.

A combined experimental and simulated training dataset was compiled to serve as the basis for ML model training and optimization, and included transmitted laser scans paired with their corresponding gas temperature and CO mole fraction determined through spectral fitting or simulation. Previously-recorded experimental data were included in the training set to facilitate robustness to various noise sources present in the transmitted signals during

112

sensor application on the production reciprocating engine. These data were recorded during natural gas-fueled engine operation over a representative load range of 2-5 kW. Subsets of 2,500 pairs of transmitted scans and gas properties were taken from data collected at 2, 3, 4, and 5 kW engine load for a total of 10,000 experimental samples to include in the training set.

Simulated synthetic training data was produced to increase the generalization of the trained models and satisfy the data volume requirement of neural network training. To generate the synthetic transmission scans, CO absorbance spectra are simulated over a uniformly distributed range of temperature (700–1300 K) and concentration (0–3.5%), shown in Fig. 6.5 (left). The range of exhaust gas temperature and composition is extended beyond the range observed during experimental testing to provide generalization and robustness over possible engine exhaust conditions including new conditions that may produce values outside of the experimental training data range. H_2O vapor absorption is also present within the transmitted scans and while these features are not utilized in the data reduction, H_2O absorption is also included in the spectral simulations for consistency with the experimental data, with the range of mole fraction estimated from equilibrium simulations of natural gas combustion. Example simulated absorption spectra are shown in Fig. 6.5 (bottom right) highlighting the broad range in absorbance magnitude across the measured spectral region. In addition, Table 6.1 lists the uniform simulation distributions of other key parameters relevant to collisional broadening affects on absorbance lineshape and superposition of absorbance on transmitted laser scans. Aggregate collisional broadening is calculated with simulated concentrations of CO, H_2O, and CO_2 and their corresponding broadening coefficients from the HITRAN and HITEMP databases, with the remainder of gas composition accounted for with air broadening coefficients [12, 11]. A further 10% variation in total collisional broadening is introduced to support generalization robust to unforeseen changes in exhaust gas composition. To generate the simulated transmitted scans that serve as inputs to the ML models, background laser scans are taken from the four experimental conditions

Parameter	Simulation range
Temperature	700 - 1300 K
X_{CO}	0 - 3.5%
X_{H2O}	15 - 22%
X_{CO2}	8%
Collisional broadening scaling	90 - 110%
Laser center wavelength	± 0.002 cm^{-1}

Table 6.1: Range of critical simulation input variables that affect measured absorbance shape and magnitude. Temperature and mole fractions ranges obtained from experimental observations and equilibrium simulations of natural gas/air combustion. Center wavelength variation matches observations from experimental data.

included in the experimental training set, and 2,500 unique simulated spectra are projected onto each of these background scans while varying the laser center wavelength to account for laser jitter. Representative examples of of these synthetic transmission scans are shown along with their corresponding absorbance spectra and output gas properties on the right of Fig. 6.5. The resulting simulated training set of 10,000 samples are added to the experimental samples to form a 20,000 sample training set with a 50/50 split between experimental and simulated data.

The training inputs and outputs are normalized in the range 0–1 to improve ML performance [add citation] while retaining simplicity for the FPGA programming. For computational simplicity, the first and last points of the raw scan act as the minima and maxima used to scale all points for that individual scan. While variations in scan shape and absorbance mean that the final data point is not always the true maximum, this was sufficient to ensure all 10 selected features (shown in Fig. 6.4 and discussed in Sec. 6.3.3) remained within the range 0-1. Scaling of output features is performed with prior knowledge of the conditions expected in the engine exhaust with over-encompassing temperature and CO mole fraction ranges of 700-1300 K and 0-3.5%, respectively. These ranges are used to normalize all training outputs from 0-1, and again used to convert normalized ML outputs back to absolute temperature and mole fraction.

6.3.3 Training and hyperparameter tuning

The machine learning model architectures and hyperparameters are tuned to optimize prediction accuracy with respect to model complexity for efficient implementation on finite-resource FPGA platforms. Multiple feature selection techniques inform the reduction in the number of input features to remove unimportant data points thereby improving learning accuracy and reducing the computational load of matrix operations during the prediction calculation [146]. The scikit-learn toolbox was used to apply Maximum Relevance—Minimum Redundancy (MRMR), Recursive Feature Elimination (RFE), and Lasso regression [146] in conjunction with prior experience in spectral fitting to isolate the data points with the greatest importance when predicting temperature and CO mole fraction from the transmitted scans. An iterative approach to feature elimination balanced FPGA-programmability with prediction accuracy. For each input layer size, both models were re-tuned, re-trained, and used for FPGA code synthesis. Ridge regression structure is well-defined for a given input layer size whereas neural networks have open-ended layer arrangements. As such, the neural network layer structure and complexity was pruned concurrently with input layer size. Feature selection converged on the final input layer size of 10 data points which lie on the two CO absorption transitions and neighboring non-absorbing regions highlighted in Fig. 6.4. Notably, the 10-feature input layer representing only 4% of the total transmitted scan data samples, with subsequently optimized ML architectures, consistently yielded higher prediction accuracy and lower bias compared to those trained with the full 250-feature input layer, where many data features or points provide no value to the prediction of temperature and mole fraction. The order of magnitude reduction in input features enabled compact neural network configurations that provided reasonable FPGA hardware utilization, as discussed in Sec. 6.4.1.

The construction and training of the ML models is performed in Python, with the scikit-learn toolbox implemented for ridge regression. The regression coefficients (weights and biases) and regularization strength λ are tuned through 20-fold cross validation and a train/test

split of 80/20 applied to the 20,000 sample training dataset. The Singular Value Decomposition (SVD) solver is used as it provides the highest prediction accuracy with the lowest training time (2.9 s on the Intel Core i7-1165G7 CPU) compared to the other available solvers. Minimum mean squared error of the two prediction variables was found with $\lambda = 0.0574$ and the resulting regression coefficients were retained for the final ridge regression model.

The neural network was developed in the TensorFlow Keras framework. For a given input layer size, KerasTuner with Bayesian optimization was used to select the fully-connected feeedforward neural network hidden layer configuration that minimized mean squared error of the regression outputs over the 20,000 training dataset. This included 50 different configurations each executed three times and trained for 50 epochs with a validation split of 20% shuffled every epoch. For a 10-feature input, the limit on hidden layers and nodes per layer were set at three and eight, respectively, to limit the computational load for FPGA programming. An experimental survey selected Adam [147] as the optimizer to train the neural networks over available alternatives such as Stochastic Gradient Descent (SGD) and Root Mean Square Propagation (RMSProp) as it consistently yielded higher prediction accuracy in this application. Similarly, the traditional ReLU (Rectified Linear Unit) activation function was replaced with the Leaky ReLU [148] (bottom of Fig. 6.4) due to an observed increase in learning accuracy especially at compact neural network configurations without significant effect on the subsequent FPGA design. The optimization required 1 hour and 38 minutes on the same Intel CPU and selected a configuration of two hidden layers with eight nodes each, a learning rate of 0.01, and a Leaky ReLU negative slope of 0.02. This final neural network configuration was then re-trained on the full training dataset for 2,000 epochs with a batch size of 32 and a shuffled 20% validation split, requiring 28 minutes to converge on final values for the 178 trainable weights and biases.
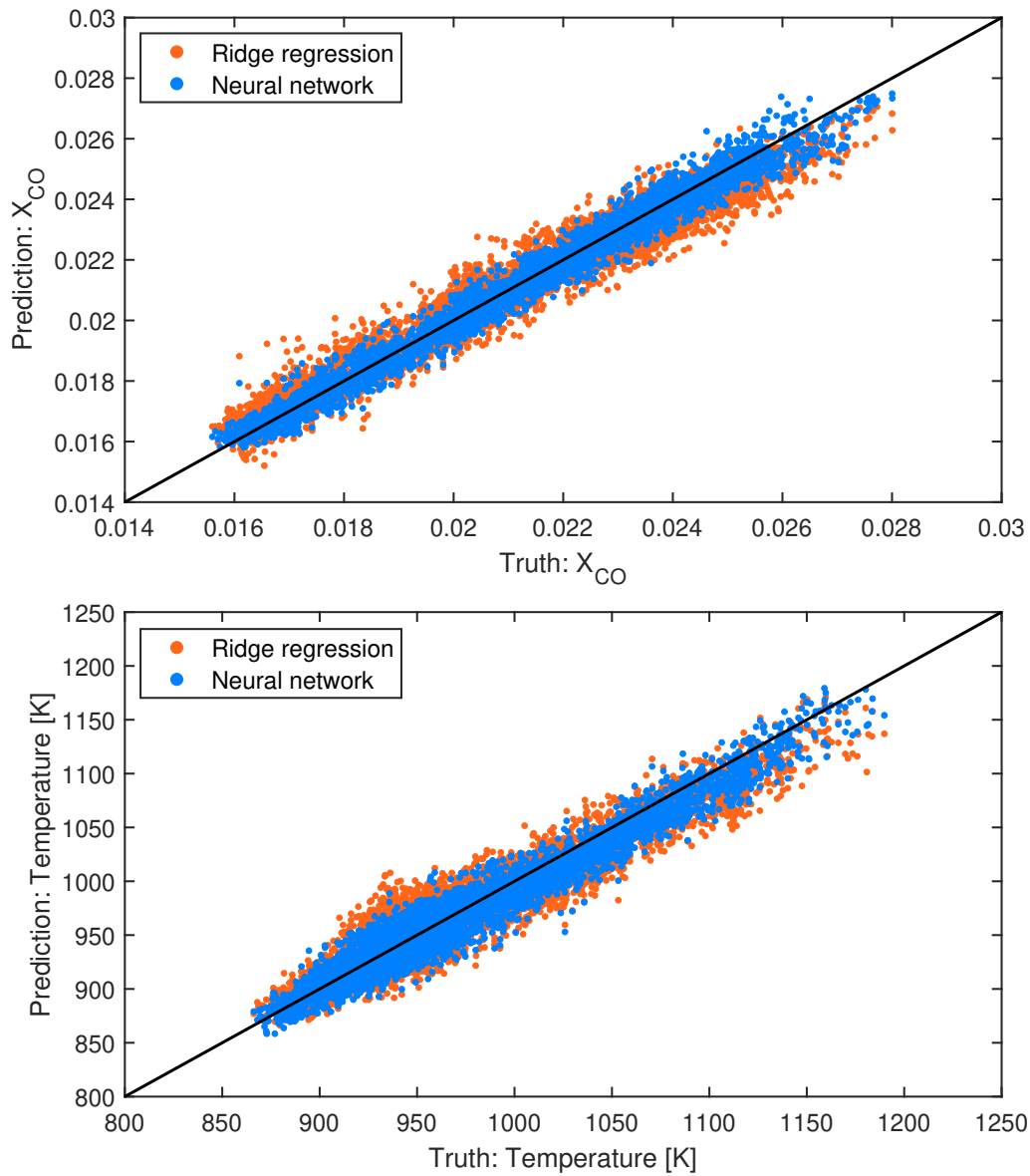
Figure 6.6: Machine learning model prediction accuracy of CO concentration *(top)* and temperature *(bottom)* compared to spectral fitting (truth). Testing dataset contains 5,000 experimental laser scans recorded during engine firing with applied load of 2 and 5 kW.

6.3.4 Prediction accuracy

The prediction accuracy of the ML models was evaluated with a test dataset of unseen experimental data collected with the LAS exhaust sensor. Two experimental datasets comprising

	Temperature		CO mole fraction	
	RMSE	R^2	RMSE	R^2
Ridge regression	20.3 K	0.8960	6.33E-4	0.9462
Neural network	15.0 K	0.9431	3.90E-4	0.9796

Table 6.2: Prediction accuracy for both ridge regression and neural network models when applied to the testing dataset shown in Fig. 6.6. RMSE: root mean square error, R^2: coefficient of determination.

2,500 transmitted spectral scans captured at 2 and 5 kW engine load are selected to represent the edge cases of normal engine operation. The spectral fitting routine serves as the ground truth and reference to evaluate the prediction accuracy of the models. The prediction accuracy of gas temperature and CO mole fraction for the 5,000-sample test dataset are shown for both the ridge regression and neural network in Fig. 6.6, with Table 6.2 listing key performance metrics. The neural network outperforms ridge regression in RMSE (root mean square error) and R^2 (coefficient of determination), showing both increased accuracy and generalization across a wide range of experimental input data. The neural network exhibits RMS error of 15.0 K and 0.0390% for predicted temperature and mole fraction, respectively. Despite some evidence of prediction bias, an R^2 value above 0.94 for both output variables illustrates that the machine learning approach adequately captures the same dependencies as spectral fitting. While the ridge regression is comprehensively outperformed by the compact neural network, the reduced complexity in training and optimization can justify its practical use in applications with lower required sensor precision. The prediction error introduced with both models is notably lower than the absolute uncertainty magnitudes of measured gas properties and the intra-cycle variation observed in previous experimental testing [19], suggesting that data reduction acceleration via machine learning does not inhibit the ability of the LAS exhaust sensor to resolve transient effects relevant to IC engine optimization.

6.3.5 Computational time

The computational acceleration achieved through ML-based data reduction is evaluated through a direct comparison with the spectral fitting procedure operating in the same MAT-LAB and CPU environment (Intel Core i7-1165G7 as in Sec. 6.2.2). The ML-based procedure to infer gas properties directly from the transmitted scans includes (1) scan normalization (2) selection of the 10 input features (3) calculation of normalized X_{CO} and temperature outputs via machine learning and (4) output scaling of the normalized model outputs to generate absolute X_{CO} and temperature. It should be noted that these computation steps do not account for time-constants associated with real-time data-transfer, but rather this comparative evaluation isolates the the spectral analysis computations. Across the 5,000 scans in the test dataset, average computational time was measured at 4.10 µs and 2.81 µs for the neural network and ridge regression, respectively. While average values are below 5 µs, inconsistent execution time results in a range of 2-110 µs. Despite the variability, replacing the spectral fitting procedure with a lean machine learning model represents a clear improvement in computational time of at least 10^2. Consistent sub-ms execution time to infer gas temperature and species mole fraction directly from transmitted laser scans reinforces the use of machine learning to facilitate real-time scanned-wavelength direct absorption spectroscopy at kHz rates.

6.4 Real-time FPGA demonstration

The real-time on-chip FPGA performance of the ML-based data reduction is experimentally demonstrated on a Speedgoat Performance real-time target machine. This system is equipped with an Intel Core i7 CPU and a Xilinx Kintex-7 FPGA (XC7K325T in FBG676 package) with 326,080 logic cells, 840 digital signal processor (DSP48E1) slices, and 16 MB of on-chip block RAM. The CPU and FPGA communicate via PCIe (x4 link, version 1.1) and Simulink Real-Time 2022a executes the signal processing algorithms and data transfer between the
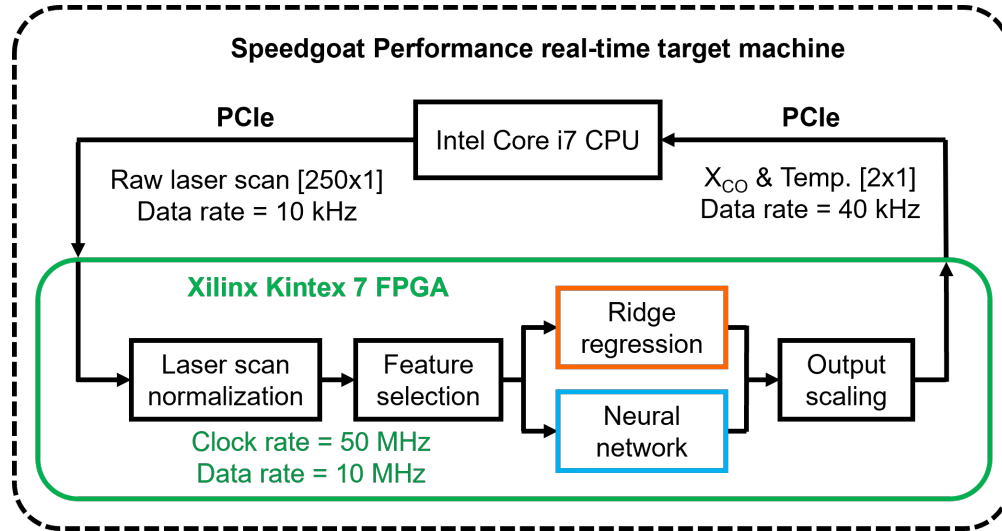
Figure 6.7: Schematic of real-time demonstration with Speedgoat Performance real-time target machine.

processing hardware. A schematic of the testing configuration is shown in Fig. 6.7. The CPU stores a subset of the experimental test dataset, with 2,500 transmitted laser scans and corresponding temperature and X_{CO} inferred via spectral fitting. The raw scans are sequentially transmitted to the FPGA over the PCIe at a rate of 10 kHz corresponding to the original laser modulation rate. This simulates the real-time data feed from the photodetector on the engine sensor module while providing a more controlled and known reference for evaluating latency and accuracy. The FPGA performs the end-to-end data reduction as described in Sec. 6.3.5 and illustrated in Fig. 6.7. The inferred gas properties are transmitted from the FPGA to the CPU over the PCIe and up-sampled at a rate of 40 kHz which is the upper limit dictated by the current Simulink Real-Time configuration and PCIe data transfer latency. Separate Simulink models are constructed for the ridge regression and neural network models for independent programming optimization and direct comparison of FPGA hardware usage and computational time. It is notable that the traditional non-linear spectral fitting algorithms (which require many steps to approximate or excessive memory and logic) are not readily implemented on the Speedgoat FPGA hardware, which trades some computational resources with rapid on-chip data handling capability as previously

120

discussed [130, 149]. As such, the foregoing comparisons of the real-time FPGA-based data reduction methods are focused on the machine learning techniques, with select comparisons to post-processed data using the traditional spectral fitting.
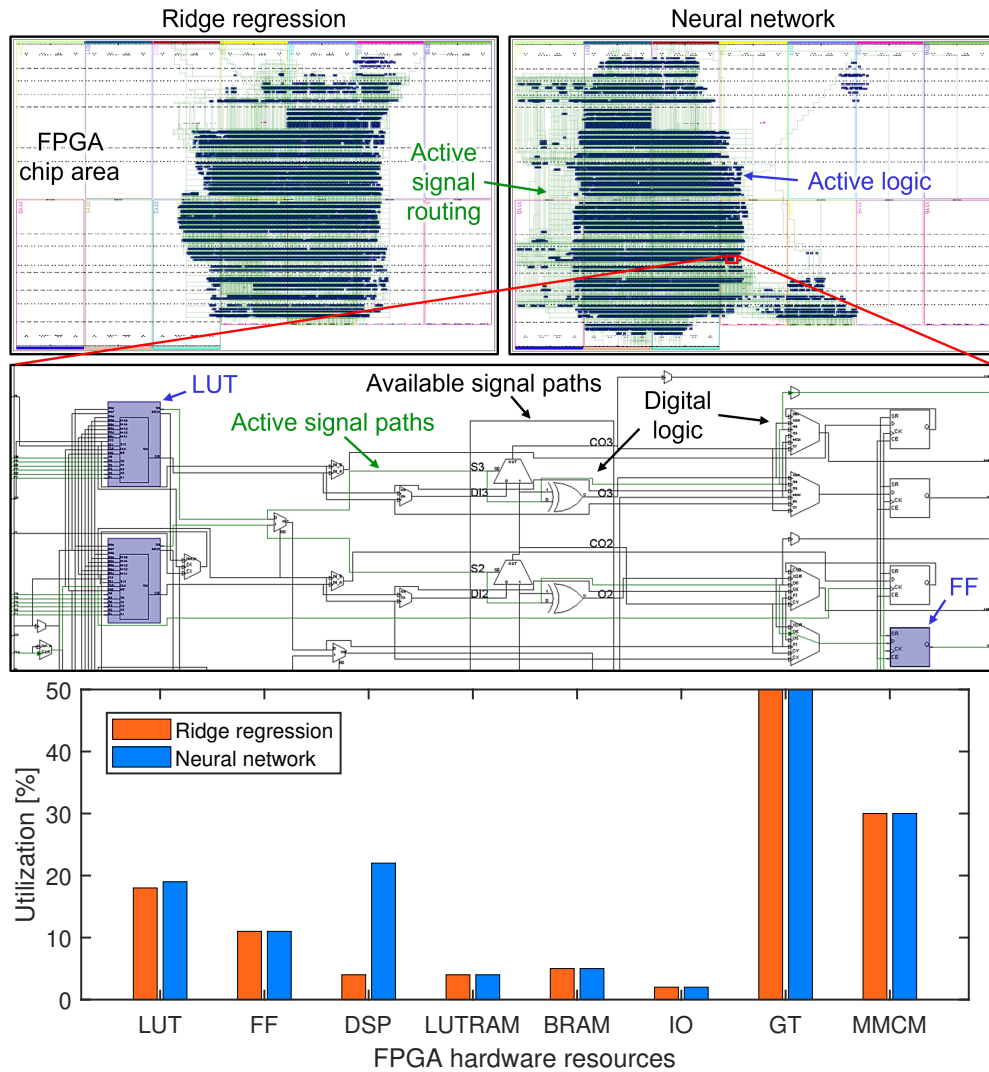
Figure 6.8: *Top:* On-chip utilization map of the FPGA designs generated in Xilinx Vivado. Blue area corresponds to allocated logic elements and green indicates the signal routing. *Middle:* Example image of programmed logic within the neural network FPGA design. *Bottom:* Resource utilization on the Kintex-7 FPGA after programming with the ML-based data reduction algorithm. FPGA hardware elements: look-up tables (LUT), flip-flops (FF), digital signal processors (DSP), LUT-based RAM (LUTRAM), block RAM (BRAM), input/output pins (IO), gigabit transceivers (GT), mixed-mode clock manager (MMCM).

6.4.1 FPGA model programming

The FPGA-based data reduction in Fig. 6.7 is constructed within the Simulink Real-Time model for conversion to an FPGA-downloadable bitstream via the Simulink HDL Coder workflow. Trained model parameters (e.g., weights and biases) are imported from Python into Simulink and used to explicitly construct the matrix multiplication sequences comprising the ridge regression and neural network. While the ML models are developed with 32-bit floating-point math, conversion to fixed-point data types increases efficient utilization of FPGA hardware resources. The FPGA design is converted to 16-bit fixed-point with fraction lengths adjusted to match the range of signal magnitudes in different stages of data reduction. The 16-bit word length proved sufficient to prevent significant loss of precision and additional error in the ML prediction accuracy. Hardware description language (HDL) code is generated within Simulink after configuring the optimization parameters including clock rate, on-chip resource sharing, and data pipelining to meet clock timing constraints and minimize resource allocation. The HDL code is converted to a bitstream with Xilinx Vivado 2020.2 as the synthesis tool that translates HDL code into an explicit flow of data signals through the configurable logic blocks of the target FPGA chip. The Vivado software enables granular analysis of exploited logic elements and timing delays due to logic and signal routing. Iteration of ML model complexity along with the FPGA data rate and pipelining was required to successfully generate a bitstream that satisfied resource and timing constraints. This process converged on the ML architectures detailed in Sec. 6.3 with the FPGA operating at a clock rate of 50 MHz, multi-cycle data rate of 10 MHz, and pipeline registers inserted between major computational stages in the data reduction. The resource utilization of the finalized FPGA designs is shown in Fig. 6.8. Both approaches require less than 50% of available resources and less than 25% of the available logic and memory elements. The largest utilization of the gigabit transceivers (GT) and mixed-mode clock manager (MMCM) is likely due to the large data transfer via PCIe and the multi-cycle clock design and do not exhibit dependence on the ML architectures at this scale. The

neural network requires slightly more look-up tables (LUTs) and significantly more digital signal processor (DSP) blocks to perform the greater number of computations characteristic of neural networks relative to linear regressions. The minimal design complexity requires on-chip memory usage of LUT-based RAM (LUTRAM) and block RAM (BRAM) below 10% which removes the need for external memory storage and additional latency due to inter-chip communication. The minimal hardware usage of the single-chip design supports flexibility in implementation both in terms of software and hardware. Complementary FPGA algorithms, multi-channel data reduction, or neural networks with increased complexity can be accommodated within the framework of the integrated real-time system. Additionally, the compact machine learning-based data reduction can provide competitive accuracy in applications constrained by smaller, lower power, or more cost effective FPGAs.

6.4.2 Real-time results
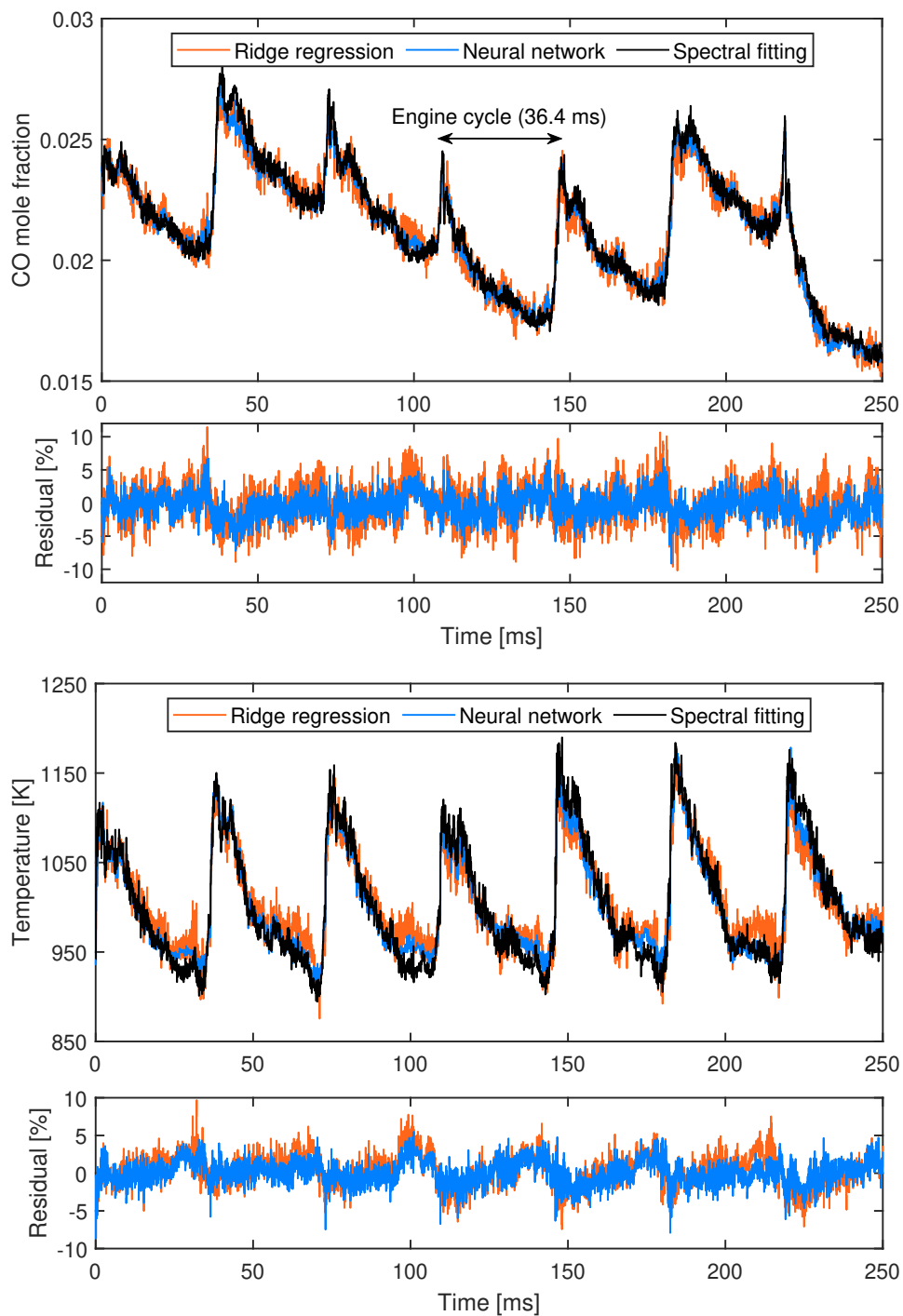
Figure 6.9: Time-resolved calculation of CO mole fraction *(top)* and gas temperature *(bottom)* obtained from ridge regression and neural network onboard the FPGA compared to spectral fitting of the raw transmitted scans.

The completed FPGA bitstream and Simulink Real-Time model were downloaded to the Speedgoat system to execute the FPGA hardware-in-the-loop test depicted in Fig. 6.7 to verify prediction accuracy and computational latency. Figure 6.9 presents the time-resolved gas properties recorded by the CPU obtained from the 10 kHz real-time prediction onboard the FPGA, overlaid with the corresponding spectral fitting reference for comparison. The demonstration data shown here represents 7 sequential engine cycles recorded by the LAS exhaust sensor, with easily-discernible intra-cycle trends in gas temperature and CO mole fraction. Notable for both ML approaches, after 16-bit conversion and FPGA programming the real-time data reduction methods capture the same intra-cycle and cycle-to-cycle trends visible after signal post-processing via spectral fitting. The combined error due to ML model accuracy and fixed-point conversion result in RMS errors in mole fraction and temperature within 3% and 2% for the ridge regression and neural network, respectively. There is also some evidence of bias in the predicted gas properties, most apparent as a slight over-prediction of temperature at lower magnitudes, where the neural network appears to consistently outperform the ridge regression prediction. This scale of imprecision displays a minimal impact on the overall characterization of the exhaust gas transients valuable for IC engine optimization.

Most critically, the real-time demonstration verifies that the FPGA data processor provides reliable 10 kHz data throughput without erroneous values or timing errors on the real-time system. The associated computational time and latency is measurable by observing the up-sampled FPGA output and generated HDL model. Figure 6.10 (top) presents a 300 μs measurement period extracted from the real-time measurements in Fig. 6.9 for the CO mole fraction output. The spectral fitting reference is sampled concurrently with the CPU-to-FPGA PCIe data transfer for the corresponding transmitted laser scan. The real-time FPGA output reveals a latency of 25 μs which corresponds to a single sample period at the 40 kHz PCIe sample rate. This total latency is composed of three major data processing and transfer processes: (1) PCIe transfer of the raw transmitted laser scan from the CPU to
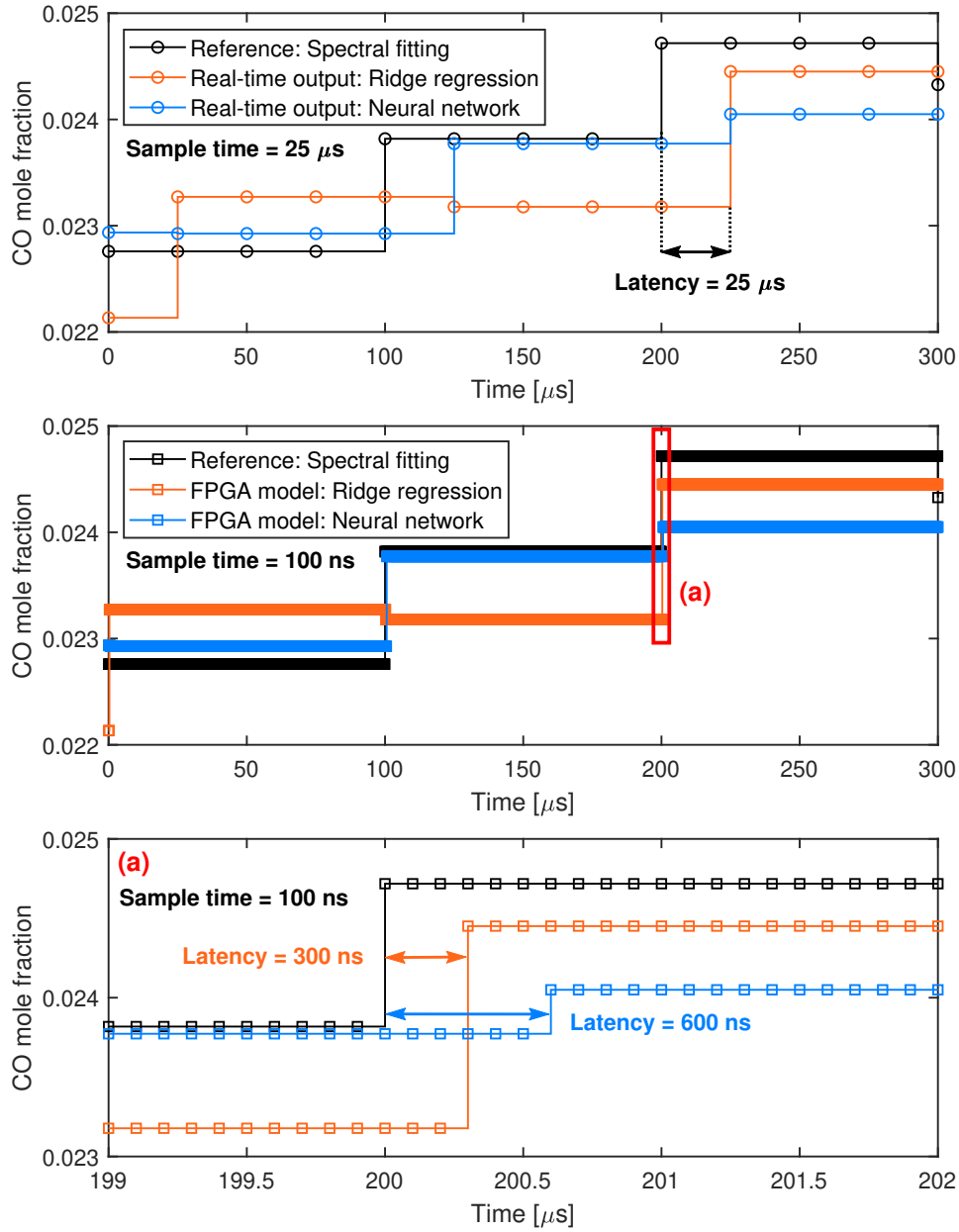
Figure 6.10: Time-resolved CO mole fraction output of the FPGA during real-time testing at 40 kHz sampled by the target machine CPU *(top)* and 10 MHz from the generated HDL model *(middle and bottom)*.

the FPGA (2) end-to-end data reduction performed on the FPGA and (3) PCIe transfer of the FPGA outputs (X_{CO} and temperature) back to the CPU.

The computational time of the FPGA design can be isolated by simulating data reduction with the generated HDL model used to program the FPGA. The HDL model simulation for the same measurement period is shown in Fig. 6.10 (middle and bottom) with a sample time of 100 ns corresponding to the 10 MHz FPGA data rate. Both ML-based FPGA models provide output predictions in less than 1 µs, with computational latency of 300 ns and 600 ns for the ridge regression and neural network, respectively. The higher latency of the neural network is due to the additional data pipelining delays between sequential matrix operations which are required to satisfy FPGA timing constraints. Compared to MATLAB-based CPU execution, adapting the ML-based data reduction for embedded FPGA implementation yields a further reduction in computational time of approximately an order of magnitude. As evident in Fig 6.9, rigid FPGA timing ensures consistent and reliable execution with this accelerated data reduction speed without the variable latencies extending above 100 µs observed on the CPU.

Overall latency in the real-time system is dominated by PCIe data transfer between the CPU. Close-coupling the FPGA processor with the ADCs used to sample the transmitted laser scans from the photodetector is expected to further reduce overall latency. The Kintex-7 FPGA module in the Speedgoat target machine houses dedicated 5 MHz 16-bit ADCs with a latency of 200 ns during data transfer to the FPGA. This would remove the need for transmitted scan transfer via PCIe and greatly reduce back-end latency of the LAS sensor below the 25 µs measured in this demonstration. In its current configuration, the proposed method already surpasses the throughput and latency requirements of the 10 kHz LAS exhaust sensor, with capability for 40 kHz data throughput and latency orders of magnitude below the period of a single engine cycle. While the overall performance of the real-time system involves a coupling of hardware design choices and on-chip data reduction algorithms, the approach utilized in this work for ML model reduction is generally applicable to different real-time systems.

6.5 Conclusions

This work presents embedded machine learning data reduction methods for real-time laser absorption spectroscopy at over 10 kHz using a field-programmable gate array for application to cycle-resolved exhaust gas sensing and low-latency sensor feedback towards adaptive reciprocating engines. A ridge regression and fully-connected feedforward neural network were systematically developed and reduced for FPGA processing to quickly and accurately infer gas temperature and carbon monoxide mole fraction directly from transmitted laser intensity signals attenuated by a pair of mid-wave infrared CO absorption transitions. The machine learning models were trained on synthetic and experimental data corresponding to an LAS sensor module integrated in a production reciprocating engine. The machine learning approach accelerates data reduction by two orders of magnitude (relative to non-linear spectral fitting) with sub-ms computational time. The compact ridge regression and neural network architectures are shown to enable FPGA on-chip deployment of end-to-end laser absorption spectroscopy signal processing with <50% resource utilization on a Kintex-7 FPGA. Real-time hardware-in-the-loop testing on a Speedgoat Performance target machine demonstrates reliable 10 kHz data throughput with a latency of 25 µs. The neural network model provides more accurate predictions relative to ridge regression with deviations within 5% relative to traditional spectral fitting and an average error of less than 2%. Transfer of the ridge regression and neural network to an FPGA design results in execution times of 300 ns and 600 ns respectively, representing a modest penalty for the added neural network complexity and accuracy. Adaptability of the machine learning data reduction methods and configuration of embedded electronics allows modification to meet variable constraints in sensor targets and hardware availability for integration into other real-time LAS systems. Importantly, the accelerated signal processing extends the capability of high-speed (>10 kHz) mid-infrared laser absorption spectroscopy for real-time exhaust emissions sensors in reciprocating engines. The high real-time bandwidth provides for intra-cycle emissions analysis and, combined with the sub-ms latency, enables adaptive cycle-to-cycle control strategies

towards more efficient and sustainable energy and combustion systems.

CHAPTER 7

Conclusions and ongoing research directions

7.1 Conclusions

The research presented here demonstrates advancements in mid-infrared laser absorption spectroscopy for high-speed, real-time sensing of exhaust gas properties in reciprocating engines valuable to characterization of low-carbon polyfuel combustion and towards enabling fast feedback for engine adaptability. Time-resolved chemical-kinetic modeling of Otto cycle combustion provides a simulation perspective on the effects of low-carbon fuel blends on engine performance and emissions. Simulation results elucidate tradeoffs between relative specific emissions, fuel efficiency, and power density with the addition of non-carbon fuels (H_2 and NH_3) to natural gas engines. Pathways to emissions reduction (CO, CO_2, and NO) are evaluated and indicate potential for optimized performance through adaptive tuning of compression ratio, equivalence ratio, and engine valve timing. An experimental approach to polyfuel engine characterization is initiated with the design of a high-temperature, high-pressure optical gas cell for fundamental mid-infrared spectroscopy studies at over 1200 K and 200 atm to facilitate sensor development and engine combustion conditions. Measurements of CO and CH_4 at elevated conditions up to 7.7 μm in wavelength enables validation of spectral parameters and inform improvements to database values for increased sensor accuracy. Mid-infrared laser absorption spectroscopy is then translated to provide in-situ measurements of CO and NO in the exhaust of a production single-cylinder natural gas engine. A novel opto-mechanical sensor module provides optical access near the exhaust port with sustained operation in the high-temperature, high-vibration environment. Scanned-wavelength direct

130

absorption spectroscopy using quantum and interband cascade lasers targeting CO and NO absorption features near 4.8 µm and 5.2 µm at 10 kHz provides intra-cycle temporal resolution of exhaust gas dynamics exposing significant cycle-to-cycle variation in the production engine. The exhaust sensor is implemented to characterize emissions response to low-carbon fuel blending with up to 10% H_2 and NH_3 in the natural gas fuel stream, highlighting 50% reduction in CO concentration and increases of NO emissions up to an order of magnitude during NH_3 fuel addition. To expand sensor utility for real-time applications, a machine learning approach is developed to accelerate signal processing and bypass computationally-intensive nonlinear Voigt fitting of absorption lineshapes. Compact neural network and linear regression models are trained on simulated and experimental engine exhaust data and provide average prediction accuracy in temperature and CO mole fraction within 2% with orders of magnitude reduction in computational time. The machine learning data reduction methods are adapted for on-chip deployment on a Xilinx field-programmable gate array (FPGA), with hardware-in-the-loop demonstrations yielding sub-µs computational time and 25 µs latency. The advancements presented in this work expand laser absorption sensors for real-time sensing applications in practical reciprocating engines, and future work will leverage this new capability in efforts towards adaptive engine architectures for fuel-flexible low-carbon power generation.

7.2 Ongoing and future research directions

7.2.1 Ammonia exhaust sensing

The increasing interest in ammonia combustion in reciprocating engines elicits characterization of emissions of unburned NH_3 as a toxic pollutant [20, 150, 21]. Chemical kinetics of ammonia oxidation in combustion engines is not fully understood, and experimental sensing of NH_3 emissions can provide a valuable tool to expedite research and development of ammonia-fueled engines with fuel-flexible and low-emission operating strategies. Nasir et

al. [151] have demonstrated detection of trace ammonia concentrations in the exhaust of a diesel IC engine using laser absorption spectroscopy near 10.4 µm. A quantum cascade laser and related optical hardware has been obtained to develop a similar laser absorption sensor at the absorption feature shown in Fig. 7.1 within the ν_2 fundamental rovibrational absorption band of NH_3.
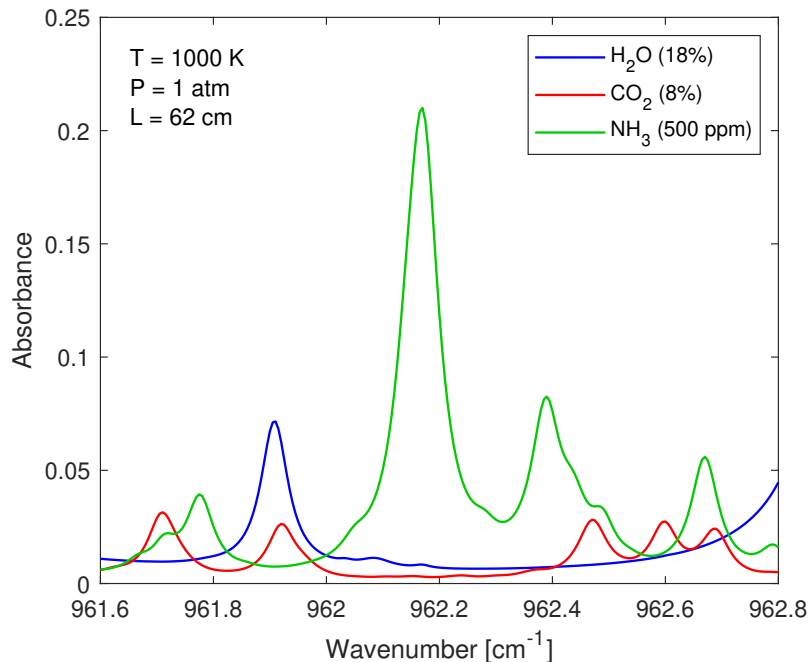
Figure 7.1: Simulated absorption of NH_3 near 10.4 µm at representative temperature and pressure in the Honda EU7000is engine exhaust at the pathlength reflective of the multi-pass exhaust sensor module. H_2O and CO_2 absorption spectra are simulated with HITEMP line-by-line parameters at concentrations estimated from combustion simulations. NH_3 is simulated with HITRAN parameters at a representative concentration taken from literature observations during moderate ammonia addition to reciprocating engine fuel [20, 21].

Future work may involve implementing the light source for NH_3 emissions sensing in the exhaust of the Honda EU7000is engine. Initial fundamental spectroscopy studies will focus on validation of the absorption spectra of NH_3 and interfering species CO_2 and H_2O at this spectral region, including measurements of temperature-dependent linestrengths and collisional broadening. Experimental studies can utilize the high-temperature, high-pressure

optical gas cell presented in Chapter 4 after installing ZnSe or BaF$_2$ optical rods to enable laser transmission at 10.4 µm. This will facilitate studies of the NH$_3$ absorption spectrum at the elevated temperatures (>1200 K) expected in the engine exhaust. Upon completion of the spectral validation study, the sensor may be implemented in the exhaust sensor module for emission studies on the test engine. This will similarly necessitate the use of alternative optical materials. Sapphire optical windows and calcium fluoride focusing lenses can be replaced with ZnSe or BaF$_2$ for transmission at longer wavelengths, although the durability of ZnSe and BaF$_2$ at high-temperature conditions is expected to be a challenge. The indium fluoride optical fibers can be replaced with hollow-core or polycrystalline solid-core optical fibers for light delivery and capture above 10 µm. Once integrated, the new sensor may be used in an experimental procedure similar to that discussed in Chapter 5 to explore exhaust emissions of NH$_3$ when the test engine is fueled with blends incorporating various volume fractions of ammonia in hydrogen and natural gas. This will provide insights into polyfuel strategies for low-carbon and low-emission engine fueling and inform future work in both engine and sensor development.

7.2.2 In-cylinder sensing

The sensing techniques used to achieve cycle-resolved exhaust sensing may be adapted for in-cylinder sensing of temperature and species concentrations throughout the engine cycle. The optical gas cell will enable validation of the spectral models of the mid-infrared absorption transitions at the high pressures representative of peak in-cylinder conditions (>40 bar). Additional testing in the high-enthalpy shock tube at UCLA will provide additional validation testing at temperatures above 1200 K if needed. Opto-mechanical techniques used in the exhaust sensor module can be adapted to provide optical access to the combustion chamber through modification of the engine cylinder head or spark plug as has been demonstrated previously [62]. Cycle-resolved thermochemical sensing during the compression and expansion strokes will provide direct analysis of combustion progress and the transient formation

of emissions at the point of sharp species evolution gradients. Time-resolved thermochemical measurements will be valuable in refining simulation approach and chemical kinetic mechanisms for polyfuel reciprocating engines. Coupling in-cylinder and exhaust manifold sensing will provide a complete diagnosis of combustion processes and resulting engine-out emissions and their dependence on fuel composition as well as tunable engine operating parameters including ignition timing and variable valve actuation.

7.2.3 Simulation model development

The engine simulation model presented in Chapter 2 can be further developed to improve accuracy when predicting emissions concentrations during low-carbon fueling of the single-cylinder test engine. Experimental data presented in Chapter 5 provides points of comparison to evaluate the simulations. Additional measurements of the engine test setup (e.g., natural gas fuel composition, intake air mass flow rate, intake manifold pressure and temperature) will help improve utility of the experimental datasets for simulation validation. Refinement of the Cantera simulation can be achieved with increased detail in the reactor network to better match real engine properties. Additional heat transfer mechanisms can be added to the constant volume reactor, and valve actuation mechanics expanded to include time-dependent flow coefficients representative of the cam-driven lift profiles. Modeling of fluid motion and gas mixing between the intake, cylinder, and exhaust domains due to backflow and valve overlap can be increased by replacing reservoirs with additional reactors. Limitations in modeling of fluid dynamics and spatial flame propagation may be addressed by modifying reactor governing equations to include conservation of momentum and discretization of the constant volume, with one common approach to implement a two-zone model of the in-cylinder combustion volume [152, 153]. Improvement of the simulation mechanics would concurrently involve evaluation of chemical kinetic mechanisms to capture species evolution in novel low-carbon blends with a desire to minimize mechanism complexity and reduce computational load of the time-resolved simulations. Simulation development informed by

laser absorption measurements in a controlled environment will support future interpretation of sensor results during dynamic or uncontrolled operating conditions and inform adjustment to tunable engine parameters including spark timing, fuel-air mixing, and valve actuation.

7.2.4 Camless valvetrain development
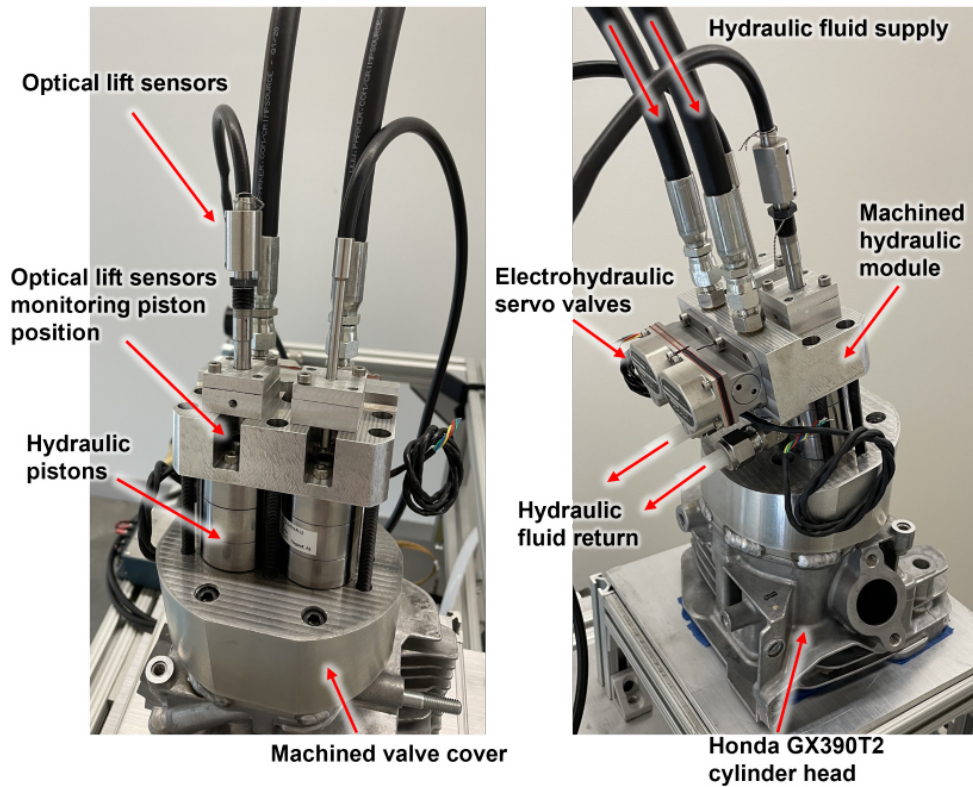
Figure 7.2: Electrohydraulic valvetrain for camless conversion of HondaEU7000is electricity generator.

An electrohydraulic valve actuation system is currently under development to convert the single-cylinder test engine to camless valve actuation. Camless engine systems have demonstrated capability to improve engine performance and reduce emissions by utilizing electronically-controlled actuators to replace mechanical camshafts with limited adjustability in standard variable valve actuation systems. Higher valve velocities coupled with the infinite control over intake and exhaust valve lift, duration, and phase enables optimization

of fluid flow throughout the engine operating range including engine speed, load, and fuel quality. The fast response of electronic control allows on-the-fly adjustment to transient disturbances such as environmental conditions, engine start-up and shut-down, and fluctuations in load demand. This system will increase adaptibility to variable-composition low-carbon fuel mixtures by adjusting valve actuation to match the differing combustion requirements.

A custom camless valvetrain for the GX390T2 engine has already been designed and manufactured and is shown in Fig 7.2. A machined aluminum valve cover provides the alignment and mounting of the double-acting hydraulic pistons that are rigidly connected to the engine valves with lightweight machined aluminum adapters to minimize valve assembly mass. The double-acting hydraulic pistons (MackCorp SS6133-5-ITW-R-LS) with 0.5 in. piston travel provide both lifting and seating of the engine valves, removing the need for a valve spring. The moving piston is visible from the top of the piston housing which enables monitoring of valve position during actuation via optical displacement sensors (Philtec D170) with 20 kHz measurement bandwidth. The hydraulic fluid inlets and outlets are also on the top side of the piston housing, and a custom machined hydraulic module mates with the fluid ports while securing the pistons in place on the valve cover. Internal flow passages within the hydraulic module lead to mounted electro-hydraulic servo valves (MOOG 30 Series -1003) which control hydraulic flow to each side of the double-acting pistons. The servo valves provide fast response (<100 Hz 3 dB cutoff frequency) actuation and flowrates up to 3.8 gallons per minute (gpm) at a 4,000 psi pressure drop. The hydraulic module provides additional mounting points for the optical displacement sensors and visual access to the moving hydraulic pistons.

Figure 7.3 shows the hydraulic power bank developed to supply the high-pressure, high-flowrate hydraulic fluid to the valvetrain. A gear pump driven by a three-phase electric motor at 1,800 rpm to supply 3.6 gpm of hydraulic fluid to the valvetrain at 1,500 psi which is limited by the pressure rating of the hydraulic pistons. Valvetrain supply pressure is controlled by an adjustable backpressure regulator, with a diaphragm accumulator connected to the fluid
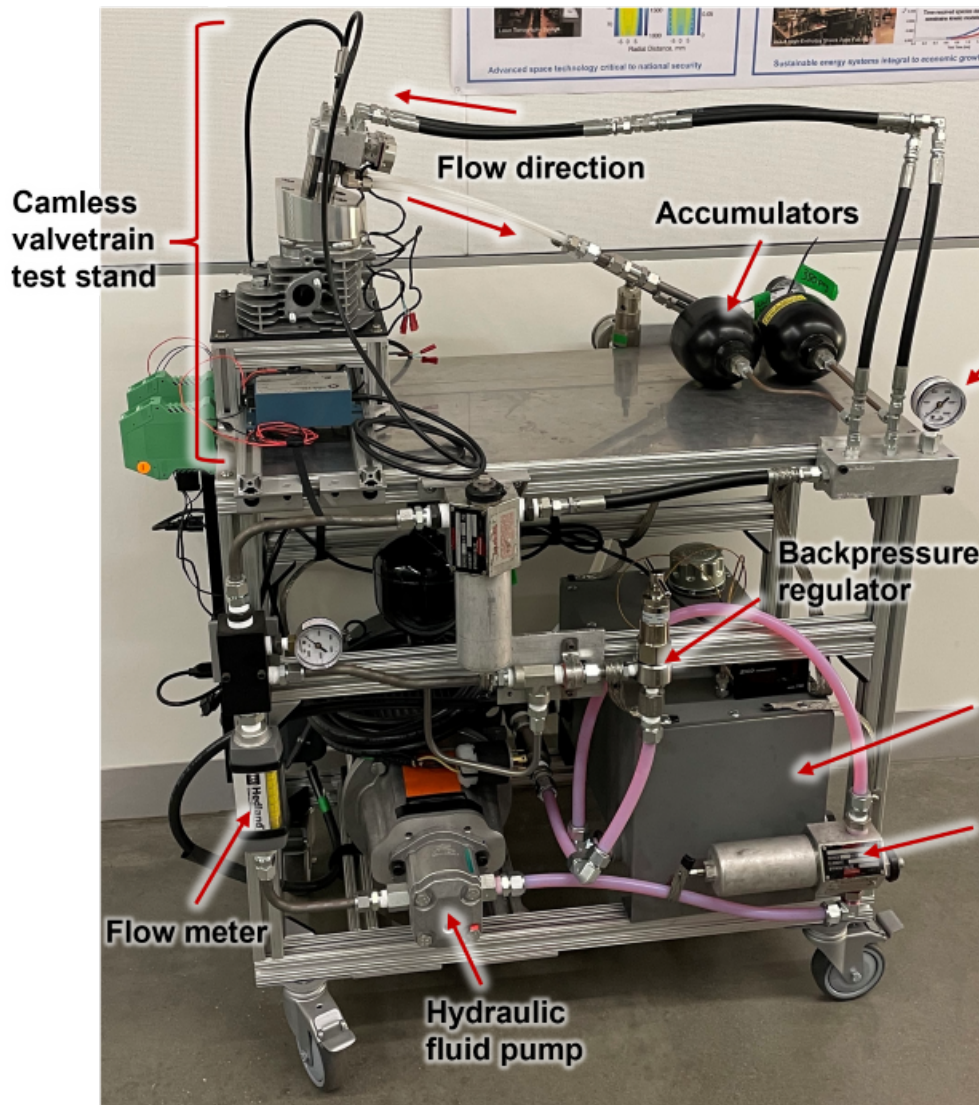
Figure 7.3: Hydraulic power bank with camless valvetrain test stand.

supply circuit to damp pressure fluctuations from the pump and pressure control. Fluid cleanliness is critical for smooth and reliable operation of the hydraulic pistons and servo valves, and filtering is achieved with multiple in-line fluid filters (Schroeder NF30) rated for 20 gpm and 3,000 psi. Hydraulic supply is split into separate lines for each servo valve, with check valves and additional independent diaphragm accumulators for pressure stability, flow consistency, and reduced cross-talk. Fluid pressure downstream of the servo valves, set to less than 500 psi, is controlled with another adjustable backpressure regulator and

additional check valves on each flow channel. Pressure gauges throughout the hydraulic flow path are used to monitor system pressure and stability, and the 5 gallon hydraulic fluid reservoir is equipped with a thermocouple to monitor fluid temperature during testing. This setup provides a mobile, compact ($<$4ft^3) platform for hydraulic supply, and an additional test stand mounted to the top of the power bank frame facilitates preliminary testing of the camless valvetrain.

The electronic control and data acquisition for the electrohydraulic valvetrain is executed by the Speedgoat Performance real-time target machine operating with Simulink Real-Time 2022a as described in Chapter 6. Analog voltage signals from the optical displacement sensors reading valve position are sampled at 200 kHz by the IO131 analog I/O module. Analog voltage control signals for the servo valves generated by the Speedgoat system are transmitted by the IO131 outputs (10 µs settling time) through buffer amplifiers which convert voltage signals to current signals compatible with the servo valves. An initial pulse method is used to perform the valve actuation and is shown in the top of Fig. 7.4. Fluid flowrate through the servo valve and resulting engine valve velocity is controlled by the pulse magnitude, with pulse duration corresponding to the duration of fluid flow and valve motion. The sign of the command signal indicates direction of flow and valve motion, with positive signals corresponding to valve lift. A constant negative control signal provides seating of the engine valves, and an initial opening pulse opens the valve at maximum velocity. A sustain pulse maintains constant maximum valve lift, followed by a closing pulse to return the valve to its seated position. The resulting camless valve lift profiles are displayed in the middle of Fig. 7.4. The valve lift profiles (timing, phase, duration, and lift) are executed to replicate the original valve timing from the cam-driven system on the GX390T2 engine at an engine speed of 1,000 rpm, shown in the bottom of Fig. 7.4. The fast-response hydraulic actuation system meets the timing requirements of the 1,000 rpm engine with the telltale trapezoidal profiles of camless valvetrains in contrast to the lobed profiles of the original cam-driven actuation. The pulse control signal method provides a simple method to execute
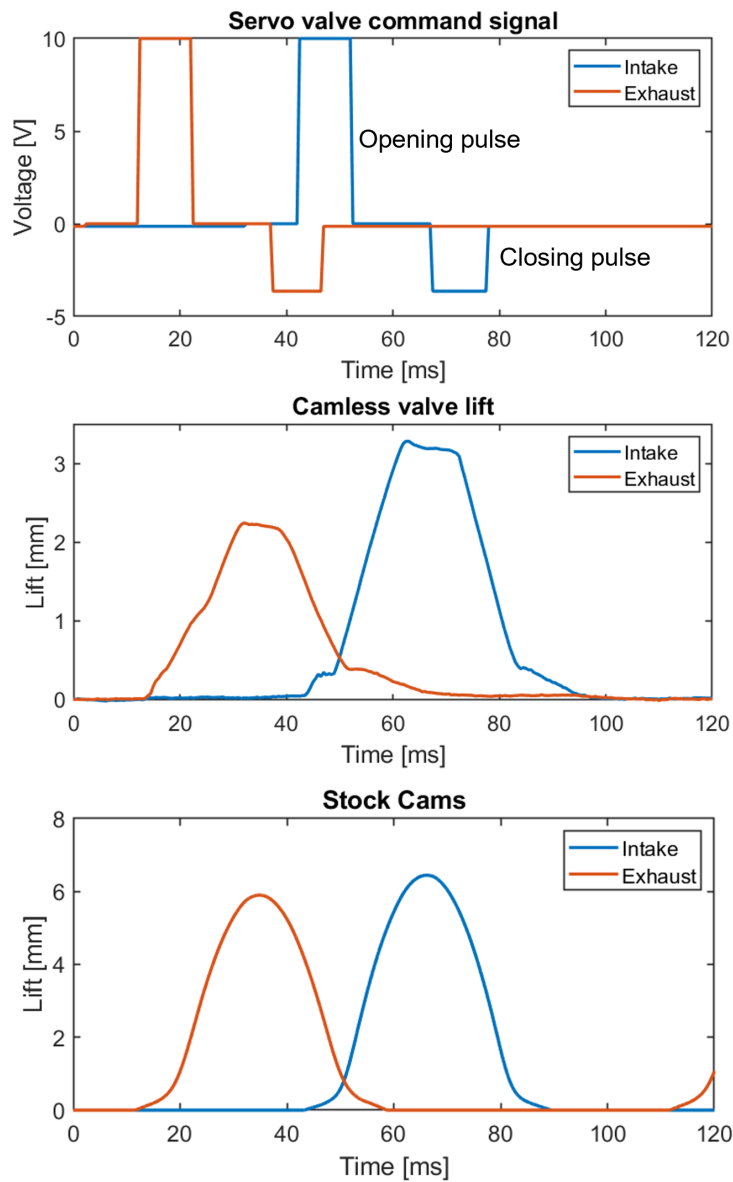
Figure 7.4: Camless actuation signals and valve lift during experimental testing, compared to original mechanical cam lift profiles on the test engine.

these profiles while providing a low valve seating velocity to prevent damage or unreliable valve seating. However, the maximum lift of the camless valvetrain at this speed is lower than the original cam-driven system. Fluid flow restriction within the compact hydraulic pistons likely leads to flow saturation and limits flowrates below what is achievable with the

hydraulic power bank and servo valves, thus limiting the maximum engine valve velocities. Modification of the hydraulic actuator strategy, either through custom high-flow pistons or alternative actuator geometries, is expected to be a main focus of future work to remove the flow limitation and increase the lift performance of the valve actuation system. Additionally, characterization of the system dynamics will enable the use of more advanced valve actuation control strategies and lead to improved performance with built-in adaptability. After valve actuation performance and control methods have reached a satisfactory readiness level, the camless system can be installed on the Honda EU7000is test engine to provide variable valve actuation control. This will facilitate experimental studies on the effect of valve actuation strategies on engine performance and emissions with low-carbon fuel blends.

7.2.5 Adaptive engine control
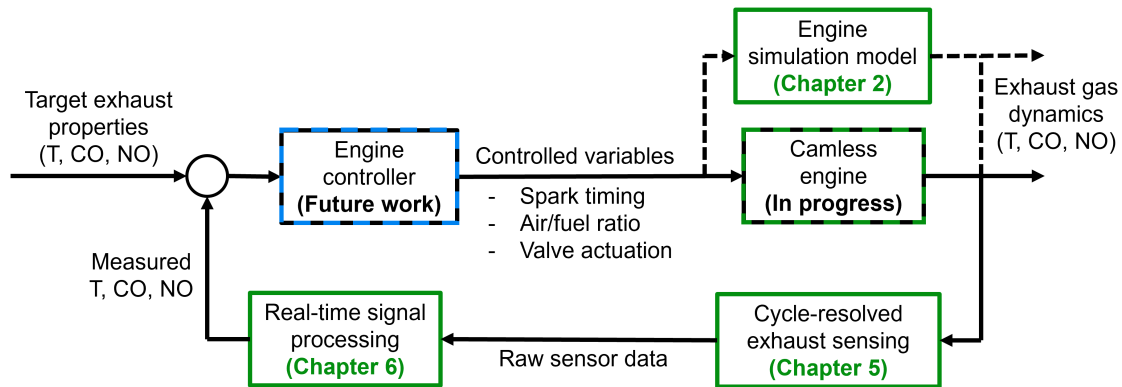
Figure 7.5: Simplified control diagram of the adaptive camless engine control informed by emissions feedback provided by the developed laser absorption exhaust sensor. The engine simulation model acts as a test bench and possible aspect of controller development depending on future work on the real-time control algorithms.

The research presented here is part of a greater effort to provide adaptive power generation reciprocating engines capable of real-time fuel-flexible operation with low-carbon polyfuel blends. The laser absorption sensors, combustion modeling, and variable valve actuation hardware are contributions to provide real-time emissions feedback for fast closed-loop con-

trol in this adaptive engine architecture. Figure 7.5 illustrates a simplified schematic of the components of the emissions feedback control loop of the in-progress adaptive camless engine. High-data-throughput LAS exhaust sensing capability has been successfully demonstrated in this dissertation, along with engine modeling to inform engine strategies and controller design. Once the camless valvetrain is completed and integrated into the test engine, this will provide a platform for electronic control of infinitely-variable valve actuation. Existing engine systems (e.g., fuel flowrate control, ignition timing, throttle, on-board sensors) may be modified if needed for similar electronic control and offloaded from the existing engine control model for integration with a new engine control system. This new engine control system can be a focus of future work to leverage the advancements in sensor development, combustion modeling, and adaptive engine hardware for real-time optimization. Model predictive control schemes may be explored for this application, with potential input from the engine simulation model to construct the optimizers for predictive action. This adaptive engine configuration will serve as test platform to achieve robust, fuel-flexible operation on low-carbon fuel blends for implementation in practical power generation engines, leveraging the technical advancements described in this dissertation.

APPENDIX A

Combustion modeling codes

A.1   Chemical kinetic mechanism

This section contains exerpts from the CRECK kinetic model used in Chapter 2.

Initial description and definition of species and overall gas properties:

description:

This thermodynamic database was obtained by fitting the thermodynamic properties extracted from the following file: TOT2003.THERM The thermodynamic properties are fitted in order to preserve not only the continuity of each function at the intermediate temperature, but also the continuity of the derivatives, from the 1st to the 3rd order The intermediate temperatures are chosen in order to minimize the fitting error. Last update: 3/24/2020

generator: ck2yaml

input-files: [chem.CKI, therm.CKT, tran.TRC]

cantera-version: 2.5.1

date: Tue, 27 Jun 2023 15:15:39 -0700

units: length: cm, time: s, quantity: mol, activation-energy: cal/mol

phases:

name: gas

thermo: ideal-gas

elements: [C, H, O, N, He, Ar]

species: [AR, N2, HE, H2, H, O2, O, H2O, OH, H2O2, HO2, CO, CO2, HOCO, CH4, CH3, CH2, CH2(S), C, CH, CH3O2H, CH3O2, CH3OH, CH3O, CH2OH, CH2O, HCO, HO2CHO, HOCHO, OCHO, C2H6, C2H5, C2H5O2H, C2H5O2, C2H4, C2H3, C2H2, C2H, C2H5OH, C2H5O, PC2H4OH, SC2H4OH, C2H4O2H, C2H4O1-2, C2H3O1-2, CH3CHO, CH3CO, CH2CHO, CH2CO, HCCO, HCOOH, CH3CO3, CH3CO3H, CH2OHCHO, CHO-CHO, O2C2H4O2H, HO2CH2CHO, CH3OCHO, CH3OCO, C3H8, IC3H7, NC3H7, C3H6, C3H5-A, C3H5-S, C3H5-T, C3H5O, C3H6O, CH3CHCHO, AC4H7OOH, CH3CHCO, AC3H5OOH, C3H6OH1-2, C3H6OH2-1, HOC3H6O2, SC3H5OH, C3H5OH, CH2CCH2OH, C3H4-P, C3H4-A, C3H3, C3H2, C2H5CHO, CH2CH2CHO, RALD3, C2H3CHO, CH3COCH3, CH3COCH2, NC4H10, PC4H9, SC4H9, IC4H10, IC4H9, TC4H9, IC4H8, IC4H7, IC4H7O, C4H8-1, C4H8-2, C4H71-3, C4H71-4, C4H71-O, C4H6, C4H5, C4H4, C4H3, C4H2, C6H6, FULVENE, C6H5, C5H6, C5H5, MCPTD, C10H8, NO, N2O, NO2, HNO, HNO2, HONO, HONO2, N2H2, H2NN, HNNO, NH2NO, NH2OH, HNOH, NH3, N2H4, N, NO3, NH, NNH, NH2, H2NO, N2H3, HCN, HNC, HNCO, HCNO, HOCN, CH2NO, CH3NO, CH3NO2, CH3ONO, CH3ONO2, CH3CN, CN, NCN, NCO, HNCN, H2CN, HCNH, C2N2, CH2CN, CH2NH, CH3NH2, CH2NH2, CH3NH]

kinetics: gas

transport: mixture-averaged

state: T: 300.0, P: 1 atm

Definition of species-specific thermodynamic coefficients and transport properties:

species:

- name: N2

composition: N: 2

thermo:

model: NASA7

temperature-ranges: [200.0, 1050.0, 3500.0]

data:

- [3.73100682, -1.8315973e-03, 4.32324662e-06, -3.04378151e-09, 7.46071562e-13, -1062.87426, 2.16821198]

- [2.81166073, 1.67067353e-03, -6.79997428e-07, 1.32881379e-10, -1.02767442e-14, -869.811579, 6.6483805]

transport:

model: gas

geometry: linear

well-depth: 97.53

diameter: 3.621

polarizability: 1.76

rotational-relaxation: 4.0

Definition of chemical reactions and relevant rate equations:

equation: H + NO (+M) ¡=¿ HNO (+M) Reaction 2142

type: falloff

low-P-rate-constant: A: 2.4e+14, b: 0.206, Ea: -1550.0

high-P-rate-constant: A: 1.5e+15, b: -0.41, Ea: 0.0

Troe: A: 0.82, T3: 1.0e-30, T1: 1.0e+30, T2: 1.0e+30

efficiencies: N2: 1.6

- equation: H + HNO ¡=¿ H2 + NO Reaction 2143

rate-constant: A: 9.68e+11, b: 0.62, Ea: 360.0

- equation: O + HNO ¡=¿ OH + NO Reaction 2144

rate-constant: A: 2.29e+13, b: 0.0, Ea: 0.0

- equation: OH + HNO ¡=¿ H + HONO Reaction 2145

type: pressure-dependent-Arrhenius

rate-constants:

- P: 0.01 atm, A: 1060.0, b: 2.76, Ea: 4439.0

- P: 0.1 atm, A: 1090.0, b: 2.75, Ea: 4450.0

- P: 0.316 atm, A: 1180.0, b: 2.74, Ea: 4476.0

- P: 1.0 atm, A: 1480.0, b: 2.72, Ea: 4554.0

- P: 3.16 atm, A: 2710.0, b: 2.64, Ea: 4768.0

- P: 10.0 atm, A: 9670.0, b: 2.49, Ea: 5253.0

- P: 31.6 atm, A: 5.31e+04, b: 2.29, Ea: 6063.0

- P: 100.0 atm, A: 1.03e+05, b: 2.24, Ea: 6951.0

A.1.1   Cantera reciprocating engine model

FracH2 = 0.25;

FracNH3 = 0;

FracNG = 1-FracH2-FracNH3;

phi = 1;

SparkTime = 345;

EVC = 20;

IVC = 200;

EVO = 500;

epsilon = 12;

p_inlet = 1*101325;

NGCH4 = 0.94;

NGC2H6 = 0.04;

NGC3H8 = 0.02;

NGCO2 = 0.00;

MW_H = 1.01;

MW_O = 16.00;

MW_N2 = 28.01;

MW_O2 = 32.00;

MW_CO = 28.01;

MW_CO2 = 44.01;

MW_NO = 30.01;

MW_NO2 = 46.01;

MW_H2 = 2.02;

MW_CH4 = 16.04;

MW_C2H6 = 30.07;

MW_C3H8 = 44.10;

MW_H2O = 18.02;

MW_NH3 = 17.03;

MW_N2O = 44.01;

NH3_O2 = (3/4);

NH3_N2 = (3/4)*3.76;

H2_O2 = (1/2);

H2_N2 = (1/2)*3.76;

NG_pCO2 = (1*NGCH4) + (2*NGC2H6) + (3*NGC3H8);

NG_pH2O = 0.5*((4*NGCH4) + (6*NGC2H6) + (8*NGC3H8));

NG_AirCoeff = 0.5*((2*NG_pCO2) + (1*NG_pH2O));

NG_O2 = NG_AirCoeff*1;

NG_N2 = NG_AirCoeff*3.76;

InletH2 = phi*FracH2;

InletNH3 = phi*FracNH3;

InletNG = phi*FracNG;

InletCH4 = NGCH4*InletNG;

InletC2H6 = NGC2H6*InletNG;

InletC3H8 = NGC3H8*InletNG; if NGAir == 1

InletO2 = NG_O2;

InletN2 = NG_N2;

else

InletO2 = FracNH3*NH3_O2 + FracH2*H2_O2 + FracNG*NG_O2;

InletN2 = FracNH3*NH3_N2 + FracH2*H2_N2 + FracNG*NG_N2;

end

StoichCH4 = NGCH4*(1-StoichH2);

StoichC2H6 = NGC2H6*(1-StoichH2);

StoichC3H8 = NGC3H8*(1-StoichH2);

StoichCO2 = NGCO2*(1-StoichH2);

InletH2 = phi*StoichH2;

InletCH4 = phi*StoichCH4;

```
InletC2H6 = phi*StoichC2H6;

InletC3H8 = phi*StoichC3H8;

InletCO2 = phi*StoichCO2;

if NGAir == 1

AirCoeff = 2.11;

InletO2 = AirCoeff*1;

InletN2 = AirCoeff*3.76;

else

pCO2 = (1*StoichCH4) + (2*StoichC2H6) + (3*StoichC3H8);

pH2O = 0.5*( (2*StoichH2) + (4*StoichCH4) + (6*StoichC2H6) + (8*StoichC3H8) );

AirCoeff = 0.5*( (2*pCO2) + (1*pH2O) );

InletO2 = AirCoeff*1;

InletN2 = AirCoeff*3.76;

end

comp_inlet = strcat('O2:',num2str(InletO2),',N2:',num2str(InletN2),',H2:',num2str(InletH2)...
,',NH3:',num2str(InletNH3),',CH4:',num2str(InletCH4),',C2H6:',num2str(InletC2H6)...
,',C3H8:',num2str(InletC3H8));

InjH = 2*InletH2 + 3*InletNH3 + 4*InletCH4 + 6*InletC2H6 + 8*InletC3H8;

InjO = 2*InletO2;

InjN = 0;

InjC = 0;

InjOH = 0;

InjMoles = 3e-4;

InjMassH = InjMoles*(InjH/(InjH+InjO))*MW_H/1000;
```

```
InjMassO = InjMoles*(InjO/(InjH+InjO))*MW_O/1000;

InjMass = InjMassH + InjMassO;

f = 3300/60;

V_H = 389e-6;

d_piston = 0.088;

T_inlet = 325;

n_inlet = p_inlet*V_H/(8.3145*T_inlet);

p_outlet = 101325;

T_injector = 300;

p_injector = 100e5;

comp_injector = strcat('O:',num2str(InjO),',H:',num2str(InjH),',C:',num2str(InjC)...
,',N:',num2str(InjN),',OH:',num2str(InjOH));

T_ambient = 300;

p_ambient = 101325;

comp_ambient = 'O2:1, N2:3.76';

T_init = 1000;

p_init = 101325;

comp_init = 'CO2:0.08, H2O:0.18, N2:0.74';

reaction_mechanism = 'chem.yaml';

inlet_valve_coeff = 5e-6;

inlet_open = 0 / 180 * pi;

inlet_close = IVC / 180 * pi;

outlet_valve_coeff = 5e-6;
```

```
outlet_open = EVO / 180 * pi;

outlet_close = EVC / 180 * pi;

injector_open = SparkTime / 180 * pi;

injector_open_2 = (SparkTime+3) / 180 * pi;

injector_close = (SparkTime+1) / 180 * pi;

injector_close_2 = (SparkTime+8) / 180 * pi;

injector_mass = InjMass;

injector_t_open = (injector_close - injector_open) / (2*pi*f);

RevMultiply = 1;

sim_n_revolutions = RevMultiply*4;

tStepMultiply = 1;

sim_n_timesteps = tStepMultiply*4000*RevMultiply;

gas = Solution(reaction_mechanism);

set(gas,'T',T_inlet,'P',p_inlet,'X',comp_inlet)

r = IdealGasReactor(gas);

set(gas,'T',T_inlet,'P',p_inlet,'X',comp_inlet)

inlet = Reservoir(gas);

InletMassFrac = massFraction(gas,'H2','CH4','C2H6','C3H8','NH3');

inlet2 = Reservoir(gas);

set(gas,'T',T_injector,'P',p_injector,'X',comp_injector)

injector = Reservoir(gas);

set(gas,'T',T_ambient,'P',p_outlet,'X',comp_ambient)

outlet = Reservoir(gas);
```

```
set(gas,'T',T_ambient,'P',p_ambient,'X',comp_ambient)

ambient_air = Reservoir(gas);

inlet_valve = Valve(inlet, r);

inlet_valve_reverse = Valve(r, inlet2);

injector_mfc = MassFlowController(injector, r);

outlet_valve = Valve(r, outlet);

A = 0.015;

piston = Wall(ambient_air, r, A);

V_oT = V_H / (epsilon - 1);

A_piston = .25 * pi * d_piston^2;

stroke = V_H / A_piston;

setInitialVolume(r,V_oT)

setArea(piston,A_piston)

sim = ReactorNet(r);

t_sim = sim_n_revolutions / f;

t = linspace(1,sim_n_timesteps,sim_n_timesteps) / sim_n_timesteps * t_sim;

states = zeros(size(length(t),21));

states(1,1:31) = [temperature(gas),pressure(gas),meanMolecularWeight(gas),...

entropy_mass(gas),moleFraction(gas,'O','O2','CO2','CO','NO','H2O',...

'CH4','NO2','CH3','CH','C2H6','C3H8','H2','H','NH3','N2O','N','N2','OH')...

,massFraction(gas,'CO','CO2','NO','H2','CH4','C2H6','C3H8','NH3')];

V = zeros(size(t));

m = zeros(size(t));
```

```
test = zeros(size(t));

mdot_in = zeros(size(t));

mdot_inout = zeros(size(t));

mdot_out = zeros(size(t));

d_W_v_d_t = zeros(size(t));

heat_release_rate = zeros(size(t));

n_last_refinement = -inf;

n_wait_coarsening = 10;

for i = 1:length(t)

piston_speed_cur = piston_speed(t(i),f,stroke);

func = Func('polynomial',0,piston_speed_cur);

setVelocity(piston,func)

if (mod(crank_angle(t(i),f) - inlet_open, 4 * pi) ¡ ...

mod(inlet_close - inlet_open, 4 * pi))

setValveCoeff(inlet_valve,inlet_valve_coeff)

setValveCoeff(inlet_valve_reverse,inlet_valve_coeff)

test(i) = 1;

else

setValveCoeff(inlet_valve,0)

setValveCoeff(inlet_valve_reverse,0)

end

if (mod(crank_angle(t(i),f) - outlet_open, 4 * pi) ¡ ...

mod(outlet_close - outlet_open, 4 * pi))
```

```
setValveCoeff(outlet_valve,outlet_valve_coeff)

else

setValveCoeff(outlet_valve,0)

end

if (mod(crank_angle(t(i),f) - injector_open, 4 * pi) < ...

mod(injector_close - injector_open, 4 * pi))

setMassFlowRate(injector_mfc,injector_mass / injector_t_open)

else

setMassFlowRate(injector_mfc,0)

end

setHeatTransferCoeff(piston,120);

for k = 1:4

if k == 5

error('Error: Refinement limit reached')

end

try

advance(sim,t(i))

catch Exception

setMaxTimeStep(sim,1e-6 * 10 ^-k)

n_last_refinement = i;

end

end

if i - n_last_refinement == n_wait_coarsening
```

```matlab
setMaxTimeStep(sim,1e-5)

end

state_cur = [temperature(gas),pressure(gas),meanMolecularWeight(gas),...

entropy_mass(gas),moleFraction(gas,'O','O2','CO2','CO','NO','H2O',...

'CH4','NO2','CH3','CH','C2H6','C3H8','H2','H','NH3','N2O','N','N2','OH')...

,massFraction(gas,'CO','CO2','NO','H2','CH4','C2H6','C3H8','NH3')];

states(i,:) = state_cur;

V(i) = volume(r);

m(i) = mass(r);

mdot_in(i) = massFlowRate(inlet_valve);

mdot_inout(i) = massFlowRate(inlet_valve_reverse);

mdot_out(i) = massFlowRate(outlet_valve);

d_W_v_d_t(i) = - (pressure(gas) - pressure(ambient_air)) * A_piston * ...

piston_speed(t(i),f,stroke);

heat_release_rate(i) = - volume(r) * gasconstant * temperature(r) * ...

sum(enthalpies_RT(gas) .* netProdRates(gas), 'all');

end
```

APPENDIX B

Gas cell temperature validation

In this appendix we briefly outline a one-dimensional finite difference heat transfer model used to justify the assumptions that (1) the thermocouple measurements on the cell wall are sufficient to describe the gas temperature within reported uncertainty and (2) that the temperature in the gas test section is uniform within the range reported. For brevity, we skip the derivation of the finite-difference forms of the governing equations, but these are readily available in the literature [154, 155]. At the end of the appendix, we compare this 1-D model to a 3-D heat transfer simulation (using the same boundary conditions and heat transfer modes) using commercial software (ANSYS Mechanical APDL) on a single test case for independent verification of the thermal analysis.

B.1   Model assumptions and setup

A diagram of the computational domain depicting a symmetric half of the gas cell is shown in Fig. B.1. The domain comprises the inconel cell wall, one of the sapphire rods, and a gas in the cell. Recorded thermocouple measurements on the outside of the cell wall are shown as T_c, T_1, and T_2. For some calculations we divide the computational domain into two sections, the rod section (Domain 1), and the gas test section (Domain 2). Insets in Fig. B.1 show the considered methods of heat transfer from the center of the cell to the ends of the cell. The following assumptions are made:

- The thermal resistance along the inconel wall is much less than that between the wall

155
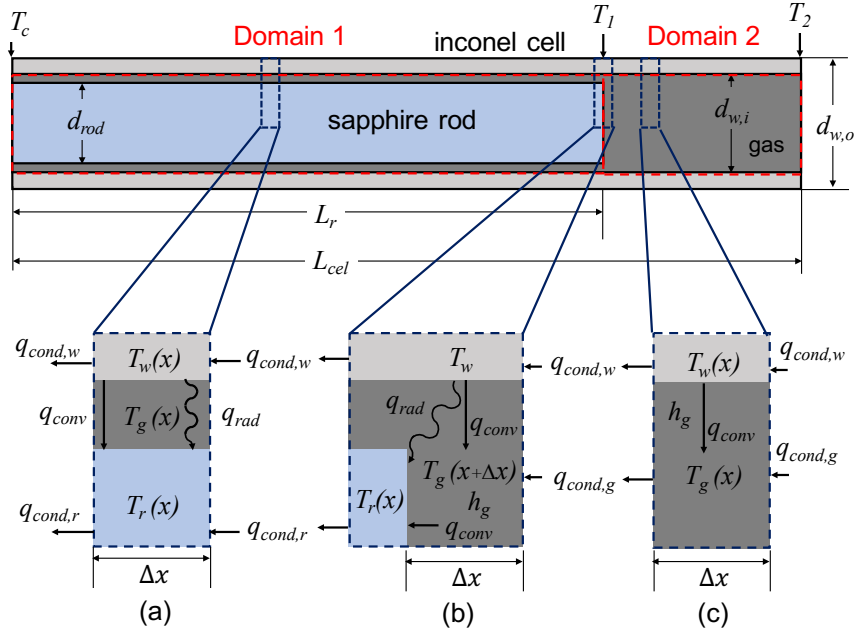
Figure B.1: Gas cell domains for 1-D finite-difference heat transfer calculation, with energy balance diagrams for the heat transfer considered in different regions of the cell.

and the gas.

- The gas has the thermal properties of air.

- The heat transfer in the sapphire rod and the inconel cell wall in Domain 1 are dominated by one-dimensional conduction axially, while natural convection and radiation dominate radially.

- For natural convection, gas temperature $T_g(x)$ in Domain 1 is assumed to be the average of the inconel wall temperature $T_w(x)$ and the rod temperature $T_r(x)$ at the same position x.

- For the gas in Domain 2, conduction between the cell wall and the gas dominates radially, while gas-gas conduction dominates axially.

B.2 Governing equations

A simplified finite-difference expression of the 1-D heat conduction equation [154] for the temperature at position x in the inconel wall, $T_w(x)$ (Figs. B.1(a–c)), utilizing the Crank-Nicholson method [155], is:

$$
\begin{aligned}
T_w(x) = & \frac{\alpha_i(x + \Delta x)\Delta t}{\Delta x^2} T_w(x + \Delta x) \\
& + \left(1 - 2\frac{\alpha_i(x)\Delta t}{\Delta x^2}\right) T_w(x) \\
& + \frac{\alpha_i(x - \Delta x)\Delta t}{\Delta x^2} T_w(x - \Delta x)
\end{aligned}
\tag{B.1}
$$

$\alpha_i(x)$ is the thermal diffusivity of inconel at position x, which changes throughout the domain due to the temperature dependence of thermal conductivity $k_i(x)$ and specific heat capacity $c_{p,i}(x)$, while the density of inconel ρ_i is assumed to be constant. The finite-difference expression for the temperature of the optical rod is similar, but includes terms for heat transfer via natural convection and thermal radiation, as indicated in Fig. B.1(a) [154]:

$$
\begin{aligned}
T_r(x) = & \frac{\alpha_s(x + \Delta x)\Delta t}{\Delta x^2} T_r(x + \Delta x) \\
& + \left(1 - 2\frac{\alpha_s(x)\Delta t}{\Delta x^2}\right) T_r(x) \\
& + \frac{\alpha_s(x - \Delta x)\Delta t}{\Delta x^2} T_r(x - \Delta x) \\
& + h_{nat}(x) \left(\frac{A_{s,r}/A_{c,r}}{\rho_s c_{p,s}(x)} \frac{\Delta t}{\Delta x}\right) (T_w(x) - T_r(x)) \\
& + h_{rad}(x) \left(\frac{A_{s,w}/A_{c,r}}{\rho_s c_{p,s}(x)} \frac{\Delta t}{\Delta x}\right) (T_w(x) - T_r(x))
\end{aligned}
\tag{B.2}
$$

In Eq. B.2, $A_{s,r}$ is the surface area of the sapphire rod for a finite length Δx, $A_{s,w}$ is the corresponding inner surface area of the inconel cell wall, and $A_{c,r}$ is the cross-sectional area of the optical rod. The heat transfer coefficient $h_{nat}(x)$ due to natural convection between two concentric cylinders and associated expressions are available in Bergman et al [154]. The ef-

fective radiation heat transfer coefficient $h_{rad}(x)$ [154] is used for computational convenience, in which the view factor for two concentric cylinders [154] is assumed. Our model assumes constant emissivities $\epsilon_i = 0.55$ [156] and $\epsilon_s = 0.55$ [154] based on available literature values for similar inconel alloys and aluminum oxide, respectively. At the boundary of Domain 2, shown in Fig. B.1(b), where $x = L_r$, the terms:

$$
\begin{aligned}
&\frac{h_g}{\rho_s c_{p,s}} \frac{\Delta t}{\Delta x} \left(T_{g,avg} - T_r(L_r) \right) \\
&+ \frac{h_{rad,f}}{\rho_s c_{p,s}} \frac{\Delta t}{\Delta x} \left(T_{w,avg} - T_r(L_r) \right)
\end{aligned}
\tag{B.3}
$$

are included in Eq. B.2 to account for axial heat transfer due to convection and radiation at the face of the optical rod from the gas and the inconel cell walls, respectively. h_g is assumed to be 25 W/m^2, and $T_{g,avg}$ is the average temperature of the gas between the rods. $T_{w,avg}$ is the average temperature of the inconel cell wall in Domain 2 and $h_{rad,f}$ is the effective radiation heat transfer coefficient, using a view factor for the inside surface of a right circular cylinder to one of its circular faces [156]. In Domain 2, shown in Fig. B.1(c), the heat transfer in the gas is modeled similarly to that of the inconel wall and optical rod:

$$
\begin{aligned}
T_g(x) = {} & \frac{\alpha_g(x + \Delta x)\Delta t}{\Delta x^2} T_g(x + \Delta x) \\
& + \left(1 - 2\frac{\alpha_g(x)\Delta t}{\Delta x^2} \right) T_g(x) \\
& + \frac{\alpha_g(x - \Delta x)\Delta t}{\Delta x^2} T_g(x - \Delta x) \\
& + h_g \left(\frac{A_{s,w}/A_{c,w}}{\rho_g(x)c_{p,g}(x)} \frac{\Delta t}{\Delta x} \right) \left(T_w(x) - T_g(x) \right)
\end{aligned}
\tag{B.4}
$$

A major difference for Eq. B.4 is that $\rho_g(x)$ is not constant, but determined by an equation of state for the gas cell test pressure and $T_g(x)$.

B.3 Boundary Conditions

The boundary conditions of Domains 1 and 2 constrain the system model and are detailed here. The cell is axially symmetric and there is a symmetric adiabat in the plane $x = L_{cel}$. This is accomplished numerically with ghost points beyond the domain boundary [155]. $T_w(x)$ has fixed temperatures near each end of each domain. For Domain 2, in the middle of the cell (the right of Fig. B.1), the temperatures at the outside surface of the inconel cell wall are specified by T_1 and T_2. Likewise, Domain 1 is bounded by T_1 and T_c. $T_w(x)$ is modeled independently of the inside of the cell since T_1, T_2, and T_c are known and the heat transfer in the cell wall is dominated by conduction. $T_w(x)$ is fixed once it is determined, and these temperatures bound the system. Additionally, all points at $x = 0$ are at T_c.

B.4 Numerical Solution

Although the model is transient, we solve for the temperature profile of the inconel cell separately from those of the optical rod and the gas, since we are primarily concerned with the steady state condition. We first solve for $T_w(x)$ using Eq. B.1, initially assuming linear temperature profiles spanning $T_w(0) = T_{cap}$ to $T_w(L_r) = T_1$ for Domain 1 and $T_w(L_r) = T_1$ to $T_w(L_{cel}) = T_2$ for Domain 2. The domains for $T_w(x)$ are solved as a single domain. A timestep Δt and grid cell size Δx are chosen to ensure numerical stability while also keeping computational cost reasonable [155], and the model is run for enough timesteps to converge on a final profile for $T_w(x)$.

Once $T_w(x)$ is known and fixed, we solve for $T_r(x)$ and $T_g(x)$ simultaneously using Eq. B.2 and Eq. B.4. For the optical rod, we estimate an initial linear temperature profile spanning $T_r(0) = T_c$ to $T_r(L_r) = 0.5T_1$ for Domain 1. For the gas, $T_g(x) = (T_w(x) + T_r(x))/2$ in Domain 1, while a uniform profile is initially assumed for Domain 2, with $T_g(x > L_r) = (T_w(L_r) + T_r(L_r))/2$. We determine appropriate Δt and Δx, and allow the model to run to convergence.

B.5 Test Case

To justify the assumptions regarding the gas temperature measurement and the test section temperature uniformity, we employ the model to analyze the test conditions shown in Fig. 4.4. The thermocouple measurements from the experiment are used as inputs for T_c, T_1, and T_2, and the results for the gas temperature distribution are shown in Fig. B.2. For the 3-D model,
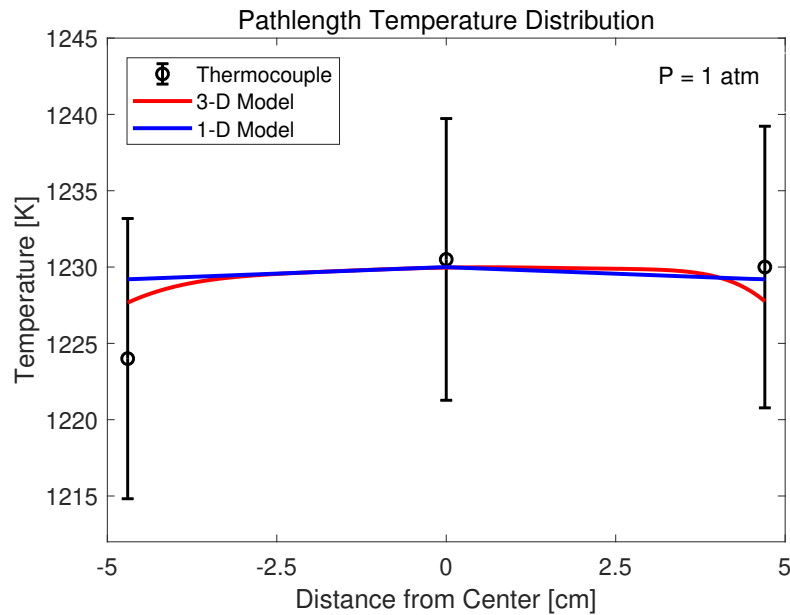
Figure B.2: Results for 1-D finite-difference heat transfer model and 3-D heat transfer model alongside thermocouple measurements for the test shown in Fig. 4.4.

asymmetries reported by the thermocouple measurements were included, while complete symmetry was assumed for the 1-D model. It is shown that the predicted gas temperature distribution for both models falls entirely within the thermocouple experimental uncertainty and reported temperature uniformity range. Importantly, the symmetric 1-D model predicts temperatures within 0.3% of those of the 3-D model (which accounts for finite wall and rod thicknesses), providing additional confidence in the assumptions of the measurements in the cell. Thus, the assumptions that the thermocouples can be used to infer the gas temperature distribution and uniformity are justified for the most extreme temperature

conditions discussed in this manuscript.

APPENDIX C

Exhaust sensor design

C.1 Exhaust pipe design

A custom exhaust pipe replaces the exhaust pipe (see Fig. C.1) that connects to to the exhaust port of the GX390T2 cylinder head. Figure C.2 shows the custom pipe assembly. A custom pipe expander matches the profile of the exhaust port flange to retain use of the original gaskets. The pipe expander interfaces with the 27 mm diameter exhaust port and expands to 50 mm to match downstream piping and the internal diameter of the exhaust sensor module. A threaded mount in the pipe expander allows installation of the original oxygen sensor. A flexible stainless steel exhaust coupling with custom flanges connects the pipe expander to the exhaust sensor module. This aids in vibration damping and alignment of the exhaust assembly and was beneficial given the inherent vibration of single-cylinder engines. Rubber bushings at the two mounting points for the muffler/catalytic converter assembly provide additional vibration damping and decoupling from the generator frame. The exhaust components are sealed with high-temperature gaskets comprised of vermiculite sandwiched between electrolytic tin plates.

C.2 High-temperature optics mounting

High-temperature epoxies used in other high-temperature combustion experiments failed to survive the harsh environment in the engine exhaust. Windows are mounted externally within a counterbore machined into the port plug, with a graphite gasket providing the high-
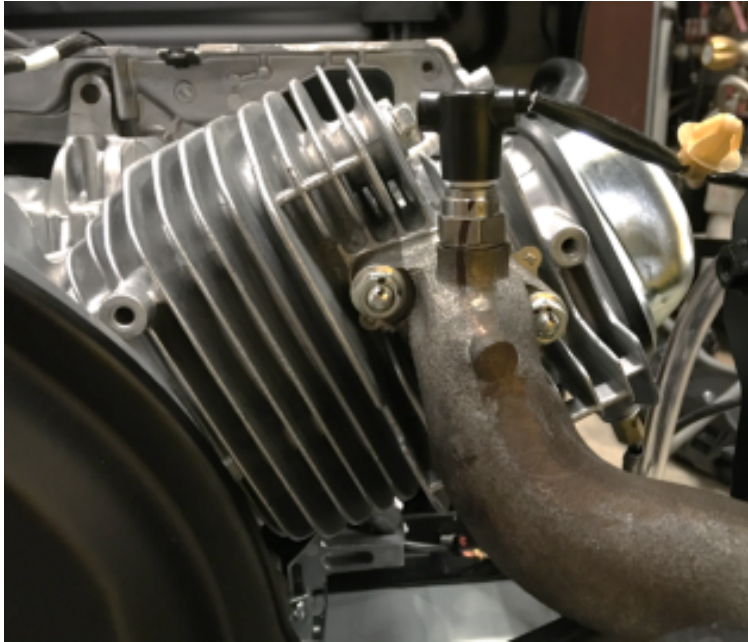
Figure C.1: Original exhaust pipe mounted on the Honda GX390T2 test engine, with O_2 sensor installed.

Figure C.2: Custom exhaust pipe with in-line exhaust sensor module body.

temperature gas-tight seal as in Fig. C.3. The 1 mm thick sapphire window is compressed against the gasket by a male-threaded retaining ring inside the female-threaded counterbore. A stainless steel shim spacer between the window and the retaining ring spans the region of

partial thread depth from the tapping process and allows full compression of the graphite gasket.
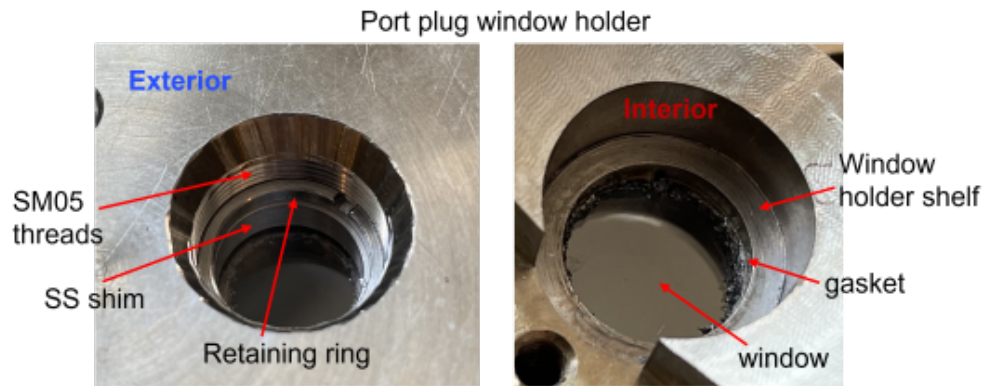
Figure C.3: Sapphire window holder within the exhaust sensor module port plugs.

Mounting of the pair of angled mirrors similarly required refinement to provide precise, secure, and stable positioning without thermal fracture of the mirror substrate. A mechanical clamping assembly was designed to achieve this and is shown in Fig. C.4.
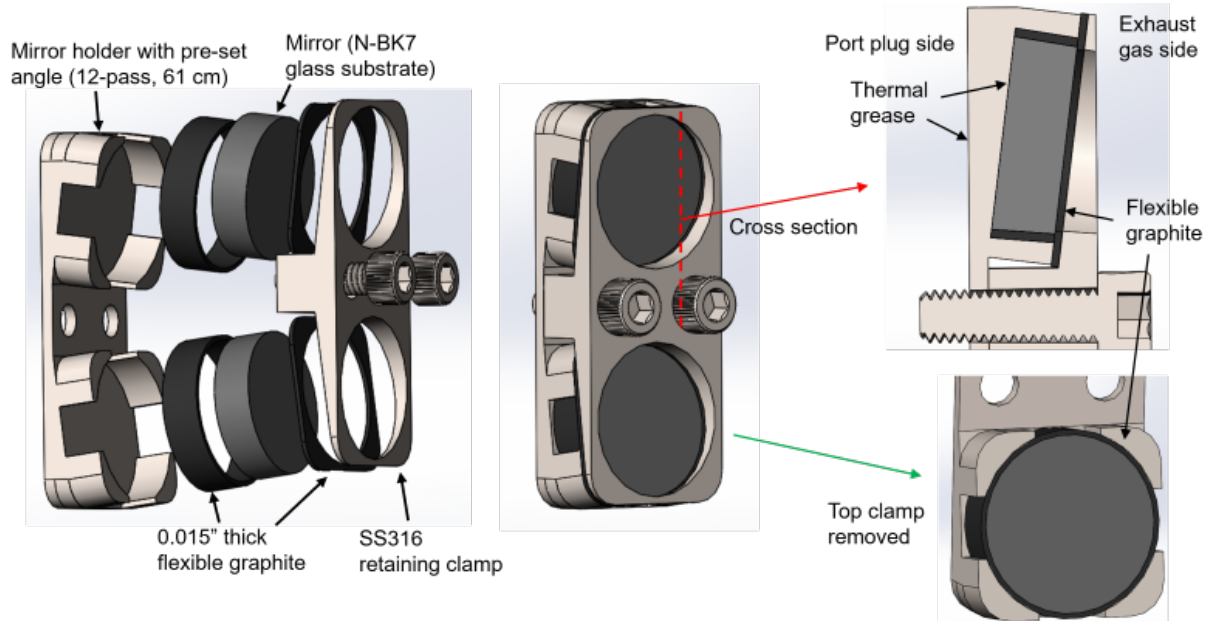
Material	Coeff. Therm. Exp. [10^{-6} K^{-1}]	Therm. Cond. [W/mK]	Spec. Heat Cap. [J/kgK]
SS 316	17.5	21.5	500
N-BK7 glass	8.3	1.12	858
Graphite	1-8	5-140	850

Figure C.4: Design and thermal properties of the mirror holder assembly for the angled White cell mirror pairs in the exhaust sensor module.

C.3   Exhaust sensor module drawings
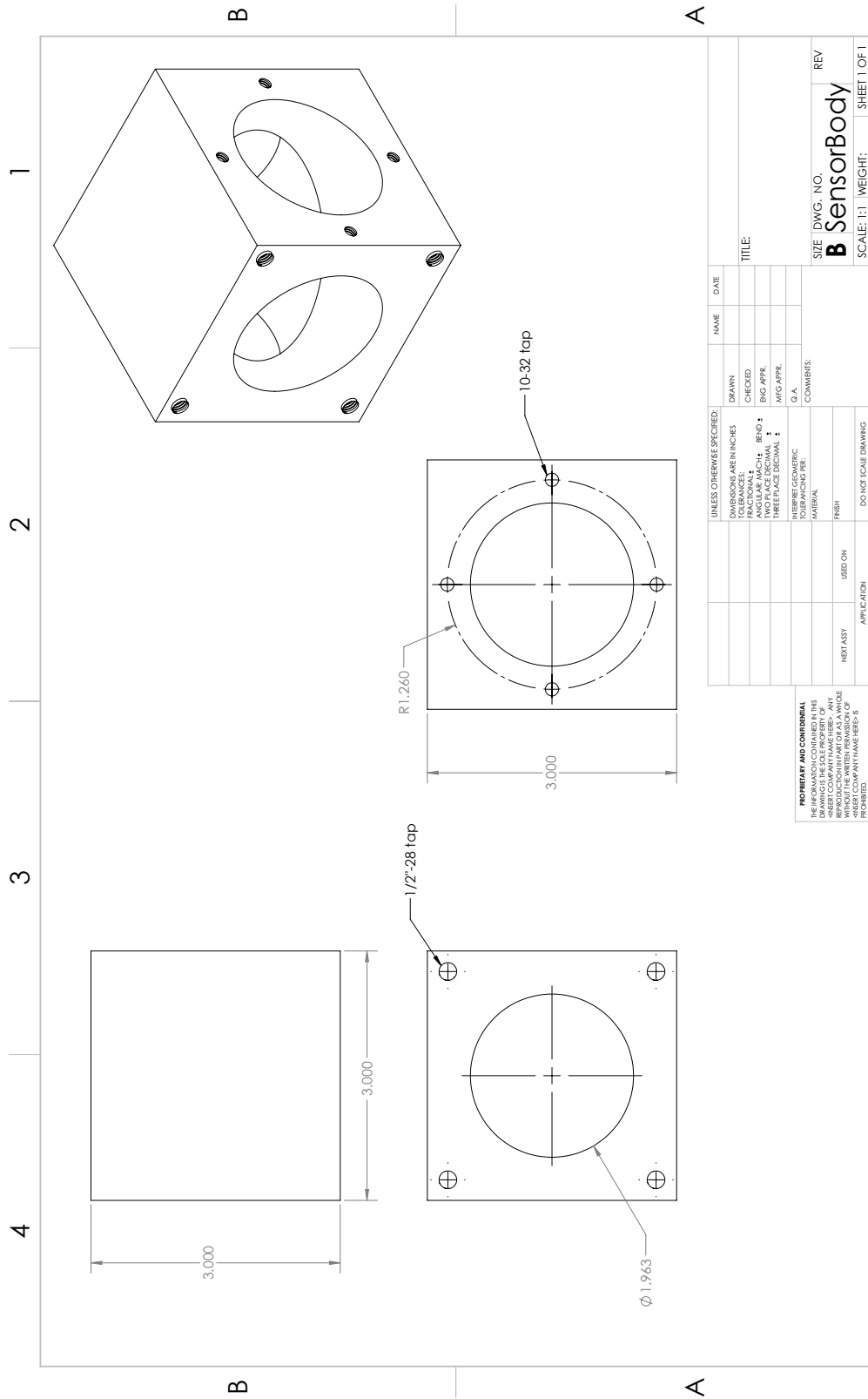
Figure C.5: Drawings for the body of the custom exhaust sensor module.
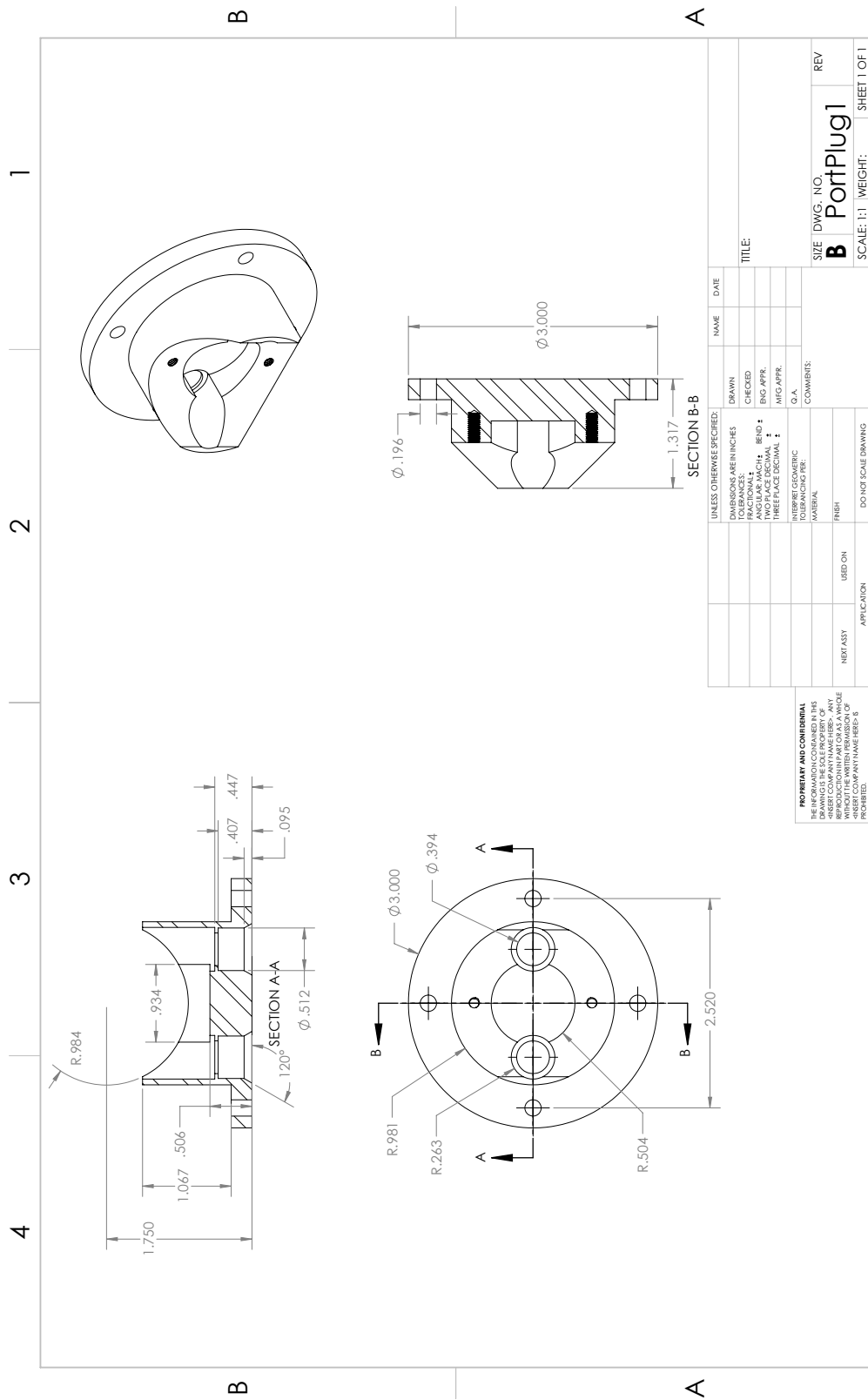
Figure C.6: Drawings for the first of two port plugs of the custom exhaust sensor module.
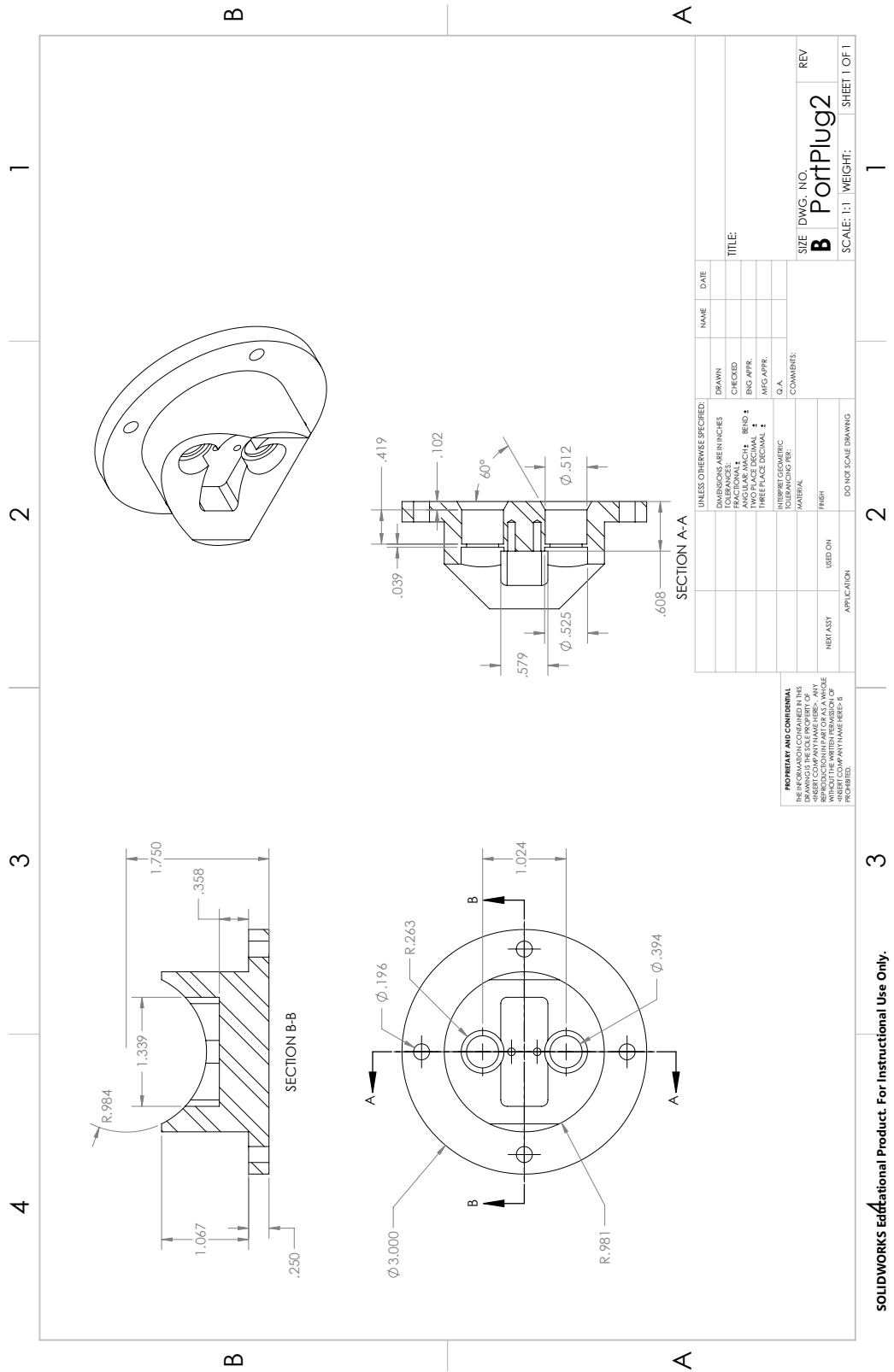
Figure C.7: Drawings for the second of two port plugs of the custom exhaust sensor module.

APPENDIX D

Machine learning models

D.1   Python ridge regression code

Helper libraries

import numpy as np

import matplotlib

import matplotlib.pyplot as plt

import scipy.io

from scipy.io import loadmat

import pandas as pd

import sklearn

TensorFlow and tf.keras

import tensorflow as tf

print("Num GPUs Available: ", len(tf.config.list_physical_devices('GPU')))

from tensorflow.keras import models

from tensorflow.keras import layers

from tensorflow.keras import regularizers

from tensorflow.keras.layers import Conv2D, Conv2DTranspose

```python
from tensorflow.keras.optimizers import RMSprop

from random import randrange


# import matlab data files

# training data

TrainingScansFile = 'ICE_ML_TrainingScans_v2.mat';

TrainingScansData = scipy.io.loadmat(TrainingScansFile);

TrainingScans = TrainingScansData['ICE_ML_TrainingScans']

TrainingOutputFile = 'ICE_ML_TrainingOutput_v2.mat';

TrainingOutputData = scipy.io.loadmat(TrainingOutputFile);

TrainingOutput = TrainingOutputData['ICE_ML_TrainingOutput']


# novel test data

TestScansFile = 'ICE_ML_TestScans_v2.mat';

TestScansData = scipy.io.loadmat(TestScansFile);

TestScans = TestScansData['ICE_ML_TestScans']

TestOutputFile = 'ICE_ML_TestOutput_v2.mat';

TestOutputData = scipy.io.loadmat(TestOutputFile);

TestOutput = TestOutputData['ICE_ML_TestOutput']


# specify x and y for model

x = TrainingScans.T

y = TrainingOutput.T


x2trim = TestScans

y2trim = TestOutput
```

```
x2 = x2trim.T
y2 = y2trim.T


#ridge regression
from sklearn.linear_model import Ridge
from sklearn.linear_model import Lasso
from sklearn.preprocessing import StandardScaler
from sklearn.model_selection import train_test_split
from sklearn.model_selection import GridSearchCV


xs = x
ys = y


ManFeatures = [4, 117, 123, 126, 129, 139, 158, 163, 168, 194]
xf = xs[:,ManFeatures]
xs = xf


#train test split
m = 20000 # number of total samples
test_size = 0.2 # test dataset   20# Split the dataset
xs_train, xs_test, ys_train, ys_test = train_test_split(xs, ys, test_size=test_size)


# parameters for grid search
alpha_array = np.linspace(0.01, 0.1, 20)
parameters = 'alpha':alpha_array
```

```
#linear regression model with ridge or lasso regularization

linear_reg = Ridge()

# define the grid search

Ridge_reg= GridSearchCV(linear_reg, parameters, scoring='neg_mean_squared_error',cv=20)


#linear_reg.fit(xs,ys)


#fit the grid search
Ridge_reg.fit(xs,ys)


# best estimator
print(alpha_array)
print(Ridge_reg.best_estimator_)


# best model
best_model = Ridge_reg.best_estimator_
best_model.fit(xs,ys)


LR_Weights = best_model.coef_


LR_Biases = best_model.intercept_
```

D.2 Python neural network hyperparameter tuning code

```python
# Helper libraries
import numpy as np
import matplotlib
import matplotlib.pyplot as plt
import scipy.io
from scipy.io import loadmat
import pandas as pd


import sklearn
from sklearn import metrics


# TensorFlow and tf.keras
import tensorflow as tf


from tensorflow.keras import models
from tensorflow.keras import layers
from tensorflow.keras.layers import *
from tensorflow.keras.models import Sequential
from tensorflow.keras.layers import Activation
from tensorflow.keras import activations
from tensorflow.keras import regularizers
#from tensorflow.keras.layers import Conv2D, Conv2DTranspose
from tensorflow.keras.optimizers import RMSprop
from random import randrange
import keras_tuner
```

```python
from keras_tuner import HyperParameters as hp


# import matlab data files

# training data

TrainingScansFile = 'ICE_ML_TrainingScans.mat';

TrainingScansData = scipy.io.loadmat(TrainingScansFile);

TrainingScans = TrainingScansData['ICE_ML_TrainingScans']

TrainingOutputFile = 'ICE_ML_TrainingOutput.mat';

TrainingOutputData = scipy.io.loadmat(TrainingOutputFile);

TrainingOutput = TrainingOutputData['ICE_ML_TrainingOutput']


# novel test data

TestScansFile = 'ICE_ML_TestScans.mat';

TestScansData = scipy.io.loadmat(TestScansFile);

TestScans = TestScansData['ICE_ML_TestScans']

TestOutputFile = 'ICE_ML_TestOutput.mat';

TestOutputData = scipy.io.loadmat(TestOutputFile);

TestOutput = TestOutputData['ICE_ML_TestOutput']


# specify x and y for model

x = TrainingScans.T

y = TrainingOutput.T


x2trim = TestScans

y2trim = TestOutput
```

```
x2 = x2trim.T
y2 = y2trim.T


ManFeatures = [4, 117, 123, 126, 129, 139, 158, 163, 168, 194]

xf = x[:,ManFeatures]

x = xf

x2f = x2[:,ManFeatures]

x2 = x2f


from keras import backend as K


def rsquared(y, y_pred):
SS_res = K.sum(K.square( y-y_pred ))
SS_tot = K.sum(K.square( y - K.mean(y) ) )
return ( 1 - SS_res/(SS_tot + K.epsilon()) )


# setup keras hyperparameter model
def build_model(hp):
model = models.Sequential()
input_shape=(InputSize,)
#model.add(layers.Flatten())
# Tune the number of layers.
for i in range(hp.Int("num_layers", 1, 3)):
model.add(
Dense(
# Tune number of units separately.
```

```
units=hp.Int(f"units_i", min_value=2, max_value=8, step=2),

activation="relu",

)

)

model.add(Dense(2))

learning_rate = hp.Float("lr", min_value=1e-5, max_value=1e-2, sampling="log")

model.compile(

optimizer=tf.keras.optimizers.Adam(learning_rate=learning_rate),

loss="mean_squared_error",

metrics=['mean_squared_error',rsquared],

)

return model


build_model(keras_tuner.HyperParameters())


tuner = keras_tuner.BayesianOptimization(

hypermodel=build_model,

objective="val_mean_squared_error",

max_trials=50,

executions_per_trial=3,

overwrite=True,

#directory="my_dir",

project_name="ICE_ML_NN_HPTune",

)


tuner.search_space_summary()
```

```
# search for best hyperparameters
tuner.search(x, y, validation_split=0.2, epochs=50, batch_size=32, shuffle=True)


tuner.results_summary()
```

D.3 Python neural network training code

```
# Helper libraries
import numpy as np
import matplotlib
import matplotlib.pyplot as plt
import scipy.io
from scipy.io import loadmat
import pandas as pd


import sklearn
from sklearn import metrics


# TensorFlow and tf.keras
import tensorflow as tf


from tensorflow.keras import models
from tensorflow.keras import layers
from tensorflow.keras.layers import *
from tensorflow.keras.models import Sequential
from tensorflow.keras.layers import Activation
from tensorflow.keras import activations
```

```python
from tensorflow.keras import regularizers
#from tensorflow.keras.layers import Conv2D, Conv2DTranspose
from tensorflow.keras.optimizers import RMSprop
from random import randrange
import keras_tuner
from keras_tuner import HyperParameters as hp


# import matlab data files
# training data
TrainingScansFile = 'ICE_ML_TrainingScans.mat';
TrainingScansData = scipy.io.loadmat(TrainingScansFile);
TrainingScans = TrainingScansData['ICE_ML_TrainingScans']
TrainingOutputFile = 'ICE_ML_TrainingOutput.mat';
TrainingOutputData = scipy.io.loadmat(TrainingOutputFile);
TrainingOutput = TrainingOutputData['ICE_ML_TrainingOutput']


# novel test data
TestScansFile = 'ICE_ML_TestScans.mat';
TestScansData = scipy.io.loadmat(TestScansFile);
TestScans = TestScansData['ICE_ML_TestScans']
TestOutputFile = 'ICE_ML_TestOutput.mat';
TestOutputData = scipy.io.loadmat(TestOutputFile);
TestOutput = TestOutputData['ICE_ML_TestOutput']


# specify x and y for model
x = TrainingScans.T
y = TrainingOutput.T
```

```python
x2trim = TestScans

y2trim = TestOutput


x2 = x2trim.T

y2 = y2trim.T


ManFeatures = [4, 117, 123, 126, 129, 139, 158, 163, 168, 194]

xf = x[:,ManFeatures]

x = xf

x2f = x2[:,ManFeatures]

x2 = x2f


from keras import backend as K


def rsquared(y, y_pred):

SS_res = K.sum(K.square( y-y_pred ))

SS_tot = K.sum(K.square( y - K.mean(y) ) )

return ( 1 - SS_res/(SS_tot + K.epsilon()) )


# build model

# calculate input size

InputSize = x.shape[1]

# setup network layers

model = models.Sequential()
```

```python
model.add(Dense(units=8,input_shape=(InputSize,)))

model.add(LeakyReLU(alpha=0.02))

model.add(Dense(units=8))

model.add(LeakyReLU(alpha=0.02))

model.add(Dense(units=2))

# specify optimizer and learning rate

ModelOptimizer = tf.keras.optimizers.Adam(learning_rate=0.01)


# parameters for training

model.compile(loss='mean_squared_error', optimizer=ModelOptimizer,...

metrics=['mean_squared_error',rsquared])

model.summary()


# train the model

history = model.fit(x,y, validation_split=0.2, epochs=2000, batch_size=32, shuffle=True);
```

APPENDIX E

Simulink FPGA programming

E.1   Simulink FPGA neural network model

This section presents images of the Simulink model constructed to perform neural network-based end-to-end data reduction of raw LAS signals for measured temperature and CO mole fraction as described in Chapter 6. Relevant weights and biases are imported into MATLAB/Simulink from the Python environment in which they are generated during model training. The following model is used to generate HDL code which is transferred into Xilinx Vivado to create the FPGA bitstream.
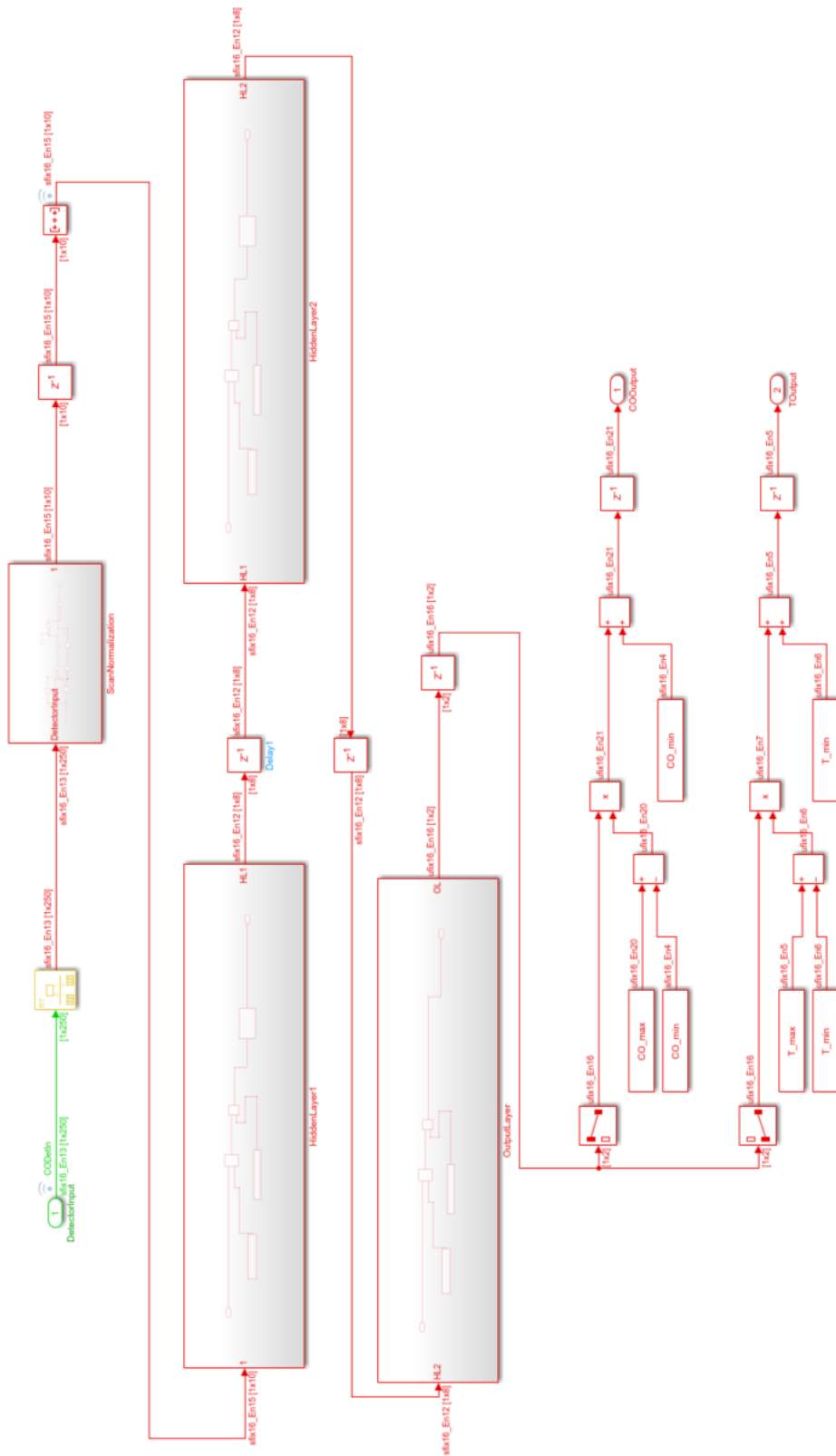
Figure E.1: Simulink model for HDL code generation for the neural network-based data reduction implemented on the Xilinx FPGA. Green signal paths correspond to a 10 kHz data rate and red paths correspond to 10 MHz data rate.
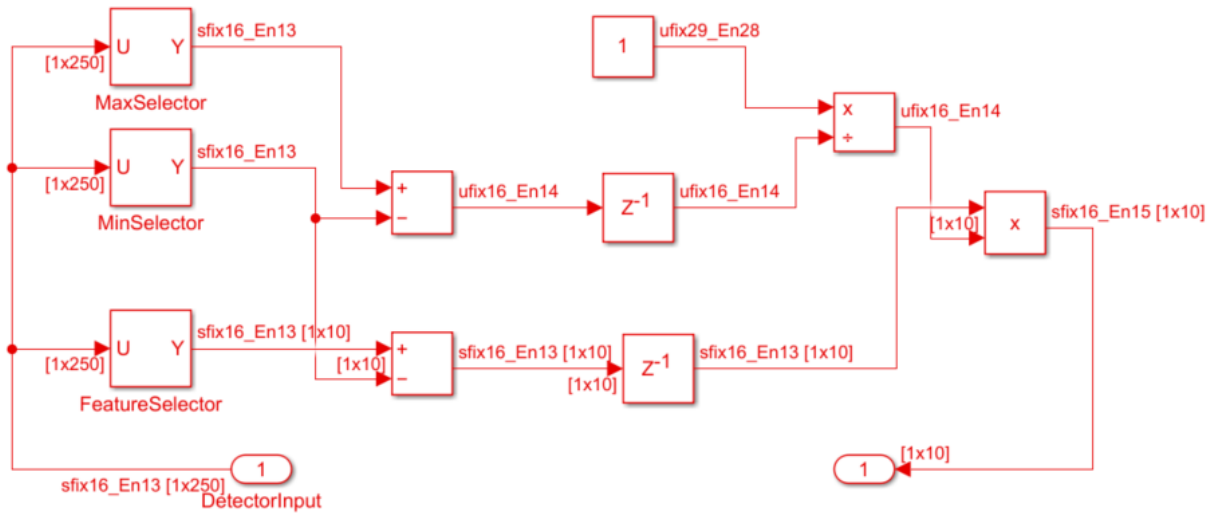
Figure E.2: "Scan normalization" Simulink model within the neural network-based Simulink model in Fig E.1.
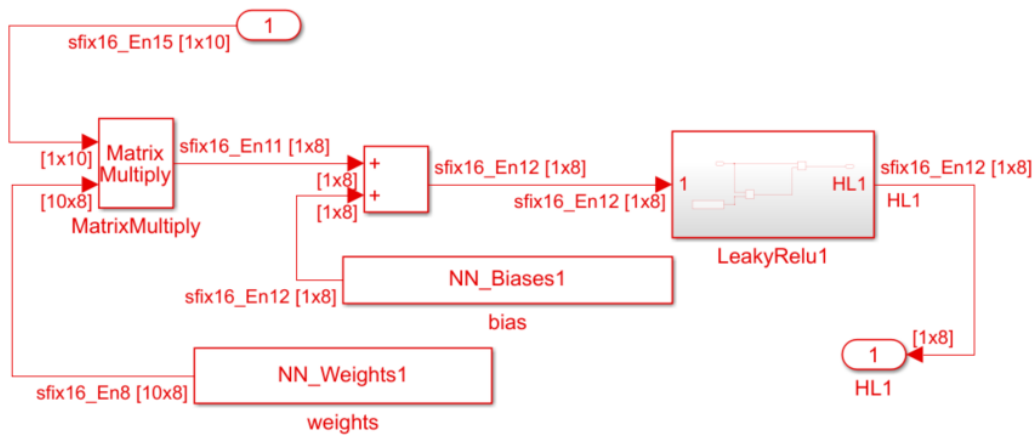
Figure E.3: "Hidden layer" Simulink model within the neural network-based Simulink model in Fig E.1.
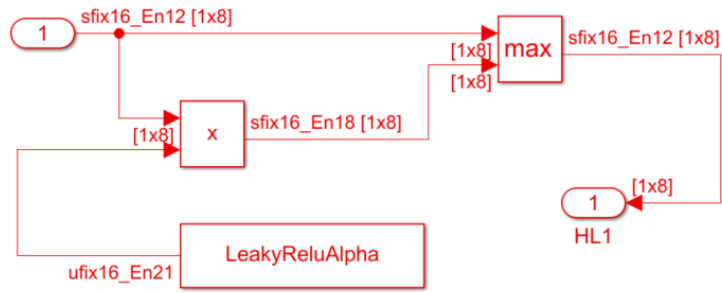
Figure E.4: "Leaky ReLU" Simulink model within the neural network-based Simulink model in Fig E.1.

APPENDIX F

Electro-hydraulic valvetrain design

F.1 Hydraulic pistons

Figure F.1: Manufacturer drawing of the MackCorp hydraulic piston. Detail includes inner hydraulic fluid flow paths.

SHORT STROKE HYDRAULIC CYLINDERS - HI-ENERGY® SERIES 125-LS-ET-PM

Double Acting-Double Ended Thru Threaded Pistons-End Trepan Ported-Pocket Mounted™
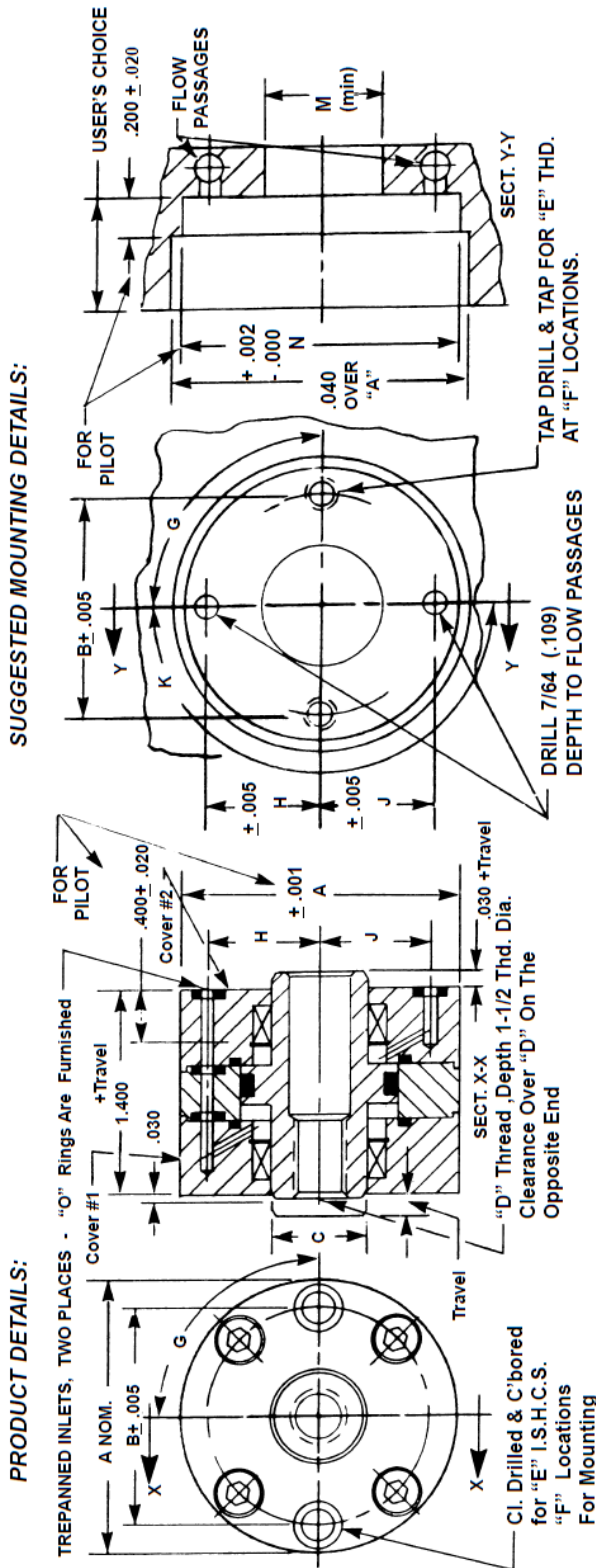
PRODUCT DETAILS:

SUGGESTED MOUNTING DETAILS:

BASIC PART NO.	O.D. A	BOLT CIRCLE B	ROD DIA. C	ROD THD. D	MTNG. SCREWS E	NO. F	DEG. G	OFF SET H	OFF SET J	DEG. K	WR. FLATS L	CL. HOLE M	PILOT N	PISTON DIA. (IN.)	NET PISTON AREA (SQ.IN.)
S6133-(-)-LS	1.500	1.142	0.438	5/16-24	8-32	2	90	0.582	0.582	180	0.375	0.469	1.503	0.738	0.277
S6134-(-)-LS	1.625	1.260	0.500	5/16-24	8-32	2	90	0.644	0.644	180	0.375	0.531	1.628	0.863	0.389
S6135-(-)-LS	1.750	1.358	0.563	5/16-24	10-32	2	90	0.690	0.690	180	0.438	0.594	1.753	0.925	0.423
S6136-(-)-LS	1.875	1.457	0.625	3/8-24	10-32	2	90	0.738	0.738	180	0.500	0.656	1.878	0.993	0.467
S6137-(-)-LS	2.000	1.575	0.688	3/8-24	10-32	2	90	0.800	0.800	180	0.500	0.719	2.003	1.118	0.610
S6138-(-)-LS	2.125	1.713	0.750	1/2-20	10-32	2	90	0.863	0.863	180	0.625	0.781	2.128	1.243	0.772
S6139-(-)-LS	2.250	1.831	0.813	1/2-20	10-32	3	60	0.925	0.925	120	0.625	0.844	2.253	1.368	0.951
S6140-(-)-LS	2.375	1.949	0.875	1/2-20	10-32	3	60	0.988	0.988	120	0.688	0.906	2.378	1.493	1.150
S6141-(-)-LS	2.500	2.067	1.000	5/8-18	10-32	3	60	1.050	1.050	120	0.750	1.031	2.503	1.600	1.226

Nom. Force (lbs) = Pressure (psi) times Area (sq.in.)

TREPANNED INLETS, TWO PLACES - "O" Rings Are Furnished

Cover #1
Cover #2

FOR PILOT

.400 + .020

1.400

.030

SECT. X-X

"D" Thread , Depth 1-1/2 Thd. Dia. Clearance Over "D" On The Opposite End

.030 +Travel

Cl. Drilled & C'bored for "E" I.S.H.C.S. "F" Locations For Mounting

Travel

USER'S CHOICE
.200 ± .020

FLOW PASSAGES

M (min)

SECT. Y-Y

+ .002 / - .000
N

.040 OVER "A"

FOR PILOT

TAP DRILL & TAP FOR "E" THD. AT "F" LOCATIONS.

DRILL 7/64 (.109) DEPTH TO FLOW PASSAGES

F.2 Hydraulic valve actuation design

The engine valves are connected to the hydraulic pistons through a custom machined alu-
minum adapter and threaded rod, visible in Figs. 7.2 and F.3. The valve mounting adapters
act as a three-piece locking collar around the top of the engine valve, which is normally used
to secure the valve spring and valve spring retainer. The top section of the valve mounting
adapter as a female thread matching the female thread on the inside of the hydraulic piston.
A threaded aluminum rod runs from the valve adapter through the entirety of the hydraulic
actuator, as seen in Fig. F.2. The top of the aluminum rod is machined flat and polished to
provide a reflective surface for the optical displacement sensors to read the hydraulic piston
and engine valve position (i.e., lift).
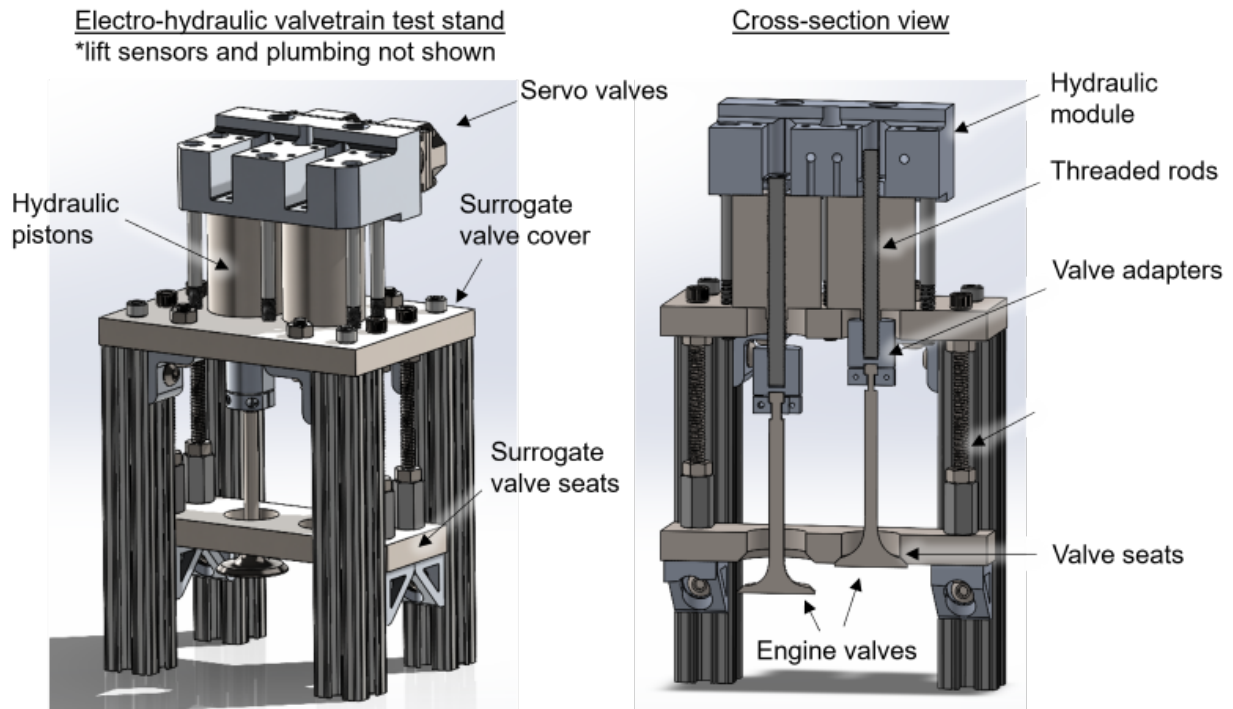
Figure F.2: CAD rendering of electro-hydraulic valvetrain test stand.

Figure F.3: Image of engine valves and adapters installed on the valvetrain test stand.
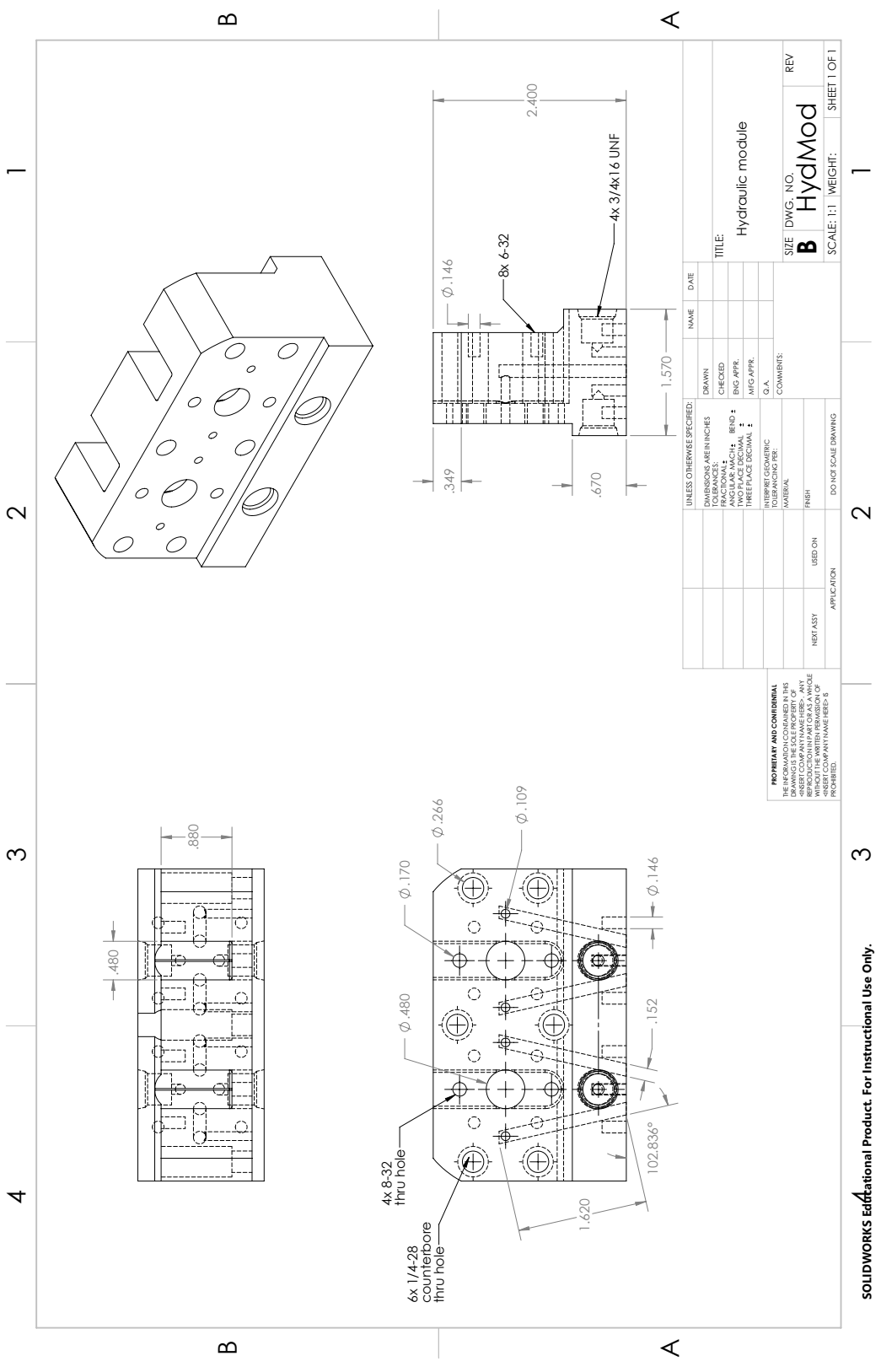
Figure F.4: Engineering drawing of the hydraulic module to interface hydraulic pistons, servo valves, and displacement sensors.
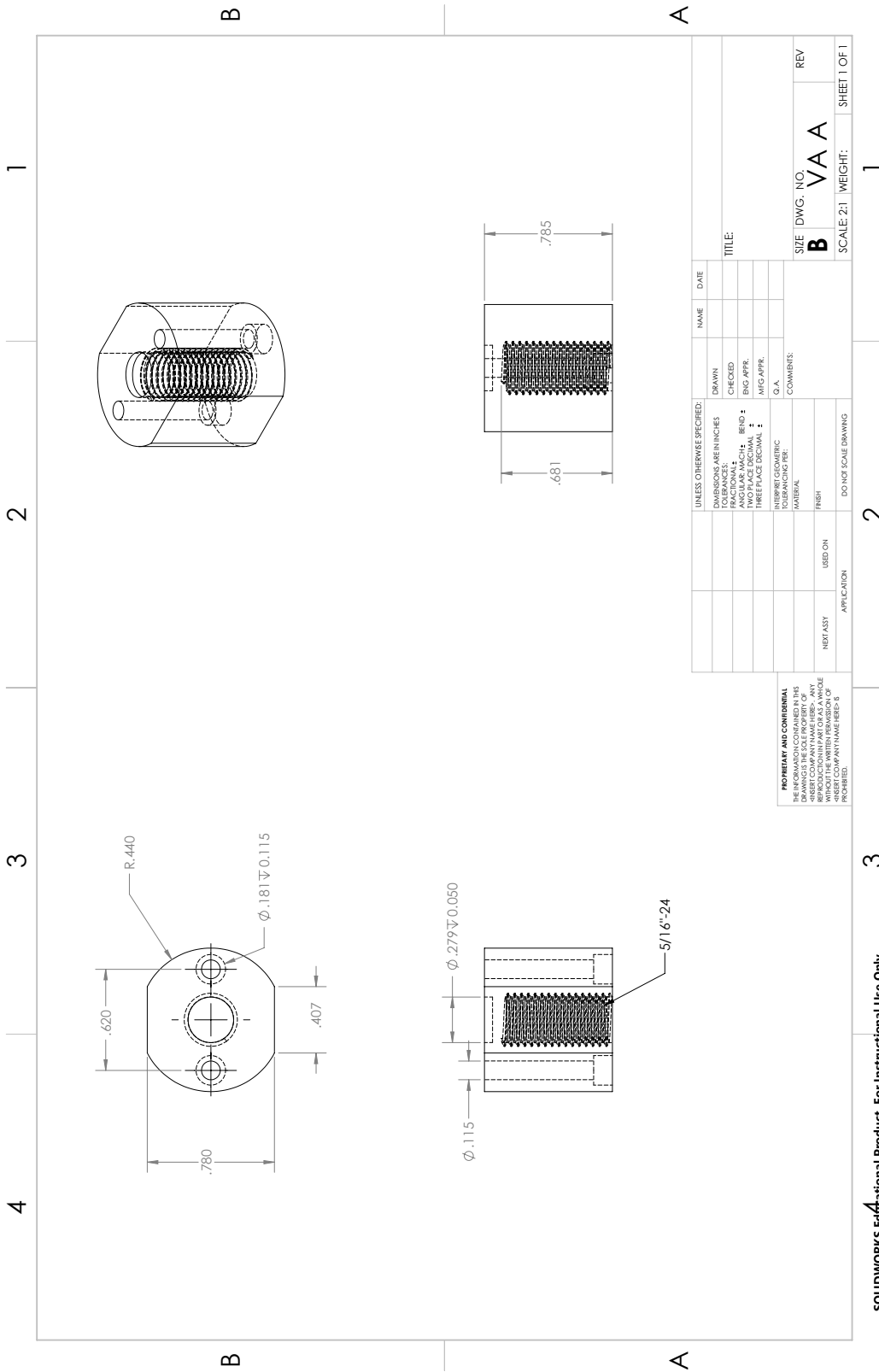
Figure F.5: Top component of the custom adapter assembly to mount the engine valves to the hydraulic pistons via a 5/16"-24 threaded rod.
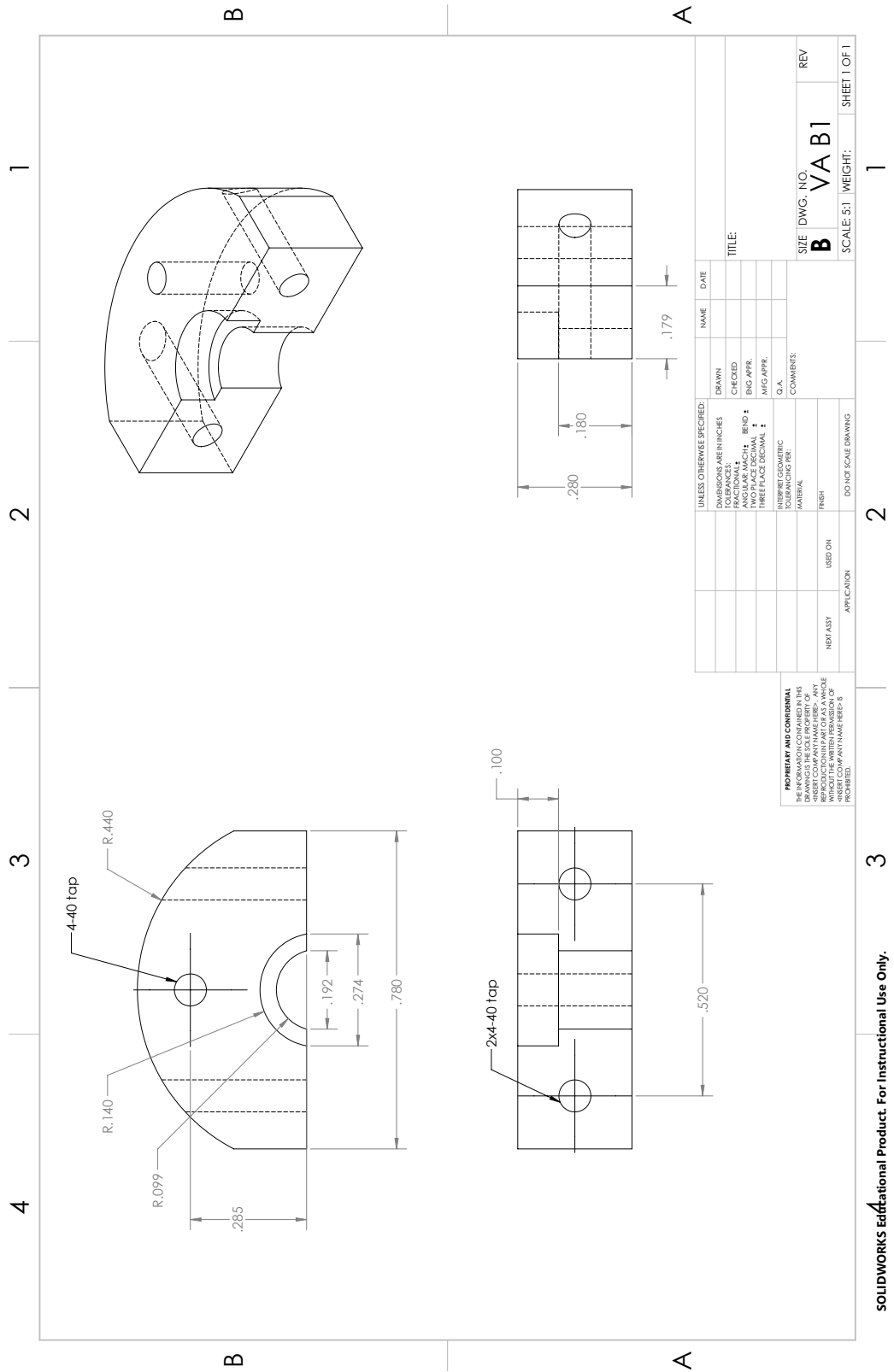
Figure F.6: First of two bottom components of the custom valve adapter assembly.
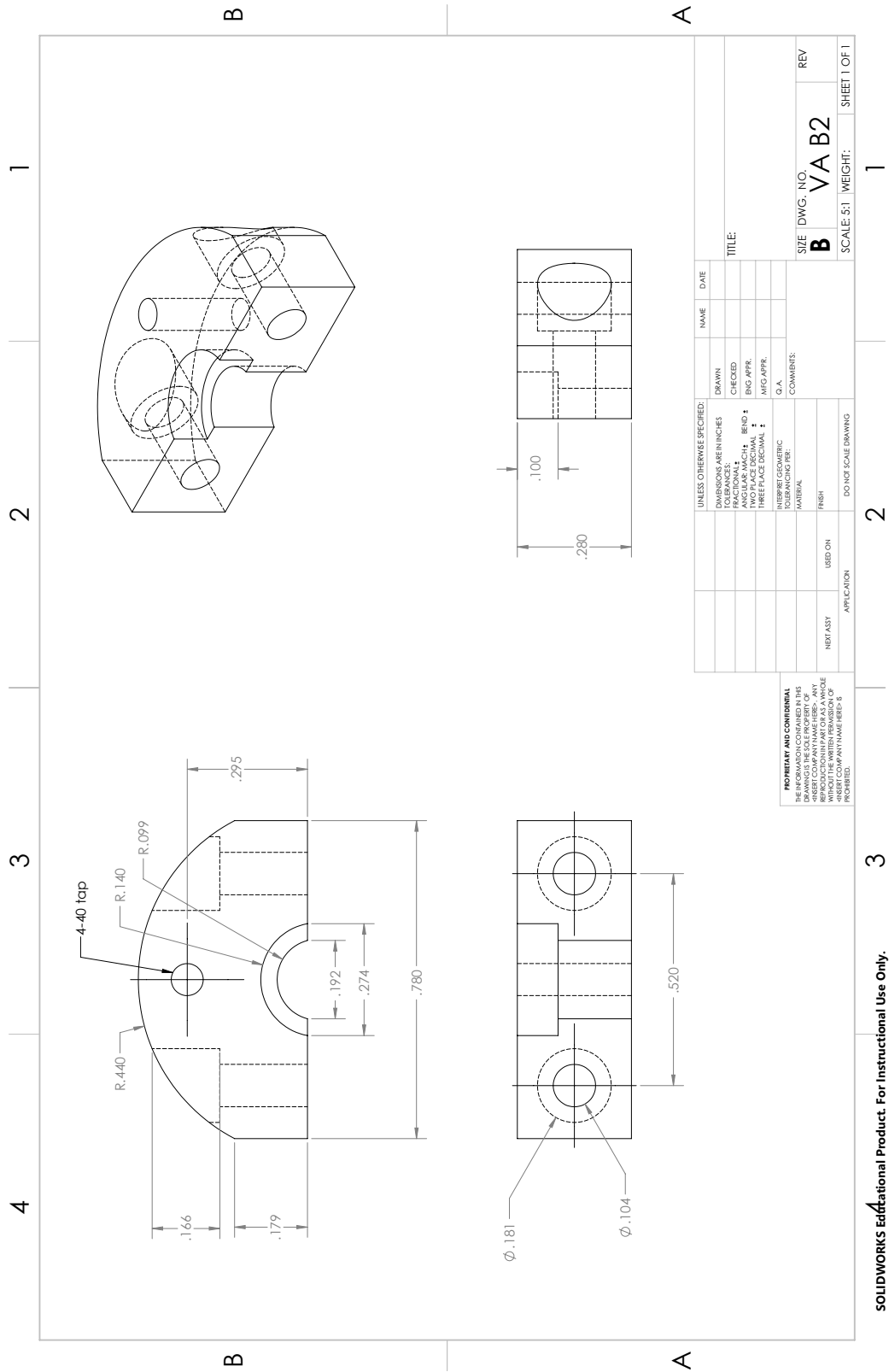
Figure F.7: Second of two bottom components of the custom valve adapter assembly.

F.3 Hydraulic actuation performance considerations

Performance of the hydraulic valve actuation is dependent on fluid flow through the actuators and varies due to fluid pressure and temperature as well as flow and valve dynamics of the electro-hydraulic servo valves. Figures F.8-F.10 depict valve actuation response to some critical operating parameters suring the pulsed command signal operation. Of critical importance is the alignment of the hydraulic piston with the driven engine valves to prevent any wear on the internal piston seals, which cause significant reduction in performance and sensitivity to fluid temperature.
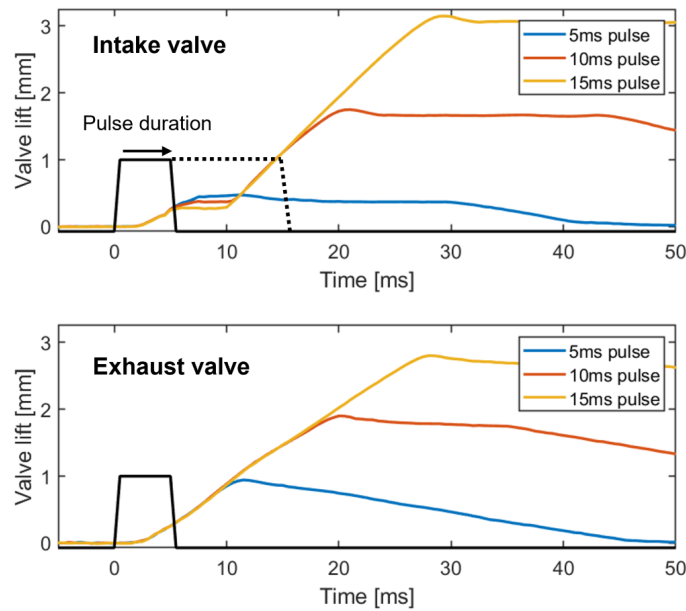
Figure F.8: Effect of servo valve input signal pulse width on valve lift at the maximum signal magnitude of 10 V (transformed into 20 mA current signal) at a supply pressure of 800 psi and return pressure of 150 psi.
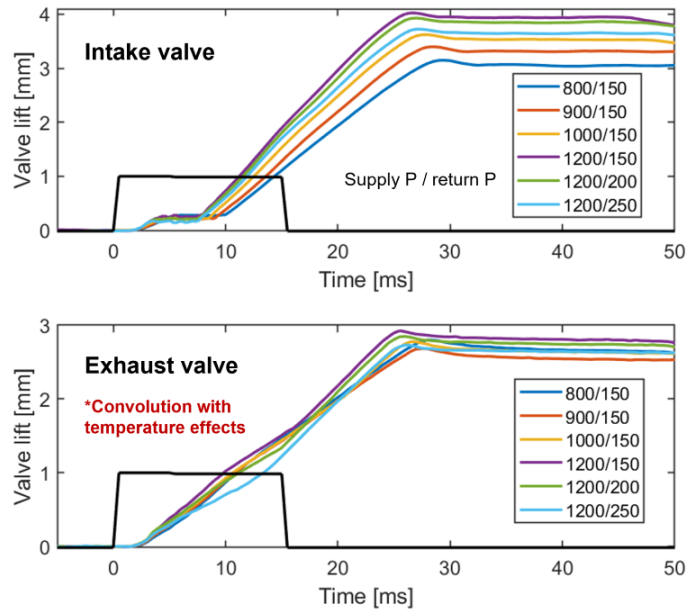
Figure F.9: Effect of hydraulic supply and return pressures on valve lift with a servo valve input signal pulse width of 15 ms and signal magnitude of 10 V.
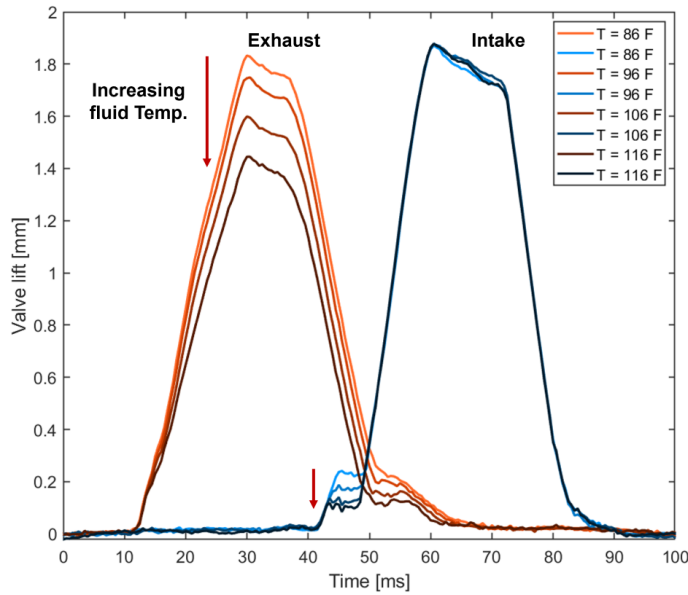
Figure F.10: Effect of hydraulic fluid temperature on valve lift during camless valve actuation representing with lift duration matching original cam profiles at 1,200 rpm on the test engine.

REFERENCES

[1] "Renewables 2018: Analysis and forecasts to 2023," tech. rep., International Energy Agency, 2018.

[2] "Renewable Energy Market Update - June 2023," tech. rep., International Energy Agency, 2023.

[3] D. F. Birol, "World Energy Outlook 2022,"

[4] R. Bowers, E. Fasching, and K. Antonio, "As solar capacity grows, duck curves are getting deeper in California," *Today in Energy - U.S. Energy Information Administration*, 2023.

[5] S. A. Shield, S. M. Quiring, J. V. Pino, and K. Buckstaff, "Major impacts of weather events on the electrical power delivery system in the United States," *Energy*, vol. 218, p. 119434, Mar. 2021.

[6] "Supercapacitors vs. Batteries," 2019.

[7] S. Fallah, *Electric and Hybrid Vehicles - Technologies, Modeling and Control: A Mechatronic Approach.* Apr. 2014.

[8] G. Pirker and A. Wimmer, "Sustainable power generation with large gas engines," *Energy Conversion and Management*, vol. 149, pp. 1048–1065, Oct. 2017.

[9] J. Miller, M. Smooke, R. Green, and R. Kee, "Kinetic Modeling of the Oxidation of Ammonia in Flames," *Combustion Science and Technology*, vol. 34, pp. 149–176, Oct. 1983. Publisher: Taylor & Francis Group.

[10] H. Kobayashi, A. Hayakawa, K. D. A. Somarathne, and E. E. C. Okafor, "Science and technology of ammonia combustion," *Proceedings of the Combustion Institute*, vol. 37, no. 1, pp. 109–133, 2019. Publisher: Elsevier Inc.

[11] I. Gordon, L. Rothman, R. Hargreaves, R. Hashemi, E. Karlovets, F. Skinner, E. Conway, C. Hill, R. Kochanov, Y. Tan, P. Wcisło, A. Finenko, K. Nelson, P. Bernath, M. Birk, V. Boudon, A. Campargue, K. Chance, A. Coustenis, B. Drouin, J. Flaud, R. Gamache, J. Hodges, D. Jacquemart, E. Mlawer, A. Nikitin, V. Perevalov, M. Rotger, J. Tennyson, G. Toon, H. Tran, V. Tyuterev, E. Adkins, A. Baker, A. Barbe, E. Canè, A. Császár, A. Dudaryonok, O. Egorov, A. Fleisher, H. Fleurbaey, A. Foltynowicz, T. Furtenbacher, J. Harrison, J. Hartmann, V. Horneman, X. Huang, T. Karman, J. Karns, S. Kassi, I. Kleiner, V. Kofman, F. Kwabia–Tchana, N. Lavrentieva, T. Lee, D. Long, A. Lukashevskaya, O. Lyulin, V. Makhnev, W. Matt, S. Massie, M. Melosso, S. Mikhailenko, D. Mondelain, H. Müller, O. Naumenko, A. Perrin, O. Polyansky, E. Raddaoui, P. Raston, Z. Reed, M. Rey, C. Richard,

R. Tóbiás, I. Sadiek, D. Schwenke, E. Starikova, K. Sung, F. Tamassia, S. Tashkun, J. Vander Auwera, I. Vasilenko, A. Vigasin, G. Villanueva, B. Vispoel, G. Wagner, A. Yachmenev, and S. Yurchenko, "The HITRAN2020 molecular spectroscopic database," *Journal of Quantitative Spectroscopy and Radiative Transfer*, vol. 277, p. 107949, 2022. Publisher: Elsevier Ltd.

[12] L. Rothman, I. Gordon, R. Barber, H. Dothe, R. Gamache, A. Goldman, V. Perevalov, S. Tashkun, and J. Tennyson, "HITEMP, the High-Temperature Molecular Spectroscopic Database," *Journal of Quantitative Spectroscopy and Radiative Transfer*, vol. 111, pp. 2139–2150, Oct. 2010.

[13] M. E. Thomas, R. I. Joseph, and W. J. Tropf, "Infrared transmission properties of sapphire, spinel, yttria, and ALON as a function of temperature and frequency," *Applied Optics*, vol. 27, p. 239, Jan. 1988.

[14] *The Crystran Handbook of Infra-Red and Ultra-Violet Optical Materials*. Poole, UK: Crystran Ltd, 2016.

[15] C. S. Goldenstein, V. A. Miller, R. Mitchell Spearrin, and C. L. Strand, "SpectraPlot.com: Integrated spectroscopic modeling of atomic and molecular gases," *Journal of Quantitative Spectroscopy and Radiative Transfer*, vol. 200, pp. 249–257, Oct. 2017. arXiv: 1709.06220 Publisher: Elsevier Ltd ISBN: 00224073.

[16] D. C. Harris, "Durable 3-5 m transmitting infrared window materials," *Infrared Physics and Technology*, vol. 39, no. 4, pp. 185–201, 1998. ISBN: 1350-4495.

[17] Special Metals Corporation, "Inconel Alloy 625," tech. rep., 2013. ISSN: 0921-5093.

[18] I. Gordon, L. Rothman, C. Hill, R. Kochanov, Y. Tan, P. Bernath, M. Birk, V. Boudon, A. Campargue, K. Chance, B. Drouin, J.-M. Flaud, R. Gamache, J. Hodges, D. Jacquemart, V. Perevalov, A. Perrin, K. Shine, M.-A. Smith, J. Tennyson, G. Toon, H. Tran, V. Tyuterev, A. Barbe, A. Császár, V. Devi, T. Furtenbacher, J. Harrison, J.-M. Hartmann, A. Jolly, T. Johnson, T. Karman, I. Kleiner, A. Kyuberis, J. Loos, O. Lyulin, S. Massie, S. Mikhailenko, N. Moazzen-Ahmadi, H. Müller, O. Naumenko, A. Nikitin, O. Polyansky, M. Rey, M. Rotger, S. Sharpe, K. Sung, E. Starikova, S. Tashkun, J. V. Auwera, G. Wagner, J. Wilzewski, P. Wcisło, S. Yu, E. Zak, and others, "The HITRAN2016 molecular spectroscopic database," *Journal of Quantitative Spectroscopy and Radiative Transfer*, vol. 203, pp. 3–69, Dec. 2017. ISBN: 0022-4073.

[19] K. K. Schwarm, N. Q. Minesi, B. Jeevaretanam, S. Enayati, T.-C. Tsao, and R. M. Spearrin, "Cycle-Resolved Emissions Analysis of Polyfuel Reciprocating Engines via In-Situ Laser Absorption Spectroscopy," in *ASME 2022 ICE Forward Conference*, (Indianapolis, Indiana, USA), p. V001T03A002, American Society of Mechanical Engineers, Oct. 2022.

[20] S. Oh, C. Park, S. Kim, Y. Kim, Y. Choi, and C. Kim, "Natural gas–ammonia dual-fuel combustion in spark-ignited engine with various air–fuel ratios and split ratios of ammonia under part load condition," *Fuel*, vol. 290, p. 120095, Apr. 2021. Publisher: Elsevier Ltd.

[21] A. Mercier, C. Mounaïm-Rousselle, P. Brequigny, J. Bouriot, and C. Dumand, "Improvement of SI engine combustion with ammonia as fuel: Effect of ammonia dissociation prior to combustion," *Fuel Communications*, vol. 11, p. 100058, June 2022.

[22] M. Korpyś and J. Wójcik, "Methods for sweetening natural and shale gas,"

[23] U. Nations, "Paris Agreement," in *UN Climate Change Conference (COP21)*, 2015.

[24] W. F. Lamb, T. Wiedmann, J. Pongratz, R. Andrew, M. Crippa, J. G. J. Olivier, D. Wiedenhofer, G. Mattioli, A. A. Khourdajie, J. House, S. Pachauri, M. Figueroa, Y. Saheb, R. Slade, K. Hubacek, L. Sun, S. K. Ribeiro, S. Khennas, S. d. l. R. d. Can, L. Chapungu, S. J. Davis, I. Bashmakov, H. Dai, S. Dhakal, X. Tan, Y. Geng, B. Gu, and J. Minx, "A review of trends and drivers of greenhouse gas emissions by sector from 1990 to 2018," *Environmental Research Letters*, vol. 16, p. 073005, June 2021.

[25] "California State Energy Profile," tech. rep., U.S. Energy Information Agency, 2023.

[26] C. Huang, Q. Hu, L. Sang, D. D. Lucas, R. Wong, B. Wang, W. Hong, M. Yao, and V. Donde, "A Review of Public Safety Power Shutoffs (PSPS) for Wildfire Mitigation: Policies, Practices, Models and Data Sources," *Policy and Regulation IEEE Transactions on Energy Markets*, pp. 1–10, 2023.

[27] P. Cicilio, D. Glennon, A. Mate, A. Barnes, V. Chalishazar, E. Cotilla-Sanchez, B. Vaagensmith, J. Gentle, C. Rieger, R. Wies, and M. H. Kapourchali, "Resilience in an Evolving Electrical Grid," *Energies*, vol. 14, p. 694, Jan. 2021.

[28] H. Chehrmonavari, A. Kakaee, S. E. Hosseini, U. Desideri, G. Tsatsaronis, G. Floerchinger, R. Braun, and A. Paykani, "Hybridizing solid oxide fuel cells with internal combustion engines for power and propulsion systems: A review," *Renewable and Sustainable Energy Reviews*, vol. 171, p. 112982, Jan. 2023.

[29] J. Figgener, P. Stenzel, K.-P. Kairies, J. Linßen, D. Haberschusz, O. Wessels, G. Angenendt, M. Robinius, D. Stolten, and D. U. Sauer, "The development of stationary battery storage systems in Germany – A market review," *Journal of Energy Storage*, vol. 29, p. 101153, June 2020.

[30] B. Faessler, "Stationary, Second Use Battery Energy Storage Systems and Their Applications: A Research Review," *Energies*, vol. 14, p. 2335, Jan. 2021.

[31] M. Tawalbeh, S. Z. M. Murtaza, A. Al-Othman, A. H. Alami, K. Singh, and A. G. Olabi, "Ammonia: A versatile candidate for the use in energy storage systems," *Renewable Energy*, vol. 194, pp. 955–977, July 2022.

[32] V. Cigolotti, M. Genovese, and P. Fragiacomo, "Comprehensive Review on Fuel Cell Technology for Stationary Applications as Sustainable and Efficient Poly-Generation Energy Systems," *Energies*, vol. 14, p. 4963, Aug. 2021.

[33] T. Korakianitis, A. Namasivayam, and R. Crookes, "Natural-gas fueled spark-ignition (SI) and compression-ignition (CI) engine performance and emissions," *Progress in Energy and Combustion Science*, vol. 37, pp. 89–112, Feb. 2011.

[34] G. Chala, A. Abd Aziz, and F. Hagos, "Natural Gas Engine Technologies: Challenges and Energy Sustainability Issue," *Energies*, vol. 11, p. 2934, Oct. 2018.

[35] Y. H. Teoh, H. G. How, T. D. Le, H. T. Nguyen, D. L. Loo, T. Rashid, and F. Sher, "A review on production and implementation of hydrogen as a green fuel in internal combustion engines," *Fuel*, vol. 333, p. 126525, Feb. 2023.

[36] J. Wang, Z. Huang, Y. Fang, B. Liu, K. Zeng, H. Miao, and D. Jiang, "Combustion behaviors of a direct-injection engine operating on various fractions of natural gas–hydrogen blends," *International Journal of Hydrogen Energy*, vol. 32, pp. 3555–3564, Oct. 2007.

[37] J. Gao, X. Wang, P. Song, G. Tian, and C. Ma, "Review of the backfire occurrences and control strategies for port hydrogen injection internal combustion engines," *Fuel*, vol. 307, p. 121553, Jan. 2022.

[38] J. S. Cardoso, V. Silva, R. C. Rocha, M. J. Hall, M. Costa, and D. Eusébio, "Ammonia as an energy vector: Current and future prospects for low-carbon fuel applications in internal combustion engines," *Journal of Cleaner Production*, vol. 296, p. 126562, May 2021.

[39] S. Oh, C. Park, J. Oh, S. Kim, Y. Kim, Y. Choi, and C. Kim, "Combustion, emissions, and performance of natural gas–ammonia dual-fuel spark-ignited engine at full-load condition," *Energy*, vol. 258, p. 124837, Nov. 2022.

[40] Z. Lou and G. Zhu, "Review of Advancement in Variable Valve Actuation of Internal Combustion Engines," *Applied Sciences*, vol. 10, p. 1216, Feb. 2020.

[41] P. Piqueras, J. D. l. Morena, E. J. Sanchis, and R. Pitarch, "Impact of Exhaust Gas Recirculation on Gaseous Emissions of Turbocharged Spark-Ignition Engines," *Applied Sciences*, vol. 10, p. 7634, Jan. 2020.

[42] S. Tripathy and D. K. Srivastava, "Effect of internal exhaust gas recirculation on performance, combustion, and emissions in a PFI camless engine," *Environmental Progress & Sustainable Energy*, vol. 41, no. 5, p. e13849, 2022.

[43] S. Asthana, S. Bansal, S. Jaggi, and N. Kumar, "A Comparative Study of Recent Advancements in the Field of Variable Compression Ratio Engine Technology," pp. 2016–01–0669, Apr. 2016.

[44] G. Xu, M. Jia, Y. Li, Y. Chang, H. Liu, and T. Wang, "Evaluation of variable compression ratio (VCR) and variable valve timing (VVT) strategies in a heavy-duty diesel engine with reactivity controlled compression ignition (RCCI) combustion under a wide load range," *Fuel*, vol. 253, pp. 114–128, Oct. 2019.

[45] T. Li, Y. Gao, J. Wang, and Z. Chen, "The Miller cycle effects on improvement of fuel economy in a highly boosted, high compression ratio, direct-injection gasoline engine: EIVC vs. LIVC," *Energy Conversion and Management*, vol. 79, pp. 59–65, Mar. 2014.

[46] C. Park, S. Lee, C. Kim, and Y. Choi, "A comparative study of lean burn and exhaust gas recirculation in an HCNG-fueled heavy-duty engine," *International Journal of Hydrogen Energy*, vol. 42, pp. 26094–26101, Oct. 2017.

[47] J. Wang, X. Duan, W. Wang, J. Guan, Y. Li, and J. Liu, "Effects of the continuous variable valve lift system and Miller cycle strategy on the performance behavior of the lean-burn natural gas spark ignition engine," *Fuel*, vol. 297, p. 120762, Aug. 2021.

[48] M. Aliramezani, C. R. Koch, and M. Shahbakhti, "Modeling, diagnostics, optimization, and control of internal combustion engines via modern machine learning techniques: A review and future directions," *Progress in Energy and Combustion Science*, vol. 88, p. 100967, Jan. 2022.

[49] D. Liao-McPherson, M. Huang, S. Kim, M. Shimada, K. Butts, and I. Kolmanovsky, "Model predictive emissions control of a diesel engine air-path: Design and experimental evaluation," *International Journal of Robust and Nonlinear Control*, vol. 30, no. 17, pp. 7446–7477, 2020. _eprint: https://onlinelibrary.wiley.com/doi/pdf/10.1002/rnc.5188.

[50] J. S. Souder and J. K. Hedrick, "Adaptive sliding mode control of air–fuel ratio in internal combustion engines," *International Journal of Robust and Nonlinear Control*, vol. 14, no. 6, pp. 525–541, 2004. _eprint: https://onlinelibrary.wiley.com/doi/pdf/10.1002/rnc.901.

[51] J. A. Badra, F. Khaled, M. Tang, Y. Pei, J. Kodavasal, P. Pal, O. Owoyele, C. Fuetterer, B. Mattia, and F. Aamir, "Engine Combustion System Optimization Using Computational Fluid Dynamics and Machine Learning: A Methodological Approach," *Journal of Energy Resources Technology*, vol. 143, Aug. 2020.

[52] L. Zhou, Y. Song, W. Ji, and H. Wei, "Machine learning for combustion," *Energy and AI*, vol. 7, p. 100128, Jan. 2022.

[53] X. Duan, Y. Liu, J. Liu, M.-C. Lai, M. Jansons, G. Guo, S. Zhang, and Q. Tang, "Experimental and numerical investigation of the effects of low-pressure, high-pressure and internal EGR configurations on the performance, combustion and emission characteristics in a hydrogen-enriched heavy-duty lean-burn natural gas SI engine," *Energy Conversion and Management*, vol. 195, pp. 1319–1333, Sept. 2019.

[54] Z. Chen, J. He, H. Chen, L. Geng, and P. Zhang, "Comparative study on the combustion and emissions of dual-fuel common rail engines fueled with diesel/methanol, diesel/ethanol, and diesel/n-butanol," *Fuel*, vol. 304, p. 121360, Nov. 2021.

[55] S. L. Ferreira, A. M. dos Santos, G. R. de Souza, and W. L. Polito, "Analysis of the emissions of volatile organic compounds from the compression ignition engine fueled by diesel–biodiesel blend and diesel oil using gas chromatography," *Energy*, vol. 33, pp. 1801–1806, Dec. 2008.

[56] Q. Fan and L. Li, "Study on first-cycle combustion and emissions during cold start in a TSDI gasoline engine," *Fuel*, vol. 103, pp. 473–479, Jan. 2013.

[57] C. Niklas, S. Bauke, F. Müller, K. Golibrzuch, H. Wackerbarth, and G. Ctistis, "Quantitative measurement of combustion gases in harsh environments using NDIR spectroscopy," *Journal of Sensors and Sensor Systems*, vol. 8, pp. 123–132, Mar. 2019. Publisher: Copernicus GmbH.

[58] J. Yoo, V. Prikhodko, J. E. Parks, A. Perfetto, S. Geckler, and W. P. Partridge, "Fast Spatially Resolved Exhaust Gas Recirculation (EGR) Distribution Measurements in an Internal Combustion Engine Using Absorption Spectroscopy," *Applied Spectroscopy*, vol. 69, pp. 1047–1058, Sept. 2015.

[59] C. Goldenstein, R. Spearrin, J. Jeffries, and R. Hanson, "Infrared laser-absorption sensing for combustion gases," *Progress in Energy and Combustion Science*, vol. 60, pp. 132–176, May 2017. Publisher: Elsevier Ltd.

[60] A. Nair, D. Lee, D. Pineda, J. Kriesel, W. Hargus, J. Bennewitz, S. Danczyk, and R. Spearrin, "MHz laser absorption spectroscopy via diplexed RF modulation for pressure, temperature, and species in rotating detonation rocket flows," *Applied Physics B*, vol. 126, p. 138, Aug. 2020.

[61] O. Diemel, R. Honza, C.-P. Ding, B. Böhm, and S. Wagner, "In situ sensor for cycle-resolved measurement of temperature and mole fractions in IC engine exhaust gases," *Proceedings of the Combustion Institute*, vol. 37, no. 2, pp. 1453–1460, 2019. Publisher: Elsevier Inc.

[62] O. Witzel, A. Klein, C. Meffert, C. Schulz, S. Kaiser, and V. Ebert, "Calibration-free, high-speed, in-cylinder laser absorption sensor for cycle-resolved, absolute H2O measurements in a production IC engine," *Proceedings of the Combustion Institute*, vol. 35, no. 3, pp. 3653–3661, 2015.

[63] S. Clees, D. H. Cha, P. Biswas, V. Boddapati, S. J. Cassady, C. L. Strand, R. K. Hanson, B. French, A. Gilmour, K. C. Hawk, J. M. Stitt, and X. Ferlet, "A laser-absorption sensor for in situ detection of biofuel blend vapor in engine intakes," *Proceedings of the Combustion Institute*, vol. 39, no. 1, pp. 1307–1316, 2023.

[64] X. Zhang, T. Wang, and J. Zhang, "Numerical analysis of flow, mixture formation and combustion in a direct injection natural gas engine," *Fuel*, vol. 259, p. 116268, Jan. 2020.

[65] G. Kosmadakis, D. Rakopoulos, and C. Rakopoulos, "Investigation of nitric oxide emission mechanisms in a SI engine fueled with methane/hydrogen blends using a research CFD code," *International Journal of Hydrogen Energy*, vol. 40, pp. 15088–15104, Nov. 2015.

[66] A. Gharehghani, R. Hosseini, M. Mirsalim, and T. F. Yusaf, "A computational study of operating range extension in a natural gas SI engine with the use of hydrogen," *International Journal of Hydrogen Energy*, vol. 40, pp. 5966–5975, May 2015.

[67] A. A, M. S, S. H, A. M, W. P, P. D, and V.-M. A, "Evolution of ammonia reaction mechanisms and modeling parameters: A review," *Applications in Energy and Combustion Science*, vol. 15, p. 100175, Sept. 2023.

[68] E. C. Okafor, Y. Naito, S. Colson, A. Ichikawa, T. Kudo, A. Hayakawa, and H. Kobayashi, "Experimental and numerical study of the laminar burning velocity of CH4–NH3–air premixed flames," *Combustion and Flame*, vol. 187, pp. 185–198, Jan. 2018.

[69] S. Wiemann, R. Hegner, B. Atakan, C. Schulz, and S. A. Kaiser, "Combined production of power and syngas in an internal combustion engine – Experiments and simulations in SI and HCCI mode," *Fuel*, vol. 215, pp. 40–45, Mar. 2018.

[70] R. Hegner and B. Atakan, "A polygeneration process concept for HCCI-engines – Modeling product gas purification and exergy losses," *International Journal of Hydrogen Energy*, vol. 42, pp. 1287–1297, Jan. 2017.

[71] D. G. Goodwin, H. K. Moffat, and R. L. Speth, "Cantera: An Object-oriented Software Toolkit for Chemical Kinetics, Thermodynamics, and Transport Processes. Version 2.3.0," Jan. 2017.

[72] G. P. Smith, D. M. Golden, M. Frenklach, N. W. Moriarty, B. Eiteneer, M. Goldenberg, C. T. Bowman, R. K. Hanson, S. Song, W. C. Gardiner, V. V. Lissianski, and Z. Qin, "GRI-MECH 3.0," 1999.

[73] Y. Song, L. Marrodán, N. Vin, O. Herbinet, E. Assaf, C. Fittschen, A. Stagni, T. Faravelli, M. U. Alzueta, and F. Battin-Leclerc, "The sensitizing effects of NO2 and NO on methane low temperature oxidation in a jet stirred reactor," *Proceedings of the Combustion Institute*, vol. 37, pp. 667–675, Jan. 2019.

[74] E. Ranzi, A. Frassoldati, A. Stagni, M. Pelucchi, A. Cuoci, and T. Faravelli, "Reduced Kinetic Schemes of Complex Reaction Systems: Fossil and Biomass-Derived Transportation Fuels," *International Journal of Chemical Kinetics*, vol. 46, no. 9, pp. 512–542, 2014.

[75] E. Ranzi, C. Cavallotti, A. Cuoci, A. Frassoldati, M. Pelucchi, and T. Faravelli, "New reaction classes in the kinetic modeling of low temperature oxidation of n-alkanes," *Combustion and Flame*, vol. 162, pp. 1679–1691, May 2015.

[76] G. Bagheri, E. Ranzi, M. Pelucchi, A. Parente, A. Frassoldati, and T. Faravelli, "Comprehensive kinetic study of combustion technologies for low environmental impact: MILD and OXY-fuel combustion of methane," *Combustion and Flame*, vol. 212, pp. 142–155, Feb. 2020.

[77] U. Demir, N. Yilmaz, G. Coskun, and H. S. Soyhan, "Evaluation of zero dimensional codes in simulating IC engines using primary reference fuel," *Applied Thermal Engineering*, vol. 76, pp. 18–24, Feb. 2015.

[78] B. J. McBride, M. J. Zehe, and S. Gordon, "NASA Glenn Coefficients for Calculating Thermodynamic Properties of Individual Species," 2002.

[79] D. J. Gardner, D. R. Reynolds, C. S. Woodward, and C. J. Balos, "Enabling New Flexibility in the SUNDIALS Suite of Nonlinear and Differential/Algebraic Equation Solvers," *ACM Transactions on Mathematical Software*, vol. 48, pp. 31:1–31:24, Sept. 2022.

[80] T. Tsujimura and Y. Suzuki, "Development of a large-sized direct injection hydrogen engine for a stationary power generator," *International Journal of Hydrogen Energy*, vol. 44, pp. 11355–11369, Apr. 2019.

[81] J. Humlíček, "Optimized computation of the voigt and complex probability functions," *Journal of Quantitative Spectroscopy and Radiative Transfer*, vol. 27, pp. 437–444, Apr. 1982.

[82] A. McLean, C. Mitchell, and D. Swanston, "Implementation of an efficient analytical approximation to the Voigt function for photoemission lineshape analysis," *Journal of Electron Spectroscopy and Related Phenomena*, vol. 69, pp. 125–132, Sept. 1994.

[83] K. K. Schwarm, H. Q. Dinh, C. S. Goldenstein, D. I. Pineda, and R. M. Spearrin, "High-pressure and high-temperature gas cell for absorption spectroscopy studies at wavelengths up to 8 μm," *Journal of Quantitative Spectroscopy and Radiative Transfer*, vol. 227, pp. 145–151, Apr. 2019.

[84] R. Hanson, R. Spearrin, and C. Goldenstein, *Spectroscopy and Optical Diagnostics for Gases*. Springer International Publishing, 2016.

[85] G. B. Rieker, X. Liu, H. Li, J. B. Jeffries, and R. K. Hanson, "Measurements of near-IR water vapor absorption at high pressure and temperature," *Applied Physics B*, vol. 87, pp. 169–178, Mar. 2007. ISBN: 0946-2171.

[86] R. M. Spearrin, I. A. Schultz, J. B. Jeffries, and R. K. Hanson, "Laser absorption of nitric oxide for thermometry in high-enthalpy air," *Measurement Science and Technology*, vol. 25, p. 125103, Dec. 2014. ISBN: 0957-0233.

[87] C. Christiansen, T. Stolberg-Rohr, A. Fateev, and S. Clausen, "High temperature and high pressure gas cell for quantitative spectroscopic measurements," *Journal of Quantitative Spectroscopy and Radiative Transfer*, vol. 169, pp. 96–103, 2016. Publisher: Elsevier.

[88] S. T. Melin and S. T. Sanders, "Gas cell based on optical contacting for fundamental spectroscopy studies with initial reference absorption spectrum of H2O vapor at 1723 K and 0.0235 bar," *Journal of Quantitative Spectroscopy and Radiative Transfer*, vol. 180, pp. 184–191, 2016. Publisher: Elsevier.

[89] M. Ghysels, S. Vasilchenko, D. Mondelain, S. Béguier, S. Kassi, and A. Campargue, "Laser absorption spectroscopy of methane at 1000 K near 1.7 m: A validation test of the spectroscopic databases," *Journal of Quantitative Spectroscopy and Radiative Transfer*, vol. 215, pp. 59–70, 2018. Publisher: Elsevier Ltd.

[90] U. P. Oppenheim and U. Even, "Infrared Properties of Sapphire at Elevated Temperatures," *Journal of the Optical Society of America*, vol. 52, p. 1078_1, Sept. 1962.

[91] R. Ritchie, "Fatigue of Brittle Materials," in *Comprehensive Structural Integrity*, pp. 359–388, Elsevier, Jan. 2003.

[92] R. C. Ropp, "Group 17 (H, F, Cl, Br, I) Alkaline Earth Compounds," in *Encyclopedia of the Alkaline Earth Compounds*, vol. 17, pp. 25–104, Elsevier, 2013.

[93] J. M. Hartmann, L. Rosenmann, M. Y. Perrin, and J. Taine, "Accurate calculated tabulations of CO line broadening by H2O, N2, O2, and CO2 in the 200–3000-K temperature range," *Applied Optics*, vol. 27, p. 3063, Aug. 1988.

[94] M. C. Phillips, M. S. Taubman, and J. Kriesel, "Use of external cavity quantum cascade laser compliance voltage in real-time trace gas sensing of multiple chemicals," in *Proceedings of SPIE - The International Society for Optical Engineering* (M. Razeghi, E. Tournié, and G. J. Brown, eds.), p. 93700Z, Feb. 2015. Issue: February 2015 ISSN: 1996756X.

[95] J. M. Kriesel, C. N. Makarem, M. C. Phillips, J. J. Moran, M. L. Coleman, L. E. Christensen, and J. F. Kelly, "Versatile, ultra-low sample volume gas analyzer using a rapid, broad-tuning ECQCL and a hollow fiber gas cell," in *Proceedings of SPIE - The International Society for Optical Engineering* (M. A. Druy, R. A. Crocombe, S. M. Barnett, and L. T. Profeta, eds.), vol. 10210, p. 1021003, May 2017. Issue: May 2017 ISSN: 1996756X.

[96] J. M. Hartmann, C. Boulet, and D. Robert, *Collisional Effects on Molecular Spectra.* Elsevier, 2008.

[97] D. Pieroni, Nguyen-Van-Thanh, C. Brodbeck, C. Claveau, A. Valentin, J. M. Hartmann, T. Gabard, J.-P. Champion, D. Bermejo, and J.-L. Domenech, "Experimental and theoretical study of line mixing in methane spectra. I. The N2-broadened 3 band at room temperature," *The Journal of Chemical Physics*, vol. 110, pp. 7717–7732, Apr. 1999. ISBN: 3316915753.

[98] H. Tran, P. M. Flaud, T. Fouchet, T. Gabard, and J. M. Hartmann, "Model, software and database for line-mixing effects in the 3 and 4 bands of CH4 and tests using laboratory and planetary measurements-II: H2 (and He) broadening and the atmospheres of Jupiter and Saturn," *Journal of Quantitative Spectroscopy and Radiative Transfer*, vol. 101, no. 2, pp. 306–324, 2006.

[99] D. D. Lee, F. A. Bendana, S. A. Schumaker, and R. M. Spearrin, "Wavelength modulation spectroscopy near 5 m for carbon monoxide sensing in a high-pressure kerosene-fueled liquid rocket combustor," *Applied Physics B*, vol. 124, p. 77, May 2018. Publisher: Springer Berlin Heidelberg ISBN: 0123456789.

[100] G. B. Rieker, J. B. Jeffries, and R. K. Hanson, "Measurements of high-pressure CO2 absorption near 2.0 $$m and implications on tunable diode laser sensor design," *Applied Physics B: Lasers and Optics*, vol. 94, no. 1, pp. 51–63, 2009.

[101] U.S. EPA, "Inventory of U. S. GHG Emissions and Sinks," tech. rep., 2022. Issue: EPA 430-R-22-003.

[102] M.-C. Chiong, C. Chong, J.-H. Ng, S. Mashruk, W. Chong, N. Samiran, G. Mong, and A. Valera-Medina, "Advancements of combustion technologies in the ammonia-fuelled engines," *Energy Conversion and Management*, vol. 244, no. April, p. 114460, 2021. Publisher: Elsevier Ltd.

[103] C. Lhuillier, P. Brequigny, F. Contino, and C. Mounaïm-Rousselle, "Experimental study on ammonia/hydrogen/air combustion in spark ignition engine conditions," *Fuel*, vol. 269, no. February, p. 117448, 2020. Publisher: Elsevier.

[104] F. Moreno, M. Muñoz, J. Arroyo, O. Magén, C. Monné, and I. Suelves, "Efficiency and emissions in a vehicle spark ignition engine fueled with hydrogen and methane blends," *International Journal of Hydrogen Energy*, vol. 37, pp. 11495–11503, Aug. 2012.

[105] Z. Lou and G. Zhu, "Review of Advancement in Variable Valve Actuation of Internal Combustion Engines," *Applied Sciences*, vol. 10, p. 1216, Feb. 2020.

[106] L. Spinelle, M. Gerboles, G. Kok, S. Persijn, and T. Sauerwald, "Review of Portable and Low-Cost Sensors for the Ambient Air Monitoring of Benzene and Other Volatile Organic Compounds," *Sensors*, vol. 17, p. 1520, June 2017.

[107] C. Niklas, S. Bauke, F. Müller, K. Golibrzuch, H. Wackerbarth, and G. Ctistis, "Quantitative measurement of combustion gases in harsh environments using NDIR spectroscopy," *Journal of Sensors and Sensor Systems*, vol. 8, no. 1, pp. 123–132, 2019. arXiv: 1810.09239.

[108] H. Cho and B.-Q. He, "Spark ignition natural gas engines—A review," *Energy Conversion and Management*, vol. 48, pp. 608–618, Feb. 2007.

[109] R. Spearrin, C. Goldenstein, I. Schultz, J. Jeffries, and R. Hanson, "Simultaneous sensing of temperature, CO, and CO2 in a scramjet combustor using quantum cascade laser absorption spectroscopy," *Applied Physics B: Lasers and Optics*, vol. 117, pp. 689–698, Nov. 2014.

[110] C. Wei, K. Schwarm, D. Pineda, and R. Spearrin, "Volumetric laser absorption imaging of temperature, CO and CO2 in laminar flames using 3D masked Tikhonov regularization," *Combustion and Flame*, vol. 224, pp. 239–247, Feb. 2021. Publisher: Elsevier Inc.

[111] O. Diemel, J. Pareja, A. Dreizler, and S. Wagner, "An interband cascade laser - based in situ absorption sensor for nitric oxide in combustion exhaust gases," *Applied Physics B*, pp. 1–8, 2017.

[112] R. Hargreaves, I. Gordon, L. Rothman, S. Tashkun, V. Perevalov, A. Lukashevskaya, S. Yurchenko, J. Tennyson, and H. Müller, "Spectroscopic line parameters of NO, NO2, and N2O for the HITEMP database," *Journal of Quantitative Spectroscopy and Radiative Transfer*, vol. 232, no. 2, pp. 35–53, 2019. arXiv: 1904.02636 Publisher: Elsevier Ltd.

[113] C. A. C. C. A. Almodovar, W. W. W.-W. Su, C. L. C. C. L. Strand, and R. K. R. Hanson, "R-branch line intensities and temperature-dependent line broadening and shift

coefficients of the nitric oxide fundamental rovibrational band," *Journal of Quantitative Spectroscopy and Radiative Transfer*, vol. 239, p. 106612, Dec. 2019. Publisher: Elsevier Ltd.

[114] J. White, "Long Optical Paths of Large Aperture," *Journal of the Optical Society of America*, vol. 32, p. 285, May 1942.

[115] P. Hannan, "White cell design considerations," *Optical Engineering*, vol. 28, no. 11, pp. 1180–1184, 1989.

[116] J. Heywood, *Internal Combustion Engine Fundamentals*. McGraw-Hill Education, 2018.

[117] P. Soltic and M. Weilenmann, "NO2/NO emissions of gasoline passenger cars and light-duty trucks with Euro-2 emission standard," *Atmospheric Environment*, vol. 37, no. 37, pp. 5207–5216, 2003.

[118] S. Tripathy, A. Das, and D. Srivastava, "Electro-pneumatic variable valve actuation system for camless engine: Part II-fuel consumption improvement through un-throttled operation," *Energy*, vol. 193, p. 116741, 2020. Publisher: Elsevier Ltd.

[119] C. K. Law, *Combustion Physics*. New York: Cambridge University Press, 2006.

[120] C. Aksu, N. Kawahara, K. Tsuboi, S. Nanba, E. Tomita, and M. Kondo, "Effect of Hydrogen Concentration on Engine Performance, Exhaust Emissions and Operation Range of PREMIER Combustion in a Dual Fuel Gas Engine Using Methane-Hydrogen Mixtures," *SAE Technical Papers*, vol. 2015-Septe, no. September, 2015.

[121] O. Mathieu and E. Petersen, "Experimental and modeling study on the high-temperature oxidation of Ammonia and related NOx chemistry," *Combustion and Flame*, vol. 162, no. 3, pp. 554–570, 2015. Publisher: The Combustion Institute.

[122] J. Otomo, M. Koshi, T. Mitsumori, H. Iwasaki, and K. Yamada, "Chemical kinetic modeling of ammonia oxidation with improved reaction mechanism for ammonia/air and ammonia/hydrogen/air combustion," *International Journal of Hydrogen Energy*, vol. 43, no. 5, pp. 3004–3014, 2018. Publisher: Elsevier Ltd.

[123] N. Kahraman, B. Çeper, S. Akansu, and K. Aydin, "Investigation of combustion characteristics and emissions in a spark-ignition engine fuelled with natural gas-hydrogen blends," *International Journal of Hydrogen Energy*, vol. 34, no. 2, pp. 1026–1034, 2009.

[124] K. K. Schwarm and R. M. Spearrin, "Real-time FPGA-based laser absorption spectroscopy using on-chip machine learning for 10 kHz intra-cycle emissions sensing towards adaptive reciprocating engines," *Applications in Energy and Combustion Science*, vol. 16, p. 100231, Dec. 2023.

[125] K. Fridrichová, L. Drápal, J. Vopařil, and J. Dlugoš, "Overview of the potential and limitations of cylinder deactivation," *Renewable and Sustainable Energy Reviews*, vol. 146, p. 111196, Aug. 2021.

[126] A. Norouzi, H. Heidarifar, M. Shahbakhti, C. R. Koch, and H. Borhan, "Model Predictive Control of Internal Combustion Engines: A Review and Future Directions," *Energies*, vol. 14, p. 6251, Oct. 2021.

[127] A. K. Agarwal, A. P. Singh, and R. K. Maurya, "Evolution, challenges and path forward for low temperature combustion engines," *Progress in Energy and Combustion Science*, vol. 61, pp. 1–56, July 2017.

[128] H. L. Yip, A. Srna, A. C. Y. Yuen, S. Kook, R. A. Taylor, G. H. Yeoh, P. R. Medwell, and Q. N. Chan, "A Review of Hydrogen Direct Injection for Internal Combustion Engines: Towards Carbon-Free Combustion," *Applied Sciences*, vol. 9, p. 4842, Nov. 2019.

[129] J. W. Stiborek, R. J. Tancin, N. J. Kempema, J. J. Szente, M. J. Loos, and C. S. Goldenstein, "A Mid-Infrared Laser Absorption Sensor for Gas Temperature and Carbon Monoxide Mole Fraction Measurements at 15 kHz in Engine-Out Gasoline Vehicle Exhaust," *SAE International Journal of Engines*, vol. 17, no. 1, 2023.

[130] L. Xu, C. Liu, D. Zheng, Z. Cao, and W. Cai, "Digital signal processor-based high-precision on-line Voigt lineshape fitting for direct absorption spectroscopy," *Review of Scientific Instruments*, vol. 85, p. 123108, Dec. 2014.

[131] J. Xia, G. Enemali, R. Zhang, Y. Fu, H. McCann, B. Zhou, and C. Liu, "FPGA-Accelerated Distributed Sensing System for Real-Time Industrial Laser Absorption Spectroscopy Tomography at Kilo-Hertz," *IEEE Transactions on Industrial Informatics*, July 2023. Publisher: Institute of Electrical and Electronics Engineers (IEEE).

[132] X. Guo, F. Zheng, C. Li, X. Yang, N. Li, S. Liu, J. Wei, X. Qiu, and Q. He, "A portable sensor for in-situ measurement of ammonia based on near-infrared laser absorption spectroscopy," *Optics and Lasers in Engineering*, vol. 115, pp. 243–248, Apr. 2019.

[133] L. Xu, R. Xue, Y. Li, H. Zhang, and Z. Cao, "FPGA-Based Real-Time Implementation of Temperature Measurement via Tunable Diode Laser Absorption Spectroscopy," *IEEE Sensors Journal*, vol. 18, pp. 2751–2758, Apr. 2018.

[134] L. Ma, W. Hu, W. Wang, and Y. Wang, "Transfer-learning-based multi-wavelength laser sensor for high fidelity and real-time monitoring of ambient temperature and humidity," *Applied Optics*, vol. 62, p. 5932, Aug. 2023.

[135] J. Goldschmidt, L. Nitzsche, S. Wolf, A. Lambrecht, and J. Wöllenstein, "Rapid Quantitative Analysis of IR Absorption Spectra for Trace Gas Detection by Artificial Neural

Networks Trained with Synthetic Data," *Sensors*, vol. 22, p. 857, Jan. 2022. Number: 3 Publisher: Multidisciplinary Digital Publishing Institute.

[136] A. Winckelmann, S. Nowak, S. Richter, S. Recknagel, J. Riedel, J. Vogl, U. Panne, and C. Abad, "High-Resolution Atomic Absorption Spectrometry Combined With Machine Learning Data Processing for Isotope Amount Ratio Analysis of Lithium," *Analytical Chemistry*, vol. 93, pp. 10022–10030, July 2021.

[137] W. Zhang, R. Zhang, Y. Fu, G. Enemali, J. Si, and C. Liu, "Machine Leaning Based Wavelength Modulation Spectroscopy for Rapid Gas Sensing," *Conference Record - IEEE Instrumentation and Measurement Technology Conference*, vol. 2021-May, pp. 1–5, 2021. Publisher: IEEE ISBN: 9781728195391.

[138] Y. Yi, D. Kun, R. Li, K. Ni, and W. Ren, "Accurate temperature prediction with small absorption spectral data enabled by transfer machine learning," *Optics Express*, vol. 29, p. 40699, Dec. 2021.

[139] L. Tian, J. Sun, J. Chang, J. Xia, Z. Zhang, A. A. Kolomenskii, H. A. Schuessler, and S. Zhang, "Retrieval of gas concentrations in optical spectroscopy with deep learning," vol. 182, p. 109739, Sept. 2021.

[140] R. Novickis, D. J. Justs, K. Ozols, and M. Greitāns, "An Approach of Feed-Forward Neural Network Throughput-Optimized Implementation in FPGA," *Electronics*, vol. 9, p. 2193, Dec. 2020.

[141] A. Sanaullah, C. Yang, Y. Alexeev, K. Yoshii, and M. C. Herbordt, "Real-time data analysis for medical diagnosis using FPGA-accelerated neural networks," *BMC Bioinformatics*, vol. 19, p. 490, Dec. 2018.

[142] R. Ayachi, Y. Said, and A. Ben Abdelali, "Optimizing Neural Networks for Efficient FPGA Implementation: A Survey," *Archives of Computational Methods in Engineering*, vol. 28, pp. 4537–4547, Dec. 2021. Publisher: Springer Science and Business Media B.V.

[143] A. Huang, Z. Cao, C. Wang, J. Wen, F. Lu, and L. Xu, "An FPGA-Based On-Chip Neural Network for TDLAS Tomography in Dynamic Flames," *IEEE Transactions on Instrumentation and Measurement*, vol. 70, pp. 1–11, 2021. Conference Name: IEEE Transactions on Instrumentation and Measurement.

[144] D. Maulud and A. M. Abdulazeez, "A Review on Linear Regression Comprehensive in Machine Learning," *Journal of Applied Science and Technology Trends*, vol. 1, pp. 140–147, Dec. 2020.

[145] I. H. Sarker, "Machine Learning: Algorithms, Real-World Applications and Research Directions," *SN Computer Science*, vol. 2, p. 160, May 2021.

[146] P. Dhal and C. Azad, "A comprehensive survey on feature selection in the various fields of machine learning," *Applied Intelligence*, vol. 52, pp. 4543–4581, Mar. 2022.

[147] D. P. Kingma and J. Ba, "Adam: A Method for Stochastic Optimization," in *International Conference on Learning Representations*, (San Diego, CA), arXiv, 2015. booktitle: International Conference on Learning Representations.

[148] J. Xu, Z. Li, B. Du, M. Zhang, and J. Liu, "Reluplex made more practical: Leaky ReLU," in *2020 IEEE Symposium on Computers and Communications (ISCC)*, pp. 1–7, July 2020. ISSN: 2642-7389.

[149] A. Abba, F. Caponio, A. Geraci, and G. Ripamonti, "Implementation of high efficiency non-linear least-squares in FPGA devices for digital spectroscopy," in *IEEE Nuclear Science Symposuim & Medical Imaging Conference*, pp. 1371–1376, Oct. 2010. ISSN: 1082-3654.

[150] M. Zhou, F. Yan, L. Ma, P. Jiang, Y. Wang, S. Ho, and S. Ho Chung, "Chemical speciation and soot measurements in laminar counterflow diffusion flames of ethylene and ammonia mixtures," *Fuel*, vol. 308, no. September 2021, p. 122003, 2022. Publisher: Elsevier Ltd.

[151] E. F. Nasir and S. T. Sanders, "Laser absorption tomography for ammonia measurement in diesel engine exhaust," *Applied Physics B*, vol. 126, p. 178, Nov. 2020. Publisher: Springer Berlin Heidelberg ISBN: 0123456789.

[152] D. A. DelVescovo, D. A. Splitter, J. P. Szybist, and G. S. Jatana, "Modeling pre-spark heat release and low temperature chemistry of iso-octane in a boosted spark-ignition engine," *Combustion and Flame*, vol. 212, pp. 39–52, Feb. 2020.

[153] Y. Wang, "A Novel Two-Zone Thermodynamic Model for Spark-Ignition Engines Based on an Idealized Thermodynamic Process," *Energies*, vol. 13, p. 3801, Jan. 2020.

[154] T. H. Bergman, A. S. Lavine, F. P. Incropera, and D. P. Dewitt, *Fundamentals of Mass and Heat Transfer*. John Wiley & Sons, Inc., 2011.

[155] P. Moin, *Fundamentals of Engineering Numerical Analysis*. Cambridge University Press, 2010.

[156] M. F. Modest, *Radiative Heat Transfer*. Academic Press, 2013.